Dynamics of Rotation and Magnetism in the Sun's Convection Zone and Tachocline

by

Loren Isaac Matilsky

A.B., Cornell University, 2015

M.S., University of Colorado Boulder, 2018

A thesis submitted to the

Faculty of the Graduate School of the

University of Colorado in partial fulfillment

of the requirements for the degree of

Doctor of Philosophy

Department of Astrophysical and Planetary Sciences

2022

Committee Members:

Juri Toomre, Chair

Bradley W. Hindman

Steven R. Cranmer

Maria D. Kazachenko

Keith Julien

Matilsky, Loren Isaac (Ph.D., Astrophysical and Planetary Sciences)

Dynamics of Rotation and Magnetism in the Sun's Convection Zone and Tachocline

Thesis directed by Prof. Juri Toomre

In this thesis, we assess the theoretical dynamics achieved in the solar interior, with particular focus on the solar tachocline. We use the open-source `Rayleigh` code on parallel supercomputers to simulate 3-D, rotating spherical shells of convection. These shells cover much of the solar convection zone and in the tachocline models, a portion of the underlying radiative interior. This thesis divides solar dynamics into two distinct classes: The hydrodynamic (HD) Sun (which explores convection in the presence of differential rotation) and the magnetohydrodynamic (MHD) Sun (which explores how a self-excited solar dynamo interacts with convection and rotation).

In the HD Sun, we discuss how the Near-Surface Shear Layer (NSSL) might be generated by fast downflow plumes. We also identify a physical mechanism whereby the Sun might establish an internal latitudinal temperature gradient and thus achieve isorotation contours significantly tilted with respect to the rotation axis. In the MHD Sun, we focus on the global magnetism and rotation profiles achieved in self-excited dynamo simulations. We first describe how dynamos in convection-zone-only shells display remarkable bistability: Two distinct magnetic cycles—each reminiscent of observed behavior in the solar cycle—are supported by the convection simultaneously.

Finally, we present an MHD simulation achieving a solid-body-rotating radiative interior and differentially rotating convection zone. This shear layer, similar to the solar tachocline, is dynamically maintained by magnetic torques acting against viscous torques. Our work is thus the first to identify a "magnetic tachocline confinement scenario" operating in a fully 3-D, nonlinear global simulation. Furthermore, the magnetism is produced by dynamo action, even below the region of convective overshoot. Rather than the classical "abyssal deep"—i.e., a largely motion-free reservoir that accumulates magnetism pumped in from above—we argue that the Sun's radiative interior may contain inertial oscillations that couple to the dynamo.

Dedication

To my mother, who taught me that work meant dedication and perseverance.

To my father, who taught me that work meant force times distance.

Acknowledgements

First and foremost, I thank my thesis advisor Juri Toomre for his unwavering support of my research and career goals, as well as his mature scientific perspective, which shaped the content and structure of this thesis. Working with Juri gave me the opportunity to attack big-ticket items in solar-physics research (e.g., the magnetic tachocline) that I might not have been exposed to otherwise. I also owe thanks for the Epicurean dinners, desserts, and classroom snacks created by Juri and his wife Linda, as well as the constant supply of Costco biscotti and dried mango in LCD.

Bradley Hindman really served as my "co-advisor" during this thesis (although he has informed me that there is no such thing). As the second author of the majority of my publications to date, he has always provided invaluable guidance, support, and a common-sense approach to science that has made my writing, figures, and theoretical ideas much clearer. His no-nonsense, extremely thorough, red editing pen has torn apart most the pages that follow and allowed me to put them back together in a substantially improved state.

A wide range of scientific colloborators and acquaintances have informed my research over the last few years. At the risk of invariably neglecting someone, I thank: Connor Bice, Nicholas Featherstone, Catherine Blume, Mark Miesch, Sacha Brun, Kyle Augustson, Antoine Strugarek, Keith Julien, Ryan Orvedahl, Rachel Howe, Axel Brandenburg, Steven Tobias, Gustavo Guerrero, Benjamin Brown, Nicholas Brummell, and Pascale Garaud. I also thank the members of my thesis committee: Juri Toomre, Bradley Hindman, Maria Kazachenko, Keith Julien, and Steven Cranmer.

I owe a special thanks to Gwen Dickinson, who made all things in the "Toomre lab" run smoothly while following the complex rules designed by NASA, JILA, and the University of Col-

orado. She also read my proposals and papers, taught me interesting and unfamiliar grammar rules, and was a lovely office-neighbor to chat with. I thank JILA's expert administrative staff (Agnieszka Lynch, Cindy Torres, Kim Monteleone, and Beth Kroger) and technical staff (Jim Mckown and J.R. Raith). I also thank the graduate program assistant of the Astrophysical and Planetary Sciences Department (Michelle Hamernik, followed by Troy Latta) for their immense help in navigating the buraucracy of the Graduate School.

This thesis would not have been possible without the support of my family and friends. My mother Ruth, father Terry, siblings Matt, Athena, Jake, and Sara, and siblings-in-law Jeff, Page, and Michelle, have all fielded many phone calls from a stressed-out grad student over the years, and have always responded with sage wisdom and never exasperation :) For teaching me the importance of hide-and-seek, watching movies, and running around outside, I thank my adorable nieces and nephews: Ben, Jem, Eliza, Ivy, Kai, Wilder, and Michael.

To my many roommates over the years, thank you for keeping the kitchen clean (sometimes), the trash empty (sometimes), and the rent low (always). I owe a special thanks to Mario Castaneda, my house-mate of now almost four years, who suffered me in the best and worst of times, always got me into the mountains, and taught me that running long distances in inhospitable environments isn't always miserable, as long as there's a good view. Our cute apartment on Lee Hill Drive and extremely thorough approach to recycling kept me sane during the first two years (so far, unfortunately) of the Covid-19 pandemic. Finally, I thank Rocky Mountain Runners (RMR) for giving me the inspiration to wake up at 5 a.m. in the bitter cold on Wednesdays, for making me run up Green Mountain on Mondays, and for rescuing me from my computer to adventure outside around the Great American West. The subset of RMR known only as "Group" via WhatsApp (you know who you are) were some of the best friends anyone has ever had. Thanks for the stethoscope; after seven years working on my doctorate, I finally feel like a doctor!

I was supported directly during this work by the Future Investigators in NASA Earth and Space Sciences Technology (FINESST) award 80NSSC19K1428, by a George Ellery Hale Graduate Fellowship, and by a University of Colorado Boulder Chancellor Fellowship. This research

was additionally supported by the NASA grants NNX13AG18G, NNX17AG22G, 80NSSC18K1127, 80NSSC17K0008, 80NSSC18K1125, 80NSSC19K0267, NNX16AC92G, and NNX14AC05G. Computational resources were provided by the NASA High-End Computing (HEC) Program through the NASA Advanced Supercomputing (NAS) Division at Ames Research Center. The `Rayleigh` code is hosted by and receives support from the Computational Infrastructure for Geodynamics (CIG), which is supported by the National Science Foundation awards NSF-0949446 and NSF-1550901.

Contents

Chapter

Tables

Table

Figures

Figure

Chapter 1

Brief Introduction to the Global Solar Dynamo

The dynamical origin of the solar magnetic field remains one of the outstanding fundamental problems of stellar astrophysics. The Sun's observed surface magnetism, locally visible at the surface as sunspots and active regions, waxes, wanes, and reverses its polarity sense fairly regularly every $\sim$11 years. This cycling behavior indicates periodic changes in the Sun's global magnetic fields (the magnetism at very large length-scales). The cycling must be caused by regenerative dynamo action—the self-excited production of magnetic energy from kinetic energy—in the interior. Much is still unclear regarding what sets the dynamo's cycle period, the overall amplitudes of individual cycles, and where in the interior the dynamo operates (for recent reviews, see, e.g., Hathaway 2015; Charbonneau 2020).

The solar dynamo, as the source of sunspots and active regions, leads to surface magnetic activity (flares and coronal mass ejections—or "space weather") that profoundly influences life on Earth. Space weather causes satellite damage, power-grid interruptions, and changes to atmospheric chemistry and global climate (e.g., Webb & Howard 2012; National Research Council 2012; Benz 2016; and references therein). One of the central goals of solar physics is thus to provide a complete physical description of the dynamo. A satisfactory theory would reproduce the observed cycling behavior—which is the strongest observational constraint—and predict particularly active cycles and individual space-weather events before they occur.

In this thesis, we focus on the *global* solar dynamo. "Global" here means we investigate the large-scale spatial structure and long-time-scale temporal behavior of the Sun's interior magnetic

fields and fluid flows. We necessarily simplify the physical processes near the photosphere, since these require *local* simulations that are specially designed to treat the 3-D radiation field and complex equation of state in the near-surface layers. "Local" here means a Cartesian box straddling a localized region of the solar near-surface layers, often with sphericity and global-scale flows ignored. We describe local simulations more fully in Section 1.2.1. We discuss certain observations that are fundamentally governed by the near-surface physics, like sunspots and active regions, but only inasmuch as they inform us about the global properties of the Sun.

1.1 Solar Observations

In the past few decades, significant progress has been made in observing the Sun. The advent of space telescopes has provided an unprecedentedly detailed view of solar active regions (e.g., van Driel-Gesztelyi & Green 2015), the chromosphere (e.g., Carlsson et al. 2019), and the solar wind (e.g., Cranmer & Winebarger 2019). Both ground-based and space-based telescopes have also allowed helioseismology—the study of acoustic wave-modes as they appear at the solar surface—to precisely map interior solar thermodynamic structure and differential rotation. The differential rotation plays a key role in the dynamo through shearing poloidal magnetic field into toroidal field (the "Ω-effect"; e.g., Parker 1955; Rädler 1986; Pipin & Kosovichev 2011). A theoretical dynamo model thus needs to explain not only the observed cycles and polarity reversals, but also the differential rotation.

In this section, we provide a general background to the relevant observational aspects of the global dynamo problem. We focus on the observations that are believed to probe the global structure of the Sun's interior magnetism and differential rotation, and discuss the topics that are directly relevant to the investigations presented in this thesis. These topics are the near-surface shear layer (NSSL) at the top of the convection zone (Chapter 2), the significant tilt of the isorotation contours away from the rotation axis in the bulk of the convection zone (Chapter 3), the cyclic behaviors of the global magnetic field (Chapter 4), and finally, the tachocline of shear at the base of the convection zone (Chapter 5).

1.1.1 Cyclic Behavior in Sunspots and Solar Magnetism

Sunspots are the visual indicators of active regions, which are areas of the solar surface where intense magnetism erupts (Figure 1.1). Typically, sunspots arrive in pairs (bipolar active regions), with each spot forming the foot-point of a magnetic arc. Sunspot pairs appear against a background of tiny granular cells (individual cells about ∼1,000 km across), which are the convective motions at the solar surface known as granulation. Magnetized sunspots appear dark because the magnetic field locally suppresses the convective heat transport in the surrounding fluid and thus the radiative output of the photosphere. Sunspots are not only important as the main "output" of the solar dynamo (which, in turn, affects life on Earth via space weather), but likely also influence the dynamo itself. Their collective areas, field amplitudes, topologies, and lifetimes are quantities measured to high precision with space telescopes and have rich distributions (e.g., van Driel-Gesztelyi & Green 2015 and references therein).

An individual sunspot pair is joined by lines that fall roughly along east–west parallels. The bipolar nature of the pair (in Figure 1.1, opposite-sign line-of-sight magnetic-field components) indicates that sunspots are formed when a largely toroidal magnetic flux rope buoyantly rises to the photosphere. According to Joy's law, these emerging flux ropes are not purely toroidal, but are tilted with respect to the east–west direction. As shown schematically in Figure 1.1, the leading (east-most) sunspot is preferentially closer to the equator than the trailing (west-most) one. The polarity of the leading spot defines the "polarity sense" of the bipolar active region. Positive polarity sense is defined as positive radial magnetic field for the leading spot, and similarly for the negative polarity sense. Note that positive polarity sense means a flux rope with magnetic field lines directed in the negative azimuthal direction.

Figure 1.1 shows snapshots of the line-of-sight (∼radial) magnetic field at the solar surface in Cycles 22 and 23. In any given cycle, sunspot pairs in the North have polarity sense opposite to the pairs in the South. This is known as Hale's polarity law. The tilt angles of individual sunspot pairs are in reality widely distributed about the ∼7°-degree characteristic Joy's-law tilt (e.g., Stenflo &

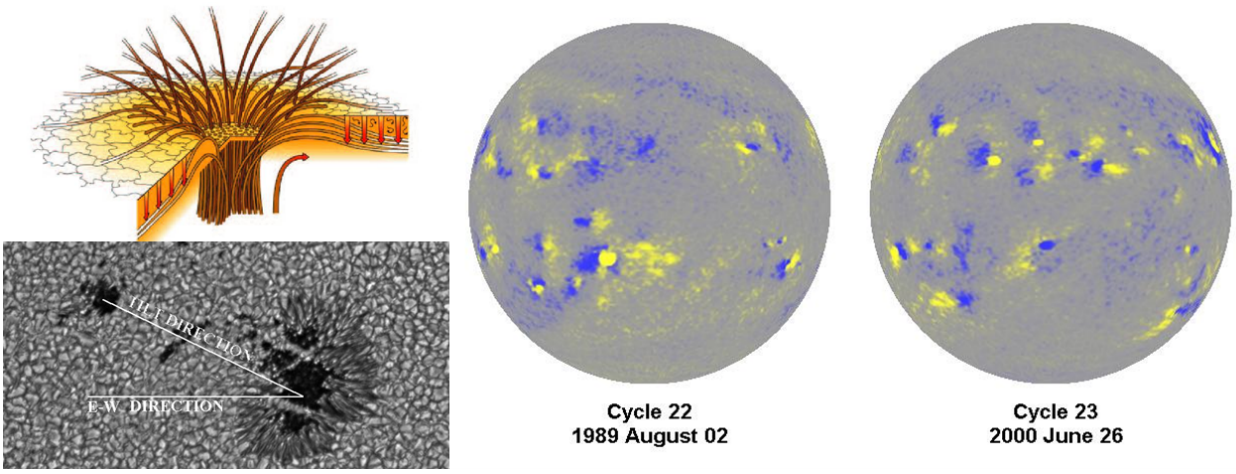

Figure 1.1: **Sunspot Schematic.** (Upper left) Sunspots are formed when magnetic field lines erupt through the photosphere. The arrows show how the magnetism flows out; in the center of the spot (net upflow), the field lines erupt outward, and surrounding the spot (net downflow), the field lines to bend back toward the surface. (Lower left) Sunspot pairs possess a characteristic tilt, known as Joy's law. The line joining two spots (tilt direction) is inclined with respect to east–west parallels. (Right) Line-of-sight magnetic field on the solar disc for two adjacent sunspot cycles. In solar-based spherical coordinates, line-of-sight field is basically radial field near disc-center. These solar-disc "magnetograms" illustrate Hale's polarity law: Sunspot groups have opposite polarity sense in the Northern and Southern Hemispheres and each hemisphere's polarity sense reverses from one cycle to the next. Image credit: David Hathaway, solarcyclescience.com.

Kosovichev 2012; Li 2018) and a non-negligible fraction (∼10%) of bipolar active regions thus have polarity senses opposite to what Hale's polarity law would predict. We discuss some implications of these "anti-Hale" active regions in Chapter 4.

Sunspots vary in number and strength every ∼11 years—a periodicity in surface magnetic energy known as the sunspot cycle. Hale's polarity law, in addition to stating that the opposite hemispheres have on average opposite polarity senses, states that the polarity sense in each hemisphere reverses from one cycle to the next. Because of the polarity reversal, a full Hale polarity cycle, 22-year cycle, or simply, solar cycle, is ∼22 years. Several such solar cycles are shown in Figure 1.2. Sunspots first appear at mid-latitudes, and then at sites (active latitudes) closer to the equator as the cycle progresses, in a pattern of equatorward propagation. This pattern also resembles butterfly wings, so time-latitude plots like Figure 1.2 are called butterfly diagrams. We note that in Figure 1.2, the sunspots themselves are *not* propagating equatorward, just the active latitudes of field emergence.

Sunspots decay slowly into small-scale flux filaments (e.g., McIntosh 1981; Wang et al. 1991; van Driel-Gesztelyi et al. 1999; Hathaway & Choudhary 2008). Opposite-polarity filaments mostly cancel, but some residual flux of a preferred polarity remains due to Joy's law. This residual flux is observed to be transported poleward (Figure 1.2) and is believed to form the seeds of the next cycle in the flux-transport, or Babcock-Leighton, dynamo theories (Babcock, 1961; Leighton, 1969). According to Figure 1.2, the poleward-propagating flux is strongest at cycle minimum. Unlike equatorward "propagation" from the emergent sunspot pattern, poleward propagation likely does represent moving flux, advected by the meridional circulation (e.g., Howe et al. 2013; Petrie 2015; and references therein). After the flux is swept poleward, the meridional circulation (or possibly downward advection by convective plumes) pumps the flux into the tachocline, where it can get sheared by the Ω-effect into the opposite-polarity toroidal field of the next cycle (e.g., Dikpati & Gilman 2009; Karak et al. 2014; Charbonneau 2020; and references therein).

We have reasonably frequent sunspot sketches and counts for the last ∼400 years. These historical sketches, or sunspot numbers, which were standardized after about 1849 by defining

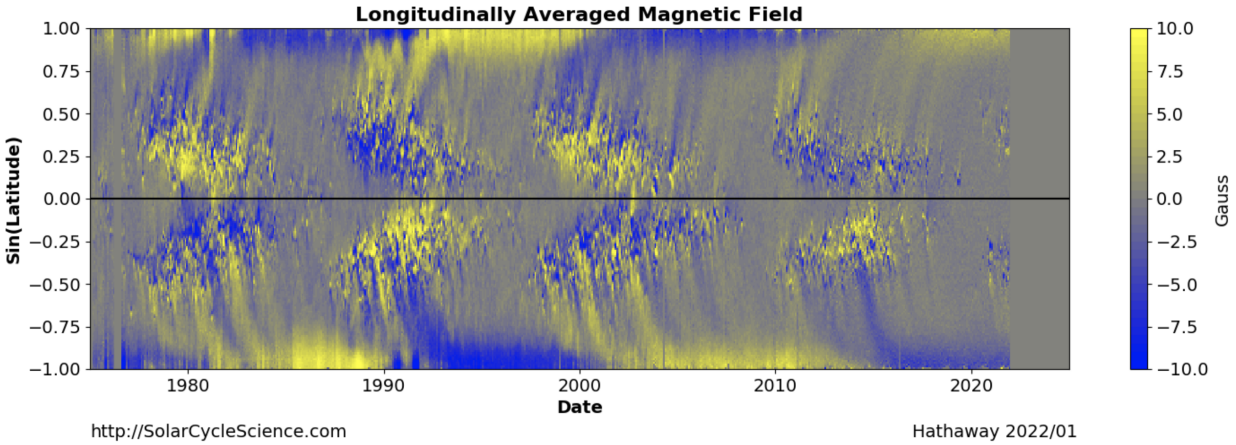

Figure 1.2: **Magnetic Butterfly Diagram.** Photospheric surface line-of-sight (∼radial) magnetic field is shown in time-latitude space. Each temporal pixel set (strip parallel to y-axis) is a longitudinal average of the field over the observed solar disc. Hale's polarity law is clearly visible, as is the migration of the average line-of-sight magnetic field to the equator (the butterfly wings). The polar regions have opposite polarity senses that switch sign from one cycle to the next near the time of solar maximum. The flux at the poles peaks near solar minimum. Image credit: David Hathaway, solarcyclescience.com.

the International Sunspot Number (Wolf, 1861), give a rough proxy of the Sun's magnetic-field strength.[1] For as long as sunspot numbers have been recorded, the ∼11-year periodicity is clearly present (Hathaway, 2015). Other proxies—the abundances of the radioisotopes ^{10}Be and ^{14}C in tree rings and glacial ice cores—yield even rougher magnetic-field activity proxies, but nonetheless clearly show the presence of the primary 11-year sunspot cycle since the beginning of the Holocene period, about 11,700 years ago (e.g., Usoskin 2013 and references therein). The isotope proxies also confirm the presence of the multi-cycle Gleissberg modulation, which has a period of ∼100 years (e.g., Gleissberg 1939; Peristykh 2003). The Gleissberg cycle is clearly a statistically significant feature, but different analyses yield different assessments of its period (e.g., Hathaway et al. 1999; Ogurtsov et al. 2002).

Another important long-term behavior of the solar cycle is the tendency toward "grand minima." These are long intervals when multiple cycles are much weaker than average. The most prominent example is the Maunder Minimum (e.g., Maunder 1890; Eddy 1976), which clearly shows record-low sunspot numbers during an extended period from 1645–1715. The grand minima also show up in the isotope proxies; 27 statistically significant minima have thus been identified during the Holocene period (Usoskin et al., 2007). All in all, the Sun appears to exist in a magnetically quiet state, corresponding to a grand minimum, about one-sixth of the time (Usoskin, 2013).

We also point out the active longitudes observed from the sunspot record, which we discuss at length in Chapter 4. Active longitudes have long been hypothesized to explain a persistent ∼27-day periodicity in the distribution of active regions in longitude and time (e.g., Svalgaard & Wilcox 1975; Bogart 1982; Balthasar & Schussler 1983; Antonucci et al. 1990; Neugebauer et al. 2000; Henney & Harvey 2002; Kitchatinov & Olemskoi 2005; Ivanov 2007). The observed periodicity is near the solar rotation rate and would indicate that there are preferential solar longitudes (longitude measured in a rotating frame) that are more active than average for long intervals. These longitudes may also correspond to increased amplitude in other activity indicators, like solar flares (e.g., Bai

[1] See Hathaway 2015 and references therein for an in-depth discussion of the historical sunspot record and its complicated correlation with the Sun's magnetic field.

& Sturrock 1987; Gyenge et al. 2016). How long active longitudes typically persist is the source of debate, but they may last up to century-long time-scales (e.g., Berdyugina & Usoskin 2003). Interestingly, the active longitudes in each hemisphere may be decoupled, with slightly different periodicities (both near ∼27 days) in the North and South (e.g., Bai 1990). This would suggest that active longitudes may be related to the Sun's hemispheric asymmetry, which we now discuss.

There is a long-observed statistically significant hemispheric asymmetry with respect to most measures of magnetic activity, which we discuss more fully in Chapter 4. The level of asymmetry ("North minus South" over "North plus South") is typically around ∼20% (e.g., Norton & Gallagher 2010). It shows up in almost all activity proxies, including sunspot number, total sunspot area, prominences, chromospheric emission, and flare occurrence (e.g., Newton & Milsom 1955; Roy 1977; Swinson et al. 1986; Chang 2009; Norton et al. 2014; Hathaway 2015; Deng et al. 2016). It is largely non-cyclic, having multiple "periodicities" (peaks in period-space with large widths) ranging between ∼10 and ∼50 years (e.g., Duchlev & Dermendjiev 1996; Ballester et al. 2005; Deng et al. 2016; and references therein). The source of the hemispheric asymmetry is still not well understood, but it is usually thought to arise from the nonlinearity inherent to the dynamo system. This results in coupling between even (equatorially symmetric) and odd (equatorially antisymmetric) dynamo modes (e.g., Kleeorin & Ruzmaikin 1984; Tobias 1997; Hotta & Yokoyama 2010; Weiss & Tobias 2016). This same coupling may lead to long periods of weak dynamo amplitudes reminiscent of grand minima. Additionally, stochastic fluctuations in realizations of the convective flows are thought to lead to "mixed-mode" solutions (typically a dipole eigenmode of the dynamo equations, mixed with a quadrupole eigenmode). There can then be frequency beating between the two modes (e.g., Moss et al. 1992; Charbonneau 2007; Usoskin et al. 2009; Belucz & Dikpati 2013; Passos & Charbonneau 2014; Brun et al. 2015), which recently has been hypothesized to yield hemispheric asymmetry with the observed periodicities (Schüssler & Cameron, 2018).

1.1.2 Helioseismology

Helioseismology is the study of the acoustic wave-modes that are trapped below the photosphere (e.g., Christensen-Dalsgaard 2002; Howe 2009; and references therein). Because the waves travel deep into the solar interior, they can be used to infer the internal structure of the Sun. Helioseismic data consists of two quantities, each spatially resolved across the solar disc: Doppler shifts of the wavelengths of various spectral lines (full-disc "Dopplergrams") and full-disc continuum-intensity maps. The Dopplergrams can be interpreted as the line-of-sight component of the fluid velocity at the photosphere (strictly, at the formation height of the given spectral line).

The velocity and intensity at the solar surface fluctuate on the timescale of $\sim$5 minutes. This was first reported by Leighton et al. (1962) as the "five-minute oscillations." Initially, the five-minute oscillations were thought to be resonant acoustic modes trapped in the solar atmosphere (e.g., Howard 1967; Frazier 1968; Tanenbaum et al. 1969). The conclusion that these waves were not surface phenomena, but rather, global normal modes of the Sun, was first discussed in Ulrich (1970) and Leibacher & Stein (1971). This interpretation was confirmed by Deubner (1975) and Rhodes et al. (1977), who showed that that the wavenumber-frequency power spectrum of the five-minute oscillations was concentrated at discrete temporal frequency (f) "ridges" for a given spherical-harmonic-degree wavenumber (ℓ). This equal spacing in frequency was predicted by the theory of global oscillations (e.g., Cox 1980; Unno et al. 1989; Gough & Kosovichev 1993). The driving mechanism for the five-minute oscillations is believed to be the highly turbulent convection near the photosphere, which in turn is driven by radiative cooling (e.g., Goldreich & Keeley 1977).

Although Deubner (1975); Rhodes et al. (1977) identified clear ridges in wavenumber-frequency space, they could not distinguish between individual normal modes of oscillation. This was first achieved by Claverie et al. (1979), who used Dopplergrams integrated across the whole solar disc to identify the low-degree (i.e., large-wavelength) normal modes. Helioseismology as we know it currently (according to Basu 2016) began when Duvall & Harvey (1983) measured the frequencies of a large number of modes that covered a wide range of horizontal wavenumbers. The frequencies

of several millions of individual modes can be measured and are used to probe the solar interior (e.g., Libbrecht et al. 1990; Thompson et al. 2003).

To precisely determine normal-mode frequencies, the acoustic power spectra must have high resolution in frequency space. This requires helioseismic data to be continuously collected for long time intervals, which can be accomplished either with a space telescope or with ground-based telescopes located at multiple points around the globe.[2] One of the most prominent ground-based observatories is the Global Oscillation Network Group (GONG; Harvey et al. 1996), managed by the National Solar Observatory (NSO). GONG collects solar-disc images at 5-arcsecond diffraction-limited resolution. The original GONG images were 512×512 pixels (corresponding to the telescope's diffraction limit), but are now 1,024×1,024 pixels since detector upgrades in 2001. GONG has continuously observed medium-degree ($\ell \lesssim 300$) acoustic modes since 1995. [3]

Higher-resolution images (composed of higher-quality data because of the absence of atmospheric seeing effects) can be obtained by space telescopes. NASA/ESA's Michelson-Doppler Interferometer (MDI) aboard the Solar and Heliospheric Observatory (SOHO; Domingo et al. 1995) collected 4-arcsecond full-disc images (1,024×1,024 pixels) from 1996–2011. A followup mission, NASA's Heliospheric and Magnetic Imager (MDI) aboard the Solar Dynamics Observatory (SDO; Scherrer et al. 2011) has collected the highest-resolution images (1 arcsecond or 4,096×4,096 pixels) and has been operational since 2011, with the SDO mission itself extended until 2030. GONG and HMI (and in the past, MDI) both collect images with a cadence of ∼1 minute, allowing the precise identification of high-frequency modes.

Global helioseismology refers to the study of the Sun's global (normal) acoustic modes (e.g., Howe 2009; Basu 2016; and references therein). For a given normal mode, properties of solar structure in the regions where the mode has high amplitude perturb the theoretical mode frequency. The measured frequency perturbation thus senses different parts of the Sun. When many frequency

[2] Another way to get continuous observations is to observe from near the South Pole (e.g., Jefferies et al. 1988; Duvall et al. 1993; Braun et al. 1996). This data yielded the first forays into time-distance helioseismology (briefly described below), and also suggested that sunspots are efficient absorbers of acoustic-mode energy.

[3] Converting angular resolution to spatial resolution on the solar disc (ignoring curvature) yields 1 arcsecond ∼ 700 km (about the size of a granule).

perturbations are collected, they can be *inverted* to yield a spatial map of the perturbing quantity in the solar interior. Spherically symmetric solar structure (e.g., hydrostatic stratification, adiabaticity, and temperature) can be obtained precisely from roughly $0.06R_\odot$ to $0.96R_\odot$ via 1-D inversions (e.g., Basu 2016). The spherically *asymmetric* rotation rate (as described below) can be obtained as a function of radius ($\sim 0.5R_\odot$ to $\sim 1R_\odot$) and latitude (equator to $\sim 75°$) via 2-D inversions. There are many unique inversion techniques, each with their own assumptions, which yield slightly different results, errors, and spatial resolution (see examples of 1-D inversions in, e.g., Gough 1985; Däppen et al. 1991; Basu et al. 2009). All inversions are similar, however, in that their spatial resolution in radius becomes much finer as the photosphere is approached from below. This is because the high-degree acoustic modes are trapped in the near-surface layers. There are many more high-degree modes than low-degree ones (decreasing the inversion error) and their radial wavelengths are shorter (making the inversion resolution finer).

The high precision of global inversions ($\sim$1% for solar structure) yielded one of the major triumphs of helioseismology in helping to resolve the solar neutrino problem. This problem can be stated as: "The number of neutrinos coming from reactions in the Sun's thermonuclear core, as measured by the first neutrino detectors, was too small by a factor of $\sim$3 compared to what standard solar models would predict." This discrepancy was first realized by Raymond Davis and John Bahcall in the 1960s. They designed the first neutrino detector, which consisted of a large $\sim$100,000-gallon tank of perchloroethylene (C_2Cl_4; i.e., dry-cleaning fluid) at the Homestake Mine in South Dakota (e.g., Davis 1964; Bahcall 1964; Davis et al. 1968). The tank was installed 4,900 feet underground in an old mineshaft, along with instrumentation to collect and count the radioactive ^{37}Ar atoms produced by the weak reaction, $\nu_e + {}^{37}Cl \rightarrow e^- + {}^{37}Ar$. Sequestering the tank like this shielded it from cosmic rays. See a detailed review of the "Homestake experiment" and its significance in Davis (2003). A solar neutrino would interact with the chlorine about 15 times every month. Note that Homestake was only sensitive to the ^{8}Be neutrinos with energies > 0.81 MeV, which come from the reaction $^8B \rightarrow {}^8Be + e^+ + \nu_e$ in the Sun's thermonuclear core (this reaction takes place on the p–p III branch, which is least dominant of all the p–p branches in the Sun). The

experiment was insensitive to the more fundamental fusion reaction $^1\mathrm{H} + {}^1\mathrm{H} \rightarrow {}^2\mathrm{D} + \mathrm{e}^+ + \nu_\mathrm{e}$ that is the first step in all the p–p branches.

Davis and Bahcall measured a neutrino flux of ∼3 SNU,[4] while the standard solar model at the time predicted ∼20 SNU (Bahcall & Shaviv, 1968). The solar models were refined and the Homestake experiment's measurements improved, but the discrepancy persisted. Final values were 2.56 ± 0.16 (statistical) $\pm$ 0.16 (systematic) SNU measured by Homestake (Cleveland et al., 1998) and solar-model predictions of ∼8 SNU (e.g., Bahcall et al. 2001). Additional neutrino experiments using other techniques were devised over the years, notably an underground tank of water at the Kamioka Mine in Japan (e.g., Suzuki 1995; Koshiba 2003) and an underground tank of gallium in Italy (the GALLEX experiment; e.g., Anselmann et al. 1995. GALLEX measured the first flux from neutrinos produced by the fundamental $^1\mathrm{H} + {}^1\mathrm{H}$ fusion reaction. All these experiments consistently measured significantly fewer neutrinos than predicted by solar models, usually fewer by a factor of ∼3. For their pioneering neutrino measurements, Raymond Davis and Masatoshi Koshiba shared the 2002 Nobel Prize in Physics, along with Riccardo Giacconi for his work in X-ray astronomy.

Nuclear physics predicts a neutrino flux that is highly sensitive to the temperature T_c of the solar core (scaling like T_c^{18} for the ^{8}Be neutrinos measured in the original Homestake experiment). After the initial results from Homestake, there were many attempts to "tweak" various solar models to make the core temperature lower (for a review, see Christensen-Dalsgaard 2021 and references therein). Such attempts involved a range of ideas: A rapidly rotating solar core to reduce the required temperature for hydrostatic balance (e.g., Bartenwerfer 1973; Demarque et al. 1973); substantial mixing of the core to increase the core hydrogen abundance and thus decrease the required T_c for solar energy production (e.g., Bahcall et al. 1968; Ezer & Cameron 1968; Dilke & Gough 1972); and even the presence in the core of the weakly interacting massive particles (WIMPs) invoked to explain dark matter, which could contribute to the solar energy transport and lessen the required radiative temperature gradient (e.g., Steigman et al. 1978; Spergel & Press 1985; Faulkner

[4] A solar neutrino unit (SNU) corresponds to 10^{-36} solar neutrino reactions per second per chlorine nucleus; hence the very large tank!

& Gilliland 1985). To remain consistent with the helioseismically inferred T_c, which was constrained to $\sim$1% precision and agreed well with the standard solar models, most of these tweaked models had to be ruled out (e.g., Elsworth et al. 1990; Dziembowski et al. 1990; Christensen-Dalsgaard 1991). It became increasingly clear that if the solar models were right, and the neutrino experiments were reliable, then the underlying assumptions of particle physics had to be revisited. The resolution, of course, was bequeathing some mass to the neutrino, which would then oscillate between three different types (or flavors) while on transit to Earth (e.g., Haxton et al. 2013). The first detectors had been designed to detect only one of these flavors (the electron-neutrino $\nu_{\rm e}$) and thus had been measuring only $\sim$1/3 of the total solar-neutrino flux. Definitive proof of neutrino oscillations came from the heavy-water (^2H_2O) solar-neutrino detector at the Sudbury Neutrino Observatory (SNO) in Canada (e.g., McDonald 2016). Arthur McDonald shared the 2015 Nobel Prize in Physics with Takaaki Kajita, who detected the oscillations of another neutrino flavor (the muon-neutrinos ν_μ), which are created by cosmic-ray interactions in the upper atmosphere (Kajita, 2016).

We note that the Sun's complicated equation of state plays a large role in any comparison of solar models with global helioseismology. Near the outer surface, partial ionization regions, kinetic effects associated with the non-collisional plasma, and non-equilibrium thermodynamics all become important. In the deep interior, the equation of state for the opacity must assume some uncertain input physics, like nuclear reaction rates, elemental abundances, and atomic cross sections. For maximum accuracy and reduced computational overhead, most solar models use pre-tabulated equations of state. Two popular choices are the Livermore-based OPAL tables (e.g., Rogers et al. 1996) and the international Opacity Project (OP) tables (e.g., Berrington 1995). The latter solves the Mihalas-Hummer-Däppen (also referred to as "MHD," unfortunately) equation of state (Mihalas et al., 1988; Hummer & Mihalas, 1988; Däppen et al., 1988; Mihalas et al., 1990). State-of-the-art tables like OPAL and OP were instrumental in bringing solar models more into accord with helioseismology, as happened during the solar-neutrino experiments (e.g., Christensen-Dalsgaard et al. 1996; Guzik & Swenson 1997; Basu et al. 2000).[5] Significant issues remain,

[5] The equation of state assumed by a particular solar model substantially affects the predicted oscillation frequen-

however, which can be summed up as the "solar modeling problem" (see the review by Buldgen et al. 2019). Quantities like the base of the convection zone, radial profiles of the sound-speed and density, and the helium abundance are precisely measured by helioseismology and disagree somewhat with those predicted by standard solar models including the most up-to-date equations of state (e.g., Basu & Antia 2008; Asplund et al. 2009; Nordlund et al. 2009; Palme et al. 2014; Asplund et al. 2021; and references therein).

Global helioseismology is the best tool for measuring solar structure and the internal rotation rate (see the next Section 1.1.3), but it is insensitive to other quantities like the meridional circulation and non-axisymmetric flows. *Local* helioseismology (e.g., Duvall 1998; Gizon & Birch 2005; and references therein) is the study of the short-lived acoustic waves that do not have time to travel all the way around the Sun. Because they do not have time to form standing waves horizontally, these waves are not normal modes and do not show up at discrete wavenumbers in the global power spectra. The waves will nonetheless travel several horizontal wavelengths before decaying and can be observed over localized horizontal regions of the solar disc. Because the waves are still resonant in radius, observing them in a given localized region for a long enough time interval can yield a 3-D view of the solar interior underneath that region.

Local helioseismology is really a combination of techniques for measuring the non-normal-mode acoustic power. In *ring-diagram analysis*, local power spectra are formed from placing a small "tile" on the solar disc, collecting a continuous stream of high-cadence "tiled" Dopplergrams, and computing a 3-D Fourier transform of the resulting data cube (e.g., Hill 1988; Schou et al. 1998; Haber et al. 2000, 2002). The Fourier transform of this cube reveals nearly circular "rings" in a k_x-k_y diagram at fixed f (where k_x and k_y are the components of the horizontal wave vector). Much as in global helioseismology, perturbations in the measured frequencies are sensitive to the properties of the Sun below the tile, and can be inverted to yield the perturbing quantities. In *time-distance helioseismology*, the travel times of acoustic modes are measured between two locations on

cies, and thus changes the level of agreement between the model and helioseismology. See Basu (2016); her Figure 6.

the solar surface, connected by a theoretically known ray path. Differences between the theoretical and measured wave travel times are sensitive to the internal fluid properties along the connecting ray path (e.g., Duvall et al. 1993; Jensen & Pijpers 2003; and references therein). Again, measured anomalies from many modes can be inverted to infer the spatial structure of the underlying anomaly.

Local helioseismic analyses have given subsurface flow maps of the horizontal velocity field (e.g., Hindman et al. 2004; Zhao & Kosovichev 2004; Haber et al. 2004; Hanasoge et al. 2012; Greer et al. 2015, 2016). These flow maps have been used to measure the Rossby number and coherence-depth of supergranulation in the outer layers (Hanasoge et al., 2012; Greer et al., 2015, 2016), the presence of diverging flows and complex vortices below a sunspot (e.g., Zhao & Kosovichev 2004; Haber et al. 2004), and the radial dependence of the recently observed solar Rossby waves (e.g., Löptien et al. 2018; Gizon et al. 2020b; Proxauf et al. 2020; Gizon et al. 2021). As described in Chapter 2, subsurface flow maps may prove helpful in constraining the interior Reynolds stress torque that is believed to drive near-surface shear. This Reynolds stress has yet to be measured.

Local helioseismology has also probed the Sun's internal meridional circulation (e.g., Giles et al. 1997; Haber et al. 2004; Hathaway 2012; Chen & Zhao 2017; Mandal et al. 2018; Gizon et al. 2020a; Braun et al. 2021), often with conflicting results. For example, there seems to be a growing body of evidence that the Sun may have multiple circulation cells in each hemisphere (e.g., Chen & Zhao 2017; Mandal et al. 2018). It should be noted that global simulations have consistently produced solar-like differential rotation (fast equator, slow poles) only with multiple circulation cells, and anti-solar differential rotation with single circulation cells (e.g., Featherstone & Miesch 2015). Part of the problem is that meridional circulation is inherently difficult to measure helioseismically, because it perturbs the acoustic-mode frequencies at second-order, unlike the differential rotation, which perturbs the frequencies at first-order (e.g., Braun & Birch 2008; Zhao et al. 2012).

1.1.3 The Internal Rotation Rate of the Sun

Throughout this thesis, we denote the interior angular velocity of the Sun (and later, of simulations), by Ω, which we also call the rotation rate. We define $\Omega \equiv \langle v_\phi \rangle / r \sin\theta + \Omega_0$, where

$\langle v_\phi \rangle$ is the longitudinally and temporally averaged azimuthal velocity in a frame rotating at Ω_0. In simulations, Ω_0 is the chosen "reference" rotation rate and for the Sun, we define $\Omega_0 \equiv \Omega_\odot$ to be the sidereal Carrington rate ($\Omega_\odot = 2.87 \times 10^{-6}$ rad s^{-1} or $\Omega_\odot/2\pi = 457$ nHz or $2\pi/\Omega_\odot = 25.38$ days). Here, r and θ are the standard spherical coordinates (radius and colatitude, respectively). We report the rotation rate in rad s^{-1}. In keeping with helioseismic tradition, we also refer to the "rotation frequency" $\Omega/2\pi$, which we report in Hz.

The helioseismically inferred rotation frequency of the Sun is shown in Figure 1.3. Closest to the photosphere is the near-surface shear layer (NSSL). This is a layer of thickness $\sim 0.05 R_\odot$, wherein the rotation frequency drops by about 5% with increasing radius. This effect is roughly latitude-independent. A 5% reduction in rotation frequency over 5% of the solar radius implies that $\Omega \sim 1/r$ in the NSSL. This dependence is notable, since a region of homogeneous angular-momentum density (as the NSSL was originally thought to be; e.g., Foukal & Jokipii 1975) would have $\Omega \sim 1/r^2$. The radial shear in the NSSL (although likely weaker than the shear in the tachocline at the base of the convection zone; discussed below) is quite strong. Given the NSSL's proximity to sunspots, it may play a more fundamental role in the solar dynamo cycle than is usually assumed. Brandenburg (2005) in particular has advocated for a "distributed dynamo shaped by near-surface shear" (see also Pipin & Kosovichev 2011). The maintenance of the NSSL is still mostly unexplained. We present our attempts to systematically model the NSSL using global simulations in Chapter 2.

Going deeper into the interior, the isorotation contours are tilted with respect to the solar rotation axis in the bulk of the convection zone. This tilt was a surprise for two reasons. First, mixing-length theory predicted that the motions in most of the convection zone should be strongly rotationally constrained, meaning a Taylor-Proudman-like constraint (i.e., invariance along the rotation axis) should hold (e.g., Pedlosky 1987; Kitchatinov & Ruediger 1995; Durney 1999; Rüdiger & Hollerbach 2004). Second, early nonlinear global simulations mostly yielded cylindrically aligned isorotation contours (e.g., Gilman 1977; Glatzmaier 1984; Miesch et al. 2000; Brun & Toomre 2002; Brun et al. 2004). Miesch et al. (2006) found that the Taylor-Proudman constraint in global

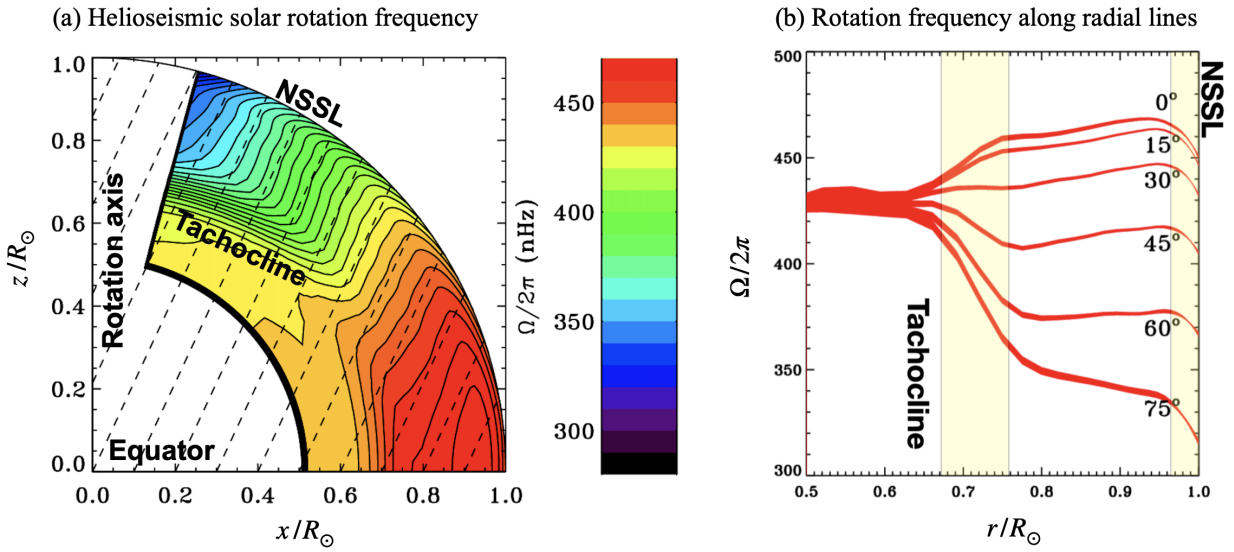

Figure 1.3: **The Internal Rotation Rate of the Sun.** The helioseismically inferred rotation frequency is shown, averaged in both longitude and time and assuming an equatorially symmetric profile. Rotation frequency $\Omega/2\pi$ is plotted in units of nHz. For geometrical reference, the base of the convection zone is $r/R_\odot \sim 0.72$ and we mark the approximate locations of the two shear layers in each panel. (a) Rotation frequency in the meridional plane. The x-axis corresponds to the solar equator and the y-axis to the axis of rotation. In the colorbar, the isorotation contours are equally spaced 10 nHz apart. The dashed lines are inclined by 25° with respect to the rotation axis and roughly match the tilt of the isorotation contours at mid-latitudes. (b) Same solar rotation frequency as depicted in panel (a), but plotted along radial lines constant solar latitudes. The thickness of the curves represents the error in the helioseismic inversion; error increases with depth. Figure adapted from Howe 2009.

simulations could be broken by imposing a latitudinal entropy gradient at the base of the convection zone. We discuss our progress in identifying a physical mechanism to drive such a latitudinal entropy gradient (and thus potentially tilt the Sun's isorotation contours) in Chapter 3.

Possibly the most striking feature of the helioseismically measured rotation profile is the tachocline, a thin, largely radial boundary layer in which the strong differential rotation in the convection zone transitions to nearly solid-body rotation in the stably stratified radiative interior (e.g., Brown et al. 1989; Thompson et al. 2003). We note that a radial shear layer in the Sun (though not the tachocline) was postulated as early as Dicke (1964). Dicke noted that if the Sun were slightly oblate due to the core rotating much more rapidly than the observed surface rotation (with an implied radial shear layer in between), the solar gravitational potential could be modified. For a rapidly rotating core (which could be caused by the solar wind torquing the outer layers of the Sun before the inner layers), classical Newtonian gravitation could explain the precession of Mercury's perihelion instead of general relativity. Dicke & Goldenberg (1967) attempted to measure the solar oblateness—$(R_{\rm eq} - R_{\rm pol})/R_\odot$, where $R_{\rm eq}$ and $R_{\rm eq}$ are the Sun's equatorial and polar radii, respectively—finding a value of 5×10^{-5}. This, in turn, would imply a core rotating about 20 times faster than the surface, which would be enough to explain the observed precession of Mercury's perihelion. [6] There have been numerous attempts to seismically measure the rotation rate of the core, with most evidence indicating approximately solid-body rotation between $\sim 0.2 R_\odot$ and $\sim 0.7 R_\odot$ (i.e., the base of the tachocline; see Howe 2009, the references in her Table 1). Helioseismology thus largely supports Einstein (and not Dicke), although rapid rotation below $\sim 0.2 R_\odot$ cannot be completely ruled out.

Because only the long-wavelength (low-ℓ) acoustic modes penetrate to the base of the convection zone (and because there are fewer of them), the spatial resolution of the global inversions in the tachocline region is fairly coarse. Different inversion techniques yield slightly different results

[6] Dicke (1964)'s initial suggestion of a rapidly rotating core incited a slew of controversy and had the upside of sparking significant interest in the Sun's internal rotation rate. Subsequent attempts to measure the solar oblateness yielded values much lower than Dicke's first measurement (e.g., Roxburgh 1967; Kraft 1967; Goldreich & Schubert 1968; Fivian et al. 2008), as was also confirmed by Dicke himself (Dicke et al., 1986, 1987). As of today, the solar oblateness still has not been precisely measured, but the situation may improve with next-generation space telescopes (see Damiani et al. 2011; Rozelot et al. 2019; and references therein).

for tachocline thickness, but generally all lie around $\sim 0.05 R_\odot$ (e.g., Howe 2009; her Table 2). That value likely reflects the resolution of the inversions at $\sim 0.72 R_\odot$, and the solar tachocline may in fact be much thinner. For example, an alternative estimate of the tachocline's thickness was given in Elliott & Gough (1999). The helioseismically measured sound-speed is discontinuously higher than the sound-speed predicted by standard solar models in the tachocline (this is known as the "tachocline anomaly"; e.g., Basu & Antia 2008). Elliott & Gough (1999) invoked enhanced mixing caused by the supposed tachocline's meridional circulation (Gough & McIntyre, 1998) to efficiently mix the tachocline layer in addition to the convection zone. This would lessen the amount of helium in the tachocline compared to standard solar models (which include effects from helium settling and the assumption that the convection zone is well mixed), lower the mean molecular weight, and thus increase the sound-speed. Using this simplified tachocline-mixing model in comparison with helioseismic structure inversions, Elliott & Gough (1999) inferred a tachocline width of $\sim 0.02 R_\odot$.

We also note that there may be a significant prolateness to the tachocline, with the equatorial thickness smaller than the high-latitude thickness (difference in thicknesses of about $0.02 R_\odot$; e.g., Charbonneau et al. 1999a; Basu & Antia 2003). Finally, Howe et al. (2000) reported a $\sim$1.3-year periodicity in the equatorial rotation rate near the tachocline using early GONG and SOHO/MDI data (1995–1999). This claim received considerable attention, since tachocline variations could yield dynamo and magnetic activity variations at a similar period, which might, in turn, explain the observed $\sim$1-year periodicity measured from heliospheric and geomagnetic data (e.g., Silverman & Shapiro 1983; Richardson et al. 1994).

Finally, both global and local helioseismology have confirmed significant *torsional oscillations* in the solar differential rotation, originally detected from the synoptic velocity maps at the Mount Wilson 150-foot tower (Howard & Labonte, 1980). See also the analysis by Ulrich (2001) using Mount-Wilson surface-velocity data. Small ($\pm 0.5\%$) variations in the subsurface rotation rate propagate equatorward with the active sunspot latitudes, indicative of deep-seated flow patterns dynamically coupled to the solar cycle. Global inversions (e.g., Howe et al. 2000; Vorontsov et al. 2002) have shown that the torsional oscillations extend deep into the convection zone, especially at

high latitudes, where they may reach all the way to the tachocline. At low latitudes, the inversions support a picture wherein the torsional-oscillation pattern originates in the convection zone and propagates both upward and equatorward (e.g., Vorontsov et al. 2002; Basu & Antia 2003). At high latitudes, by contrast, fast and slow rotation bands propagate poleward (e.g., Antia & Basu 2001; Schou 2003), suggesting they are related to the flux-transport inferred from the solar butterfly diagram (Figure 1.2).

1.2 Solar Modeling

The observational data just described imposes strong constraints on theories of the solar dynamo. A successful theory must reproduce: (1) The temporal behavior of the magnetic field (e.g., the 22-year solar cycle, the Gleissberg modulation, and the grand minima) and (2) the solar differential rotation (e.g., the tilted isorotation contours and the two shear layers). Theoretical calculations (both analytical and numerical) have made much progress in the last few decades, but still fall short of describing some of the major observed behaviors. In this section, we briefly go over recent progress in theoretical calculations, particularly the global simulations. We describe the major triumphs simulations have achieved and the fundamental mysteries that remain.

1.2.1 Modeling of Near-Surface Convection and Active Regions

Simulating sunspots and active regions generally involves utilizing the equations of magnetohydrodynamics (MHD) while simultaneously treating the radiation field (radiative MHD, or RMHD). As the photosphere is approached from below, the mean-free-path of a photon becomes comparable to the dynamical length-scales associated with the convection (in fact, the cooling caused by photons is what drives the convection). Calculating the radiation field accurately thus becomes a formidable problem, since 3-D, non-gray radiative transport must be taken into account. Because of the heavy computational overhead, near-surface simulations are usually local, treating a small Cartesian box straddling the photosphere.

The radiation field is treated by sorting it into a small number of groups in frequency space

and then solving the time-dependent radiative transfer equation (e.g., Vögler et al. 2004; Rempel et al. 2009). The "R" in RMHD then boils down to calculating a realistic equation of state for the opacities as functions of density and temperature. Usually this equation of state involves tables, like OPAL or OP, mentioned in Section 1.1.2. Several numerical tools for simulating the radiatively driven near-surface "magneto-convection" in the Sun have been developed. Comparisons of these codes appear to agree quite well with respect to observable properties like emergent intensity and granular convective topology, but have small differences that are attributable to different treatments of the radiation field and/or the equation of state (e.g., Beeck et al. 2012).

One of the triumphs of the local simulations has been the reproduction of active regions, solar flares, and coronal mass ejections, with magnetic-field strengths and flow properties remarkably similar to observations (e.g., Cheung et al. 2010; Stein & Nordlund 2012; Rempel & Cheung 2014; Rempel 2016; Chen et al. 2017). Granulation is also reproduced quite well, with the observed flux-expulsion of granules (the sweeping of small-scale magnetic flux into inter-granular lanes) correctly captured by the simulations (e.g., Stein & Nordlund 2000, 2006; Rempel et al. 2009). The local models of active regions usually treat an individual sunspot as it emerges in the outermost layers of the Sun (i.e., the outer ∼30,000 km or so). We note, however, that recently very large calculations have captured the rise of a buoyant flux rope through a whole convection zone from base to surface, including sophisticated near-surface physics. These simulations tracked the flux rope through its eruption as a bipolar active region, with results remarkably similar to observations (see Hotta et al. 2019; Hotta & Iijima 2020).

With the exception of the "hero" calculations just mentioned, the main difficulty local simulations face is the absence of self-consistently generated large-scale flows and magnetic fields. Their boundary conditions (what they are "fed") are thus inconsistent with realistic stellar circulations, differential rotation, and global magnetic-field topology. Conversely, the global models described below suffer from unrealistic treatments of near-surface physics. In this regard, progress has been made by "patching" a local near-surface simulation onto a global simulation. For example, Chen et al. (2017) simulated the buoyant rise of a flux rope to form an erupting active region, using

an initial magnetic configuration taken directly from a global simulation (Fan & Fang, 2014). We speculate that such patching of local models onto global models may be the future path by which numerical modeling makes detailed contact with solar dynamo observations. Such efforts are currently underway as part of the large multi-university "Whole Sun" collaboration, which has been funded for six years by an ERC Synergy Grant (e.g., Brun et al. 2017; Strugarek et al. 2017; Brun et al. 2022). This project aims to use advances in supercomputing power to develop next-generation numerical solar simulations (including the radiative interior, convection zone, chromosphere, and corona) to run on future exascale machines.

1.2.2 Global Spherical-Shell Dynamo Simulations

The first global dynamo models were based on mean-field theory, which is still the speaking language of the global simulation community. In light of the solar cycle, a key goal of mean-field theory is to describe the physical processes leading to a "dynamo loop," or the achievement of a polarity reversal. We previously described one such loop, the Babcock-Leighton, or flux-transport, dynamo. Another commonly invoked dynamo loop is the class of $\alpha\Omega$-type dynamos (e.g., Parker 1955). Here, the toroidal magnetic field is produced from poloidal field via mean shear by the differential rotation (the already-mentioned "Ω-effect"). The poloidal magnetic field is then produced from toroidal magnetic field by the electromotive force (emf) associated with helical convection (the "α-effect"; e.g., Moffatt 1963; Brandenburg 2005). Helical motions (or "cyclonic events," following the terminology of Parker 1970) can locally twist the toroidal magnetic field lines into loops. Each loop is associated with an elemental current, and thus an emf. If the magnetic diffusion is low enough, the net current from these cyclonic events can convert toroidal into poloidal field (see Figure 7.2 of Moffatt 1963).

In the case of the Sun, because the Coriolis force tilts the toroidal field slightly (consistent with Joy's law), the α-effect creates poloidal field in the opposite direction to its previous orientation, thus creating a polarity reversal and completing the dynamo loop.[7] While the nonlinearity of the

[7] In comparison to the flux-transport dynamos, the α-effect here takes the place of the transport of small-scale

problem is oversimplified, processes like the Ω- and α-effects consistently help the interpretations of simulations (e.g., Brown et al. 2010, 2011; Racine et al. 2011; Augustson et al. 2013; Warnecke et al. 2014; Augustson et al. 2015; Guerrero et al. 2016a; Matilsky & Toomre 2020a; Bice & Toomre 2020; Brun et al. 2022). Pipin (2012); Brandenburg (2018) give excellent reviews of mean-field theory, especially how it has recently evolved in light of ever-more-powerful numerical simulations.

In the so-called interface dynamo paradigm, the solar tachocline is invoked as the main site of magnetic field amplification through the Ω-effect (e.g., Parker 1993; Charbonneau & MacGregor 1997). The tachocline is also in a privileged position since it lies directly above the stably stratified radiative interior. The stable stratification strongly inhibits radial motion and is thought to lead to conditions for which tachocline-produced magnetic fields are stored stably for long time-intervals (e.g., van Ballegooijen 1982; Moreno-Insertis et al. 1992; Ferriz-Mas & Schuessler 1994; Gilman 2000a). In the interface dynamo paradigm, the tachocline acts as a magnetic-field generator and the radiative interior acts as a storage reservoir.[8] When concentrated bundles of magnetism within the radiative interior become strong enough for buoyancy instabilities to set in, they rise, traversing the convection zone to erupt as sunspot pairs (e.g., Cline et al. 2003; Jouve & Brun 2009; Weber et al. 2013; Fan & Fang 2014).

The concepts of mean-field theory just described have been instructive in understanding the basic operation of the solar 22-year cycle. Mean-field theories fall short, however, of addressing the fully turbulent, nonlinear processes like the helical convection (emf) that maintains the poloidal magnetic field and the Reynolds stress that maintains the differential rotation. For more insight, we must turn to global simulations, which are fully 3-D, non-axisymmetric, and self-consistent (each field is coupled to the other fields). The nonlinear effects are calculated explicitly in a global model, rather than parameterized. Finally, in contrast to the local near-surface models, global models capture the spherical geometry and large-scale transport processes of the star.

residual flux from decayed sunspots. Since the Coriolis force is believed to tilt emergent magnetic field in a manner consistent with Joy's law, the two types of α-effect are in some ways equivalent.

[8] The practice of treating the solar radiative interior as a quiescent "abyssal deep" (to borrow the oceanographic term) is longstanding. One of the central findings of this thesis is that stellar radiative interiors may be filled with strong horizontal motions that significantly affect the dynamo. We return to this point in our conclusions (Chapter 6).

To capture the long time-scales and large length-scales associated with the global solar dynamo, the complicated near-surface physics necessary for local simulations (Section 1.2.1) must be simplified. Typically, global simulations have a smooth, impenetrable outer boundary that replaces radiative cooling with thermal conduction or an artificial cooling layer. The exact form of the MHD equations solved, the numerical algorithm used to solve them, and the geometry of the domain are treated differently by different codes. In this thesis, we use the `Rayleigh` MHD code (Featherstone & Hindman, 2016a; Matsui et al., 2016; Featherstone, 2018; Featherstone et al., 2021), which solves the anelastic (sound-wave-filtering) MHD equations (see Equations (1.1)) in full spherical shells. `Rayleigh` uses a pseudo-spectral approach to evolve the equations in time, in which frequent transformations are made between "spectral space" (fluid quantities decomposed into Chebyshev polynomials radially and spherical harmonics horizontally) and "physical space" (fluid quantities described as functions of position).

We note that `Rayleigh` is one of many global MHD codes, some of which we briefly describe here. The pseudo-spectral `Anelastic Spherical Harmonic` (`ASH`) code is the precursor to `Rayleigh`, but employs a different form of the radiative heating and conductive heat flux (e.g., Clune et al. 1999; Brun & Toomre 2002; Brun et al. 2011). The `Pencil` code is a purely finite-difference partial differential equation solver (e.g., Brandenburg & Dobler 2002) and is modular, able to be used for a variety of astrophysical applications. In the context of solar models, `Pencil` has been used to simulate convection in spherical-shell wedges (e.g., Warnecke et al. 2014; Käpylä et al. 2017). The `Reduced Speed of Sound Technique` (`RSST`) code (e.g., Rempel 2005, 2006; Hotta et al. 2015) solves the fully compressible MHD equations in spherical shells, but with a continuity equation that effectively becomes anelastic in the deeper layers, reducing the sound-speed where it would become extremely large. `RSST` has given rise to a new code, `Radiation and RSST for Deep Dynamics` (`R2D2`) that can realistically treat the near-surface radiation field and essentially simulate the whole convection zone (in a large Cartesian box) on short time-scales (e.g., Hotta et al. 2019; Iijima et al. 2019; Hotta & Iijima 2020). Finally, the `Eulerian-Lagrangian-` (`EULAG-`) `MHD` code (e.g., Smolarkiewicz & Prusa 2004; Prusa et al. 2008) solves partial differential equations

via an advection scheme (specifically, the "Multidimensional positive definite advection transport algorithm," or MPDATA) that introduces numerical diffusivity wherever the simulation would be numerically unstable. MPDATA effectively introduces diffusion only on the smallest length-scales, and also allows `EULAG-MHD` simulations to remain stable even on grids with modest resolution. `EULAG-MHD` can be used for multiple geometries, and recently has been used to simulate solar and stellar dynamos in spherical shells (e.g., Racine et al. 2011; Guerrero et al. 2016a, 2019).

In many global simulations, convection is excited by a solar luminosity conducted through the inner spherical shell. This is essentially a spherical version of the "thermal instability of a layer of fluid heated from below"—i.e., classical Rayleigh-Bénard convection (see Chandrasekhar 1961; his Chapter II). In this thesis, luminosity-injection is distributed throughout the convection zone using a heating function, but the heating is still concentrated in bottom parts of the convection zone. At the top of the domain, the luminosity is carried out by thermal conduction.[9] One common feature of ignoring radiative cooling is that none of the global models have convection driven exclusively from above, or at the small granular scales. [10]

With significant advances in computing power over the last few decades, global models are now able to generate large-scale, coherent, and cycling magnetic fields. Brown et al. (2010, 2011) found that coherent magnetic "wreaths" of toroidal field, wrapping all the way around the sphere, could exist in turbulent simulations of a convection zone with no tachocline. This was initially a surprise, given the dominant role attributed to the tachocline in the classical interface dynamo paradigm, and the general belief that highly turbulent flows in the convection zone would shred apart any large-scale magnetism (e.g., Parker 1975). Large-scale wreaths have since been confirmed as robust features of multiple MHD codes in F-, G-, K-, and M-type stars (e.g., Nelson et al. 2013b; Augustson et al. 2013; Passos & Charbonneau 2014; Augustson et al. 2015; Yadav et al. 2015; Guerrero et al. 2016a; Matilsky & Toomre 2020a; Bice & Toomre 2020, 2022; Brun et al. 2022).

[9] Note that in the `RSST` and `R2D2` codes, the luminosity is shed instead via an artificial cooling layer near the top boundary.

[10] The `EULAG-MHD` code is slightly different than the others; the convection is driven by dragging the thermal perturbations to a pre-defined slightly superadiabatic background state. It is thus unclear exactly where the luminosity enters and leaves the spherical shell, or even what "luminosity" means in this context.

In all global models, any potential wreaths are necessarily maintained by fully nonlinear dynamo processes. Nevertheless, the differential rotation and helical convection still play fundamental roles, suggesting that the basic characteristics of a mean-field $\alpha\Omega$-type dynamo may survive, even at higher levels of turbulence.

Figure 1.4 shows an example of coherent magnetic wreaths in the simulations of Matilsky & Toomre (2020a) (see also Matilsky & Toomre 2020b and Chapter 4). The wreaths are strongest near mid-latitudes, and their cores lie deep in the convective shell, near the inner boundary. Although the wreaths are quite prominent and have connectivity all the way around the sphere, they are clearly advected and shredded by the turbulent convection. At the instant shown in Figure 1.4, the toroidal field is symmetric about the equator (unlike in the solar cycle). Furthermore, there are four wreaths total (two per hemisphere), whereas the butterfly diagram of Figure 1.2 would suggest two wreaths in the actual Sun (one per hemisphere, each having opposite polarity). We note, however, that the torsional oscillations (e.g., Howe et al. 2000) propagate equatorward in two bands per hemisphere, like the wreaths in Figure 1.4. It is possible that wreath-like structures, if they indeed are present in the solar convection zone, form an additional "'magnetic reservoir," distinct from the reservoir in the radiative interior that is invoked in the interface dynamo paradigm. Both reservoirs could produce buoyant magnetic loops that break off the wreath and rise to form sunspot pairs, with individual pairs bearing some type of signature from their parent reservoir.

The dynamos in global models have also been able to achieve some striking cycling behavior. In the early wreath-building simulations of Brown et al. (2011) and Nelson et al. (2013b), the cycles were fairly irregular and the fields sometimes non-axisymmetric. Passos & Charbonneau (2014), by contrast, achieved highly regular polarity-reversing cycles (with large-scale axisymmetric wreaths) that remained stable for over 1650 years ($\sim$40 polarity reversals at $\sim$40 years per cycle). The long-term behavior of the cycles was reminiscent of the Gleissberg modulation, and even-numbered cycles had different amplitude than odd-numbered cycles, as is observed for the Sun as the Gnevyshev-Ohl rule (Gnevyshev & Ohl, 1948). Notably, Passos & Charbonneau (2014) included a tachocline of shear between the stable and unstable layers (more on this in Section 1.2.4).

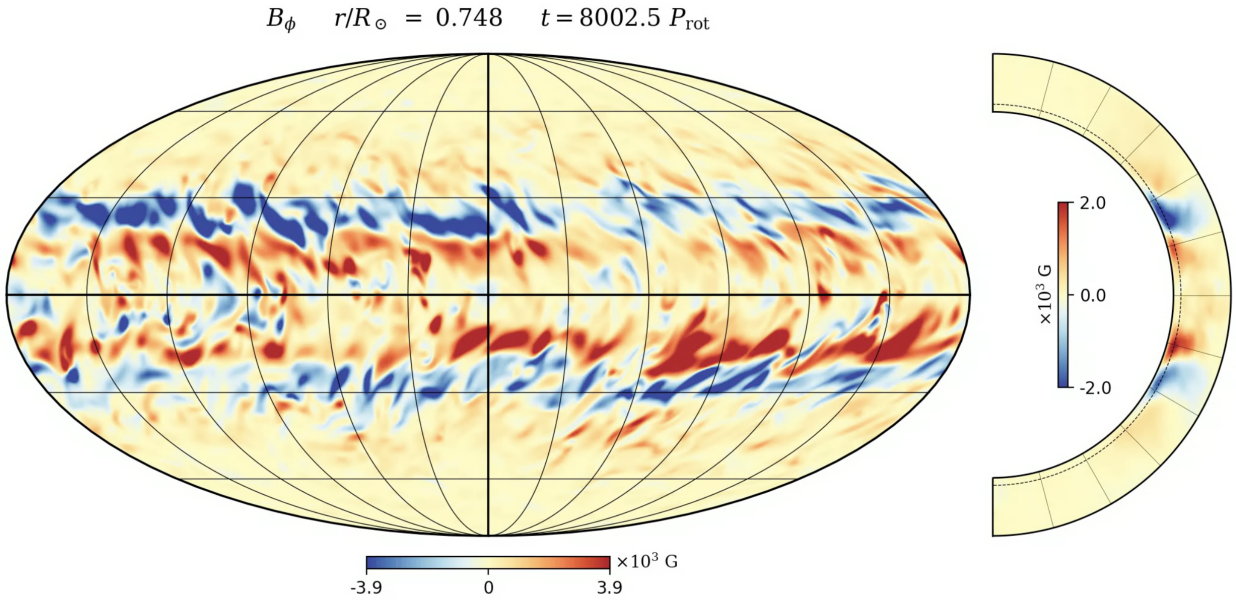

Figure 1.4: **Magnetic Wreaths in Global Dynamo Simulations.** (Left) Toroidal magnetic field (B_ϕ) on a spherical slice in the deep convection zone of a global dynamo simulation (Matilsky & Toomre, 2020a). Red tones indicate field in the prograde direction ($B_\phi > 0$) and blue tones indicate field in the retrograde direction ($B_\phi < 0$). The field is plotted in full Mollweide view (all longitudes are shown) and is composed of four toroidal "wreaths" of strong magnetism—two in each hemisphere. Parallels and meridians are shown every 30 degrees, with the equator, sphere boundary, and central meridian lines plotted slightly thicker. (Right) Longitudinally averaged magnetic field $\langle B_\phi \rangle$ at the same instant as the Mollweide slice on the left, shown in the meridional plane. The four wreaths have maximum amplitude close to the base of the convection zone. The curved boundaries of the meridional plane represent the inner and outer radii of the spherical shell, the radial level of the Mollweide slice is shown as a dotted black curve, and radial lines (lines of constant θ) are marked every 15 degrees. The top labels indicate the toroidal magnetic field, the radial level in the shell, and the simulation-time sampled in rotations.

Augustson et al. (2015) also achieved remarkably regular cycles, which displayed equatorward propagation of wreaths at low latitudes and poleward propagation of small-scale magnetism at high latitudes. The high-latitude magnetic field had average polarity opposite to that of the low-latitude wreaths—highly reminiscent of the solar butterfly diagram (Figure 1.2). Furthermore, the simulation in Augustson et al. (2015) stopped cycling for an extended interval, similar to a solar grand minimum, and then resumed cycling afterward. Finally, Matilsky & Toomre (2020a) found a "bistable" dynamo, consisting of two types of cycle operating simultaneously. One was a regularly-reversing equatorward-propagating system of axisymmetric wreaths (Figure 1.4), and the other was a longitudinal modulation of non-axisymmetric (azimuthal wavenumber $m = 1$) "partial wreaths," similar to those presented in Brown et al. (2011) and Nelson et al. (2013b). The partial wreaths in Matilsky & Toomre (2020a) were further recognized to possess striking similarities to the observed active longitudes and hemispheric asymmetry on the Sun. The bistable simulations are described in detail in Chapter 4. Recently, Bice & Toomre (2022) made progress in understanding the generation of non-axisymmetric magnetic cycling via so-called patchy convection (active nests of strong convection localized to a particular longitude—e.g., Brown et al. 2008).

1.2.3 Insights into the Solar Differential Rotation from Global Simulations

All dynamos in global modeling so far encountered are intimately coupled to the achieved differential-rotation profile via the Ω-effect. Here, we discuss some of the successes and shortcomings of global models in explaining the helioseismically inferred solar rotation rate. At zeroth-order, solar-like differential rotation consists of the rapidly rotating equator and slowly rotating polar regions. The maintenance of solar-like differential rotation is now widely believed to arise from angular momentum transport by interior convective rolls, also known as "Busse columns," "Taylor columns," "convective Rossby waves," and/or "banana cells" in the literature. We usually refer to these rolls as Busse columns in this thesis (Taylor columns in Chapter 4). The possibility for Busse columns to drive the solar differential rotation was first suggested in the pioneering work of Busse (1970a,b), Gilman (1972), and Busse (1973). The presence of Busse columns (and their ability to

maintain differential rotation) was subsequently confirmed in nonlinear 3-D convection simulations (e.g., Glatzmaier 1984; Gilman & Miller 1986; Elliott et al. 2000; Brun & Toomre 2002).

An example of a spherical-shell convection simulation is shown in Figure 1.5. The radial velocity acts as a fairly good tracer of the flow. Between about ± 30 degrees latitude, the convection consists of fairly coherent columnar rolls aligned with the rotation axis, which are the Busse columns. Above the mid-latitude regions, the convection appears more isotropic and vortical, although some of the downflow lanes are clearly the ends of Busse columns. The flow field shown in Figure 1.5 is typical of reasonably turbulent global simulations. Figure 1.5 also shows the asymmetry between upflows (broad and slow) and downflows (thin and fast) that arises from the density contrast across the shell, and is not present in Rayleigh-Bénard convection.

Busse columns arise in regions of strong rotational constraint, which in this thesis is defined by low Rossby number (ratio of rotation period to convective turnover time) and low Ekman number (ratio of the rotation period to viscous diffusion time).[11] In other words, strong rotational constraint occurs when the rotation is so fast that it influences all other dynamical processes. The solar NSSL (Figure 1.3) presented the first indication that rotational constraint may break down near the photosphere, where the velocities are high and the convective turnover time is short. As described in Section 1.1.3, the rotation rate decreases with radius in the NSSL. In fact, this behavior was inferred even before helioseismology by observing that magnetic tracers—which are believed to be anchored below the photosphere—rotate faster than the surrounding plasma (e.g., Howard & Harvey 1970; Wilcox et al. 1970; Foukal 1972). Foukal & Jokipii (1975) proposed that high-velocity, rotationally unconstrained fluid in the NSSL could homogenize angular momentum in radius, thus yielding $\Omega \sim 1/r^2$. Helioseismology, of course, revealed that $\Omega \sim 1/r$ in the NSSL, so clearly Foukal & Jokipii (1975)'s mechanism did not entirely work. Nevertheless, the general idea that near-surface turbulence maintains the NSSL remains prevalent (e.g., Miesch & Hindman 2011; Hotta et al. 2015; Matilsky et al. 2019. As we will discuss in-depth in Chapter 2, some recent numerical simulations

[11] All simulations in this thesis have low Ekman numbers $\sim 10^{-4}$–10^{-3}, so we need only technically consider the Rossby number when assessing rotational constraint. However, it is still useful to invoke the Ekman number when discussing certain aspects of rotational constraint.

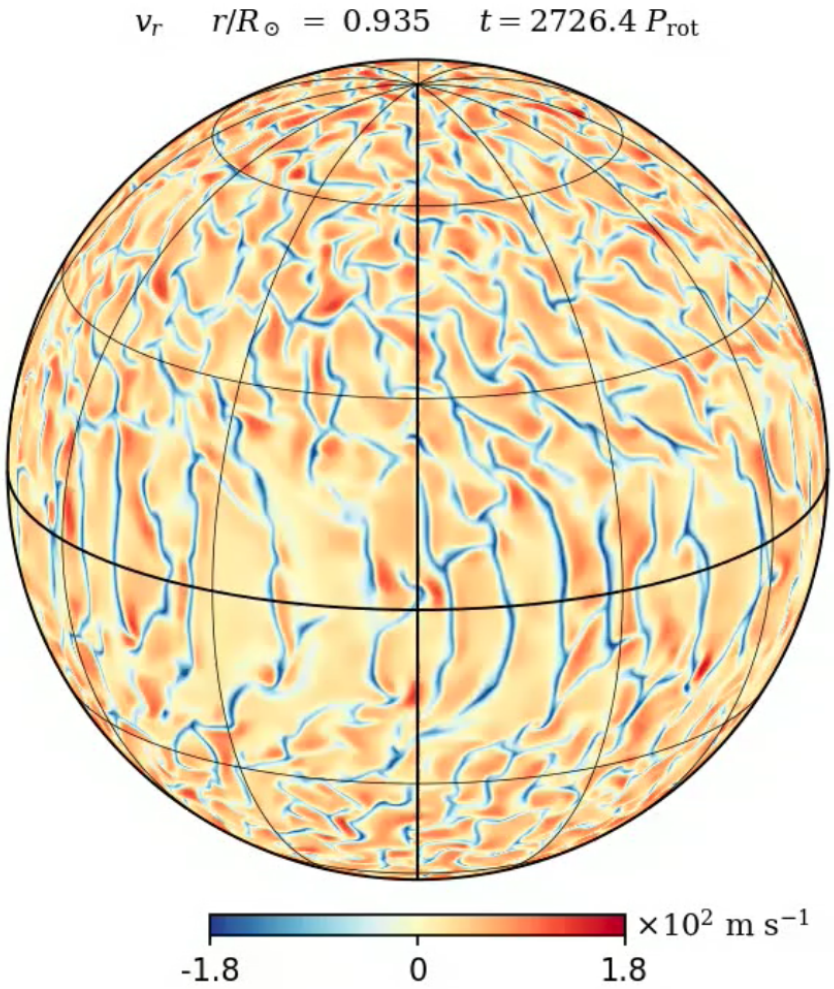

Figure 1.5: **Spherical-Shell Convection.** Snapshot of the radial velocity v_r field near the outer surface a convection simulation in a rotating spherical shell (Matilsky & Toomre, 2020a). The velocity is plotted in color (red tones indicate upflow, blue tones indicate downflow) on a spherical surface just below the outer boundary in orthographic projection. The sphere is viewed from above the 20th parallel in the Northern Hemisphere. Meridians and parallels are shown as black curves every 30 degrees, and the equator, sphere boundary, and central meridian are plotted slightly thicker. Where the meridians meet at the top of the figure is the North Pole, which also lies on the rotation axis. The top labels indicate the radial velocity, the radial level in the shell, and the simulation-time sampled in rotations.

have attempted to capture the NSSL with an outer layer of rotationally unconstrained fluid (Hotta et al. 2015; Matilsky et al. 2019). These attempts have so far not succeeded.[12] Some phenomenon in addition to the NSSL—likely the near-surface meridional circulation or magnetic fields—is likely not being faithfully captured by the global simulations.

As already mentioned, the substantial tilts of the isorotation contours have been difficult for global simulations to capture. Rempel (2005) suggested that the cylindrical contours usually achieved in global simulations were the result of too much rotational constraint (or equivalently, Taylor-Proudman constraint). A "thermal wind," or an equator-to-pole entropy gradient, can break the Taylor-Proudman constraint. Rempel (2005) suggested that such a thermal wind might arise from the convection zone's coupling to the tachocline. Inspired by this idea, Miesch et al. (2006) imposed an equator-to-pole entropy gradient at the bottom boundary in a global simulation. The result was significant contour tilt, with the tilt angle basically adjustable in proportion to the strength of the imposed entropy gradient. It remains unclear, however, how a thermal wind in the tachocline would couple to the solar convection zone (the thermal conductivity is very low in the Sun) and also what would drive this thermal wind in the first place. In Matilsky et al. (2020) (Chapter 3), we show that Busse columns transport heat poleward, in addition to transporting angular momentum outward. This gives a physical mechanism to drive a thermal wind and tilt the Sun's isorotation contours.

We finally note that all global models currently suffer from a fundamental problem with the differential rotation as simulations are pushed to more turbulent regimes. This "convective conundrum" may be stated following (O'Mara et al., 2016): "The convective velocities required to transport the solar luminosity in global models of solar convection appear to be systematically larger than those required to maintain the solar differential rotation and those inferred from solar observations." More specifically, if simulations are pushed to increasingly turbulent regimes (while keeping the rotation rate and luminosity fixed at the solar values), the velocities at large scales grow

[12] The exception are some quite solar-like NSSLs achieved (at high latitudes only) in some of the MHD simulations of Guerrero et al. (2016a,b, 2019). Guerrero et al. (2016a,b) invoke rotationally unconstrained turbulence as causing the NSSLs, but do not perform any further dynamical analysis.

larger than helioseismology would predict. The large-scale flows lose their rotational constraint, and thus their columnar nature (Figure 1.5), failing to transport angular momentum outward. The simulation as a whole becomes "anti-solar," with fast polar regions and a slow equator. We note that the physical origin of the anti-solar states is still not well understood (e.g., Featherstone & Hindman 2016b; Hindman et al. 2020; and references therein). It should also be noted that only some helioseismic studies (e.g., Hanasoge et al. 2012) yield small velocities on the large scales. Other helioseismic investigations (Greer et al., 2015, 2016) yield substantially higher flow velocities, and so it is not entirely clear how unrealistic the simulations' large-scale flow velocities are.

In any case, it is likely that the flows achieved in global models are somewhat unrealistic (in general) because of the way the system is driven. A solar convection zone is required to carry out the solar luminosity via convective heat transport, which depends on the flow structures' temperature, speed, and size. The efficiency of the transport also depends on the thermal conductivity, since a given fluid parcel can only transport energy for as long as it can retain its hotness or coldness. In the Sun, the energy leaves the system via radiative cooling, which drives the convection and occurs at much different length-scales than those set by the thermal conductivity. In most global simulations, by contrast, the luminosity exits via conduction, implying that flow structures are driven at the same scales as they dissipate heat. We speculate that using more realistic near-surface physics, in which the buoyant driving occurs at scales totally separate from the scales of dissipation, may help to solve the convective conundrum.

Practically, global simulations could achieve a reduction in large-scale flow amplitudes via a reduction in the buoyant driving at the large scales. O'Mara et al. (2016) suggest that this could be accomplished via small-scale magnetic field acting to enhance the viscosity, but not the thermal conductivity. This effective "high-Prandtl-number" regime would lead to small-scale downflow plumes carrying more thermal content (i.e., driving the small scales harder), and require a weaker velocity at large scales to carry out the solar luminosity. Some recent very-high-resolution global simulations ($\ell_{\max} \sim 4{,}096$) lend support to the magnetically enhanced viscosity, yielding solar-like differential rotation at the solar rotation rate and luminosity, with large-scale flows inhibited by a

small-scale dynamo (Hotta & Kusano, 2021).

1.2.4 Global Models Including a Tachocline

The helioseismically inferred tachocline (why it is observed to be so thin, at $\sim 0.05 R_\odot$) presents a major puzzle for solar physics. Spiegel & Zahn (1992) first recognized that left to its own devices, the tachocline should have spread to a thickness (at minimum) of $\sim 0.4 R_\odot$ by the current age of the Sun. This "thermal" or "radiative" spread occurs when the tachocline's thermal wind (latitudinal entropy gradient) and accompanying meridional circulation imprint downward via radiative diffusion. The burrowing meridional circulation transports angular momentum and thus carries with it the differential rotation (the phenomenon of radiative spread is discussed extensively in Chapter 5). In the Sun, there must be a torque that forces the radiative interior to remain in solid-body rotation and thus prevent the spread of the tachocline. The origin of this torque is the subject of various tachocline confinement scenarios (e.g., Miesch 2005; Brun & Strugarek 2019; and references therein). The two most commonly invoked scenarios are hydrodynamic (HD; e.g., Spiegel & Zahn 1992) and magnetohydrodynamic (MHD; e.g., Gough & McIntyre 1998). In Chapter 5, we clearly demonstrate for the first time that magnetism can force solid-body rotation in the radiative interior of a fully 3-D, nonlinear, global simulation. In contrast to previously hypothesized magnetic confinement scenarios (Gough & McIntyre, 1998; Forgács-Dajka & Petrovay, 2001), the confining magnetism in our simulation is primarily non-axisymmetric. Furthermore, the magnetism is produced by induction, *even below the layer of convective overshoot*. Our work thus hints that the solar radiative interior may be dynamically active, rather than the usually supposed "abyssal deep." This is one of the central findings of this thesis, as we discuss at length in Chapters 5 and 6.

With the exception of Brun & Zahn (2006) and Strugarek et al. (2011a,b), global models have not focused on addressing the tachocline confinement problem. [13] Instead, they have

[13] In the Brun and Strugarek models, a poloidal magnetic field was put into the radiative interior as an initial condition in a 3-D simulation. This was meant to assess whether the poloidal field could confine the tachocline—as in Gough & McIntyre (1998)—with null results. The initially confined poloidal field spread diffusively into the convection zone and imprinted the differential rotation inward along magnetic-field lines, seeming to follow Ferraro's law of isorotation (Ferraro, 1937).

implemented a tachocline artificially and explored its effects on the differential rotation, global dynamo, and MHD waves and instabilities. This was first done in Browning et al. (2006), who used an explicit forcing term to create a steady-state tachocline in a global, MHD `ASH` simulation. In the more recent simulations, tachocline spread is controlled diffusively. In the `ASH` and `Rayleigh` models (e.g., Brun et al. 2011; Alvan et al. 2014, 2015; Brun et al. 2017; Bice & Toomre 2020), the sub-grid-scale diffusions (which appear in the equations as enhanced Newtonian diffusions) are explicitly dropped by ∼3–4 orders of magnitude in the radiative interior. A similar lowering of the sub-grid-scale diffusions is implemented in the `EULAG-MHD` simulations (e.g., Passos & Charbonneau 2014; Guerrero et al. 2016a; Beaudoin et al. 2018; Guerrero et al. 2019). In `EULAG-MHD`, there are no explicit diffusions, but implicit numerical diffusions associated with the advection operator, MPDATA. These numerical diffusions roughly scale with the convective velocities, and since the velocities are so small in the radiative interior, the diffusions are effectively very low. However the diffusions are lowered, the same effect is accomplished: the tachocline still spreads inward, but very slowly. For the time-scales over which the simulations can be run, the tachocline is effectively stationary and its influence on the dynamics can be assessed.

Browning et al. (2006) were the first to show that the tachocline could produce large-scale, coherent magnetic structures in the radiative interior in a 3-D simulation. This lent support to notion of the radiative interior as a magnetic-field reservoir that could act to stabilize the global dynamo. Furthermore, although the early convection-zone-only simulations of Brun et al. (2004) (upon which Browning et al. 2006's tachocline simulation was based) possessed largely incoherent magnetic field at many scales and irregular polarity reversals of the mean field, the introduction of the tachocline yielded steady polarity of the mean poloidal field, even in the convection zone. It was clear that even in turbulent 3-D simulations, the magnetic field in the convection zone could "feel" the influence of the tachocline.

The initial results of Browning et al. (2006) were also supported by `EULAG-MHD` simulations (e.g., Ghizaru et al. 2010; Racine et al. 2011; Passos & Charbonneau 2014). The simulation of Ghizaru et al. (2010) contained both coherent magnetism (field strengths peaking just below the

tachocline) and regular polarity reversals. Racine et al. (2011) ran Ghizaru et al. (2010)'s simulation further and identified significant torsional oscillations. Racine et al. (2011) also fitted the turbulently generated emf to a full α-tensor. This mean-field analysis suggested that the dynamo cycle was driven primarily by the torsional oscillations. Furthermore, the presence of strong magnetic field significantly reduced the differential rotation contrast by a factor of $\sim$3, an effect we also observe in the MHD simulation with magnetically confined tachocline discussed in Chapter 5. Finally, Passos & Charbonneau (2014) ran a simulation similar to that of Ghizaru et al. (2010) and Racine et al. (2011), but with the addition of explicit numerical diffusion for the purpose of stabilizing the solution. This "Millennium Simulation" was run for an extended interval, achieving stable, regular cycling behavior for over 1650 years. Passos & Charbonneau (2014) identified several behaviors similar to the solar cycle: A "sunspot" cycle (with a period of $\sim$40 years), a Gleissberg modulation (with a long-term periodicity of $\sim$100 years), and a Gnevyshev-Ohl rule (adjacent cycles alternating in strength; Gnevyshev & Ohl 1948).

Magneto-shear (or magneto-rotational) instabilities (Balbus & Hawley, 1991) and magneto-buoyancy instabilities are likely important effects in the solar tachocline, where concentrations of toroidal magnetic field exist amidst strong gradients in the rotation rate. These effects can make magnetic fields at certain horizontal wavenumbers unstable, possibly contributing to the low latitudes of sunspot emergence and the high latitudes of ephemeral active regions (Gilman, 2018a,b). Lawson et al. (2015) searched the Millennium Simulation for such MHD instabilities, using a slightly different version of the simulation that included an additional friction term at the base of the stable layer to damp out numerically unstable gravity modes (this was also done in Alvan et al. 2014, 2015). Lawson et al. (2015) calculated the phasing between various components of the magnetic and kinetic energies in the tachocline, and identified the same non-axisymmetric magneto-shear instability (azimuthal wavenumber $m = 1, 2$) of Miesch (2007).

More `EULAG-MHD` tachocline simulations were presented in Guerrero et al. (2016a,b, 2019), with results largely in-line with previous work. In Guerrero et al. (2016a,b), the simulations with a tachocline were shown to produce larger-scale, longer-cycle, more coherent, and stronger magnetic

fields than their convection-zone-only counterparts. Similar results were also obtained by Bice & Toomre (2020), who used the `Rayleigh` code to simulate M dwarfs with and without a tachocline, by Augustson et al. (2012, 2013), who used `ASH` to simulate dynamos in F-type stars, and by Brun et al. (2022), who used `ASH` to simulate dynamos in G- and K-type stars. The models of Guerrero et al. (2019) were unique in that they reproduced the observed increase of dynamo cycle period (e.g., Noyes et al. 1984; Böhm-Vitense 2007, whereas the opposite trend (decrease in cycle period with rotation period) was reported in the prior investigation of Strugarek et al. (2017). It should finally be noted that many of the simulations in Guerrero et al. (2016a,b, 2019) achieved some striking solar-like differential rotation, including a tachocline (as was expected from their sub-grid-scale diffusion technique), tilted isorotation contours, and the most solar-like NSSL achieved to date in a global model. The tilt of the isorotation contours was further observed in the `EULAG-MHD` models of Beaudoin et al. (2018) and attributed to the build-up of an equator-to-pole temperature contrast caused by rotationally influenced convective overshoot.

1.3 Our Approach to Global Simulations

Here, we briefly describe the numerical attributes of the global simulations presented in this thesis. Our models were all run with the `Rayleigh` code and shared many of the same properties, like boundary conditions, background states, and geometry. We describe these common properties here, to avoid repeating them in the subsequent Chapters when possible. In all cases, we consider a spherical shell of fluid, representative of the solar interior, governed by the one-fluid equations of (magneto)hydrodynamics, or (M)HD. The shell extends from a deep inner radius ($r_{\rm i} \sim 0.49 R_\odot$ or $r_{\rm i} \sim 0.72 R_\odot$) to a near-surface outer radius $r_{\rm o} \sim 0.95 R_\odot$, and thus covers $\sim$75% of the convection zone (by radius), and sometimes a portion of the radiative interior. We describe the shell using the standard spherical coordinates r (radius), θ (colatitude), and ϕ (azimuth angle), and the corresponding unit vectors $\hat{\mathbf{e}}_r$, $\hat{\mathbf{e}}_\theta$, and $\hat{\mathbf{e}}_\phi$. We also use the cylindrical coordinates $(\lambda, \phi, z) = (r \sin\theta, \phi, r\cos\theta)$ and unit vectors ($\hat{\boldsymbol{e}}_\lambda$, $\hat{\boldsymbol{e}}_\phi$, $\hat{\boldsymbol{e}}_z$). We use the following terms interchangeably: "vertical" $\leftrightarrow$ "radial," "toroidal" $\leftrightarrow$ "ϕ component," and "poloidal" $\leftrightarrow$ "r and θ components."

1.3.1 The Anelastic MHD Equations

In stellar interiors, the plasma is less dense further from the core, and this density contrast (or stratification) is an essential feature. For example, there is pronounced asymmetry between upflows and downflows in stratified solar-like convection (e.g., Miesch et al. 2000; Brun & Toomre 2002; also see Figure 1.5), whereas there is up-down symmetry in classical Rayleigh-Bénard convection (e.g., Chandrasekhar 1961). In the anelastic approximation (e.g., Gough 1969; Glatzmaier 1984; Jones et al. 2011), compressibility is kept in the sense that the density (ρ) can vary weakly in space and time so that the overall radial stratification is captured. However, the rapid fluctuations in ρ as occur in sound waves are filtered out. This allows the simulations to have long time-steps and run for decades-long time-scales (thus capturing dynamo behavior), which is not possible if the simulations are required to track the fast sound waves. The approximation is appropriate for a low-Mach-number flow, wherein the velocities are much smaller than the sound-speed and the sound waves are thus decoupled from the rest of the dynamics. Mathematically, the anelastic approximation simply corresponds to setting the time-derivative of density ($\partial\rho/\partial t$) in the continuity equation to zero.

We denote the total density, temperature, specific entropy, and pressure of the fluid by ρ, T, S, and P (respectively) and the fluid velocity and magnetic fields by $\boldsymbol{v}$ and $\boldsymbol{B}$ (respectively). The anelastic approximation is then $\nabla\cdot(\rho\boldsymbol{v})=0$. Additionally, it is assumed (as in the Boussinesq equations—e.g., Spiegel & Veronis 1960) that perturbations in the thermodynamic variables away from the 1-D background are small. Each thermodynamic variable is thus written as, e.g., $\rho=\overline{\rho}+\hat{\rho}$, where $\overline{\rho}$ is the "background," or "reference" density (which can vary slowly in space, and technically also in time) and the "perturbed" density $\hat{\rho}$ is small, so $|\hat{\rho}|\ll\overline{\rho}$. In the `Rayleigh` code (and all the other global codes we are aware of), slow rotation, well below break-up, is assumed. The Sun is thus treated as spherically symmetric to first-order and the centrifugal force is neglected. We also assume that the reference thermodynamic state is time-independent and spherically symmetric—i.e., $\overline{\rho}=\overline{\rho}(r)$ and $\nabla\overline{\rho}=(d\overline{\rho}/dr)\hat{\boldsymbol{e}}_r$, and similarly for the other reference thermodynamic variables

$\overline{P}(r)$, $\overline{T}(r)$, and $\overline{S}(r)$.

In stellar radiative interiors, energy is transported solely by radiation, which can be regarded as a thermal diffusion (e.g., Eddington 1916; Rosseland 1930; Collins 1989). In global MHD codes, the complicated thermodynamics governing the interior opacity is usually neglected. In `ASH` (e.g., Brun & Toomre 2002) and `Pencil` (e.g., Brandenburg 2016), the radiative diffusive coefficient is treated as a simple function of radius. In `Rayleigh`, the "radiative diffusion" does not operate like a conductive flux, and instead is treated as a source of heat, $Q(r)$. The heat source is fixed a priori and is independent of density and temperature perturbations, chemical composition, etc. $Q(r) \rightarrow 0$ near the outer surface so that instead of radiative cooling, a thermal flux $\boldsymbol{\mathcal{F}}_{\rm cond}$ carries away the solar luminosity. More specifically, $Q(r)$ is chosen to have the fixed radial profile $Q(r) = \alpha[\overline{P}(r) - \overline{P}(r_{\rm o})]$ (nonzero only in the convection zone), with the normalization constant α chosen such that a solar luminosity $L_\odot = 3.846 \times 10^{33}$ erg s^{-1} is forced through the domain (see Featherstone & Hindman 2016a). This prescription for the internal heating function coincides well with the radiative heating calculated by more sophisticated solar models (see model S described in Christensen-Dalsgaard et al. 1996, for example). In particular, $Q(r)$ is concentrated roughly in the bottom third of the convection zone and thus resembles (to some degree) the "heating from below" in Rayleigh-Bénard convection and in other global simulations.

With these assumptions, the MHD equations reduce to

$$\begin{aligned}\overline{\rho}(r)\frac{\partial \boldsymbol{v}}{\partial t} =& -\overline{\rho}(r)\boldsymbol{v}\cdot\nabla\boldsymbol{v} - 2\overline{\rho}(r)\boldsymbol{\Omega}_0\times\boldsymbol{v} - \overline{\rho}(r)\nabla\left[\frac{\hat{P}}{\overline{\rho}(r)}\right] \\ &+ \overline{\rho}(r)\left(\frac{\hat{S}}{c_{\rm p}}\right)g(r)\hat{\boldsymbol{e}}_r + \nabla\cdot\boldsymbol{D} + \frac{1}{4\pi}(\nabla\times\boldsymbol{B})\times\boldsymbol{B}, \qquad (1.1a)\end{aligned}$$

$$\begin{aligned}\text{and}\qquad \overline{\rho}(r)\overline{T}(r)\frac{\partial \hat{S}}{\partial t} =& -\overline{\rho}(r)\overline{T}(r)\boldsymbol{v}\cdot\nabla\hat{S} - \overline{\rho}(r)\overline{T}(r)v_r\frac{d\overline{S}}{dr} \\ &+ \nabla\cdot[\overline{\rho}(r)\overline{T}(r)\kappa(r)\nabla\hat{S}] + Q(r) + \boldsymbol{D}:\nabla\boldsymbol{v} + \frac{\eta}{4\pi}|\nabla\times\boldsymbol{B}|^2, \qquad (1.1b)\end{aligned}$$

$$\frac{\partial \boldsymbol{B}}{\partial t} = \nabla\times[\boldsymbol{v}\times\boldsymbol{B} - \eta(r)\nabla\times\boldsymbol{B}], \qquad (1.1c)$$

$$\nabla\cdot[\overline{\rho}(r)\boldsymbol{v}] = 0, \qquad (1.1d)$$

$$\text{and}\qquad \nabla\cdot\boldsymbol{B} = 0, \qquad (1.1e)$$

which are the momentum, entropy (equivalently, energy or heat), and induction equations, followed by the continuity equation and "no magnetic monopoles" (or "solenoidal") condition, respectively (e.g., Clune et al. 1999; Featherstone & Hindman 2016a). Here, $\boldsymbol{D} = \overline{\rho}(r)\nu(r)[\nabla\boldsymbol{v} + \nabla\boldsymbol{v}^T - (2/3)(\nabla\cdot\boldsymbol{v})\boldsymbol{I}]$, $\boldsymbol{I}$ is the identity tensor, $c_{\rm p} = 3.5\times10^8$ erg g^{-1} K^{-1} is the specific heat at constant pressure, $\nu(r)$, $\kappa(r)$, and $\eta(r)$ are the momentum, thermal, and magnetic diffusivities (respectively), and $\boldsymbol{g}(r)$ is the body force. All simulations in this thesis have a thermal Prandtl number of unity (Pr $\equiv \nu/\kappa = 1$, or $\nu = \kappa$), though the magnetic Prandtl number (Pr$_{\rm m} \equiv \nu/\eta$) takes on other values (Pr$_{\rm m}$ is nevertheless never far from unity). All diffusivity profiles have the same radial shape, so each Prandtl number is constant. Strictly, $\boldsymbol{g}(r)$ should be the "effective" gravity, including both the gravitational and centrifugal accelerations. Since the centrifugal term is ignored, $\boldsymbol{g}(r) = \nabla(GM_\odot/r)$, where G is the gravitational constant and $M_\odot \equiv 1.9989\times10^{33}$ g is the mass of the Sun (the self-gravity of the shell is ignored). We also denote the magnitude of gravitational acceleration by $g(r) \equiv |\boldsymbol{g}(r)| = GM_\odot/r^2$.

In a real star, the molecular diffusivities are almost entirely negligible, and so here $\nu(r)$, $\kappa(r)$, and $\eta(r)$ must be regarded as sub-grid-scale representations of unresolved turbulence. For simplicity, they appear in Equations (1.1) as turbulently enhanced values with the same form as the Newtonion diffusivities. The actual turbulent transport is not a diffusive process, however, and the choice of enhanced diffusivities is made primarily for computational tractability. For full consistency with classical theory, $\nu(r)$, $\kappa(r)$, and $\eta(r)$ would be chosen based on various mixing-length-theory assumptions for the Sun (e.g., Brandenburg 2016 and references therein). In our work, however, we simply choose the diffusivities to be arbitrary functions of density. We note that the heat conduction diffuses the entropy instead of the temperature: the conductive heat flux is $\boldsymbol{\mathcal{F}}_{\rm cond} = -\overline{\rho}(r)\overline{T}(r)\kappa(r)\nabla\hat{S}$, which is meant to capture the unresolved turbulent mixing of heat. A moving fluid parcel carries heat energy that is proportional to its entropy content, $\hat{S}$, which initially is the same as the entropy of the background fluid. If the fluid parcel moves adiabatically and then mixes its heat energy with the surrounding fluid after traveling a small distance, there will be an associated unresolved (or "eddy") thermal-energy flux proportional to $\nabla\hat{S}$.

Our models employ a perfect gas for the equation of state. Combined with the first law of thermodynamics and the assumption of small thermodynamic perturbations, the perfect gas equation takes the form

$$\frac{\hat{\rho}}{\overline{\rho}} = \frac{\hat{P}}{\overline{P}} - \frac{\hat{T}}{\overline{T}} = \frac{\hat{P}}{\gamma \overline{P}} - \frac{\hat{S}}{c_{\rm p}}, \tag{1.2}$$

where $\gamma = c_{\rm v}/c_{\rm p}$ ($c_{\rm v}$ is the specific heat at constant volume, or equivalently, constant density). We assume full ionization and three translational degrees of freedom, yielding $\gamma = 5/3$ throughout the Sun. We note that although the thermodynamics is linearized in Equation (1.2), the velocity and magnetic fields are fully nonlinear in Equations (1.1).

The reference state is required to be in hydrostatic balance,

$$\frac{d\overline{P}}{dr} = -\overline{\rho} g, \tag{1.3}$$

satisfy the first law of thermodynamics,

$$\frac{1}{c_{\rm p}} \frac{d\overline{S}}{dr} = \frac{1}{\gamma \overline{P}} \frac{d\overline{P}}{dr} - \frac{1}{\overline{\rho}} \frac{d\overline{\rho}}{dr}, \tag{1.4}$$

and be a perfect gas,

$$\overline{P} = \overline{\rho} \mathcal{R} \overline{T}, \tag{1.5}$$

where $\mathcal{R} = (\gamma - 1) c_{\rm p}/\gamma$ is the gas constant. We note that strictly $\mathcal{R} = k_B/\mu m_H$ (with μ the mean molecular weight, k_B Boltzmann's constant, and m_H the mass of the hydrogen atom) should be radially varying, especially between the well-mixed convection zone and slowly-circulating radiative interior. For simplicity, we do not consider compositional mixing and treat $\mu = 0.59$ as a constant in both space and time, its value determined from the canonical mass fractions for hydrogen ($X = 0.75$) and helium ($Y = 0.25$). We ignore the nonzero metallicity and assume full ionization.[14] This in turn yields $c_{\rm p} = 3.5 \times 10^8$ erg g^{-1} K^{-1}.

Once Equations (1.3)–(1.5) are assumed, the background state can be specified entirely by the choice of $g(r)$ (we have chosen $g(r) = GM_\odot/r^2$) and $d\overline{S}/dr$ (see Chapter 5 for details). All of

[14] Recall that $\frac{1}{\mu} = 2X + \frac{3}{4}Y$ for a fully ionized gas with no metals.

the simulations in this thesis include a convection zone, which we enforce by choosing $d\overline{S}/dr = 0$. This stratification is equivalent to a polytrope with index $n = 1.5$ (see Jones et al. 2011 for details). Although the background state is thus technically not unstable (but marginally stable), the system still convects, driven both by the internal heating (concentrated in the lower layers) and the outer conductive cooling layer (concentrated in the upper lowers). Once the convection is established, the spherically symmetric part of $\partial\hat{S}/\partial r$ becomes < 0, i.e., the convection zone becomes slightly superadiabatic. Thus, our simulations act conversely to classical mixing-length theory: the convection drives the superadiabatic gradient.

In writing Equation (1.1a), the Lantz-Braginsky-Roberts (LBR) approximation (Lantz, 1992; Braginsky & Roberts, 1995) is used. Equations (1.3)–(1.5) show that the buoyancy force is

$$-\frac{1}{\overline{\rho}}\nabla\hat{P} - \frac{\hat{\rho}}{\overline{\rho}}g\hat{\boldsymbol{e}}_r = -\nabla\left(\frac{\hat{P}}{\overline{\rho}}\right) + \left(\frac{\hat{S}}{c_{\rm p}}\right)g\hat{\boldsymbol{e}}_r + \frac{\hat{P}}{\overline{\rho}}\frac{1}{c_{\rm p}}\frac{d\overline{S}}{dr}\hat{\boldsymbol{e}}_r. \tag{1.6}$$

The LBR momentum equation (1.1a) thus consists of ignoring the term due to the background entropy gradient in the buoyancy, which will be exact for an adiabatic ($d\overline{S}/dr = 0$) reference state—in our models, the convection zone. Of course, for simulations including a tachocline and layer of strong stable stratification ($d\overline{S}/dr > 0$), the LBR approximation should be inapplicable. Research on this topic is far from conclusive, but simulations of small Cartesian boxes of fluid show that LBR may be the best form of the anelastic approximation in stable layers, despite being mathematically incorrect. LBR correctly conserves energy in the excited gravity-wave field, whereas anelastic formulations that keep the entropy-gradient term in the buoyancy do not (Brown et al., 2012; Vasil et al., 2013). Notably, these Cartesian investigations only explored an isothermal atmosphere, and so the energy-conserving properties of LBR in our stable layers, which have radially varying $\overline{T}(r)$, are unknown.

1.3.2 Initial and Boundary Conditions

Equations (1.1), combined with Equations (1.2), form a system of nonlinear partial differential equations in eight variables ($\hat{S}$, $\hat{P}$, and the three components each of $\boldsymbol{v}$ and $\boldsymbol{B}$) that is first-order

in time and second-order in space. The system thus requires eight initial conditions (one for each variable) and sixteen boundary conditions (one at both the inner and outer boundaries for each variable; see Equation (1.7) below). The coefficients of the system are non-constant but only depend on the radial coordinate r.

In the HD variables ($\hat{S}$, $\hat{P}$, and the three components of $\boldsymbol{v}$), we initialize the system with randomly distributed small ($\sim$10 erg g^{-1} K^{-1}) fluctuations in $\hat{S}$ (equivalent to $\hat{S}/c_\mathrm{p} \sim 10^{-8}$) and set the other fluid variables to zero. These thermal perturbations quickly yield nonzero fluctuations in $\boldsymbol{v}$ and $\hat{P}$, and then become convectively unstable, reaching amplitudes of $\hat{S} \sim 10^3$ erg g^{-1} K^{-1} (and corresponding buoyantly-driven radial velocities of $v_r \sim 100$ m s^{-1}) in the most turbulent cases. If the simulation is MHD (including $\boldsymbol{B}$), small ($\sim$1 G) magnetic perturbations B' are included as an initial condition in parallel with the thermal perturbations (equivalent to $\sqrt{(B'^2/8\pi)/\overline{P}} \sim 10^{-8}$). Dynamo action (exponential amplification of the initial seed field to amplitudes of $\sim 10^4$ G for the strongest dynamos) is possible, but not guaranteed.

Each boundary of the shell is treated as an impenetrable sphere that is stress-free. In the MHD simulations, the magnetic field is matched onto a potential field at both boundaries. At the inner boundary, there is no conductive heat flux, and at the outer boundary, there is either an outward conductive flux of the solar luminosity $L_\odot$, or else fixed entropy. All simulations in this thesis thus share the following boundary conditions:

$$v_r = 0 \qquad \text{at } r_\mathrm{i} \text{ and } r_\mathrm{o} \qquad \text{(impenetrable)}, \tag{1.7a}$$

$$\frac{\partial}{\partial r}\left(\frac{v_\theta}{r}\right) = \frac{\partial}{\partial r}\left(\frac{v_\phi}{r}\right) = 0 \qquad \text{at } r_\mathrm{i} \text{ and } r_\mathrm{o} \qquad \text{(stress-free)}, \tag{1.7b}$$

$$\boldsymbol{B} = \nabla\Phi \quad \text{where} \quad \nabla^2\Phi = 0 \qquad \text{at } r_\mathrm{i} \text{ and } r_\mathrm{o} \qquad \text{(match to potential field)}, \tag{1.7c}$$

$$\frac{\partial \hat{S}}{\partial r} = 0 \qquad \text{at } r_\mathrm{i} \qquad \text{(fixed flux)}, \tag{1.7d}$$

$$\text{and} \quad \hat{S} = 0 \quad \textit{or} \quad \frac{\partial \hat{S}}{\partial r} = -\frac{L_\odot}{4\pi r_\mathrm{o}^2 \overline{\rho}(r_\mathrm{o})\overline{T}(r_\mathrm{o})\kappa(r_\mathrm{o})} \qquad \text{at } r_\mathrm{o}$$

$$\text{(fixed flux } \textit{or} \text{ fixed entropy)}. \tag{1.7e}$$

The outer boundary condition on the entropy (either one) ensures that as the system equilibrates, a

sharp gradient in the spherical mean of $\hat{S}$—i.e., a thermal boundary layer—develops near the outer surface, which carries out the solar luminosity via thermal conduction. Recall that in a stellar convection zone, by contrast, the luminosity is ultimately carried out by radiative cooling.

1.3.3 The `Rayleigh` Code

The `Rayleigh` code (Featherstone & Hindman, 2016a; Matsui et al., 2016; Featherstone et al., 2021) solves the LBR anelastic equations of (M)HD. The underlying serial algorithm of `Rayleigh` closely follows that of the `Anelastic Spherical Harmonic (ASH)` code (e.g., Clune et al. 1999; Brun et al. 2004) but is open-source and has a highly efficient parallel algorithm, scaling well on up to half a million CPU cores. To strictly enforce the anelastic approximation, $\nabla \cdot (\rho \boldsymbol{v}) = 0$, and solenoidal condition, $\nabla \cdot \boldsymbol{B} = 0$, the vector velocity field is decomposed into two streamfunctions and the vector magnetic field into two flux-functions:

$$\rho \boldsymbol{v} = \nabla \times \nabla \times (W \hat{\boldsymbol{e}}_r) + \nabla \times (Z \hat{\boldsymbol{e}}_r), \tag{1.8a}$$

$$\boldsymbol{B} = \nabla \times \nabla \times (C \hat{\boldsymbol{e}}_r) + \nabla \times (A \hat{\boldsymbol{e}}_r) \tag{1.8b}$$

This formalism satisfies Equations (1.1d)–(1.1e) by construction, and further reduces the other Equations (1.1a)–(1.1b) to a system in six unknowns ($\hat{S}$, $\hat{P}$, W, Z, C, and A), requiring six initial conditions and twelve boundary conditions. Physically, the streamfunctions W and Z are related to the radial velocity and vorticity, respectively (C and A are related to the radial magnetic field and current density, respectively). For example, if we decompose $W(r, \theta, \phi, t) = \sum_{\ell m} W_{\ell m}(r, t) Y_{\ell m}(\theta, \phi)$, where the $Y_{\ell m}(\theta, \phi)$ are the spherical harmonics (and similarly for v_r), we find that the spectral coefficients are related by $(v_r)_{\ell m} = [\ell(\ell+1)/r^2] W_{\ell m}$.

Each variable is expanded on a discretized grid, using spherical harmonics in the horizontal directions (directions tangent to spherical surfaces) and Chebyshev polynomials in the vertical (radial) direction. The vertical grid is composed of one or more stacked domains of Chebyshev collocation points, which cluster near the ends of each domain. One Chebyshev domain is used for the convection-zone-only models and multiple domains are used for the models including a

radiative interior. Both the Chebyshev polynomials and the Legendre polynomials are dealiased by approximately one-third the number of collocation points. For example, if the vertical grid has N_r radial (Chebyshev) collocation points in a given domain, $2N_r/3$ Chebyshev polynomials are used in the vertical expansion for that domain. Similarly, if the horizontal grid has N_θ colatitudinal (Legendre) collocation points, spherical harmonics of maximum degree $\ell_{\max} = 2N_\theta/3$ are used in the expansion. The number of longitudinal (Fourier) collocation points is $N_\phi = 2N_\theta$ so that the azimuthal order m of the highest-degree spherical harmonics ranges from $-\ell_{\max}$ to $+\ell_{\max} - 1$.

The linear terms (e.g., diffusion and buoyancy) in Equations (1.1) are evaluated in spectral (Chebyshev and spherical-harmonic) space, while the nonlinear terms (e.g., advection, induction, and the Coriolis force even though it is technically linear) are evaluated in physical space. The time is advanced using a semi-implicit Crank-Nicolson scheme for the linear terms and an explicit Adams-Bashforth scheme for the nonlinear terms. The use of both spectral and physical space at each time step makes the code "pseudo-spectral." See, e.g., Clune et al. (1999) for details on Rayleigh's anelastic, pseudo-spectral algorithm, and Featherstone et al. (2021) for details on its parallel structure.

1.4 Structure of this Thesis

In the subsequent four Chapters, we describe the research results of this thesis. Chapters 2–4 are essentially restatements of the three publications, Matilsky et al. (2019) (see also the conference proceedings paper, Matilsky et al. 2018), Matilsky et al. (2020), and Matilsky & Toomre (2020a) (see also the conference proceedings paper, Matilsky & Toomre 2020b), respectively. The work presented in Chapter 5 is currently being prepared for an upcoming publication, Matilsky et al. (2022) and was briefly described in the conference proceedings paper, Matilsky & Toomre (2021). We broadly divide our research into two classes: dynamics of the Sun without magnetism (HD) and dynamics with magnetism (MHD). In Chapter 2 (first HD Chapter), we present our findings on the torque balance achieved in the solar Near-Surface Shear Layer (Matilsky et al., 2018, 2019). In Chapter 3 (second HD Chapter), we present our substantial progress in understanding the cause of the

helioseismically observed isorotation contour tilts (Matilsky et al., 2020). In Chapter 4 (first MHD Chapter), we describe in detail the remarkable phenomenon of "bistability," in which the global solar dynamo is found to be capable of supporting two very different cycles simultaneously (Matilsky & Toomre, 2020a,b). In Chapter 5 (second MHD Chapter), we present and dynamically analyze an MHD simulation that appears to yield a magnetically confined tachocline self-consistently (Matilsky & Toomre, 2021; Matilsky et al., 2022). Finally, in Chapter 6, we present some concluding remarks and directions of future research.

Chapter 2

The Role of Downflows in Establishing Solar Near-Surface Shear

As discussed in Section 1.1.3, the fine structure of the internal rotation of the Sun is intimately tied to the solar dynamo. The dynamo therefore cannot be understood without explaining the salient features of the differential rotation. Because the two problems are coupled through mean-shear induction ($\Omega \rightarrow \boldsymbol{B}$) and the Lorentz force ($\boldsymbol{B} \rightarrow \Omega$), it is likely that a complete understanding of each is only accessible through reproducing both the butterfly diagram and the differential rotation simultaneously. We begin the research portion of this thesis by describing our work treating the differential rotation separately—i.e., in a purely hydrodynamic (HD) setting.

Often, the tachocline is invoked as the main source of the interior shear that must create large-scale solar toroidal magnetic field. However, as pointed out in Brandenburg (2005), the dynamo may in fact be "distributed," operating in both the tachocline and Near-Surface Shear Layer (NSSL). The NSSL, though it has weaker shear than the tachocline does, is closer to the surface and thus may play a larger role in sunspot emergence than is usually assumed. The NSSL is also the oldest known feature of the Sun's internal rotation rate. Before helioseismology confirmed its presence (and mapped its latitudinal structure), it was discovered through tracking sunspots over 50 years ago. Sunspots were believed to be "magnetically anchored" below the photosphere and were observed to move with the solar rotation faster than the surrounding gas. This implied that the rotation rate increased with depth close to the surface (Howard & Harvey, 1970; Wilcox et al., 1970). The magnitude of the shear estimated back then (rotation rate falling with radius by $\sim$5% over the outer $\sim$5% of the Sun) still agrees with current helioseismic deductions.

We have attempted to self-consistently reproduce the solar NSSL in numerical simulations of a solar-like convection zone by increasing the density contrast across rotating, 3-D spherical shells. We explore the hypothesis that high density contrast leads to near-surface shear by creating a rotationally unconstrained layer of fast flows near the outer surface. Although our high-contrast models do have near-surface shear, it is confined primarily to low latitudes (between $\pm 15^{\circ}$). Two distinct types of flow structures maintain the shear dynamically: rotationally constrained *Busse columns* that transport angular momentum outward, and rotationally unconstrained *downflow plumes* that deplete angular momentum from the outer fluid layers. The plumes form at all latitudes, and in fact are more efficient at transporting angular momentum inward at high latitudes. The presence of Busse columns at low latitudes thus appears essential to creating near-surface shear in our models. We conclude that a solar-like NSSL is unobtainable from a rotationally unconstrained outer fluid layer alone. In numerical models, the shear is eliminated through the advection of angular momentum by the meridional circulation. Therefore, a detailed understanding how the solar meridional circulation is dynamically achieved will be necessary to elucidate the origin of the Sun's NSSL.

This Chapter is primarily a restatement of the publication Matilsky et al. (2019) (also see the related conference proceedings paper, Matilsky et al. 2018). However, we add some additional perspectives informed by recent NSSL studies over the last few years. As the primary author of the paper, I conducted the simulations, performed their analyses, created the Figures, and wrote the text. My two coauthors Juri Toomre and Bradley Hindman provided advice and guidance throughout the process, gave detailed text edits, and suggested schematic designs of some of the Figures. Special thanks is owed to Nicholas Featherstone, who formulated the idea of creating a rotationally unconstrained near-surface fluid layer in simulations by increasing the density contrast, and also for providing me with a pre-release version (`0.9.1`) of the `Rayleigh` code.

2.1 Introduction: Our Theoretical Understanding of the Solar Near-Surface Shear Layer (NSSL)

Helioseismology has revealed the presence of two boundary layers of shear at the top and bottom of the solar convection zone (CZ). In the *tachocline* at the bottom, differential rotation in the CZ transitions sharply to solid-body rotation in the radiative zone below (see Figure 2.1). At the top of the CZ, there is a 5% reduction in rotation rate with increasing radius over a radial distance of ∼35,000 km, which is largely a uniform feature at all latitudes. This latter feature is known as the *Near-Surface Shear Layer* (NSSL). Both boundary layers may play a significant role in the solar dynamo, since rotational shear creates toroidal magnetic field from poloidal field through the Ω-effect. However, the dynamical origins of these boundary layers are still not well understood.

The solar differential rotation (from Figure 2.1, the equator rotates about 30% faster than the poles) is believed to be the result of convectively driven Rossby waves, which manifest in the solar CZ as *Busse columns*, also known as *banana cells* in the literature (e.g., Gilman 1972; Busse 2002; Brun & Toomre 2002; Nelson et al. 2018). Busse columns are convective rolls of fluid aligned with the rotation axis. Each roll has a cross-sectional tilt in the equatorial plane such that upflows move prograde and downflows move retrograde, the net result being the transport of angular momentum away from the rotation axis (see Figure 6 of Busse 2002). The Busse columns thus tend to spin up the equator (which is far from the rotation axis) compared to the polar regions, which are close to the rotation axis.

By contrast, in the NSSL (see Figure 2.1), the surface layers rotate 5% *slower* than the layers just below. Foukal & Jokipii (1975) hypothesize the following explanatory mechanism for the formation of the NSSL: Fluid parcels conserve their specific angular momentum $\mathcal{L}$ in the outermost layers of the Sun as they move in the radial direction. Thus, for a steady-state system, the angular-momentum profile $\mathcal{L}(r)$ should be constant with radius. Since specific angular momentum is related to the local fluid rotation rate Ω through $\mathcal{L} = \Omega r^2 \sin^2\theta$, this would imply $\Omega \propto 1/r^2$ along a radial

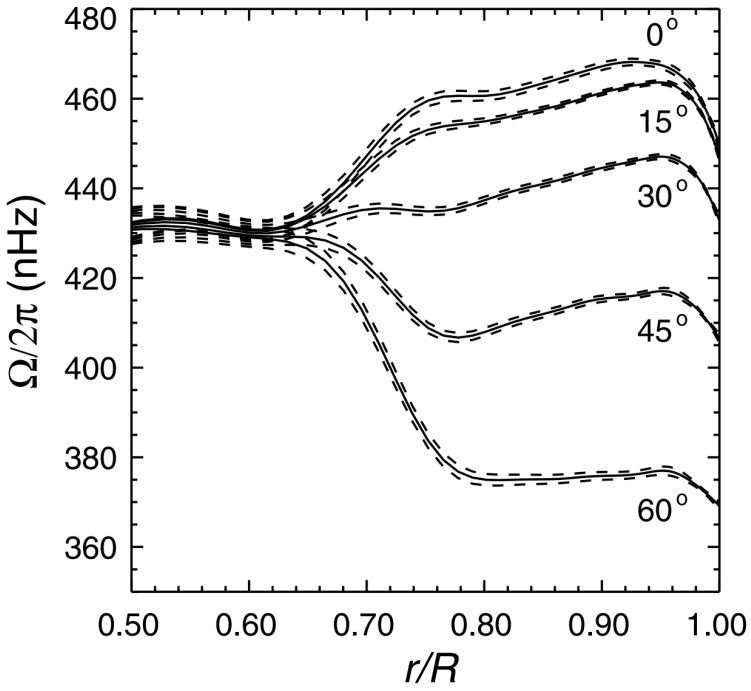

Figure 2.1: **Helioseismically Inferred Rotation Rate (with Errors)**. Temporally and longitudinally averaged solar rotation rate $\Omega/2\pi$ obtained from an inversion of GONG frequency splittings. Rotation rate is plotted as a function of the fractional solar radius at different latitudes. The dashed lines represent 1σ error bounds for a single inversion. Figure credit: Howe et al. (2000).

line in the outermost fluid layers—a decrease in rotation rate with radius.

In order to successfully homogenize angular momentum, the flows need to be free from rotational constraint so that they do not get captured by Busse-column rolls. The degree of rotational constraint is parameterized by the *Rossby number* Ro, which is the ratio of rotation period to convective overturning time. Thus, according to Foukal & Jokipii (1975), the Sun must possess a region near the outer surface in which

$$\mathrm{Ro} \equiv \frac{v'}{2\Omega_0 L} \gtrsim 1, \tag{2.1}$$

where v' is a typical velocity of the convective flow structures (that may vary with radius), L is their typical length scale and Ω_0 is the background rotation rate. Thus, a *rotationally unconstrained* fluid structure is one that is either fast, small-scale, or both. In the models explored here, we find that only the downflows (in particular, structures we call *downflow plumes*) are sufficiently fast and small-scale to be rotationally unconstrained.

Previous numerical simulations of rotating, spherical-shell convection that captured aspects of the solar NSSL have all possessed a layer of rotationally unconstrained fluid near the outer surface. Guerrero et al. (2013) saw an NSSL arise near the equator of their models due to the mixing of angular momentum by fast, high-Rossby-number convective motions. In modeling the banded "zonal jets" observed in longitudinal flows on the gas and ice giants, Gastine et al. (2013) found that high density contrast across the spherical shell ($\sim$150) enabled low-Rossby-number Busse columns to exist in the deep fluid layers and high-Rossby-number, small-scale convection to occur near the outer surface. Hotta et al. (2015) have come closest to a self-consistent reproduction of an NSSL in a model with density contrast across the shell of $\sim$613. They successfully achieved a Rossby-number transition with a thin rotationally unconstrained outer layer, and reported prominent near-surface shear at high latitudes.

Features of near-surface shear thus seem to appear in models with high density contrast. This is because increasing the density contrast across the spherical shell—while keeping the density at the inner surface fixed—decreases the near-surface density scale-height, which is thought to be a

good representative length-scale of the convection. The luminosity pumped into the system is also shed near the outer surface; if the fluid parcels there are much less dense, they will be endowed with a much greater temperature deficit and be accelerated higher (downward) speeds via the buoyancy force. Both effects serve to increase the Rossby number near the outer surface.

In this work, we systematically investigate the nature of rotationally unconstrained near-surface layers across a range of density contrasts in rotating spherical shells. We explicitly analyze the simulations at the two ends of this range, with contrasts of $\sim$20 and $\sim$150. We find the low-contrast simulation is entirely dominated by Busse columns at low latitudes, as expected. The high-contrast simulation, on the other hand, exhibits rotationally unconstrained fast flows near the outer surface, as in previous work. However, our analysis reveals that *only* the downflows are rotationally unconstrained and transport angular momentum inward, creating shear. The upflows still exist in Busse columns and transport angular momentum outward, even near the outer surface.

In Section 2.2, we describe the parameter space we explore. In section 2.3, we discuss the global character of the flows achieved, both instantaneously and averaged over time. In Sections 2.4 and 2.5, we describe the structure and evolution of Busse columns and downflow plumes, respectively. In Section 2.6, we discuss the dynamical balance of torques in our models and its relation to the simulated features of near-surface-shear. In section 2.7, we examine in detail the Reynolds stress from Busse columns and downflow plumes, which manifests in the separate upflow- and downflow-contributions to the angular-momentum flux. In Section 2.8, we discuss our results in the general context of meridional force balance.

2.2 Numerical Model

As described in Section 1.3, we numerically evolve a rotating, stratified shell of ideal gas using the `Rayleigh` code, here the pre-release version `0.9.1` (Featherstone & Hindman, 2016a; Matsui et al., 2016; Featherstone, 2018). The computational domain of the layer here consists of the CZ only: A spherical shell with inner radius $r_{\rm i} = 5.000 \times 10^{10}$ cm $= 0.719\ R_\odot$ and outer radius $r_{\rm o} = 6.586 \times 10^{10}$ cm $= 0.947\ R_\odot$, where $R_\odot \equiv 6.957 \times 10^{10}$ cm. Recall that `Rayleigh` makes

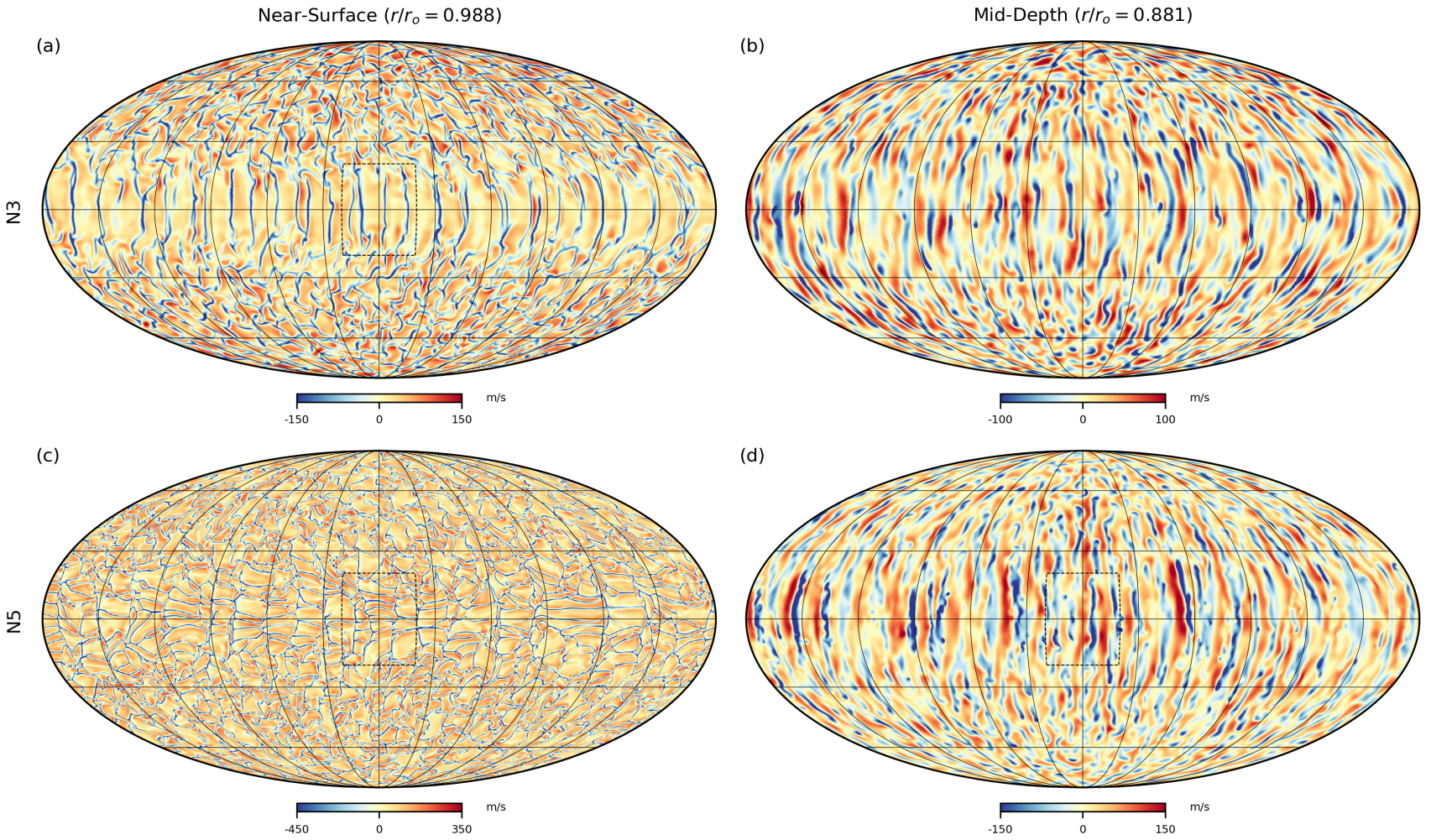

Figure 2.2: **Influence of Density Stratification on Flow Structures**. Mollweide projections of the radial velocity v_r on spherical surfaces for cases N3 and N5. Red tones indicate upflows ($v_r > 0$) and blue tones indicate downflows ($v_r < 0$). Two radial levels are sampled: a near-surface level ($r/r_\mathrm{o} = 0.988$) and a level mid-way through the domain ($r/r_\mathrm{o} = 0.881$). In panel (c), the colorbar is binormalized to highlight the asymmetry between upflows and downflows near the outer surface for case N5. The dashed $40^\circ \times 40^\circ$ box at the centers of panels (a), (c) and (d) show the regions that are magnified in later Figures.

use of the anelastic approximation to increase the maximum allowable time step by removing sound waves. Specifically, `Rayleigh` here solves Equations (1.1) with no magnetic terms and no reference-entropy-gradient term. The temporally steady and spherically symmetric reference state has adiabatic stratification ($d\overline{S}/dr = 0$; this is equivalent to a polytrope with index $n = 1.5$; see Jones et al. 2011 for a complete description), but develops a slightly superadiabatic spherical mean in $\hat{S}$ due to the convection. Setting the values of the density at the inner boundary and the overall density contrast across the shell fully determines the background state.

Recall that for all simulations described in this thesis, a solar luminosity $L_\odot$ is driven through the layer via a fixed internal heating function $Q(r)$ and is carried out via thermal conduction at the top boundary. Furthermore, all simulations have impenetrable, stress-free bottom and top boundaries, fixed-flux ($\partial\hat{S}/\partial r = 0$) bottoms. Here, the simulations have fixed-entropy ($\hat{S} = 0$) tops, they rotate at three times the solar Carrington rate ($3\Omega_\odot$) to ensure that a solar-like differential rotation (fast equator and slow polar regions) is attained,[1] and they have a Prandtl number ($\mathrm{Pr} \equiv \nu/\kappa$) of unity ($\nu$ and κ are spatially constant, each equal to 2×10^{12} cm^2 s^{-1} throughout the shell; all simulations in this thesis have a Prandtl number of unity). In this work, we compare two models with different density contrasts. The relevant model parameters are shown in Table 2.1. Here, N_ρ refers to the number of density scale heights across the domain. The density contrast from the inner to the outer boundaries (also shown in Table 2.1) is related to the number of scale heights by $\overline{\rho}_\mathrm{i}/\overline{\rho}_\mathrm{o} = \exp(N_\rho)$, where $\overline{\rho}_\mathrm{i}$ and $\overline{\rho}_\mathrm{o}$ refer to the values of $\overline{\rho}$ at the inner and outer boundaries, respectively. The *thermal diffusion time* T_diff (equivalently, the *viscous diffusion time*) estimates how long it takes for heat (momentum) to diffuse across the full spherical shell. The *averaging time* refers to the time interval used in the temporal averages of fluid quantities—e.g., differential rotation, meridional circulation and Reynolds stress. This interval coincides with the time from equilibration (total energy flux constant with radius) to the end of the simulation. All

[1] In this Chapter only, $\Omega_\odot = 2.6 \times 10^{-6}$ rad s^{-1}, which is the value of the solid-body rotation of the radiative interior according to Spiegel & Zahn (1992). It was thus often used in the early `ASH` models (e.g., Brun & Toomre 2002; Browning et al. 2006; Brown et al. 2010). In subsequent Chapters, $\Omega_\odot = 2.87 \times 10^{-6}$ rad s^{-1}, which is the sidereal Carrington rate.

input parameters are fixed in the two models, except for N_ρ, which takes on the values 3 and 5 (for density contrasts across the shell of $\sim$20 and $\sim$150, respectively). We refer to the resulting models as cases N3 and N5, respectively.

2.3 Global Flow Properties

Figure 2.2 shows the radial velocity of the flow on spherical surfaces near the outer boundary and at mid-depth for cases N3 and N5. At low latitudes, the alternating lanes of upflow and downflow are parallel to the rotation axis and indicate the locations of Busse-columns pairs. The columns at mid-depth have connectivity to their counterparts in the near-surface layers, but they are significantly slower and the downflow lanes are thicker, which is a consequence of the density stratification. At high latitudes, there is less noticeable alignment of the fluid structures with the rotation axis, although this may in part be due to angular distortion effects of the spherical projection. We note that in the near-surface layers of case N5, there are downflow lanes oriented north–south (parallel to meridians) *and* lanes oriented east–west (parallel to lines of latitude). The places where the two types of lanes cross we call *interstices*. We shall see that the interstices are sources of prominent *downflow plumes*, which evolve independently from the Busse columns and transport angular momentum in the opposite direction.

We turn next to the mean-flow properties of our models. The average radial profile of rotation rate at various latitudes for cases N3 and N5 is shown in Figure 2.3 and the full rotation rate in the meridional plane is shown in Figure 2.4. Case N3 exhibits the stronger differential rotation, with a variation of $\Delta\Omega = 155$ nHz from equator to pole. This corresponds to a *differential rotation fraction* of $\Delta\Omega/\Omega_0 = 0.125$. As the density contrast across the layer increases, the overall differential rotation $\Delta\Omega$ decreases, along with the differential rotation fraction. Case N5 has a differential rotation from equator to pole of only 81 nHz and a differential rotation fraction of $\Delta\Omega/\Omega_0 = 0.065$. We note that both these values of fractional differential rotation are significantly smaller than the value $\Delta\Omega_\odot/\Omega_\odot \sim 0.3$ observed in the Sun.

While the rotation rate in case N3 increases monotonically in both radius and latitude, case

Table 2.1: **Model Parameters for the NSSL Experiment**. Input Model Parameters for Cases N3 and N5. All parameters are displayed to 4 significant digits. N_r, N_θ, and N_ϕ refer to the number of grid points in the radial, colatitudinal, and longitudinal directions (respectively) in the computational domain. The *global* Ro refers to the Rossby number defined in Equation 2.1, averaged over the full spherical shell. We take the typical convective length scale to be $L = H_\rho(r) = -1/(d \ln \overline{\rho}/dr)$ (the local density scale height) and the typical speed $v'(r)$ to be the rms amplitude of the convective velocity (the velocity with the longitudinally averaged component subtracted), with the mean in the rms referring to an average in time and over a spherical surface of radius r.

Parameter	N3	N5
r_i	5.000×10^{10} cm	
r_o	6.586×10^{10} cm	
c_p	3.500×10^{8} erg K^{-1} g^{-1}	
ν	2.000×10^{12} cm^2/s	
κ	2.000×10^{12} cm^2/s	
γ	1.667	
$\overline{\rho}_\mathrm{i}$	0.1805 g/cm^3	
Ω_0	7.800×10^{-6} rad/s	
$\Omega_0/2\pi$	1,241 nHz	
$P_0 \equiv 2\pi/\Omega_0$	9.323 days	
$T_\mathrm{diff} \equiv (r_\mathrm{o} - r_\mathrm{i})^2/\kappa$	1,456 days (3.985 yr)	
N_ρ	3.000	5.000
$\overline{\rho}_\mathrm{i}/\overline{\rho}_\mathrm{o}$	20.10	148.4
(N_r, N_θ, N_ϕ)	(128, 768, 1536)	256, 1152, 2304)
Global Ro	0.1345	0.4793
Averaging time	53.78 yr	34.07 yr
	2,107 P_0	1,335 P_0
	13.50 T_diff	8.550 T_diff

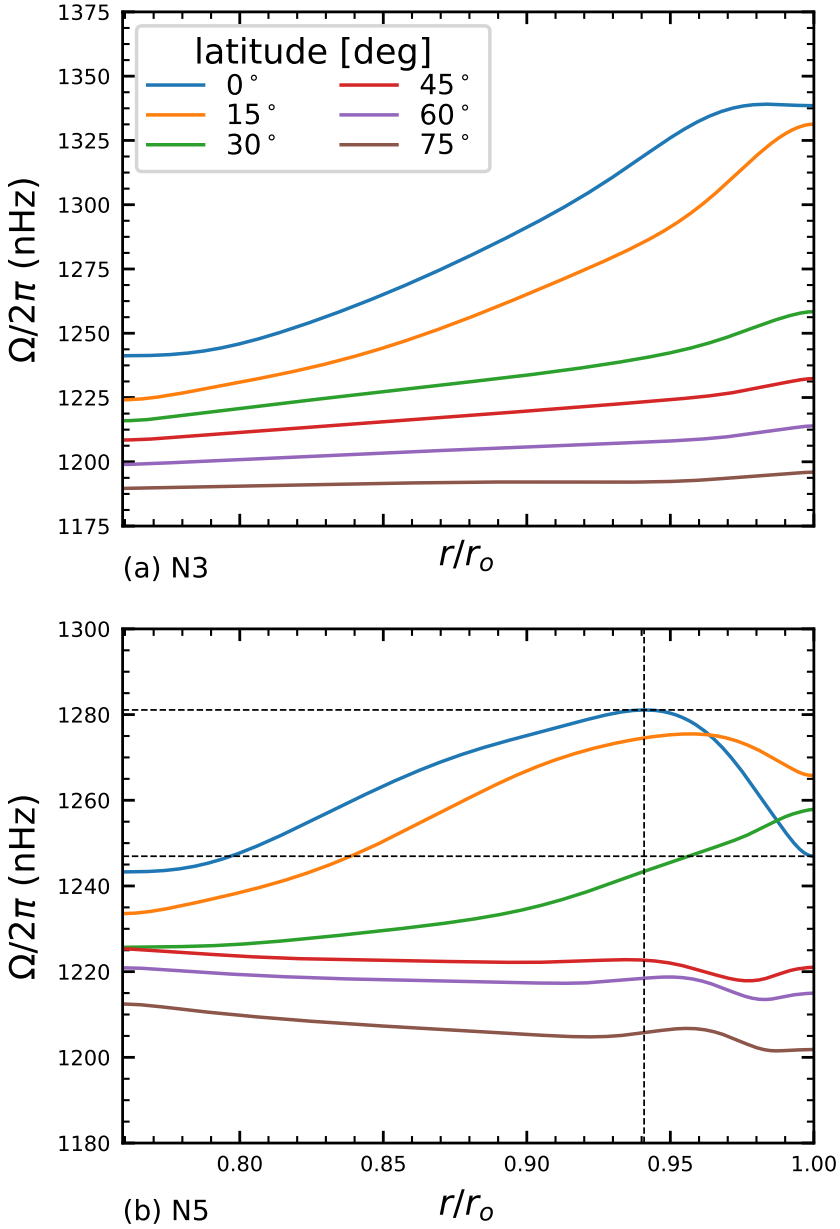

Figure 2.3: **Influence of Density Contrast on Rotation Profiles along Radial Lines**. Temporally and longitudinally averaged rotation rate as a function of radius at various latitudes for cases N3 and N5 (compare to the Sun's rotation rate in Figure 2.1). The location of the prominent *dip* in rotation rate in the equatorial region of case N5 is indicated by the vertical dashed line at $r/r_o = 0.941$ in panel (b). The amplitude of the dip is indicated by the two horizontal dashed lines separated by 34.1 nHz.

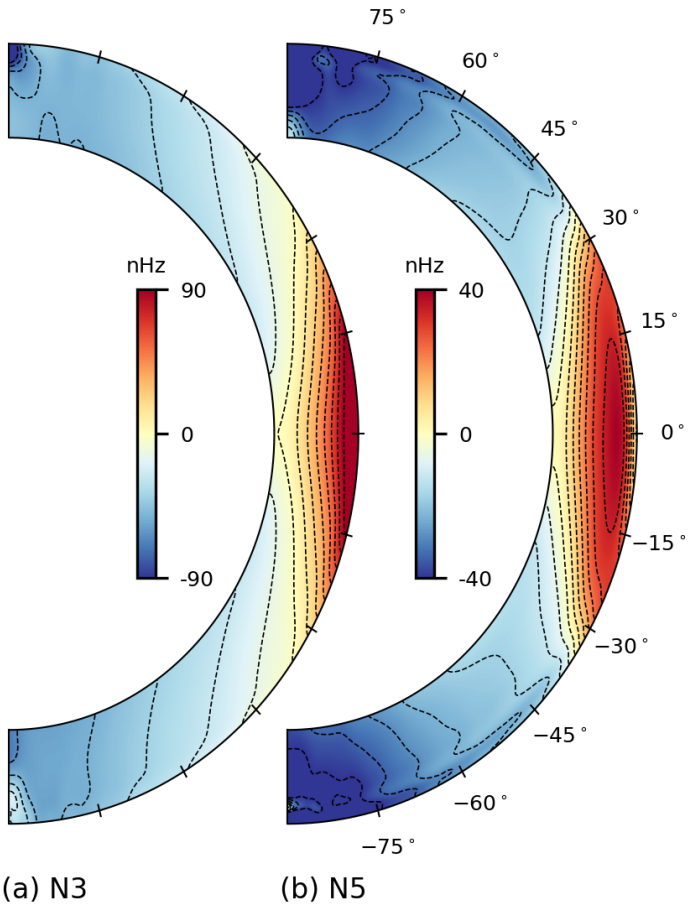

Figure 2.4: **Influence of Density Contrast on Rotation Frequency**. Temporally and longitudinally averaged rotation frequency in the meridional plane for cases N3 and N5, respectively. The frame rotation frequency $\Omega_0/2\pi$ has been subtracted off, so that positive values (red tones) indicate prograde rotation, while negative values (blue tones) indicate retrograde rotation. In each panel, there are 15 dashed contours, corresponding to rotation-frequency values that evenly divide the range indicated by the colorbar.

N5 exhibits features reminiscent of near-surface shear. The most prominent of these is a *dip* in the rotation rate at low latitudes near the outer surface. Here, the rotation rate decreases with radius by ∼2.7%. The effect is comparable in magnitude to the Sun's NSSL, which is characterized by a ∼5% decrease in rotation rate near the top of the CZ. This low-latitude dip has been a robust feature of other work (e.g., Brun & Toomre 2002; Brandenburg 2007; Guerrero et al. 2013; Gastine et al. 2013; Hotta et al. 2015) and is also referred to as a *dimple* in the literature. At high latitudes in case N5, there are some signs of shear as well, although the overall effect is much weaker, corresponding to a reduction in angular velocity of only ∼0.5%. Furthermore, the shear has both a negative and positive radial gradient. Hotta et al. (2015) saw this phenomenon as well.

The meridional circulation (here, represented by the magnitude of the longitudinally averaged mass flux, with circulation streamlines overplotted) for cases N3 and N5 is shown in Figure 2.5. At low latitudes in the Northern Hemisphere (for both cases), there are three cylindrically stacked circulation cells. The inner and outer cells are counterclockwise and the sandwiched inner cell is clockwise. The sandwiched clockwise cell is large in case N3, but small in case N5, while the opposite is true for the counterclockwise cell near the outer surface. Furthermore, case N5 has two additional clockwise cells at high latitudes, one near the outer boundary and one near the inner boundary. For both cases, the large counterclockwise cell at high latitudes is concentrated in a thin band near the outer surface, where there is strong poleward flow. In the Southern hemisphere for each case, the circulation patterns are the same, but with the clockwise/counterclockwise sense of each cell reversed.

Figure 2.6 shows the breakdown of radial energy fluxes for case N5. These fluxes are defined

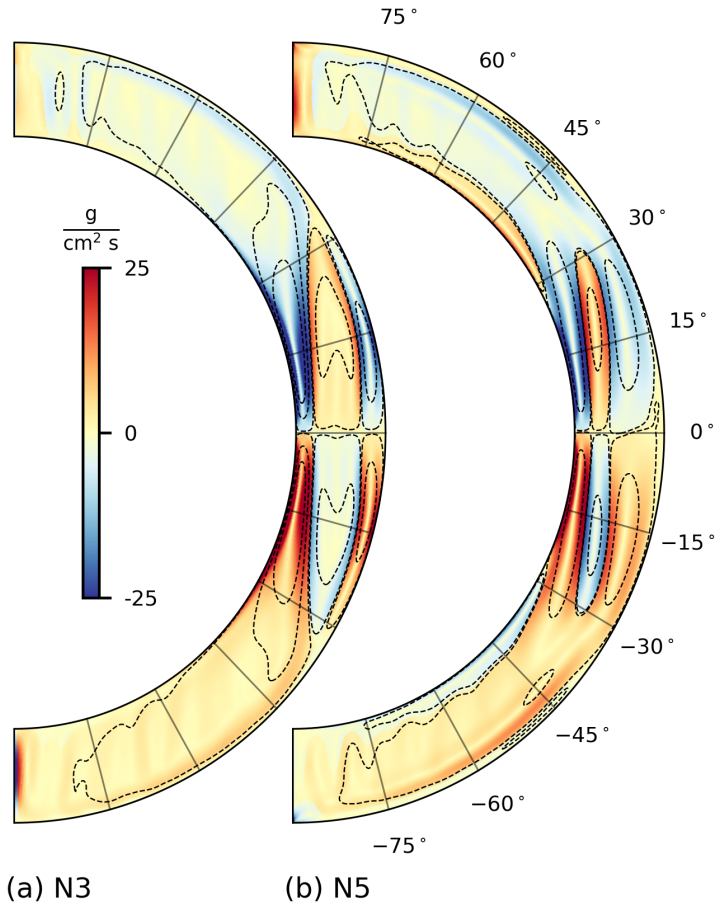

Figure 2.5: **Influence of Density Contrast on Meridional Circulation**. Vector-magnitude of the temporally and longitudinally averaged mass flux—$|\,\langle\overline{\rho}\boldsymbol{v}_{\rm pol}\rangle\,|$—in the meridional plane for cases N3 and N5. The vector-magnitude of the mass flux corresponds to the density of meridional circulation streamlines, several of which are denoted by the dashed contours. Here $\boldsymbol{v}_{\rm pol} = v_r\hat{\boldsymbol{e}}_r + v_\theta\hat{\boldsymbol{e}}_\theta$ refers to the poloidal part of the velocity. Red (positive values) indicates clockwise circulation, while blue (negative values) indicates counterclockwise circulation.

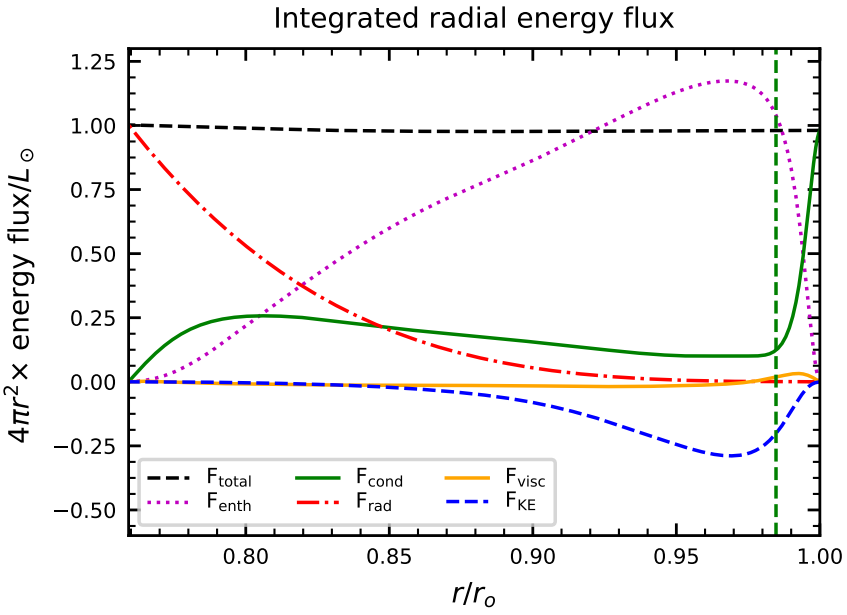

Figure 2.6: **Radial Energy Fluxes for High Density Contrast**. Decomposition of the spherically integrated radial energy flux for case N5, as defined in Equation (2.2). The location of the base of the thermal boundary layer is shown as the dashed vertical green line, chosen by eye to coincide with the near-surface local minimum (in radius) of the conductive energy flux.

(e.g., Featherstone & Hindman 2016a) to be

$$F_{\text{enth}}(r) \equiv \overline{\rho}(r) c_{\text{p}} \left\langle v_r \hat{T} \right\rangle, \tag{2.2a}$$

$$F_{\text{cond}}(r) \equiv -\kappa \overline{\rho}(r) \overline{T}(r) \left\langle \frac{\partial \hat{S}}{\partial r} \right\rangle, \tag{2.2b}$$

$$F_{\text{KE}}(r) \equiv \frac{1}{2} \overline{\rho}(r) \left\langle v^2 v_r \right\rangle, \tag{2.2c}$$

$$F_{\text{visc}}(r) \equiv -\left\langle \boldsymbol{v} \cdot \boldsymbol{D} \right\rangle, \tag{2.2d}$$

$$\text{and} \qquad F_{\text{rad}}(r) \equiv \frac{1}{r^2} \int_r^{r_{\text{o}}} Q(x) x^2 dx. \tag{2.2e}$$

Here, the angular brackets denote spherical averages. For the most part, four main fluxes contribute to the outward transport: the radiative flux F_{rad}, the conductive flux F_{cond}, the enthalpy flux F_{enth} (which represents the convective transport of heat), and the kinetic energy flux F_{KE}. In the bottom layers ($r/r_{\text{o}} \lesssim 0.85$), energy is transported primarily by the radiative flux and about 25% of the energy is transported by the conductive flux. As the radiative flux decreases with radius, the enthalpy flux begins to take over. Around $r/r_{\text{o}} \sim 0.97$, the convective heat flux is dominant. Finally, near the outer surface, the boundary conditions on the velocity and entropy force all fluxes to vanish except for the conductive flux, which carries a solar luminosity out of the domain in a narrow thermal boundary layer. The extreme flatness of the total energy flux in case N5 indicates a mature state of statistical equilibrium for the energy transport.

2.4 Busse Columns

We recall that *Busse columns* are convective rolls of fluid aligned with the rotation axis. Adjacent rolls have opposite senses of spin, so that each columnar downflow lane traces the region in between two Busse-column rolls. In Figure 2.8, we show the equatorial cross section of radial velocity for case N3. The prograde tilt of the downflow lanes is obvious: the portions of the lane close to the outer surface are at a higher longitude than the portions of the lane close to the inner surface. As a general rule, the columns extend in depth all the way through the layer; however, several structures (especially the downflows in the upper half of the layer) only extend through

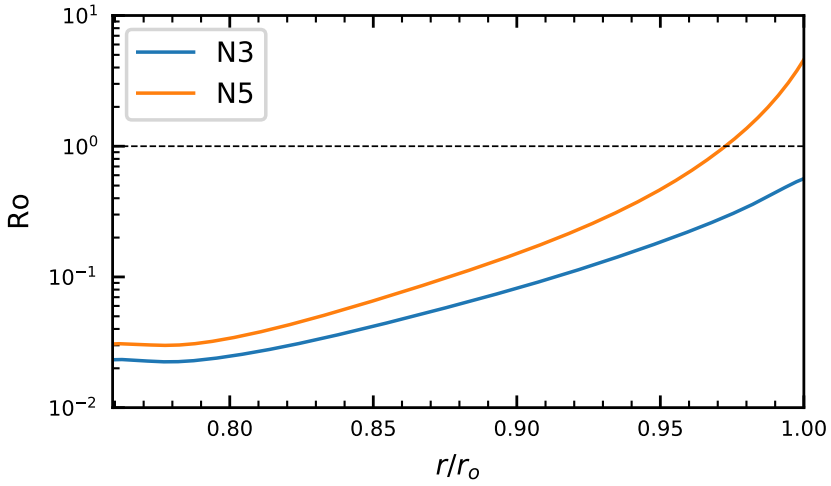

Figure 2.7: **Influence of Density Contrast Rossby Number**. Radial profile of the local Rossby number defined in Equation (2.1) for cases N3 and N5. The spherically averaged rms velocity $v'(r)$ and the typical length scale $L = H_\rho(r)$ are defined as in the caption to Table 2.1. The dashed line shows the critical value of the Rossby number Ro = 1, which is reached only for case N5.

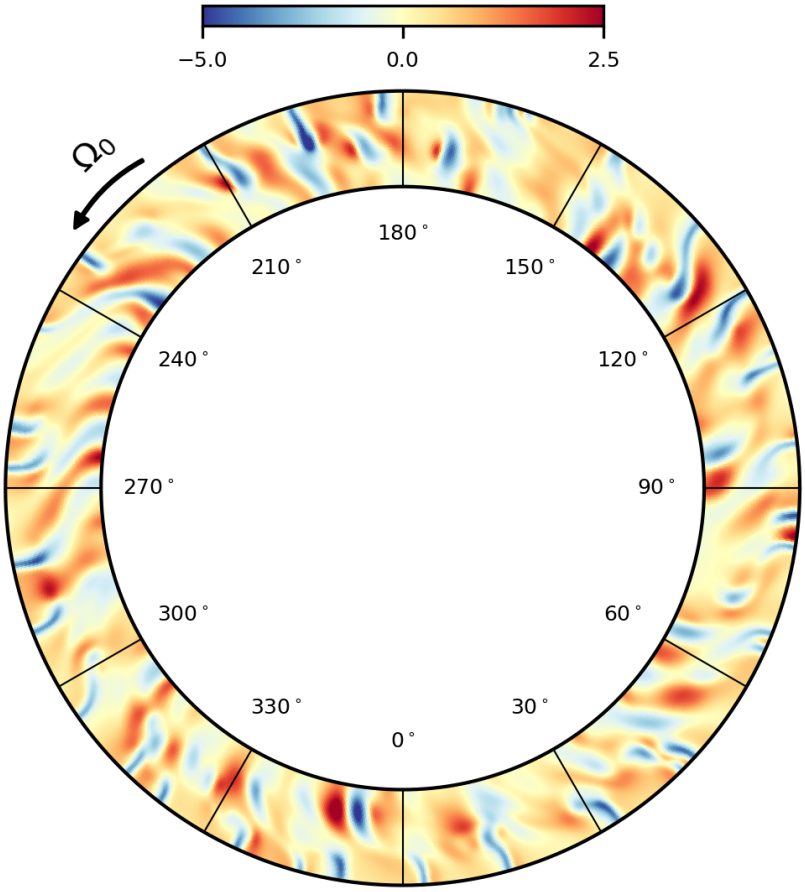

Figure 2.8: **Busse Columns on Equatorial Cuts**. Instantaneous profile of the radial velocity v_r on an equatorial cut of the computational domain for case N3. The view is from the North Pole, so the longitude ϕ increases in an counterclockwise sense. The radial velocity has been divided by its rms value at each radius and the colorbar is binormalized to show the asymmetry in the upflow- and downflow-speeds with respect to the rms.

about half the layer or less.

The character of the Busse columns depends on the level of rotational constraint in the simulations. We show the radial profile of Ro for cases N3 and N5 in Figure 2.7. The near-surface outer layers of case N5 are rotationally unconstrained (Ro > 1), in contrast to those of case N3 (see also Figures 2.2(a, c)). In the deep layers, on the other hand, both cases are rotationally constrained, with low Rossby numbers and definitive Busse-column structure (Figures 2.2(b, d)).

In the deep layers of the shell, the Busse-column structure is clearest (e.g., Figures 2.2 and 2.8). We estimate the longitudinal wavenumber of the Busse columns in each case by finding the peak of the power spectrum of the sectoral spherical harmonics (first averaging the spectrum in time and in radius over the inner half of the shell). We find a clear peak in each power spectrum, with $m_{\rm peak} \sim 28$ for case N3 and $m_{\rm peak} \sim 24$ for case N5. For both cases, a typical Busse column thus has a longitudinal extent ($2\pi r_{\rm i}/m_{\rm peak} \sim 1.3 \times 10^{10}$ cm) comparable to the depth of the shell ($\sim 1.6 \times 10^{10}$ cm). Featherstone & Hindman (2016b) show that the wavenumber of Busse columns scales with the Rossby number like $m_{\rm peak} \sim {\rm Ro}^{-1/2}$. Near the inner surface, the ratio of the Rossby numbers between cases N3 and N5 is ~ 0.76 (see Figure 2.7). This corresponds to a ratio of Busse-column wavenumbers of $(0.76)^{-1/2} \approx 1.15$, in agreement to lowest order with our estimates of $m_{\rm peak}$ from the power spectra ($28/24 \sim 1.17$). The comparable values of the Busse-column wavenumbers in cases N3 and N5 illustrate the fact that although the near-surface layers of the two cases have very different flow structures, the deep layers of the two simulations (where the Rossby numbers are only slightly different) have similar flow structures.

Figure 2.9 shows the temporal evolution of the near-surface flow field in case N3. To better see the evolution, we magnify a $40^\circ \times 40^\circ$ patch centered at the equator, indicated by the dashed box in Figure 2.2(a). Some downflow lanes (which trace the regions in between adjacent Busse-column rolls) have been labeled with capital letters to indicate how they are advected and distorted by the flow. Although the downflow lanes are rather long-lived (lane A, for instance, maintains its structure for several rotation periods before getting absorbed by another lane), they are not simply advected passively by the flow. They frequently merge, disappear, and reappear, indicating

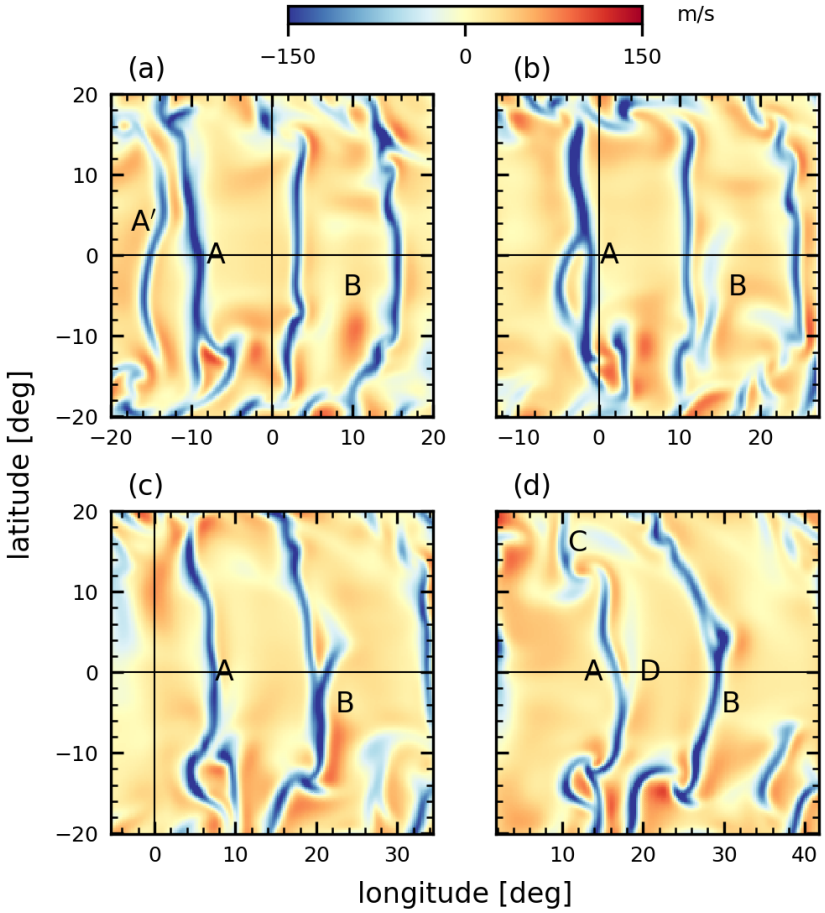

Figure 2.9: **Following the Movement of Busse Columns**. Temporal evolution of a patch of radial velocity v_r for case N3. Spherical cuts of the full velocity field are taken at the near-surface radial level $r/r_o = 0.988$. Each panel shows a 40 °× 40° patch of the spherical surface centered at the equator, with successive patches equally spaced in time by roughly a quarter of a rotation period. The frame of the patch is rotating at the local equatorial rotation rate in order to see the super-rotation of the columns.

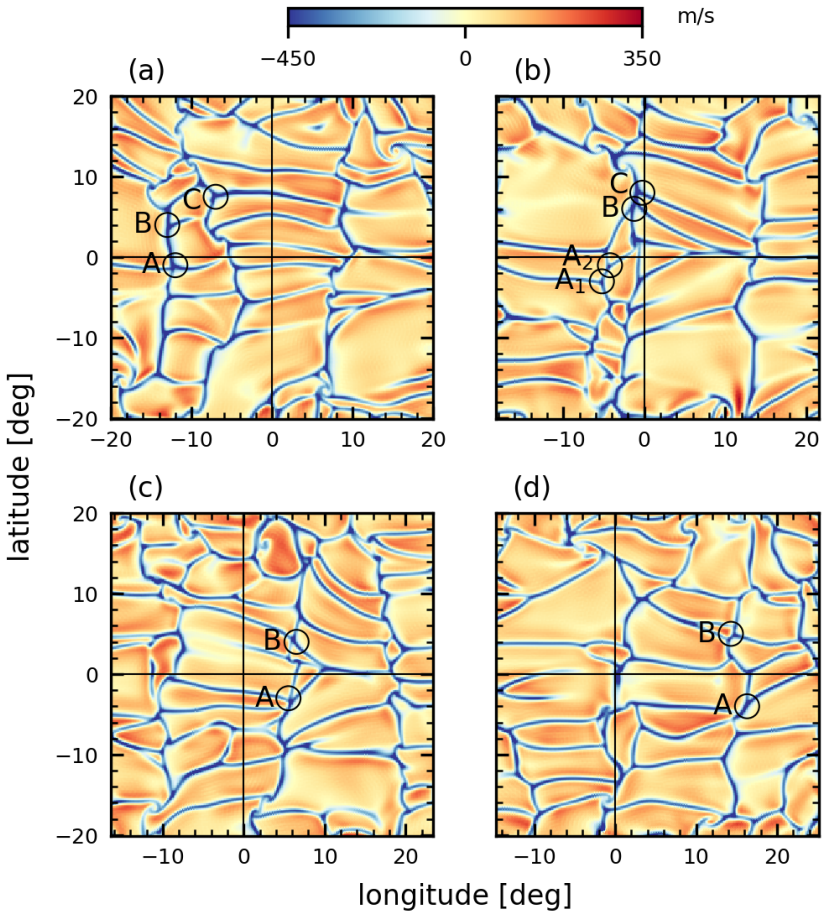

Figure 2.10: **Following the Movement of Intense Downflow Plumes**. Similar to Figure 2.9, but for case N5. Spherical cuts are taken at $r/r_o = 0.988$ and each panel shows a $40° \times 40°$ patch of the full surface centered at the equator, equally separated in time by roughly a quarter of a rotation period. The frame of the patch is rotating at the local equatorial rotation rate.

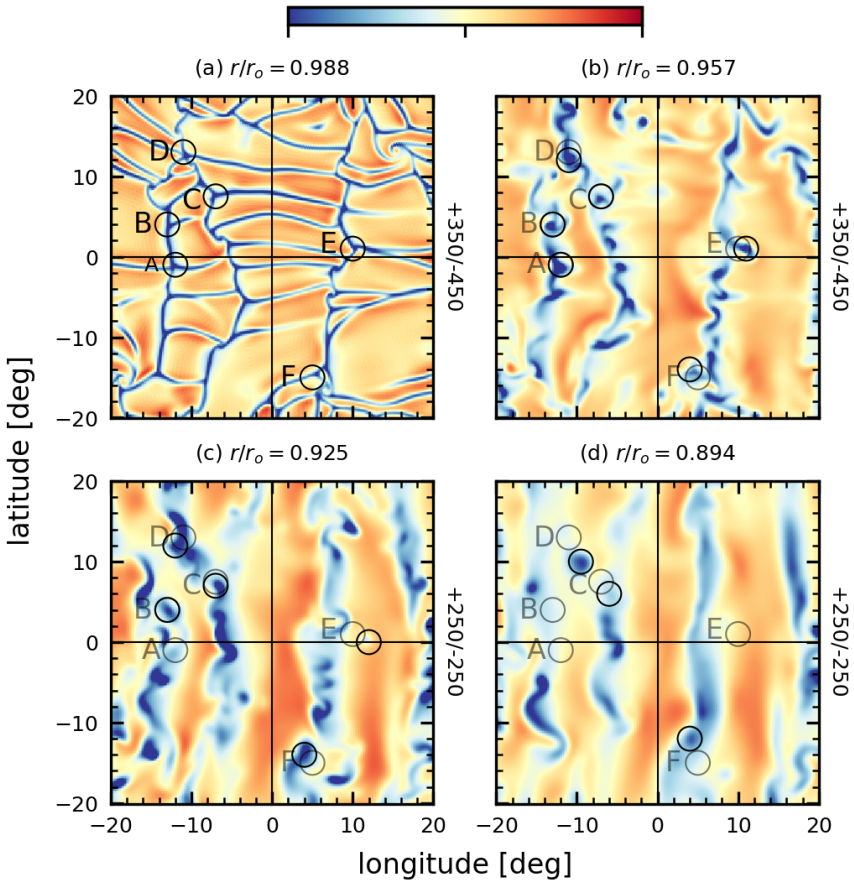

Figure 2.11: **Following the Vertical Structure of Downflow Plumes**. Magnified view of the $40^\circ \times 40^\circ$ equatorial patch of radial velocity denoted by the dashed box in Figure 2.2(c). Each panel shows the same patch at a common time for successively deeper layers, evenly spaced throughout approximately the upper half of the spherical shell. The saturation values (in m/s) for the colorbar are shown to the right of each panel. Several downflow plumes (beginning as interstices in panel a) have been traced in depth by small black circles. These plumes/interstices are labeled in panel (a) by capital letters A–F. Interstices A–C correspond to the same interstices identified in Figure 2.10. The near-surface plume locations and labels are shown in gray in panels (b–d).

that no single Busse column lives for a protracted interval. Furthermore, the lanes (and hence, the columns) only extend coherently to about $\pm 15^\circ$; beyond this latitude range, the lanes move more slowly, eventually breaking off and joining the swirling small-scale flow at high latitudes. We note that the differential rotation of Figure 2.3(a) correspondingly occupies mainly the narrow latitude band between $\pm 15^\circ$. Each lane is advected by several degrees over the whole rotation period, corresponding to a pattern speed of the Busse columns that is $\sim$40 m/s *faster* than the background rotation rate. In other words, the Busse columns *super-rotate* with respect to the background flow.

2.5 Downflow Plumes

Figure 2.10 shows the evolution of the near-surface flow field for case N5, with several interstices (regions where the north–south and east–west downflow lanes cross) labeled by capital letters. We see that each upflow is surrounded by a more-or-less polygonal network of downflow lanes and thus may be regarded as a *cell*. The cells are stacked in the axial direction such that there are 10 or so downflow lanes that connect throughout the whole patch north–south, analogous to the downflow lanes between pairs of Busse-column rolls in case N3 (Figure 2.9). On average, the interstices move in the prograde direction, indicating that they are super-rotating like the Busse columns. The interstices have much shorter lifetimes than the Busse columns, splitting up and merging several times over the course of a rotation period. In panel (b), for example, interstice A has split into two interstices A_1 and A_2, while in panel (c), the two interstices have merged again.

At any given instant of time, the interstices shown in Figure 2.10 are the sources of *downflow plumes*. The plumes can be seen by following the interstices down in depth. In Figure 2.11, we consider the patch from Figure 2.10(a) and examine the connectivity of the downflows from the near-surface layers to mid-depth. As the patches get successively deeper, the downflow associated with each interstice intensifies in amplitude and becomes more localized. We refer to the entire structure (interstice to localized downflow near mid-depth) as a downflow plume. It is important to note that the plumes do *not* coincide with the trajectory of a fluid parcel launched downward from the interstice. Since the interstices move prograde in time, each radial point on the plume

corresponds to a fluid parcel that was launched when the parent interstice (top of the plume) was positioned retrograde from its present location.

The coherence of the north–south downflow lanes in Figure 2.11 increases with depth and the plumes slowly fade. No single plume extends in depth more than $\sim$0.1 $r_{\rm o}$ (or about 2/5 the depth of the layer) from the near-surface layer shown in panel (a). This is consistent with the ephemeral nature of the interstices; over the radial extent of a plume, the fastest speeds are on average $\sim$400 m/s in the plume core, while the lifetime of an individual interstice is $\sim$2 days. Thus, the total depth-extent of the plumes should be $\sim$ (400 m/s) $\times$ (2 days) $\sim$ 0.1 $r_{\rm o}$.

2.6 Torque Balance

The steady-state distribution of angular momentum (and by extension, the differential rotation) can be understood in terms of the angular momentum transport, or torque, due to various aspects of the flow. In equilibrium, the torque balance (e.g., Elliott et al. 2000; Brun & Toomre 2002; Miesch & Hindman 2011) is expressed as

$$\tau_{\rm rs} + \tau_{\rm mc} + \tau_{\rm v} \equiv 0, \tag{2.3}$$

where

$$\tau_{\rm rs} \equiv -\nabla \cdot [\overline{\rho} r \sin\theta \left\langle v'_\phi \boldsymbol{v}'_{\rm pol} \right\rangle], \tag{2.4a}$$

$$\tau_{\rm mc} \equiv -\left\langle \overline{\rho} \boldsymbol{v}_{\rm pol} \right\rangle \cdot \nabla \mathcal{L}, \tag{2.4b}$$

$$\text{and} \qquad \tau_{\rm v} \equiv \nabla \cdot [\overline{\rho} \nu r^2 \sin^2\theta \nabla \Omega]. \tag{2.4c}$$

Here $\boldsymbol{v}_{\rm pol} \equiv v_r \hat{\boldsymbol{e}}_r + v_\theta \hat{\boldsymbol{e}}_\theta$ is the poloidal part of the fluid velocity and $\mathcal{L} \equiv r \sin\theta (\Omega_0 r \sin\theta + \langle v_\phi \rangle) = \Omega r^2 \sin^2\theta$ is the fluid's specific angular momentum in the non-rotating lab frame. Angular brackets indicate a combined temporal and longitudinal average and the primes indicate deviations from the average.

Figure 2.12 shows the balance of torques for cases N3 and N5. At each point in the meridional plane, the magnitude of the sum of the torques is a factor of $\sim$100 smaller than the magnitude of

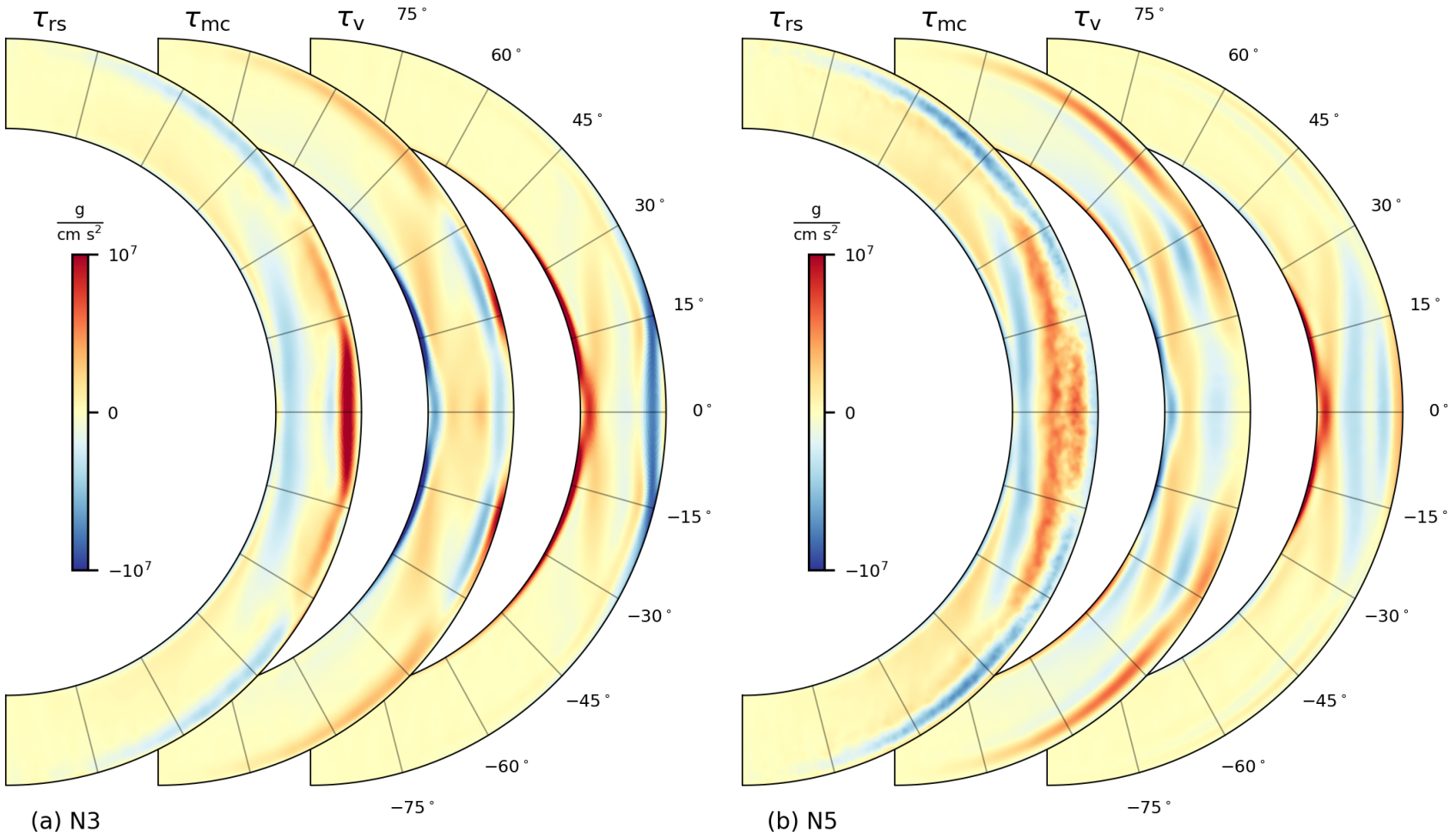

Figure 2.12: **Torque Balance for High and Low Density Contrast**. Temporally and longitudinally averaged torque balance in the meridional plane for cases N3 and N5. In each panel, overlapping plots show the torque densities due to Reynolds stress, meridional circulation, and viscosity from left to right. Positive torque, which tends to increase angular momentum in the axial direction $\hat{\boldsymbol{e}}_z$ (or equivalently, tries to accelerate the fluid in the longitudinal direction $\hat{\boldsymbol{e}}_\phi$) is shown in red and negative torque in blue.

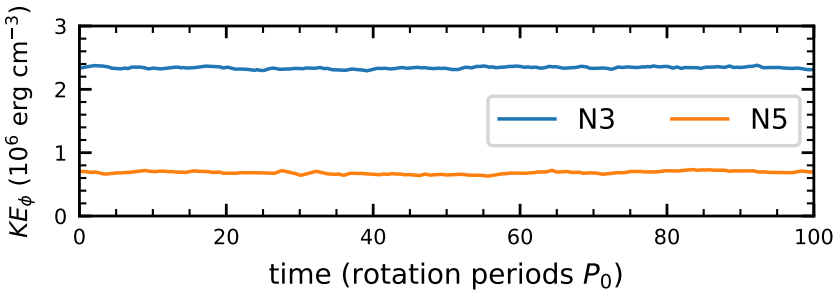

Figure 2.13: **Equilibrium of the Steady-State Differential Rotation**. Temporal variation of the kinetic energy density in the differential rotation ($\mathrm{KE}_\phi \equiv (1/2)\overline{\rho}\,\langle v_\phi \rangle^2$) for cases N3 and N5 over 100 rotation periods. Here, the kinetic energy has been averaged over the entire shell. Time is measured from the beginning of equilibration for each case.

any of the three torques individually. Furthermore, following equilibration in each simulation, the kinetic energy in the differential rotation (KE_ϕ) varies by only a few percent from its temporally averaged value, as shown in Figure 2.13. We have also confirmed that there is no secular drift in the kinetic energy with time over several thousand rotation periods, indicating a mature state of equilibrium in the torque balance.

For each case, the torque is roughly constant on cylinders near the equator, whereas it is roughly constant on spheres at high latitudes. The main feature that sets case N5 apart from case N3 is the strong band of negative Reynolds-stress torque near the outer surface of case N5, extending across all latitudes; in case N3, there is only negative Reynolds-stress torque at high latitudes, and it is significantly weaker than in case N5.

A decomposition of $\left\langle v'_\phi \boldsymbol{v}'_{\mathrm{pol}} \right\rangle$ into its two component-correlations $\left\langle v'_r v'_\phi \right\rangle$ and $\left\langle v'_\theta v'_\phi \right\rangle$ reveals that the Reynolds-stress torque is almost entirely dominated by the *radial* turbulent angular-momentum flux

$$\mathcal{F}_r \equiv \overline{\rho} r \sin\theta \left\langle v'_r v'_\phi \right\rangle \tag{2.5}$$

for both cases N3 and N5. We now argue that this radial flux is produced by the two types of flow structures mentioned previously, Busse columns and downflow plumes. [2]

[2] Note that here in Chapter 2, we keep the notation of Matilsky et al. (2019). We use a capital Roman "F" to denote the spherically integrated radial energy flux (units of luminosity) and a curly "$\mathcal{F}$" to denote the angular

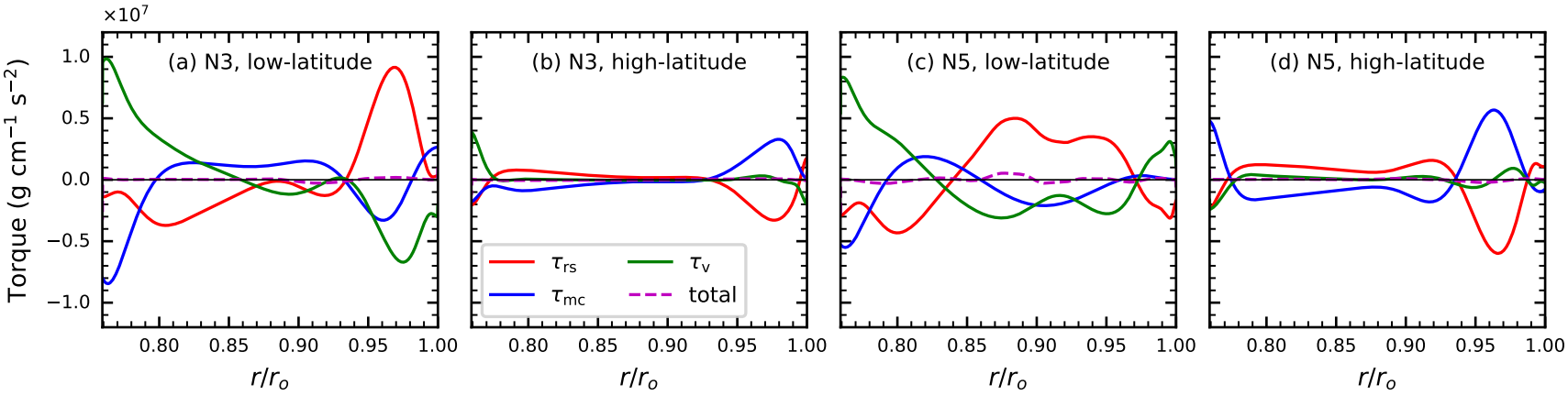

Figure 2.14: **Torque Balance in High- and Low-Latitude Ranges**. Torque balance averaged over low latitudes (between ±15°) and high latitudes (between ±45° and ±60°) for cases N3 and N5. Each curve shows a torque averaged over its particular latitude region and plotted as a function of radius.

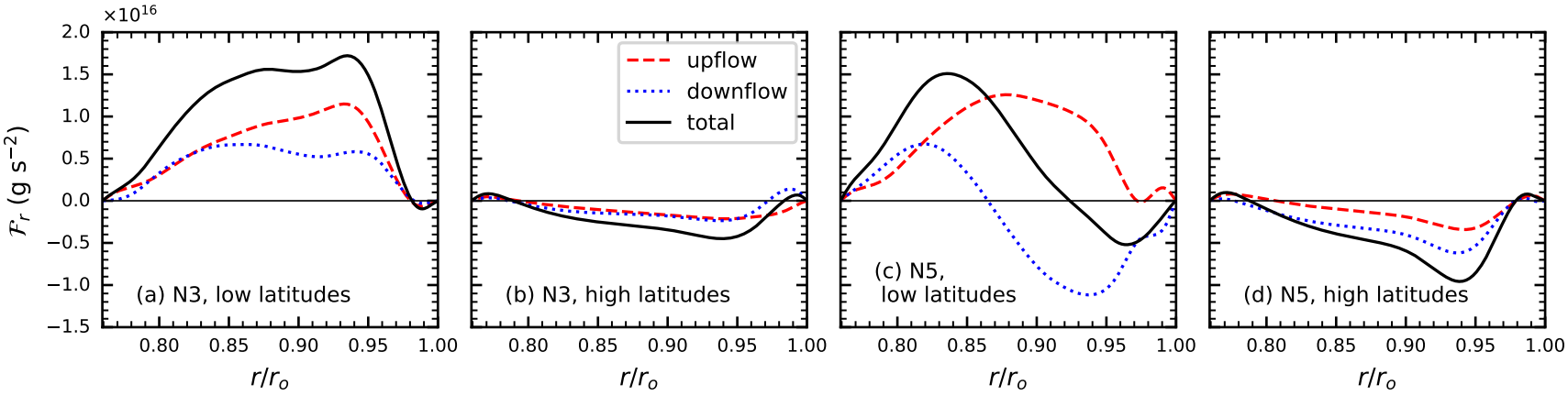

Figure 2.15: **Angular Momentum Flux Due to Upflows and Downflows**. Radial angular-momentum flux from the Reynolds stress ($\mathcal{F}_r$) averaged over low latitudes (between $\pm 15°$) and high latitudes (between $\pm 45°$ and $\pm 60°$) for cases N3 and N5. The flux has been divided into the component from the upflows ($v_r > 0$) and the component from the downflows ($v_r < 0$). The sum of these components is equal to the total flux.

The cross-sectional tilt of the Busse columns (Figure 2.8) tends to give upflows ($v_r' > 0$) a positive v_ϕ' and downflows ($v_r' < 0$) a negative v_ϕ'. Within a Busse column, both upflows and downflows thus yield a positive (radially outward) angular-momentum flux. The net result is that angular momentum is taken away from the inner layers (negative torque) and deposited in the outer layers (positive torque). Figure 2.14(a) shows the low-latitude torque balance for case N3. The Reynolds-stress torque is positive in roughly the upper quarter of the domain and negative in the lower three-quarters, indicating that Busse columns dominate the Reynolds stress at all depths. In case N5, however, the Reynolds-stress torque is negative near the outer surface (Figure 2.14(c)), indicating the influence of an additional transport mechanism.

The downflow plumes do not follow the Busse column tilt. There are only a few other physical mechanisms to create correlations in v_r' and v_ϕ', and the most obvious of these is deflection by the Coriolis force. For downflow plumes ($v_r' < 0$), the deflection is prograde ($v_\phi' > 0$), corresponding to a negative (radially inward) transport of angular momentum. This picture is consistent with the Reynolds-stress torque at high latitudes for both cases (Figures 2.14(b, d)): the Reynolds-stress torque is negative in the outer layers and positive in the inner layers, corresponding to the inward transport of angular momentum from the outer surface to the deeper layers.

At low latitudes, the presence of downflow plumes is most prominent in case N5 near the outer surface, where the Reynolds-stress torque is negative. Correspondingly, there is a dip in rotation rate at low latitudes for case N5, but not for case N3. This lends substantial support to the argument of Foukal & Jokipii (1975), at least at low latitudes: downflow plumes are Coriolis-deflected (or equivalently, they conserve their angular momentum), transporting angular momentum radially inward and creating near-surface shear.

The torque from the meridional circulation is determined by the alternating pattern of clockwise and counterclockwise cells in Figure 2.5, coupled with the fact that angular momentum in our models is roughly constant on cylinders (λ = constant). From Equation (2.4), this means that

momentum flux. In Chapter 3, we use "$\mathcal{F}$" to denote the non-integrated energy flux (units of luminosity per unit area) and "$\mathscr{I}_r$" to denote the spherically integrated energy flux.

the torque has a sign opposite to that of $\langle \overline{\rho} v_\lambda \rangle$. Near the equatorial boundaries of the circulation cells, the meridional flow is dominated by the radial component $\langle \overline{\rho} v_r \rangle = \langle \overline{\rho} v_\lambda \rangle$. Consequently, $\tau_{\rm mc}$ changes sign in Figures 2.14(a, c) at the radial locations of the north–south cell boundaries.

At high latitudes, a decomposition of the meridional circulation into its radial and latitudinal components reveals that only the latitudinal term $-\langle \overline{\rho} v_\theta \rangle \left(\partial \mathcal{L} / r \partial \theta \right)$ contributes significantly to the torque. Geometrically, this is due to the shape of the near-surface counterclockwise cell of meridional circulation in both cases, which is most intense in a region highly elongated in the latitudinal direction. The resultant poleward flow carries high-angular-momentum fluid from the equator and brings it to high latitudes, thereby creating a positive near-surface torque.

The viscous flux of angular momentum $-\overline{\rho} \nu r^2 \sin^2 \theta \nabla \Omega$ is proportional to the negative gradient of the rotation rate. This is similar to a Fickian diffusivity (acting on the rotation rate, not the specific angular momentum), meaning that viscosity simply tends to bring the rotation rate to a constant value (i.e., it eliminates shear). In this sense, the viscous torque is "passive," responding only to counteract the shear produced by the Reynolds stress and meridional circulation. Thus, in Figure 2.14, the viscous torque is simply negative or positive according to the sign of the combined Reynolds stress and meridional circulation torques.

2.7 Angular Momentum Transport by Upflows and Downflows

Figure 2.15 shows the Reynolds-stress angular-momentum flux $\mathcal{F}_r$ broken up into upflow- and downflow-components for cases N3 and N5 in the high- and low-latitude regions. For case N3 at low latitudes, both components of the flux have the same sign—positive in most of the domain except for a narrow region of very weak negative flux near the outer boundary. The strong positive fluxes are consistent with the tilts of the Busse columns in the equatorial plane, which makes the correlation $\left\langle v_r' v_\phi' \right\rangle$ positive for both upflows and downflows. In the middle layers, the magnitude of the upflow-flux is about twice as large as that of the downflow-flux. This asymmetry may be attributed to the fact that although *most* downflows are part of a Busse column, there are also downflows whose speeds are large enough that they are really plumes that lack a negative v_ϕ'. The

overall positive correlation $\left\langle v_r' v_\phi' \right\rangle$ is thus weaker for the downflows.

For case N5, the low-latitude upflow-flux looks rather similar to the upflow-flux in case N3, except that it peaks in the middle of the layer, as opposed to peaking in the upper half. The downflow-flux in the bottom half of the layer ($r/r_{\rm o} \lesssim 0.87$) is positive, consistent with the organization of both upflows and downflows into Busse columns in the deeper layers. The top half of the shell, by contrast, has negative downflow-flux, whose maximum magnitude is over twice as great as the maximum magnitude of the positive downflow-flux. Thus, at low latitudes, the inward transport of angular momentum comes *only* from the downflow plumes; the upflows are dominated by Busse columns.

When the low-latitude upflow and downflow-fluxes are added, there is a positive slope in the radial profile of the total angular-momentum flux $\mathcal{F}_r$. The effect on the Reynolds stress *torque*, which scales like the radial derivative of $r^2\mathcal{F}_r$, is to produce the narrow region of negative torque near the outer boundary as seen in Figure 2.14(c). This negative torque is responsible for maintaining the low-latitude near-surface shear against viscosity.

At high latitudes in both cases, the upflow- and downflow-fluxes have the same sign: negative in most of the fluid layer, except near the shell boundaries. Near the outer surface, there is significant asymmetry in the flux magnitudes between cases N3 and N5, and separately between the upflow- and downflow-flux of case N5. We argue that this arises mostly from the asymmetry in upflow- and downflow-speeds. Figure 2.16 shows the rms radial speeds of upflows and downflows in cases N3 and N5 as functions of radius. In case N5, the downflows are about twice as fast as the upflows near the outer surface. The Reynolds stress, which scales like v_r^2, is correspondingly larger for the downflows than the upflows. Similarly, since both the upflows and downflows are about twice as fast in case N5 than in case N3 near the outer surface, both the upflow- and downflow-fluxes are greater in case N5.

We note here that the Rossby number associated with the rms radial downflow speed at the base of the thermal boundary layer is $\sim$0.2 for case N3 and $\sim$1.2 for case N5. Here we define the *downflow Rossby number* as $v'_{\rm rms}(r)/2\Omega_0 H_\rho(r)$, where $v'_{\rm rms}(r)$ is the rms convective speed of the

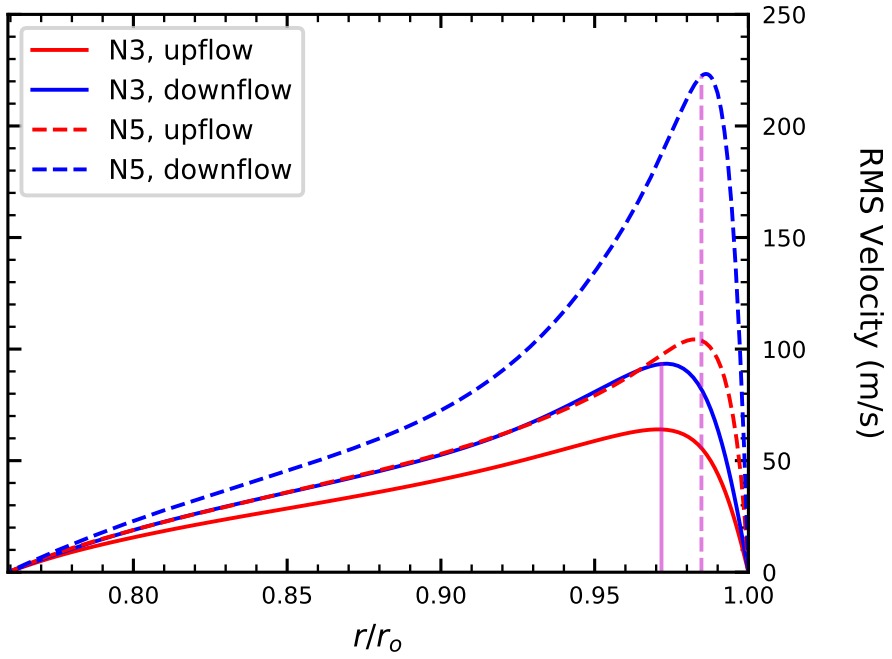

Figure 2.16: **Coupling of Thermal Boundary-Layer Depth to Rotational Constraint**. Spherically and temporally averaged radial convective velocity amplitudes for cases N3 and N5. The rms amplitudes are computed separately for the upflows and downflows. The vertical magenta lines indicate the location of the base of each thermal boundary layer for cases N3 and N5 (compare to Figure 2.6).

downflows, averaged over spherical surfaces of radius r. Hence, the *downflows* in case N5 are, on average, rotationally *unconstrained* according to Equation (2.1). This agrees with the fact that the downflow-flux is negative in the outer layers of case N5; the downflow plumes conserve their angular momentum and thus transport it radially inward.

We now verify that it is only the downflow *plumes* that carry angular momentum inward at low latitudes, and not the slower downflow lanes associated with Busse columns. Figure 2.17 shows a similar "dive" through the fluid layer as in Figure 2.11, but this time illustrates the instantaneous angular-momentum flux in the patch. We see that at $r/r_{\rm o} = 0.957$ (which is close to $r/r_{\rm o} = 0.942$—the extremum of the flux from the downflows in Figure 2.15(b)), the central region of nearly every plume is associated with a positive v'_ϕ and thus a negative angular-momentum flux. The notable exception is plume D, which has the deepest extent of any of the plumes. However, plume D has negative flux in the deepest layers, as seen in Figure 2.17(d).

In contrast to the plumes, the columnar downflow lanes in the deep layers (Figures 2.17(b–d)) mostly have positive angular-momentum flux, consistent with the tilt of Busse columns. It is also interesting to note that in between the axially aligned downflow lanes, the upflows are split into two regions with alternating sign of the flux—positive on the right and negative on the left. This is simply due to the manner in which upflows diverge and recirculate (in the center of the upwell) to accommodate the impenetrable outer boundary and maintain mass conservation. Note, however, that in the deeper layers, the positive flux in the upflows dominates the negative flux. This explains the weakness of the positive upflow-flux between $r/r_{\rm o} \sim 0.96$ and $r/r_{\rm o} \sim 1$ in Figure 2.15(c). Near the outer surface, the upflow rolls diverge symmetrically in both the positive and negative longitudinal directions and their net angular momentum transport cancels out almost completely.

Finally, we note that near the outer surface, the east–west downflow lanes have largely the opposite sign of flux compared to the upflows in which they are embedded—negative on the right and positive on the left for the upflow column straddling the central meridian. This is due to the tendency of the fluid in the east–west lanes to flow sideways toward the interstices, which have an

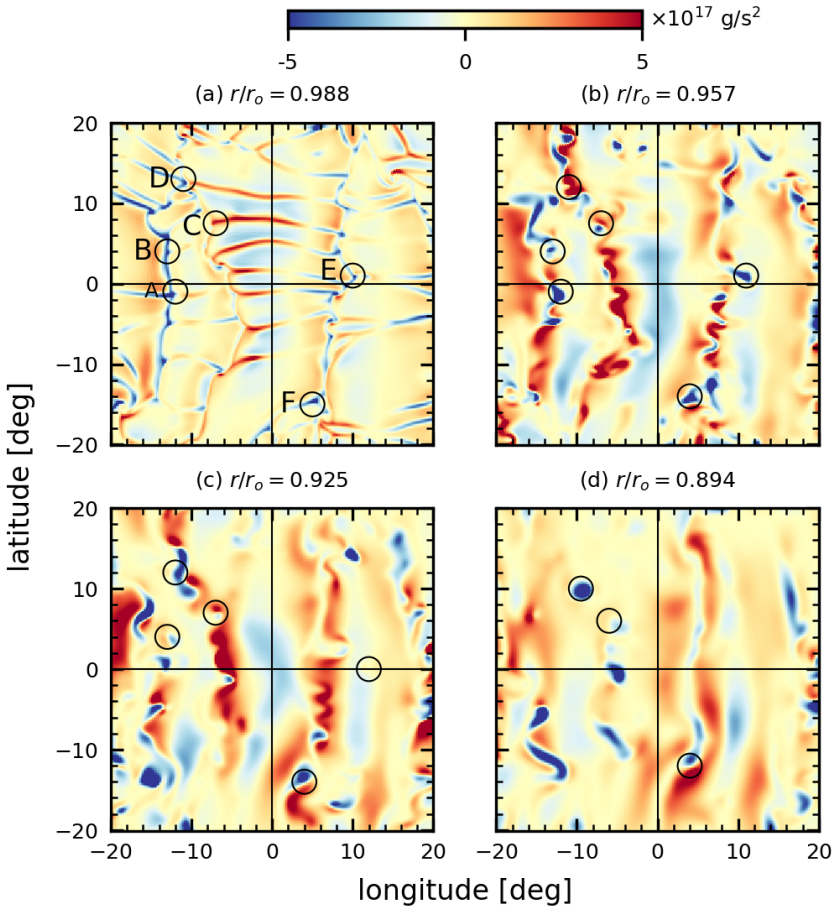

Figure 2.17: **Angular Momentum Transport by Downflow Plumes**. Radial structure of the angular-momentum transport by downflow plumes in the $40^\circ \times 40^\circ$ equatorial patch for case N5 (compare to Figure 2.11). Each panel shows the instantaneous Reynolds-stress angular-momentum flux $\overline{\rho} r \sin\theta v_r' v'_\phi$ in the patch for successively deeper layers at a common time. Here the colorbar is saturated to the same values for all four panels. The locations of the downflow plumes identified in Figure 2.11 are again traced in depth by small black circles, labeled in the first panel by capital letters A–F.

extremely low pressure compared to their surroundings.

2.8 Discussion

In this work, we have explored the development of near-surface shear in 3-D spherical-shell models of solar-like convection as a natural consequence of increasing the density contrast across the shell. We find that increased stratification does indeed foster more rapid flow structures with Reynolds stresses that enhance near-surface shear. However, this proves insufficient to create a solar-like Near-Surface Shear Layer.

Our highest-contrast model (case N5) contains two types of flow structures that influence differential rotation: rotationally constrained Busse columns and rotationally unconstrained downflow plumes. The Busse columns transport angular momentum outward at low latitudes and thus maintain a fast equator and slow polar regions. The plumes transport angular momentum inward in the outer half of the layer at all latitudes. The influences of Busse columns and downflow plumes on the Reynolds stress is cleanly summarized in Figure 2.18, which shows the correlation coefficient $C \equiv \left\langle v_r' v_\phi' \right\rangle / \left[\left\langle (v_r')^2 \right\rangle \left\langle (v_\phi')^2 \right\rangle \right]^{1/2}$ plotted in the meridional plane for the upflows and downflows in case N5. This correlation contains the same information as the angular-momentum fluxes depicted in Figure 2.15, but the signal has been normalized and the geometric factor $r \sin\theta$ has been removed.

For the upflows, the correlation is everywhere positive at low latitudes, implying outward angular momentum transport—and thus dominance by Busse columns—at all depths. It is negative (except near the inner boundary) at high latitudes, consistent with inward angular momentum transport through Coriolis-deflection. The correlation for the downflows is mostly negative everywhere, except in the inner half of the shell at low latitudes (where the Busse columns dominate) and near the inner boundary at high latitudes. The strong positive correlation near the inner boundary for both upflows and downflows is due to the impenetrability condition maintained by the pressure force, which we do not investigate in detail here.

Figure 2.18 shows that the dip in angular velocity at low latitudes in case N5, while similar

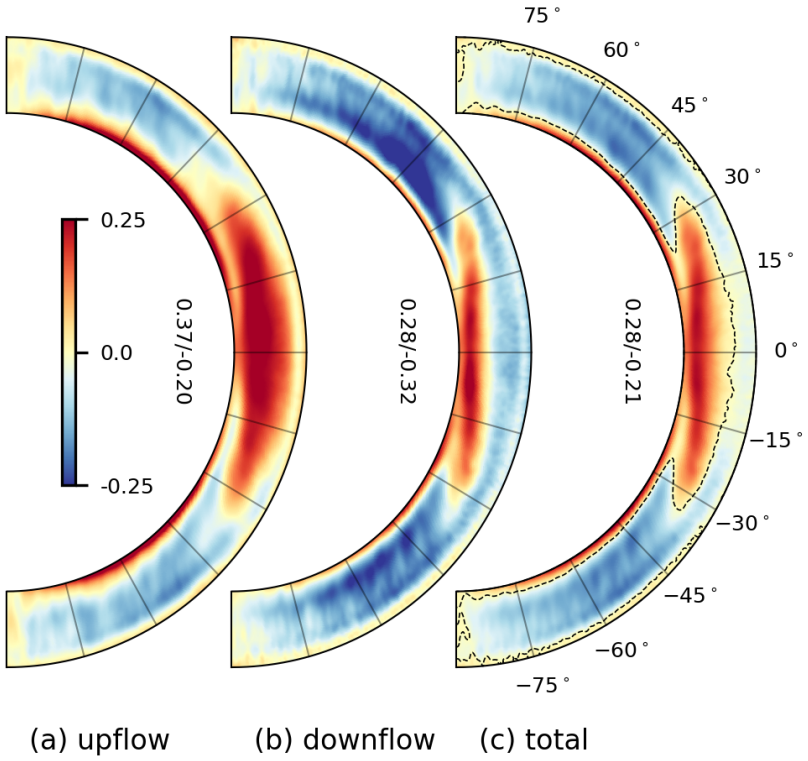

Figure 2.18: **Reynolds-Stress Correlation in Upflows and Downflows for High and Low Density Contrast**. Correlation coefficient of the convective velocities v'_r and v'_ϕ for the upflows, downflows, and total flow in the meridional plane for case N5. The numbers beside each panel indicate the extremum values for the correlation coefficient. The dashed contour in panel (c) denotes the surface in the meridional plane where the total correlation coefficient vanishes.

in amplitude and radial extent to the solar NSSL, arises for the wrong reasons. The Busse columns transport angular momentum outward, while the plumes transport angular momentum inward. The radial location where the upward flux from the Busse columns cancels the downward flux from the plumes—i.e., the spherical surface where the total correlation is zero in Figure 2.18(c)—corresponds roughly to the peak in rotation rate at low latitudes. The low-latitude NSSL in case N5 thus does not represent a layer that the downflow plumes slow down, but rather a layer that the Busse columns fail to speed up. In the Sun, by contrast, the rotation curves have only a small positive slope with radius (see Figure 2.1), implying that Busse columns, if they are present in the Sun, do not transport angular momentum in the same way as they do in simulations, or that the plumes reach more deeply than in our models.

The essential role played by Busse columns in maintaining numerical models' near-surface shear is even more apparent at high latitudes in case N5. Here the Busse columns have little effect on angular momentum transport (the correlations in Figure 2.18 are mostly negative for both upflows and downflows), while fast, small-scale downflow plumes conserve angular momentum in radial motion, transporting it inward. Although this Coriolis-deflection effect is, in fact, *stronger* at high latitudes than at low latitudes, there is basically no high-latitude near-surface shear in case N5. Thus, the mechanism described by Foukal & Jokipii (1975)—namely, that there is a rotationally unconstrained fluid layer near the outer surface of the solar CZ—cannot, by itself, explain the NSSL, at least not using current numerical models.

Miesch & Hindman (2011) make a similar point in their investigation of how meridional circulation and differential rotation respond to a negative axial torque. In our case N5, there is a negative torque due to the Reynolds stress. At high latitudes, the torque balance is primarily between the Reynolds stress and meridional circulation, reducing the torque balance in Equation (2.3) to $-\tau_{\rm mc} = \tau_{\rm rs}$. The definition of $\tau_{\rm mc}$ in Equation (2.4) then leads to the following equilibrium relationship between meridional circulation and differential rotation:

$$\overline{\rho}\,\langle \boldsymbol{v}_{\rm pol}\rangle \cdot \nabla(\Omega r^2 \sin^2\theta) = \tau_{\rm rs}. \tag{2.6}$$

The preceding equation may be satisfied in multiple ways, since both the rotation rate Ω *and* the meridional circulation $\overline{\rho}\,\langle \boldsymbol{v}_{\rm pol} \rangle$ appear on the LHS. All local models that seek to explain the solar NSSL by inward angular momentum transport—for example, the Coriolis-deflection of downflow plumes in our case N5—prescribe a negative right-hand side, e.g., a negative $\tau_{\rm rs}$. This does *not*, however, constrain the rotation rate until another equation—namely, that of meridional force balance—is specified to determine the meridional circulation. Since the meridional circulation is fundamentally a global phenomenon, it is unlikely that any local model of angular momentum transport will explain the NSSL.

An examination of the high-latitude meridional circulation profile in the context of Equation (2.6) reveals why near-surface shear is nearly absent at high latitudes in our case N5 and in the simulation of Hotta et al. (2015). In both simulations, there is a narrow band of poleward meridional circulation near the outer surface (see Figure 2.5 of this work and Figure 10 of Hotta et al. 2015), which brings high-angular-momentum fluid from equator to pole. If, on long timescales, this process pumps angular momentum to high latitudes more efficiently than the Reynolds stress can remove it, there will be no shear at high latitudes in equilibrium.

Figure 2.19 shows the radial profiles of Reynolds-stress torque, latitudinal mass flux and rotation rate averaged over high latitudes for case N5. Clearly, case N5 satisfies Equation (2.6) in its outer layers by having the meridional circulation near the outer surface inherit the radial profile of negative Reynolds-stress torque, while the near-surface rotation rate is mostly flat. In other words, although we might expect the strongly negative Reynolds-stress torque created by downflow plumes in the outer layers of case N5 to drive near-surface shear, the particular profile of the near-surface meridional circulation opposes this driving mechanism almost completely.

Because the molecular viscosity in the solar interior is so low, the balance in Equation (2.6) likely holds in the Sun, possibly with the added complication of a Maxwell torque from the magnetic field. This work has shown explicitly that the only way to understand the solar NSSL in the context of local angular momentum transport—i.e., the right-hand side of Equation (2.6)—is through a detailed understanding of how the meridional circulation is established in the Sun. Once this is

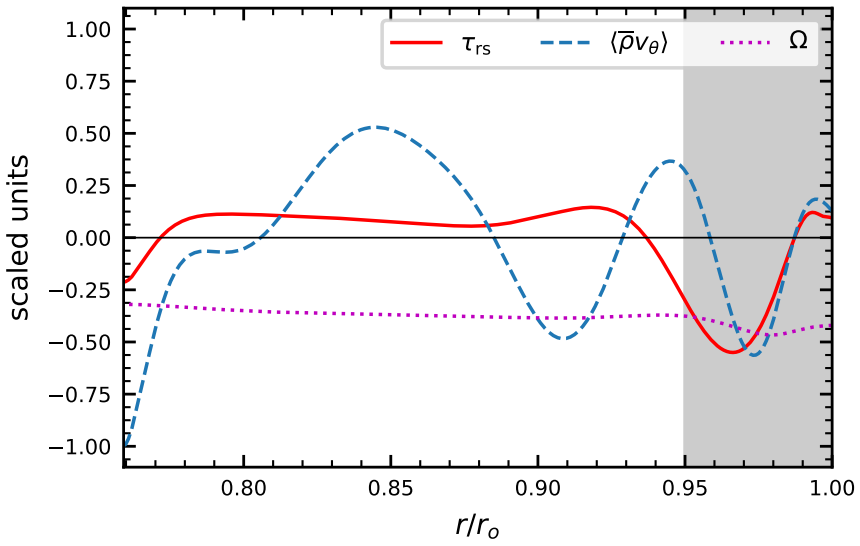

Figure 2.19: **The Relation Between Meridional Circulation, Rotation Rate, and Reynolds Stress in the NSSL**. Radial profiles of $\tau_{\rm rs}$, $\langle\overline{\rho}v_\theta\rangle$, and Ω, averaged over high latitudes (between $\pm45°$ and $\pm60°$) for case N5. We scale $\langle\overline{\rho}v_\theta\rangle$ by its maximum absolute value to make its radial profile lie in the range $(-1, 1)$. We scale Ω and $\tau_{\rm rs}$ to match the shape of their profiles in Figures 2.3 and 2.14, respectively. The shaded region indicates the near-surface layers in which the radial profile of the meridional circulation follows that of the Reynolds-stress torque.

understood, the origins of the NSSL may be determined by Equation (2.6).

Hotta et al. (2015) and Featherstone & Miesch (2015) have made substantial progress in understanding meridional force balance, with the former being concerned specifically with the balance required to maintain a NSSL. Hotta et al. (2015) argue that the high-latitude features of near-surface shear achieved in their simulation represent a significant deviation from the Taylor-Proudman state, which is achieved by turbulent transport of latitudinal momentum in the radial direction—i.e., the correlation $\langle v_r' v_\theta' \rangle$. This correlation is, they claim, produced by the sign of the radial derivative of the meridional flow ($\partial \langle v_\theta \rangle / \partial r$) in their NSSL. Although this indeed appears to be a promising mechanism to break the Taylor-Proudman constraint, we argue that it cannot provide the full picture for meridional force balance in the solar NSSL. The Sun has rotation rate constant roughly on radial lines at high latitudes and thus is not in a Taylor-Proudman state either within the shear layer or without. Thus, breaking the Taylor-Proudman state is a necessary, but insufficient condition to create near-surface shear.

Although the detailed dynamical maintenance of the solar meridional circulation is unclear, helioseismic observations provide fairly rigorous constraints on the circulation profile itself, at least in the NSSL. In particular, the there is little near-surface variation of latitudinal flow $\langle \overline{\rho} v_\theta \rangle$ with radius in the Sun as compared to case N5 (e.g., Giles et al. 1997; Zhao & Kosovichev 2004; Hathaway 2012; Chen & Zhao 2017; Mandal et al. 2018). Given that both the meridional circulation $\langle \overline{\rho} \boldsymbol{v}_{\rm pol} \rangle$ and rotation rate Ω are observationally constrained in the NSSL, it would be worthwhile to measure the Reynolds-stress torque in the NSSL as well, for example using high-resolution ring-diagram analysis (e.g., Greer et al. 2014; Greer et al. 2015). Once this is done, the relationship between meridional circulation and differential rotation in the NSSL will be elucidated. This will be an important guide for future simulations attempting to capture near-surface shear.

In summary, we have determined that the solar NSSL is still an unsolved problem. The argument that a rotationally unconstrained layer near a convecting spherical shell's outer surface efficiently mixes angular momentum (and thus, creates a NSSL) is oversimplified, since *only* the downflows are sufficiently rotationally unconstrained to pump angular momentum inward. At low

latitudes, the downflows must continually fight the upflows, which still exist in Busse columns and transport angular momentum outward. In our models, this battle between upflows and downflows seems essential to create substantial shear. By contrast, at high latitudes, the inward transport of angular momentum by both upflows and downflows only produces very weak shear due to the global character of the meridional circulation.

In future work, it would be useful to analyze the nature of the feedback between the meridional circulation and differential rotation achieved in spherical-shell models of convection, in particular its behavior in highly stratified regimes and in the presence of magnetic fields. This feedback is likely relevant in a broader context than simply NSSL dynamics. Since the meridional circulation is dynamically linked to the solar dynamo cycle both observationally and theoretically (e.g., Wang et al. 1989; Chou & Dai 2001; Ghizaru et al. 2010; Charbonneau 2014; Komm et al. 2015), dissecting the nature of feedback between the solar NSSL and meridional circulation will provide important theoretical constraints on the processes by which the Sun forms its magnetic field.

2.9 More Recent Modeling of the NSSL

As mentioned in Section 1.2.2 some of the magnetic tachocline simulations of Guerrero et al. (2016a,b) achieve shear layers strikingly similar to the solar NSSL, mostly at high latitudes. Guerrero et al. claim that their NSSLs arise from rotationally unconstrained turbulence (a negative torque from the Reynolds stress, as in cases N3 and N5), but their torque balances are not reported. (The torques are technically plotted in Figure 3 of Guerrero et al. 2016b, but the choice of colorbar renders the balance in the NSSL invisible). These `EULAG-MHD` models also have no explicit diffusion, and the transport properties associated with the unresolved scales are unknown. Still, the NSSLs in Guerrero et al. (2016a,b) are the most convincing of any of the global models. Isolating the role of the meridional circulation, magnetic fields, and coupling to a tachocline in such models would shed much light on the solar NSSL problem.

More recently, Choudhuri (2021) developed a simple model of the NSSL without using global simulations. His work posits that the NSSL is in thermal wind (geostrophic) balance, in addition

to the bulk of the CZ. As mentioned in Section 1.2.3, thermal wind balance is assumed to hold for high rotational constraint. This is usually considered a good approximation in the deep solar interior, but not in the near-surface layers (e.g., Miesch & Hindman 2011; Augustson et al. 2015; Karak et al. 2014; Hotta et al. 2015). The assumption that geostrophy is broken in the NSSL is, however, still an open question.

Choudhuri (2021) presents the thermal wind equation in the following form:

$$\lambda \frac{\partial \Omega^2}{\partial z} = \frac{g(r)}{r c_{\rm p}} \frac{\partial \left\langle \hat{S} \right\rangle}{\partial \theta} = \frac{g(r)}{r \overline{T}(r)} \frac{\partial \left\langle \hat{T} \right\rangle}{\partial \theta}. \tag{2.7}$$

The right-most equation is valid if isochores (surfaces of constant density) coincide with spheres, yielding $\langle \hat{\rho} \rangle = 0$ everywhere in the meridional plane and thus $\left\langle \hat{S} \right\rangle / c_{\rm p} = \left\langle \hat{T} \right\rangle / \overline{T}(r)$. It should be noted that no simulation we are aware of has yielded $\langle \hat{\rho} \rangle = 0$ (more often they yield $\left\langle \hat{S} \right\rangle \approx 0$—see Figure 3.8).

In any case, Choudhuri's argument goes as follows. The background temperature $\overline{T}(r)$ decreases rapidly radius, while $\partial \hat{T} / \partial \theta \sim \Delta \hat{T}$—the pole-to-equator temperature contrast—remains the same.[3] . We thus have that $\Delta \hat{T} / \overline{T}$ should skyrocket near the outer surface. If we also require Equation (2.7) to hold, then $\partial \Omega^2 / \partial z$—which is proportional to the tilt of the isorotation contours—must become large, thereby creating the NSSL.

Jha & Choudhuri (2021) show that Equation (2.7), assuming a radially independent $\Delta \hat{T} =$ 2.5 K (this value is taken from continuum and Ca II K intensity observations of the solar disc in Rast et al. 2008; see the following Chapter 3) reproduces the NSSL very well. They take the helioseismically inferred rotation profile from below the NSSL and then integrate Equation (2.7) outward, yielding a rotation profile in the NSSL matching helioseismology to within ∼5%. Of course, it is unclear what happens if the correct form of the thermal wind equation—employing the latitudinal entropy gradient, which unconstrained, either by helioseismology or theory—is used. If thermal wind balance is applicable in the NSSL, however, Choudhuri (2021); Jha & Choudhuri

[3] Rotationally unconstrained convection is argued to homogenize $\partial \hat{T} / \partial r$ in latitude so that the buoyant driving is not influenced by rotation. The temperature contrast $\Delta \hat{T}$ should then be constant in the rotationally unconstrained layer, which Choudhuri also assumes to be the depth of the NSSL.

(2021) have effectively shown that $\hat{\rho} = 0$ near the outer surface, which would be an interesting finding in and of itself.

Chapter 3

Revisiting the Sun's Strong Differential Rotation along Radial Lines

Current state-of-the-art models of the solar convection zone consist of solutions to the Navier-Stokes equations in rotating, 3-D spherical shells. Such models are highly sensitive to the choice of boundary conditions. In this Chapter, we present two suites of simulations differing only in their outer thermal boundary condition. This boundary condition is either one of fixed-entropy or fixed-entropy-gradient, as in Equation (1.7)(e). We find that the resulting differential rotation is markedly different between the two sets. The fixed-entropy-gradient simulations have strong differential rotation contrast and isorotation contours tilted along radial lines (in good agreement with the Sun's interior rotation profile revealed by helioseismology), whereas the fixed-entropy simulations have weaker contrast and contours tilted in the opposite sense. We examine in detail the force balances in our models and find that the poleward transport of heat by Busse columns drives a thermal wind responsible for the different rotation profiles. We conclude that the Sun's strong differential rotation along radial lines may result from the solar emissivity being invariant with latitude (which is similar to the fixed-entropy-gradient condition in our models) and the poleward transport of heat by Busse columns. In future work on convection in the solar context, we strongly advise modelers to use a fixed-gradient outer boundary condition.

This Chapter is primarily a restatement of the work published in Matilsky et al. (2020). As the primary author of the paper, I conducted the simulations, performed their analyses, created the Figures, and wrote most of the text. My coauthor Bradley Hindman wrote some of the initial drafts of Sections and 3.5 and 3.6. Both my coauthors Juri Toomre and Bradley Hindman provided

advice and guidance throughout the process, gave detailed text edits, and suggested schematic designs of some of the figures.

3.1 Introduction: The Sun's Tilted Isorotation Contours

Helioseismology has revealed in detail the internal rotation profile of the solar convection zone (CZ; e.g., Thompson et al. 2003; Howe et al. 2005), as shown in Figure 3.1. The most notable properties of the rotation rate are that the equator rotates significantly faster than the high-latitude regions and that the isorotation contours are tilted significantly with respect to the rotation axis, falling largely along radial lines. Furthermore, there are two shear layers at the top and bottom of the CZ: at the top, the contours bend toward the equator in a region known as the *Near-Surface Shear Layer* (NSSL; see Chapter 2), and at the bottom, the differential rotation in the CZ transitions to solid-body rotation, over a narrow boundary layer called the *tachocline*. Prior to helioseismic probing, most theoreticians had assumed that the differential rotation that is observed directly at the surface would imprint into the interior along isosurfaces parallel to the rotation axis, hence satisfying the Taylor-Proudman theorem. The helioseismic observations have clearly demonstrated that this theoretical supposition was wrong.

For the last several decades, global, 3-D supercomputer simulations of hydrodynamic convection in rotating spherical shells have succeeded in achieving rotation profiles that are fast at the equator and slow at the poles. However, simulations generally have a weaker overall differential rotation contrast than that of the Sun. If the contrast is defined to be the difference in rotation rate between the equator and 60° latitude, expressed as a percentage of the "frame" rotation rate, then for the Sun, this magnitude is ∼20% (using the solar Carrington rate $\Omega_\odot$ as the frame rate, for example). Most simulations, on the other hand, have rotation-contrast magnitudes of ∼10%, although there are some notable exceptions (e.g., Brun & Toomre 2002; Brown et al. 2010; Matilsky & Toomre 2020a). To date, however, there is no systematic physical explanation for why these particular simulations have high rotation contrast.

Simulations have also struggled to achieve rotation contours in the bulk of the CZ that are

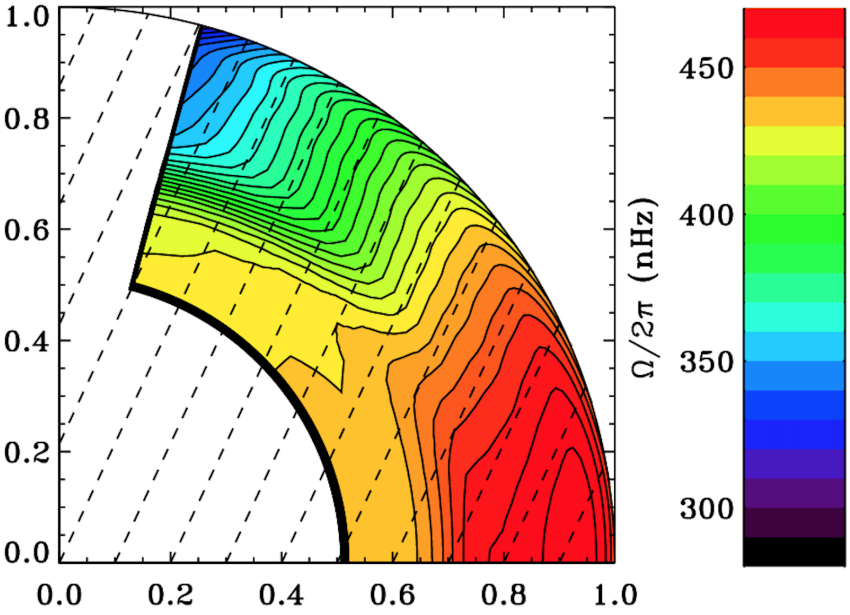

Figure 3.1: **The Solar Rotation Profile in the Meridional Half-Plane (Again).** Contour map in the upper meridional plane of the internal rotation profile of the Sun, in and below the CZ, averaged in longitude and time from 1995–2009. The rotation rate has been obtained using a regularized least-squares (RLS) inversion, which is sensitive only to the equatorially symmetric part of the rotation. The dashed lines are at a 25° angle to the rotation axis and align with the isorotation contours at mid-latitudes. Image credit: Howe et al. (2005), extended to include GONG data until 2009.

significantly tilted from the axis, as seen in Figure 3.1. With some exceptions (e.g., Elliott et al. 2000; Miesch et al. 2006), the simulations generally have cylindrically aligned contours. In the case of Miesch et al. (2006), the contours were tilted systematically by imposing a modest latitudinal entropy gradient at the base of the CZ. By modifying the magnitude of this entropy gradient, Miesch et al. (2006) controlled the magnitude of the contour tilt. Imposing this boundary condition was inspired by thermal wind balance in the tachocline imprinting up into the CZ.

There is also good evidence for thermal wind balance operating in the deep CZ from analytical models. Balbus (2009a) and Balbus et al. (2009) assumed a simple functional relationship between the entropy and angular velocity and solved explicitly for the combined isorotational and isentropic contours as characteristics of the thermal wind equation. This yielded tilted contours in good agreement with helioseismology for the bulk of the CZ (away from the boundary layers of shear at the top and bottom). Such analytical work—in addition to lending strong support for the presence of a thermal wind in the solar interior—points to the need to better understand the dynamical coupling between entropy and angular velocity in global numerical simulations, something we address in the present paper.

In this work, we explore the role that the outer thermal boundary condition plays, in conjunction with an interior thermal wind, in modifying the resulting differential rotation. We consider the two most commonly used options: fixed-entropy (FE), in which the entropy at the outer boundary is fixed to a constant value, and fixed-flux (FF), in which the radial entropy gradient at the outer boundary is fixed, therefore implying an outward conductive flux that is independent of latitude. See Hurle et al. (1967) and Edwards (1990) for descriptions of these boundary conditions in the context of linear theory, and Anders et al. (2020) for a detailed analysis of the boundary conditions in nonlinear simulations of Rayleigh-Bénard convection. The FF condition is more appropriate for the Sun, since the radiant flux from the solar photosphere does not appear to vary substantially with latitude. Rast et al. (2008) analyzed full-disk images from the Precision Solar Photometric Telescope at the Mauna Loa Solar Observatory and calculated non-magnetic contributions to the solar photospheric intensity. In both continuum and Ca II K intensity distributions, only a

$\sim$0.1–0.2% variation was observed, corresponding to a solar pole that is at most $\sim$2.5 K warmer (in terms of effective temperature) than the equator. The deduced near-spherical-symmetry of the solar emissive flux is a significant observation, since a thermal wind strong enough to drive the observed differential rotation would require greater differences in the interior temperature between equator and pole. We return to this point in our concluding remarks.

We do not address the dynamics of the near-surface nor tachocline shear layers in this work. In particular, our models have an impenetrable lower boundary that does not allow for the convective overshoot of downflow plumes into the stable region that may play a role in the origin of the tachocline. The dynamical maintenance of the NSSL is still an open question, as discussed in Hotta et al. (2015) and Matilsky et al. (2019), and models tend to only display signs of near-surface shear if they have high density contrast ($\gtrsim$100) across the CZ. To avoid high computational cost, the models in this work have a smaller density contrast of $\sim$20.

Solar-like differential rotation (fast equator and slow poles) in spherical-shell convection is thought to be due to the outward transport of angular momentum by Busse columns (also called "Taylor columns" and "banana cells"; e.g., Busse 2002; Jones et al. 2011; Matilsky et al. 2019). In this work, we show that Busse columns also transport heat poleward and equivalently drive a solar-like differential rotation through a thermal wind. We find that in our FF cases, the thermal wind drives stronger differential rotation magnitudes and achieves more significant tilts of the isorotation contours than in the corresponding FE cases. Elliott et al. (2000) noted this effect for one simulation, but did not explore the underlying mechanism.

In Section 3.2, we describe the parameter space explored by our simulation suite, as well as the mathematical details of the FF and FE boundary conditions. In Section 3.3, we describe the basic results of our experiment, focusing on the achieved differential rotation. In Section 3.4, we quantify the force balance achieved in our models, which, for the radial and latitudinal directions, consists of a thermal wind in spherical geometry. In Section 3.5, we examine the latitudinal transport of energy by Busse columns that is responsible for the thermal wind. In Section 3.6, we discuss how the effects of the thermal wind are modified by the outer thermal boundary condition. In Section

Table 3.1: **Common Input Parameters for All Simulations**. Each shell covers three density scale heights of the solar convection zone, as in case N3 (see Chapter 2 and Table 2.1).

r_i	5.00×10^{10} cm $= 0.719\ R_\odot$
r_o	6.59×10^{10} cm $= 0.947\ R_\odot$
c_p	3.50×10^{8} erg K^{-1} g^{-1}
γ	1.67
$\overline{\rho}_\mathrm{i}$	0.181 g cm^{-3}
$L_\odot$	3.85×10^{33} erg s^{-1}
$M_\odot$	1.99×10^{33} g
$R_\odot$	6.96×10^{10} cm
$\mathrm{Pr} \equiv \nu/\kappa$	1.00

3.7, we discuss our simulation results in the context of the Sun.

3.2 Numerical Experiment

We consider time-dependent, 3-D simulations of a rotating, stratified spherical shell of fluid representative of the solar CZ. As in Chapter 2, we use the open-source code `Rayleigh 0.9.1` (Featherstone & Hindman, 2016a; Matsui et al., 2016; Featherstone, 2018), which solves the equations of hydrodynamics in spherical geometry. All notation and equations solved are identical to that laid out in Chapter 2. Each simulation is similar to case N3 from that Chapter. In particular, the background thermodynamic state is one of an adiabatically stratified polytrope and the density contrast across all our spherical shells is $\exp(N_\rho) = \exp(3) \sim 20$. Each simulation differs only by the value of $\nu = \kappa$ (the Prandtl number for all simulations described in this thesis is unity), the rotation rate, and the outer thermal boundary condition. Input parameters common to all the simulations explored here are shown in Table 3.1.

The main purpose of this work is to characterize the influence of the outer thermal boundary condition on the behavior of the resulting differential rotation. Recall that in Chapter 2, both cases considered (N3 and N5) had top thermal boundary conditions of fixed entropy. Here we consider models with different background rotation rates Ω_0 and diffusion values ($\nu = \kappa$). For each model,

we analyze two sub-cases:

$$\hat{S} = 0 \text{ at } r = r_{\mathrm{o}} \qquad \text{(fixed entropy, or FE)} \tag{3.1}$$

and

$$\frac{\partial \hat{S}}{\partial r} = -\frac{L_{\odot}}{4\pi r_{\mathrm{o}}^2 \overline{\rho}\overline{T}\kappa} \text{ at } r = r_{\mathrm{o}} \qquad \text{(fixed flux, or FF).} \tag{3.2}$$

The solar luminosity that is injected into the system via internal heating is ultimately carried out through the outer surface via thermal conduction, which in our models arises from entropy gradients (see Equation (1.1b)). For the fixed-entropy condition (3.1), the interior is initially heated (leading to $\hat{S} > 0$ in the lower parts of the CZ) while the entropy at the outer surface is "pinned" to zero. This naturally establishes a thermal boundary layer (sharp entropy gradients $\partial\hat{S}/\partial r < 0$) just below the outer surface. The steepness of the gradient (i.e., the strength of the outward conductive loss of energy) is allowed to vary with latitude.

For the fixed-flux condition (3.2), the outer thermal boundary layer is present from the beginning of the simulation. The steepness of the entropy gradient (and thus the energy loss) at the outer surface is independent of latitude by construction, and is forced to have exactly the value needed to carry out a solar luminosity. The fixed-flux condition is thus more "solar-like," since in the Sun there is little observed latitudinal dependence of the emergent intensity (Rast et al., 2008), which is equal to the energy lost via radiative cooling at the photosphere.

For both the FE and FF cases, the thermal conductive boundary layer stands in contrast to the real solar photosphere, in which radiative cooling removes the heat from a very thin ($\sim$100 km) outer layer. The cooling drives very small temporal and spatial scales of motion compared to the deep interior (such as granulation and supergranulation), making its direct inclusion in global models problematic. Researchers have sought to address this difficulty in various ways. Nelson et al. (2018) implemented stochastic driving of convection by near-surface plumes designed to mimic the effects of supergranulation, finding that that the flow structures and transport properties were significantly altered in the deep CZ. Hotta et al. (2019) simulated the whole CZ with no rotation or

magnetic field, coupling a global spherical shell that captured large-scale flows in the deep interior to a Cartesian box that solved the equations of radiative transfer in the photosphere (they used the `RSST` code mentioned in Chapter 1). They found that the near-surface motions had a weak influence on the deep interior. Regardless of its relevance to interior flow structures, correctly capturing the small-scale near-surface flows in global models is currently prohibitively expensive computationally. In order to explore a wider range of parameter space, we thus only consider the FE and FF boundary conditions here.

3.3 Simulation Results

We label simulations with a prefix that signifies the outer boundary condition ("FE" for Equation (3.1) and "FF" for Equation (3.2)), followed by the value of the diffusion constant $\nu = \kappa$ (in units of 10^{12} cm^2 s^{-1}), followed by the value of the rotation rate (in units of the sidereal Carrington value for the Sun, $\Omega_\odot \equiv 2.87 \times 10^{-6}$ rad s^{-1}, or $\Omega_\odot/2\pi \equiv 456$ nHz). For example, "case FE4-3" refers to a simulation with an FE outer boundary, for which $\nu = \kappa = 4 \times 10^{12}$ cm^2 s^{-1} throughout the domain, and $\Omega_0 = 3\Omega_\odot$. We note that except for the slightly differing definitions of $\Omega_\odot$, case FE2-3 here is identical to case N3 from Chapter 2. [1]

Table 3.2 in Section 3.8 contains the values of the non-dimensional parameters, as well as the grid resolution, for each of the 18 simulations considered in this work. Table 3.2 has four groupings according to FE or FF at two different rotation rates. Following the notation of Featherstone & Hindman (2016b), we parameterize the strength of the imposed driving in each simulation through a bulk "flux Rayleigh number" (imposed a priori),

$$\mathrm{Ra_F} \equiv \frac{\tilde{g}\tilde{F}H^4}{c_\mathrm{p}\tilde{\rho}\tilde{T}\nu^3} \tag{3.3}$$

[1] In Chapter 2, we used $\Omega_\odot \equiv 2.6 \times 10^{-6}$ rad s^{-1}, which is the value of the interior rotation rate of the Sun as predicted from the tachocline model of Spiegel & Zahn (1992). This convention likely began in Brun & Toomre (2002) and does not agree with the results of helioseismology (e.g., Howe et al. 2000). In this and subsequent Chapters, we instead choose $\Omega_\odot$ to be the solar Carrington value. In any case, these different conventions likely make little difference, since we cannot achieve solar-like differential rotation for models rotating near the solar rate anyway.

and the level of turbulence through bulk Reynolds or Péclet numbers (calculated a posteriori),

$$\mathrm{Re} = \frac{\mathrm{Pe}}{\mathrm{Pr}} = \frac{\tilde{v}' H}{\nu}. \tag{3.4}$$

Since the Prandtl number for all models is unity, the Péclet number $\mathrm{Pe} = \tilde{v}' H \kappa^{-1}$ equals the Reynolds number.

Similarly, we parameterize the influence of rotation through an Ekman number (imposed a priori),

$$\mathrm{Ek} \equiv \frac{\nu}{2\Omega_0 H^2} \tag{3.5}$$

and a bulk Rossby number (calculated a posteriori),

$$\mathrm{Ro} \equiv \frac{\tilde{v}'}{2\Omega_0 H}. \tag{3.6}$$

In the preceding equations, the length scale H is taken to be the shell depth $r_\mathrm{o} - r_\mathrm{i}$, the tildes refer to volume averages over the full spherical shell. For the volume averages of the thermodynamic variables (e.g., $\tilde{\rho}$), we take the average of the background variable (e.g., $\overline{\rho}(r)$). F refers to the energy flux associated with conduction and convection in equilibrium (see Featherstone & Hindman 2016b). The typical convective velocity amplitude $\tilde{v}'$ refers to the rms of the velocity with the longitudinally averaged part subtracted, the mean being taken over time and over the full volume of the shell. Throughout this work, temporal averages are taken during the latter portion of run time for which there is statistical equilibrium—generally $\sim$3/4 of the total run time listed in Table 3.2.

Before discussing our results in detail, we note that all our models have fairly high levels of thermal and viscous diffusion. Furthermore, all our models rotate at either two or three times the solar Carrington rate. These choices, which stand in contrast to the physics of the solar interior, ensure that our models have low enough Rossby numbers to avoid antisolar differential rotation (fast polar regions, slow equator). All global spherical-shell convection codes produce high velocities at large scales in the solar context when sufficiently turbulent. The influence of rotation on the large scales is therefore weak, which causes less coherence in the outward angular momentum transport

by the convection, and ultimately less angular momentum in the outer layers than the inner layers (i.e., an antisolar differential rotation). The overall problem—that increasing the turbulence in simulations leads to antisolar states—is now called the "convective conundrum" (O'Mara et al., 2016). The antisolar states can be avoided by raising the rotation rate, raising the diffusions, or lowering the luminosity. We choose a combination of the former two, which requires that our models are only moderately turbulent. Nonetheless, the viscous force and heat flux are small to leading order in the primary dynamical balances.

Returning to our simulation results, we quantify the magnitude of the overall differential rotation contrast as the difference in the outer-surface rotation rate between the equator and 60°-latitude, normalized by the frame rotation rate:

$$\frac{\Delta\Omega}{\Omega_0} \equiv \frac{\Omega(r_\mathrm{o}, \pi/2) - \Omega(r_\mathrm{o}, \pi/6)}{\Omega_0}, \tag{3.7}$$

where

$$\Omega(r, \theta) \equiv \Omega_0 + \frac{\langle v_\phi \rangle}{r \sin\theta} \tag{3.8}$$

is the rotation rate of the fluid as a function of r and θ and the angular brackets denote a combined temporal and longitudinal average. From Table 3.2, the FF cases have differential rotation contrasts $\Delta\Omega/\Omega_0$ that are significantly greater—on average, by ∼40%—than those of the FE cases. For comparison, the solar value of the rotation contrast is substantially higher than in any of our models: $\Delta\Omega_\odot/\Omega_\odot = 0.20$ (see Howe et al. 2000, Figure 1). For the solar estimate, we have taken $\Omega_\odot$ to be the sidereal Carrington rate and r_o to lie just below the Near-Surface Shear Layer.

Figure 3.2 shows how the differential rotation fraction scales with the reduced Rayleigh number, which accounts for the increase to the critical Rayleigh number for convective onset caused by rotation (Chandrasekhar, 1961). The reduced Rayleigh number thus serves as a better parameterization of the supercriticality of the system than simply the Rayleigh number. From Figure 3.2, each type of boundary condition yields a similar scaling with the reduced Rayleigh number $\mathcal{R}$. For the $\Omega_0 = 3\Omega_\odot$ cases (circles in Figure 3.2), the rotation contrast increases monotonically

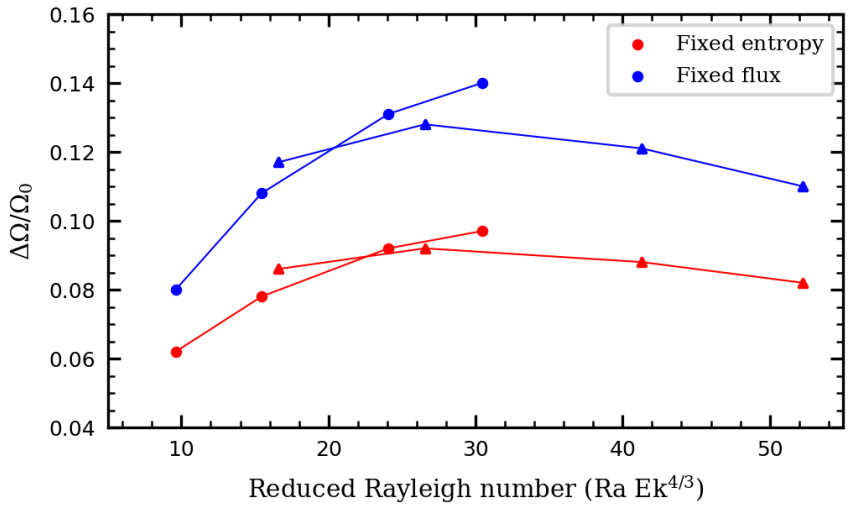

Figure 3.2: **Simulated Rotation Contrasts for Upper Thermal Boundary Conditions**. Rotation contrast achieved by the suite of simulations plotted as a function of the reduced Rayleigh number $\mathcal{R} \equiv \mathrm{Ra\ Ek}^{4/3}$. Circles mark the $\Omega_0 = 3\Omega_\odot$ cases and triangles the $\Omega_0 = 2\Omega_\odot$ cases.

(but with decreasing slope) with increasing $\mathcal{R}$, so that the curves connected by circles in Figure 3.2 are concave-down. For the $\Omega_0 = 2\Omega_\odot$ cases (triangles in Figure 3.2), the curves "overturn" so that a peak value of the rotation contrast (at around $\mathcal{R} \sim 27$) is achieved. This behavior (concisely described in Gastine et al. 2013) is a symptom of the convective conundrum; as models grow more turbulent, the rotation contrast increases at first, but then decreases and eventually becomes negative (i.e., antisolar).

To illustrate exactly where the "extra" rotation contrast in the FF cases is located, we plot the rotation rate at the outer surface for three of the cases rotating at $3\Omega_\odot$ in Figure 3.3. Most of the additional contrast occurs at high latitudes, where the polar regions in the FF cases rotate significantly more slowly than in their FE counterparts. Additionally, the equator in the FF cases rotates slightly faster than in the FE cases. For all simulation pairs, the difference in contrast between the FE case and the FF case is greater the smaller the value of the diffusion (or the higher the level of turbulence).

Figure 3.4 shows contour plots of rotation rate in the upper meridional plane for some of the simulation suite. Clearly there is a striking difference between the tilts of the rotation contours in

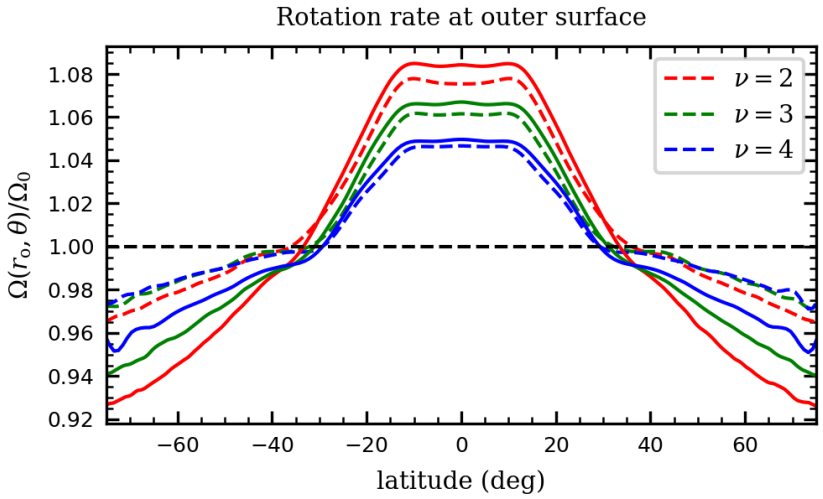

Figure 3.3: **Simulated Latitudinal Rotation Profiles for Each Thermal Boundary Condition**. Temporally and longitudinally averaged rotation rate (normalized by the frame rate Ω_0) at the outer surface for three of the cases rotating at $\Omega_0 = 3\Omega_\odot$, plotted versus latitude. Dashed lines correspond to the FE cases and solid lines to the FF cases. In the legend, $\nu = \kappa$ is given in units of 10^{12} cm^2 s^{-1}.

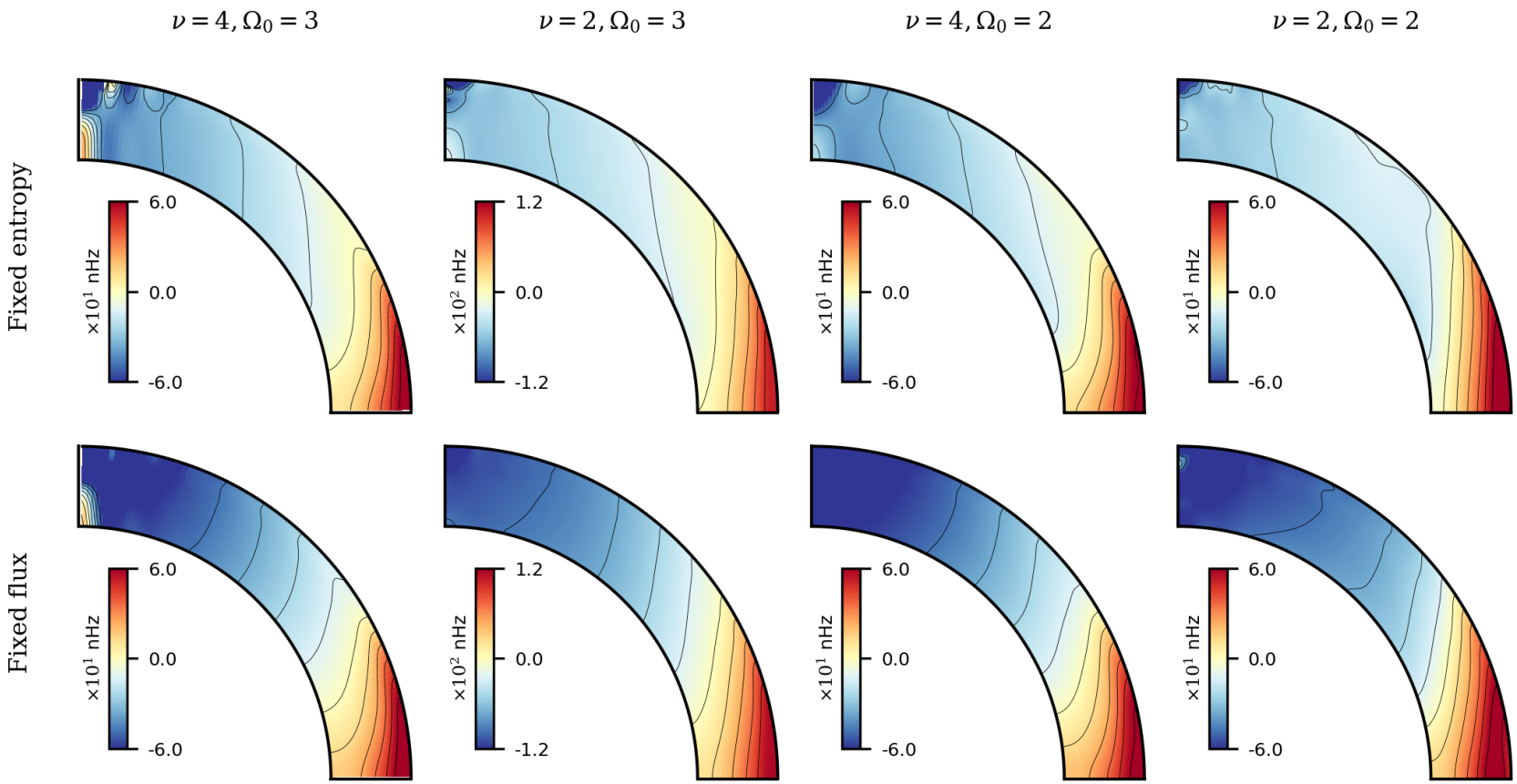

Figure 3.4: **Simulated Latitudinal Rotation Profiles for Each Thermal Boundary Condition**. Temporally and longitudinally averaged rotation rate in the meridional plane for some of the simulations in the suite, with the two hemispheres averaged assuming even symmetry about the equator. In the titles at the top, $\nu = \kappa$ is given of units of 10^{12} cm^2 s^{-1}, and Ω_0 in units of $\Omega_\odot$.

the FE and FF simulations.

In this paper, we define all rotation-contour *tilt angles* (or simply *tilts*) with respect to the rotation axis, with zero tilt corresponding to alignment of the contour with the rotation axis. We use the sign convention for tilt angle illustrated in Figure 3.5. Under this convention, the solar rotation contours have positive tilts at all latitudes in the bulk of the CZ (above the tachocline and below the NSSL, as shown in Figure 3.1). We thus define the tilt angle of a rotation contour at a given point in the meridional plane as

$$\text{tilt} \equiv -\tan^{-1}\left[\frac{\partial\Omega/\partial z}{\partial\Omega/\partial\lambda}\right], \tag{3.9}$$

which is consistent with the sign convention shown in Figure 3.5 for solar-like differential rotation, in which the contours further from the rotation axis correspond to a higher rotation rate.

Describing the solar rotation contours as "tilted along radial lines," as is often done, is technically misleading. Radial tilt implies a specific dependence of the contour tilt angle with latitude, namely, contours that fan radially outward from the center of the Sun. In Figure 3.1, by contrast, the bulk-CZ tilts are roughly constant at $\sim 25^\circ$ for mid-latitudes, are smaller than $\sim 25^\circ$ for low latitudes (where radially aligned tilts would be greater), and are greater than $\sim 25^\circ$ for high latitudes (where radially aligned tilts would be smaller). To avoid confusion, we will henceforth not use the term "radial tilt" and instead describe the rotation-contour tilt (in the Sun and in our simulations) simply as "positive" or "negative," using the sign convention illustrated in Figure 3.5.

In Figure 3.6, we show the values of the rotation-contour tilt angle at mid-depth for a subset of our models and for the Sun. The positive tilt for the FF cases is obvious, with the maximum tilt angle being about $+15^\circ$ for the highest value of the diffusion ($\nu = 4 \times 10^{12}$ cm^2 s^{-1}). This is still substantially lower than the solar value for contour tilt, which attains a maximum value of $\sim 25^\circ$ in the middle of the solar CZ. The contours in the FE cases all have positive tilt at low latitudes. At high latitudes, however, they have negative tilt, and are tilted the most (with a tilt angle of about -10°) for the *lowest* value of the diffusion ($\nu = 2 \times 10^{12}$ cm^2 s^{-1}).

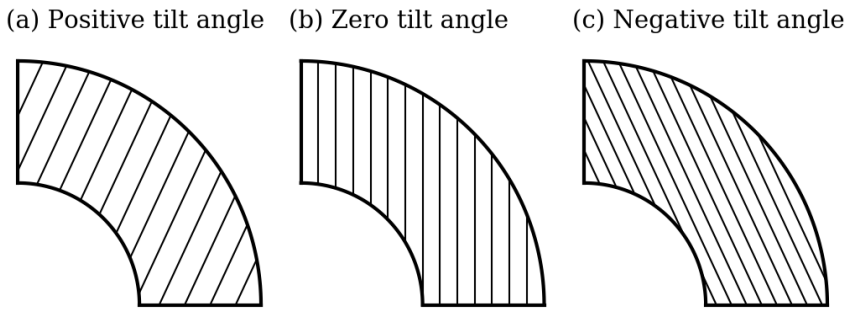

Figure 3.5: **Schematic of the Different Types of Contour Tilt**. Here we show our definition of contour tilts: (a) Positive contour tilt (all contours tilted at a constant $+25°$), (b) zero contour tilt, and (c) negative contour tilt (all contours tilted at a constant $-25°$).

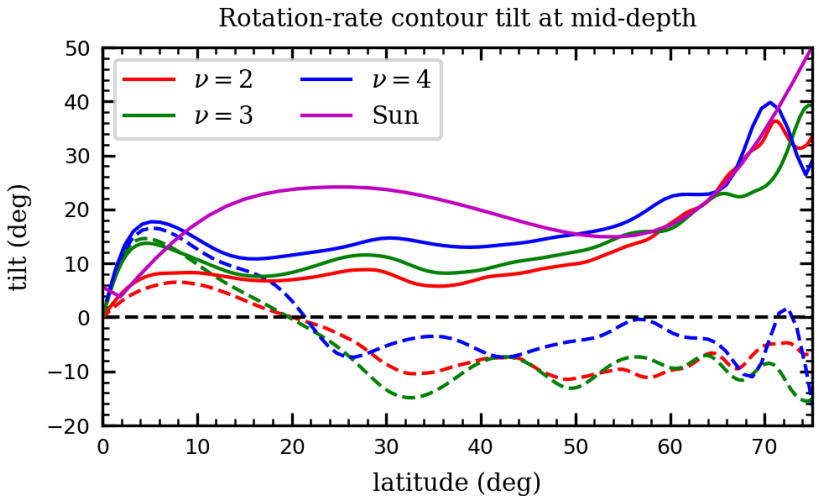

Figure 3.6: **Latitudinal Tilt-Angle Profiles for Each Thermal Boundary Condition**. Tilt angle of Equation (3.9) shown as a function of latitude for three of the cases rotating at $3\Omega_\odot$ and for the Sun. The profiles are taken at the middle of the shell for our models and the middle of the CZ for the Sun. The Northern and Southern Hemispheres have been averaged assuming odd symmetry for tilt angle. Dashed lines correspond to the FE cases and solid lines to the FF cases. For the solar tilt angle, we use the inversion from GONG data 1995–2004 as reported in Howe et al. (2005) and shown in Figure 3.1.

3.4 Thermal wind balance

We find that to leading order, the longitudinally and temporally averaged force balance in the meridional directions r and θ (or λ and z) is dominated by the Coriolis, pressure, and buoyancy forces for each simulation in this work:

$$-\nabla\left(\frac{\langle P\rangle}{\overline{\rho}}\right)+\frac{\langle S\rangle}{c_{\mathrm{p}}}g(r)\hat{\boldsymbol{e}}_r+2\left\langle v_\phi\right\rangle\hat{\boldsymbol{e}}_\phi\times\boldsymbol{\Omega}_0\approx 0. \tag{3.10}$$

Here, the angular brackets denote a combined temporal and longitudinal average.

In the Earth's atmosphere, a "thermal wind" describes a situation in which geostrophic balance (pressure balancing the Coriolis force) holds in the horizontal directions and hydrostatic balance (pressure balancing gravity) holds in the vertical direction. Equation (3.10) thus represents the generalization of a thermal wind to the solar geometry, in which the vertical (radial) and horizontal extents of the flow structures are comparable (unlike in the Earth's atmosphere where the vertical extent is very small). Furthermore, the flows in the solar geometry generally have a vertical component, unlike in a classical thermal wind for which the flows are purely horizontal.

The colatitudinal component of Equation (3.10) may be rearranged to yield

$$\Omega(r,\theta)\approx\Omega_0+\frac{1}{\Omega_0\overline{\rho}r^2\sin 2\theta}\left\langle\frac{\partial P}{\partial\theta}\right\rangle, \tag{3.11}$$

which is a purely geostrophic equation, since the buoyancy force is radial. Figure 3.7 shows a representative example of geostrophic balance for the FE2-3/FF2-3 pair. Clearly Equation (3.11) is very well satisfied for both cases, with deviations from geostrophy being no more than 1 part in 10^3 in the bulk of the meridional plane and 1 part in 10^2 at isolated regions by the equator and pole. The same is true for all the cases considered in this work, indicating that the differential rotation profile in our simulations is almost completely determined by the pressure profile, and vice versa. The fact that the differential rotation magnitudes are $\sim$40% greater in the FF cases compared to the FE cases is thus a consequence of greater latitudinal pressure gradients. Figure 3.7 also indicates that viscosity plays a relatively insignificant role in the force balance at large scales.

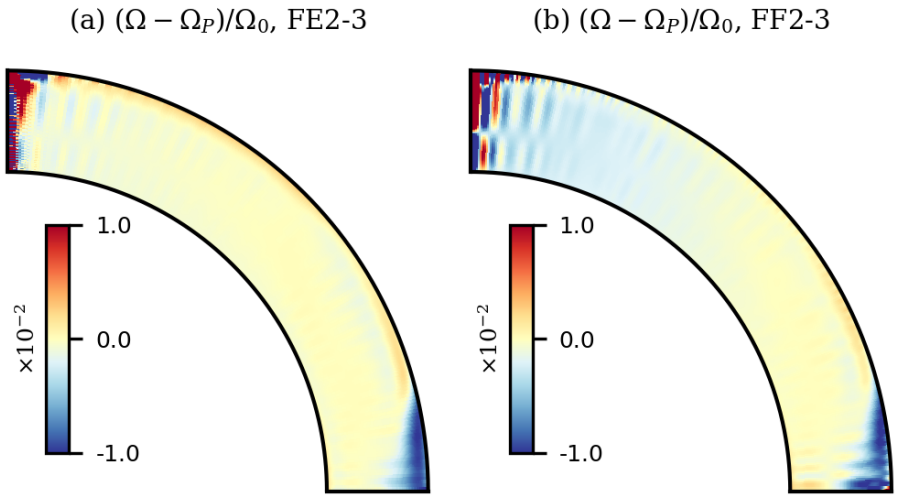

Figure 3.7: **Thermal Wind Balance: The Pressure Perspective**. Point-by-point colatitudinal force balance in the meridional plane for representative pair (a) case FE2-3 and (b) case FF2-3. We show the difference between the temporally and longitudinally averaged rotation rate Ω and the right-hand side of Equation (3.11), which we denote by Ω_P (rotation rate from the pressure), normalized by the frame rotation rate Ω_0. The two hemispheres have been averaged assuming even symmetry about the equator.

To assess why there are opposite signs of tilt for the rotation contours in the FF and FE simulations, we differentiate Equation (3.11) with respect to the axial coordinate z and use the radial component of Equation (3.10) to eliminate terms (or equivalently, take the ϕ-component of the curl of Equation (3.10)), yielding

$$\frac{\partial \Omega}{\partial z} \approx \frac{g}{2\Omega_0 r^2 \sin\theta c_{\rm p}} \left\langle \frac{\partial S}{\partial \theta} \right\rangle. \tag{3.12}$$

The tilt of the rotation contours is thus determined by the entropy distribution in the final thermodynamic state.

In Figure 3.8, we show the average profiles for entropy, pressure, and temperature in the meridional half-plane for the FE2-3/FF2-3 pair. Case FF2-3 (which is representative of all the FF cases in the simulation suite) displays a monotonically increasing entropy from equator to pole. Case FE2-3, on the other hand, has a non-monotonic entropy profile: except on the outer boundary, the entropy from equator to pole increases up to $\sim 20^\circ$ latitude, then decreases. In both cases, the pressure and temperature deviations (normalized by the background reference state) are substantially greater (by a factor of $\sim$30 in the case of the pressure) than the entropy deviation. The profiles of pressure and temperature in the meridional plane thus tend to mirror one another, with high temperature regions corresponding to high pressure regions and vice versa (compare the last two columns of Figure 3.8).

The balance described by Equation (3.12) is shown for the representative simulation pair FE2-3/FF2-3 in Figure 3.9. There is good balance in the deep layers, although significant departures near the outer surface, which has been noted frequently in past work (e.g., Brun et al. 2011; Augustson et al. 2012; Hotta et al. 2015). Quantitatively, the error in Equation (3.12) (shown in the right-hand column of Figure 3.9) is $\sim$10% in the lower 80% of the layer and $\sim$50% in the upper 20% of the layer. For solar-like differential rotation (fast equator and slow poles), positively tilted rotation contours (the FF cases) correspond to $\partial\Omega/\partial z < 0$, which arises from $\langle \partial S/\partial\theta \rangle < 0$ at all latitudes, as in Figure 3.8(d). Similarly, the FE cases (which have contours tilted negatively at high-latitudes and positively at low latitudes) all have $\langle \partial S/\partial\theta \rangle > 0$ at high latitudes and $\langle \partial S/\partial\theta \rangle < 0$

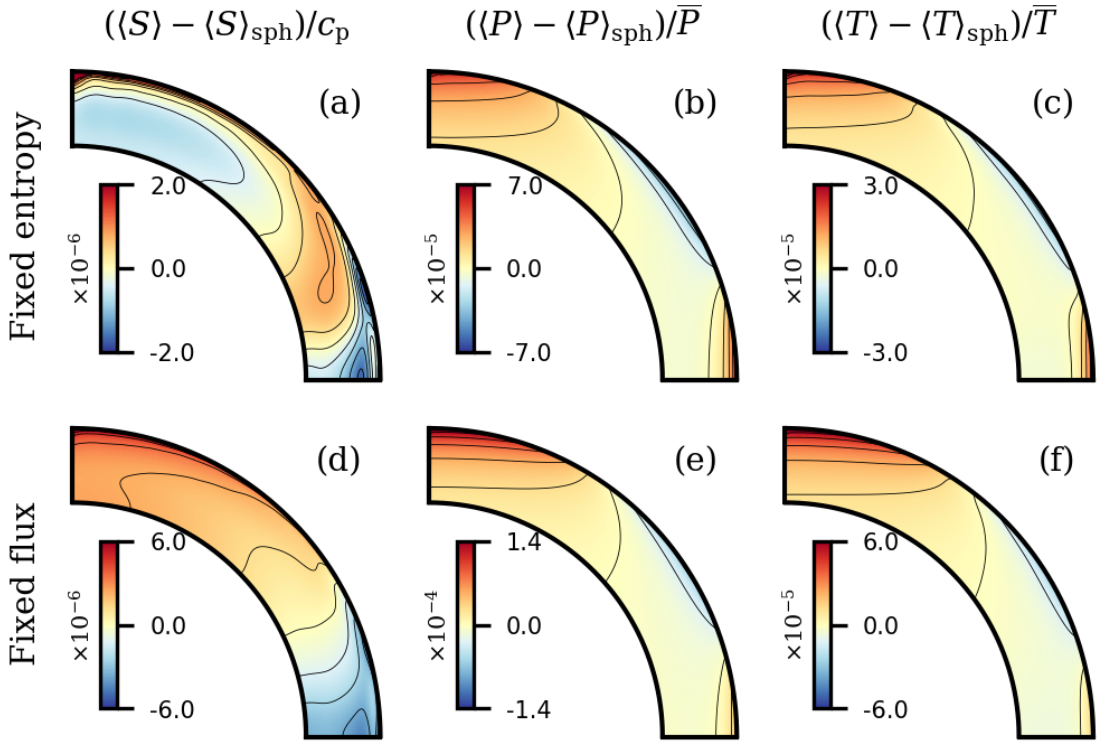

Figure 3.8: **Thermodynamic Profiles for Each Thermal Boundary Condition**. Temporally and longitudinally averaged entropy, pressure, and temperature deviations from the spherically symmetric mean in the meridional half-plane (averaged assuming even symmetry about the equator) for cases FE2-3 and FF2-3, normalized by the reference state profiles. The spherical mean $\langle\cdots\rangle_{\rm sph}$ has been removed to show the variation from equator to pole. There should be "hats" over some of the thermodynamic variables in the panel labels; in Matilsky et al. (2020), we used overbars to indicate reference quantities and the lack of overbars to indicate perturbation quantities.

at low latitudes, as in Figure 3.8(a).

3.5 Poleward energy transport from Busse columns

In light of Equations (3.11) and (3.12), a thermal wind in spherical geometry fundamentally consists of pressure and entropy differences in latitude. Polar regions that are high-pressure and high-entropy relative to lower latitudes (which we have shown lead to strong differential rotation with positively tilted contours) are expected to be established by the preferentially poleward transport of energy. In our simulations, this transport arises from the action of the convective Busse-column rolls. These rolls manifest at convective onset as an overstable, low-frequency prograde wave (e.g., Unno et al. 1989) or, as it is called in the geophysics literature, a thermal Rossby wave. This wave consists of a series of convective rolls, or Busse columns, that gird the equator. Each roll is rotationally aligned and the sign of the vorticity alternates from roll to roll. Furthermore, each roll is in geostrophic balance; hence, the alternating sign of the vorticity corresponds to every other roll being a zone of high pressure, with low-pressure rolls in between. Since the ends of the columns (at mid-latitudes) have neutral pressure, the pressure anomalies at the equator cause poleward axial flow in the high-pressure rolls and equatorward flow in the low-pressure rolls (e.g., Figure 1 in Gilman 1983). The resulting strong correlation between pressure and the direction of axial flow leads to a net poleward enthalpy flux through pressure work.

The effect just described is easiest to illustrate for models that are barely supercritical. Here, the profiles for the velocity and thermodynamic variables are dominated by the wavenumber associated with the most unstable mode. For the range of Ekman numbers spanned by our simulation suite, the resulting Busse columns are mostly localized in the outer half of the shell by radius and at low latitudes (see Jones et al. 2009 for a linear stability analysis of the problem). Figures 3.10(a, b) show the instantaneous convective radial velocity and convective colatitudinal energy transport in the highly diffusive case FE10-3, which lies in the barely supercritical regime. Each upflow and downflow (pairs of which trace one Busse column roll) has an associated colatitudinal energy transport that is, on average, negative in the Northern Hemisphere and positive in

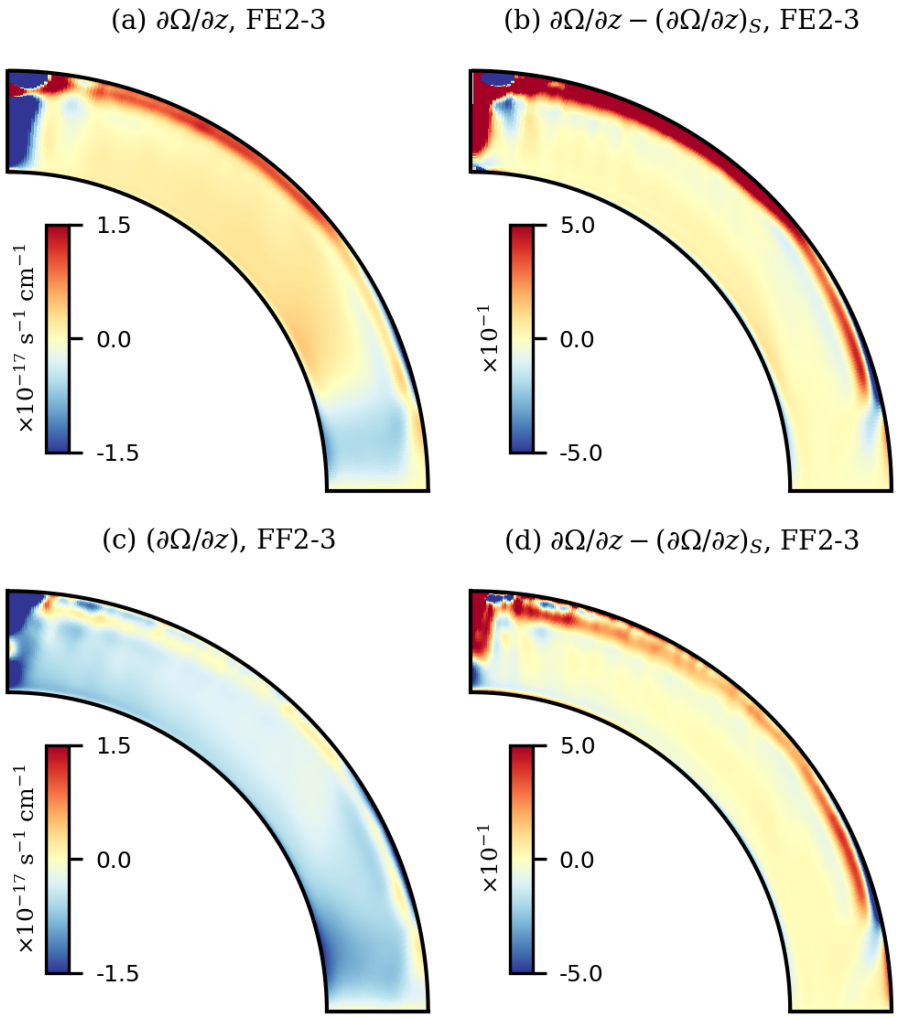

Figure 3.9: **Curl of Thermal Wind Balance: The Entropy Perspective**. Temporally and longitudinally averaged azimuthal vorticity balance in the meridional plane for representative pair FE2-3 and FF2-3. The two hemispheres have been averaged assuming odd symmetry about the equator. The left-hand column (a, c) shows the axial derivative of the rotation rate, $\partial\Omega/\partial z$. The right-hand column (b, d) shows the difference between $\partial\Omega/\partial z$ and the right-hand side of Equation (3.12) ($(\partial\Omega/\partial z)_S$, or the axial derivative of rotation rate from the entropy), normalized by 1.5×10^{-17} s^{-1} cm^{-1}.

the Southern Hemisphere, implying preferentially poleward energy transport. Note that under the spherical-coordinate convention, with θ as the colatitude, the positive-θ direction is always oriented north–south. Thus equatorward (poleward) transport of energy corresponds to positive (negative) colatitudinal transport in the Northern Hemisphere and negative (positive) transport in the Southern Hemisphere.

Figures 3.10(c, d) show the radial velocity and convective energy transport in the comparatively more turbulent case FF2-3. The flow structures are more intricate and fine-scale than in the barely supercritical regime, but the imprint of the most unstable mode remains. Many Busse column rolls—which can be seen at low latitudes as columnar red and blue features in Figure 3.10(c)—correspond to sites of negative colatitudinal energy transport (blue in Figure 3.10(d)) in the Northern Hemisphere and positive transport (red in Figure 3.10(d)) in the Southern Hemisphere. Overall, there are more sites of poleward energy transport (from the Busse columns) than sites of equatorward transport in each hemisphere. Under an azimuthal average, the Busse columns in the more turbulent case FF2-3 thus yield preferentially poleward energy transport, just as in the barely supercritical case FE10-3.

The geostrophic nature of the Busse columns is illustrated in Figure 3.11, as is the resulting axial component of the flow. In the top row (case FE10-3), panel (a) shows that the Busse-column rolls alternate between high and low pressure. Panel (b) shows that the high-pressure rolls are each anticyclonic (have negative vorticity), while the low-pressure rolls are cyclonic. Finally, panel (c) shows that each high-pressure anomaly corresponds to poleward flow ($v_z > 0$ in the Northern Hemisphere), while each low-pressure anomaly corresponds to equatorward flow ($v_z < 0$). In the bottom row (the more supercritical case FF4-3), the Busse columns are less regularly spaced, but still largely alternate between anticyclonic regions of high pressure and cyclonic regions of low pressure (panels d, e). The axial flow associated with the Busse columns in case FF4-3 (panel f) then leads to poleward energy transport through pressure work, just as in case FE10-3.

It has long been known that Busse columns transport angular momentum outward. We have just shown that Busse columns also transport heat poleward. The Busse columns thus define

a purely hydrodynamic mechanism coupling entropy and angular velocity. Balbus et al. (2009) posited the presence of such a convective mechanism in the Sun and further argued that the motions responsible should fall along surfaces of both constant entropy and constant angular velocity. In that picture, the isorotational and isentropic contours should thus coincide. The Busse columns in our simulation suite do not completely behave in this way, as evidenced by none of our simulations having good alignment of the isorotational and isentropic contours. Independent of whether the constant-entropy and constant-angular-velocity surfaces coincide in the Sun, a key point from our work is that the Busse columns provide an explicit convective mechanism to couple entropy and angular velocity.

3.6 Effect of outer thermal boundary condition

Given that Busse columns direct energy poleward, equilibrium can be achieved by forming conductive gradients that balance the poleward convective enthalpy flux. In general, such conductive transport can be achieved in two distinct ways. As the pole heats up and the equator-to-pole contrast increases, a latitudinal gradient will form that transports heat equatorward. Additionally, the increased temperature of the pole can lead to enhancement of the radial gradients in the outer thermal boundary layer, thus causing the poles to lose heat more efficiently (i.e., become superluminous). In the FF cases, the outer thermal boundary condition precludes the second of these options because the radial gradients are fixed. Hence, the FF models must rely solely on the development of a pole-to-equator conductive gradient. In the FE models, both types of gradients are possible. Therefore, the amount that the pole must be heated before equilibrium can be achieved is less for the FE models than it is for the FF models. The outer thermal boundary condition thus has a direct influence on the latitudinal contrast in the temperature, entropy, and pressure, with the FF boundary condition being conducive to strong contrast in all the thermodynamic variables. In the presence of thermal wind balance, the FF boundary condition thus leads to enhanced contrast in the differential rotation and positively tilted contours in the rotation rate.

Mathematically, we illustrate the combined effects of the outer thermal boundary condition

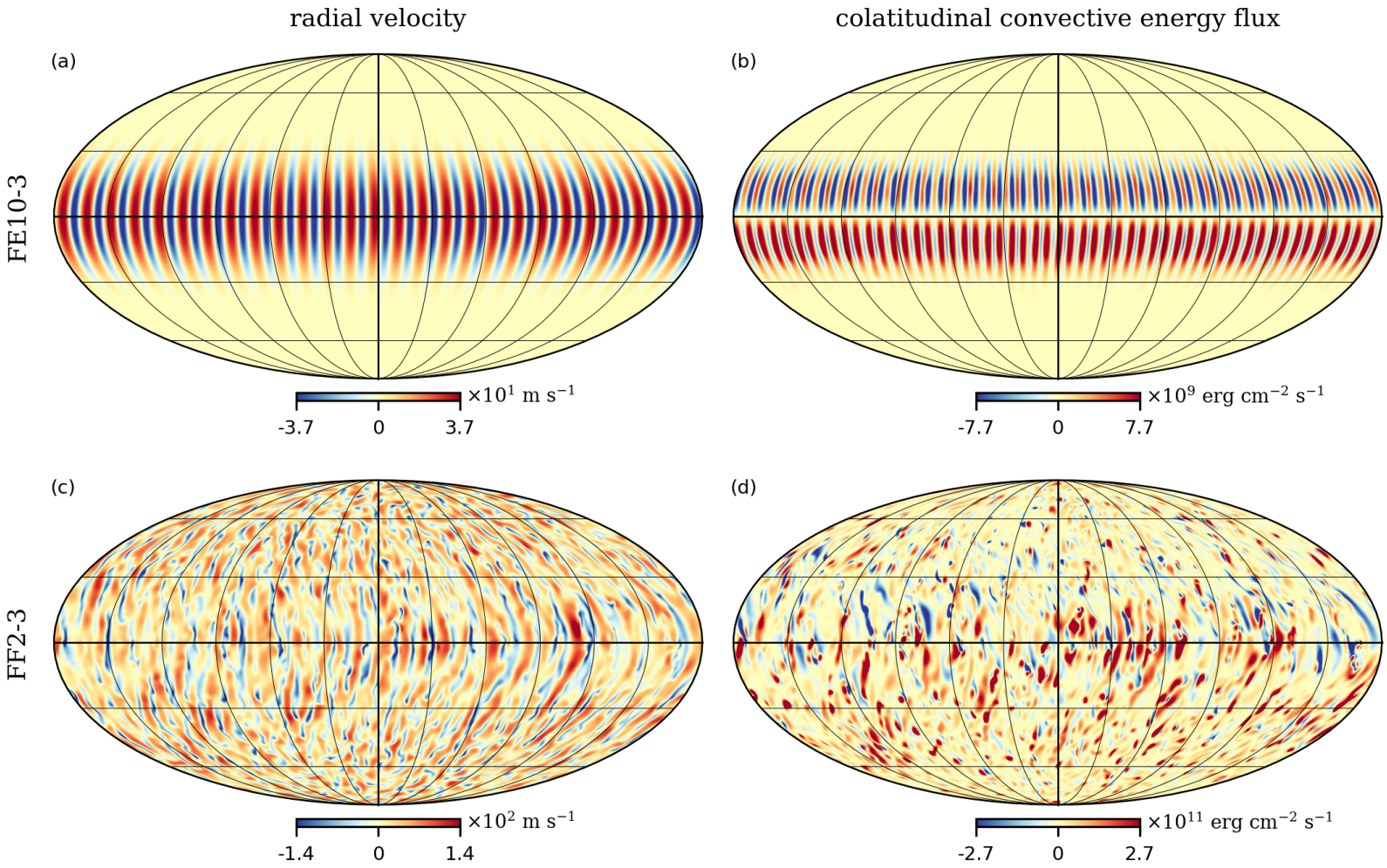

Figure 3.10: **Heat Transport by Busse Columns: Laminar and Turbulent**. Spherical snapshots (at $r/r_o = 0.910$) of the radial velocity v'_r (left-hand panels) and colatitudinal convective energy flux $v'_\theta[\overline{T}\hat{S} + \hat{P} + (1/2)\overline{\rho}(v')^2]$ (right-hand panels), shown in global Mollweide projections. The three terms in the convective energy flux correspond to advection of heat, pressure work, and advection of kinetic energy, respectively. The top row of panels is taken from the highly diffusive, barely supercritical case FE10-3 and the bottom row of panels is taken from case FF2-3. In both cases, the Busse-column sites in the left-hand panels are associated with sites of poleward convective energy flux in the right-hand panels—i.e., panels (b) and (d) are on average blue in the North and red in the South.

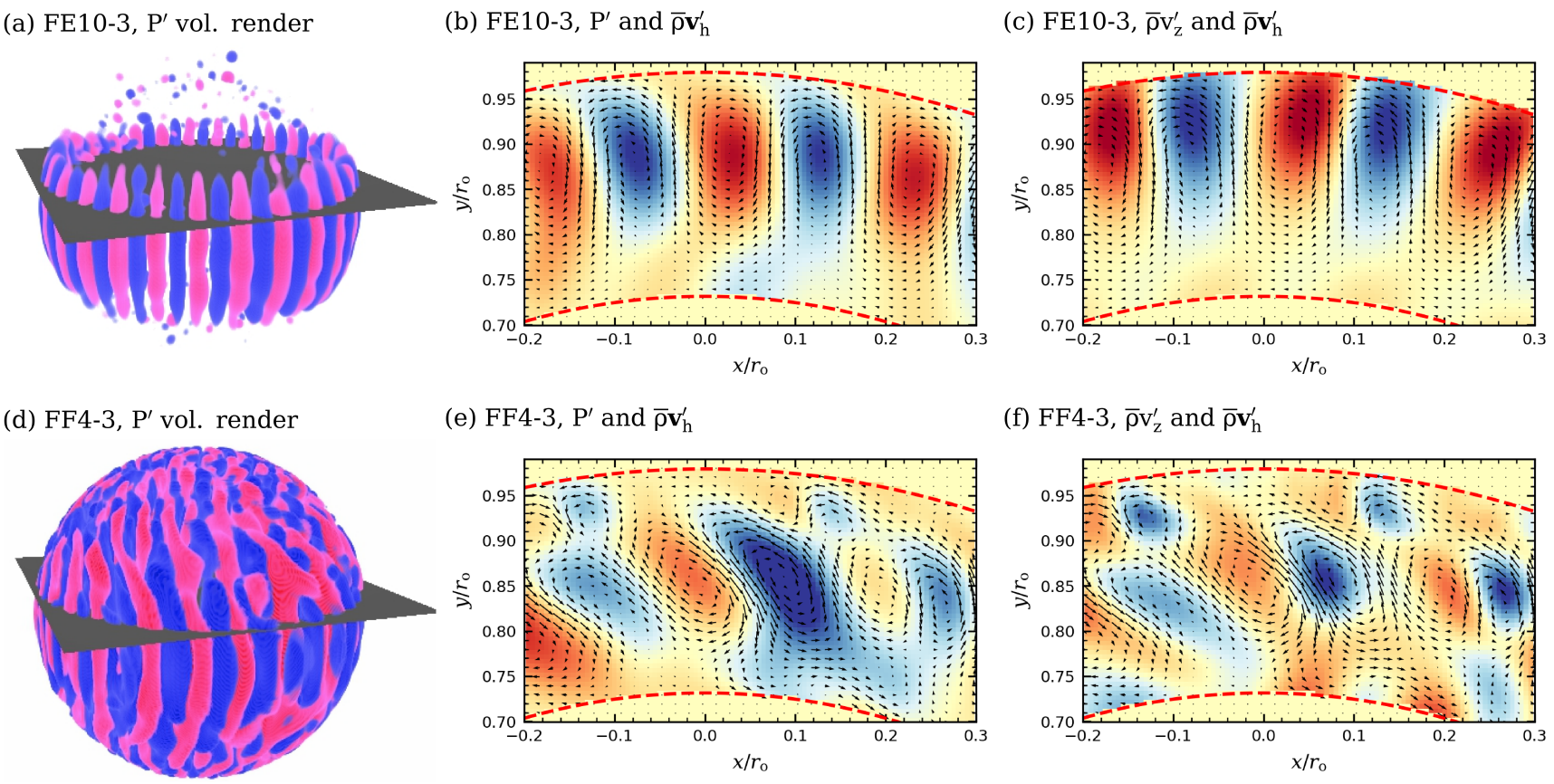

Figure 3.11: **Geostrophic Balance within Busse Columns: Laminar and Turbulent**. This figure illustrates the balance between pressure and Coriolis force for Busse columns in cases FE10-3 (laminar; top row) and FF4-3 (turbulent; bottom row). Here, we use the standard Cartesian coordinates x, y, and z. (a, d) Snapshots of the non-axisymmetric pressure ($\hat{P}' = \hat{P} - \left\langle \hat{P} \right\rangle$) shown as 3-D volume renderings, with the view from slightly north of the equator and the scene cut by the plane $z/r_o = 0.2$. (b, e) Closeup views of $\hat{P}'$ (shown in color) and $\overline{\rho}\boldsymbol{v}'_h \equiv \overline{\rho}(v'_x\hat{\boldsymbol{e}}_x + v'_y\hat{\boldsymbol{e}}_y)$ (shown as a vector field) in a portion of the plane $z/r_o = 0.2$. (c, f) Closeup views of $\overline{\rho}v'_z$ and $\overline{\rho}\boldsymbol{v}'_h$ in the same portion of the plane as in panels (b) and (e). In all panels, red tones indicate positive values and blue tones indicate negative values. There should be "hats" over the pressure $\hat{P}$ in the panel labels; in Matilsky et al. (2020), we used overbars to indicate reference quantities and the lack of overbars to indicate perturbation quantities.

and latitudinal energy transport using the steady-state total energy equation for the fluid. Using Equations (1.2), this equation takes the form of a balance of fluxes:

$$\nabla \cdot \boldsymbol{\mathcal{F}} = 0, \tag{3.13}$$

where

$$\boldsymbol{\mathcal{F}} \equiv \boldsymbol{\mathcal{F}}_{\rm conv} + \boldsymbol{\mathcal{F}}_{\rm cond} + \boldsymbol{\mathcal{F}}_{\rm rad} + \boldsymbol{\mathcal{F}}_{\rm visc} + \boldsymbol{\mathcal{F}}_{\rm circ} \tag{3.14}$$

is the temporally and longitudinally averaged total energy flux in the meridional plane and we have defined the averaged convective, conductive, radiative, viscous, and meridional-circulation fluxes through

$$\boldsymbol{\mathcal{F}}_{\rm conv} \equiv \overline{\rho}\left(c_{\rm p} \left\langle \hat{T}' \boldsymbol{v}' \right\rangle + \frac{1}{2} \left\langle v^2 \boldsymbol{v} \right\rangle \right), \tag{3.15a}$$

$$\boldsymbol{\mathcal{F}}_{\rm cond} \equiv -\kappa \overline{\rho} \overline{T} \left\langle \nabla \hat{S} \right\rangle, \tag{3.15b}$$

$$\boldsymbol{\mathcal{F}}_{\rm rad} \equiv \left(\frac{1}{r^2} \int_r^{r_o} Q(x) x^2 dx \right) \hat{\boldsymbol{e}}_r, \tag{3.15c}$$

$$\boldsymbol{\mathcal{F}}_{\rm visc} \equiv - \left\langle \boldsymbol{D} \cdot \boldsymbol{v} \right\rangle, \tag{3.15d}$$

$$\text{and} \qquad \boldsymbol{\mathcal{F}}_{\rm circ} \equiv \overline{\rho} c_{\rm p} \left\langle \hat{T} \right\rangle \left\langle \boldsymbol{v} \right\rangle \tag{3.15e}$$

respectively. Note that $\overline{\rho}\overline{T}\hat{S} + \hat{P} = c_{\rm p}\hat{T}$, so the terms with $\left\langle \hat{T}' \boldsymbol{v}' \right\rangle$ and $\left\langle \hat{T} \right\rangle \left\langle \boldsymbol{v} \right\rangle$ in the convective and meridional-circulation fluxes represent the combined effects of heat advection and pressure work. Technically, the flux due to transport of kinetic energy (proportional to $\left\langle v^2 \boldsymbol{v} \right\rangle$) has convective terms (e.g., $\left\langle (v')^2 \boldsymbol{v}' \right\rangle$) *and* meridional-circulation terms (e.g., $\left\langle \boldsymbol{v} \right\rangle^2 \left\langle \boldsymbol{v} \right\rangle$). For simplicity, we include all the kinetic-energy terms in the convective flux since they are in general small. [2]

We are interested in the total latitudinal transport of energy, and so we integrate the total flux in Equation (3.14) over conical surfaces at constant latitude:

$$\mathscr{I}_\theta(\theta) \equiv 2\pi \sin\theta \int_{r_{\rm i}}^{r_{\rm o}} \mathcal{F}_\theta(r,\theta) r dr. \tag{3.16}$$

[2] Recall that in Chapter 2, we use a capital Roman "F" to denote the spherically integrated radial energy flux (units of luminosity) and a curly "$\mathcal{F}$" to denote the angular momentum flux. Here in Chapter 3, we keep the notation of Matilsky et al. (2020). We use "$\mathcal{F}$" to denote the non-integrated energy flux (units of luminosity per unit area) and "$\mathscr{I}_r$" to denote the spherically integrated energy flux.

For the FF cases, there can be no net transport of energy in latitude due to the absence of conductive losses in the polar regions through the outer boundary. In other words, $\mathscr{I}_\theta(\theta) \equiv 0$. For the FE cases, by contrast, there is a net poleward energy transport because the poles are allowed to be superluminous. Thus, $\mathscr{I}_\theta(\theta)$ will in general be negative in the Northern Hemisphere and positive in the Southern Hemisphere. Recall that equatorward (poleward) transport of energy corresponds to positive (negative) $\mathscr{I}_\theta(\theta)$ in the Northern Hemisphere and negative (positive) $\mathscr{I}_\theta(\theta)$ in the Southern Hemisphere.

Figure 3.12(a) shows the integrated colatitudinal energy fluxes in case FF2-3 after the system has achieved statistical equilibrium. The total flux is very close to zero at all latitudes, indicating a well-equilibrated state. The dominant transport components are the convective flux, which transports energy preferentially poleward due to the Busse columns, and the conductive flux, which transports energy equatorward. The monotonic entropy gradient of Figure 3.8(d) and (by extension) the radially tilted isorotation contours in the FF cases, is thus seen to be a result of the response by conduction to the convective transport of energy to the poles.

Figure 3.12(b) shows the integrated colatitudinal energy transport in case FE2-3. The poles are clearly superluminous—i.e., there is a net poleward energy transport due to the convection. For all the FE cases explored here, the energy loss at the poles is even greater than the heating by the convection; the conductive flux is thus forced to change sign at mid-latitudes (around $\pm 20^\circ$), transporting energy poleward in concert with the Busse columns. This results in the non-monotonic entropy profile of, e.g., Figure 3.8(a). The tilts of the rotation contours are thus negative at high latitudes and positive at low latitudes, as in the top row of Figure 3.4.

3.7 Discussion and conclusions

We have shown that the differential rotation achieved in global, 3-D convection simulations is well described by a thermal wind and highly sensitive to the outer thermal boundary condition. The FF boundary tends to yield more solar-like rotation profiles (strong contrast with positively tilted contours), while the FE boundary yields weaker contrast and negatively tilted contours. In light of

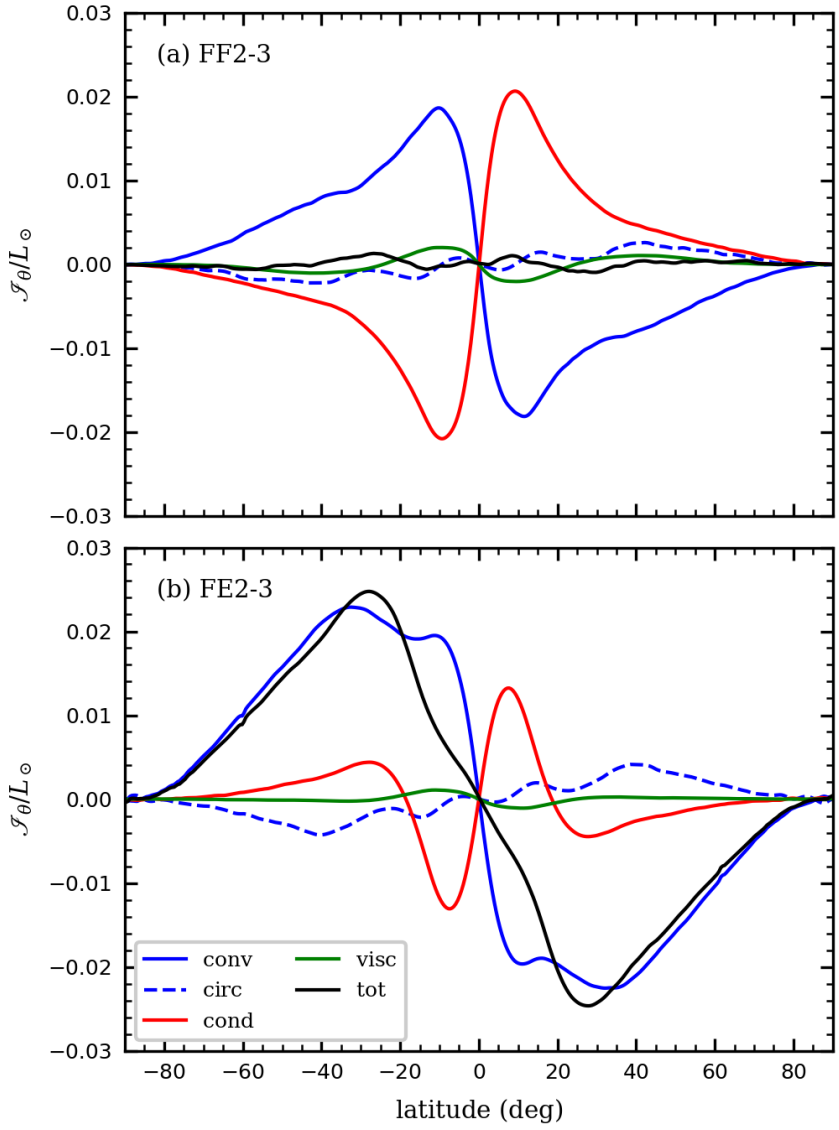

Figure 3.12: **Colatitudinal Energy Transport for Each Thermal Boundary Condition**. This figure shows the total colatitudinal energy transport for (a) case FF2-3 and (b) case FE2-3—i.e., the integrals of the fluxes in Equations (3.15) over conical surfaces at constant latitude. The integrated fluxes are plotted as functions of latitude ($= \pi/2 - \theta$). Contributions from the various fluxes are indicated in the legend, "tot" denoting the sum of all the other fluxes. Positive (negative) $\mathscr{I}_\theta$ indicates equatorward (poleward) transport in the Northern Hemisphere and poleward (equatorward) transport in the Southern Hemisphere.

these results, we now discuss the likelihood that the Sun's strong rotation contrast and positively tilted contours arise from thermal wind balance in the deep interior coupled with the observation that the radiative flux from the solar photosphere does not vary appreciably with latitude.

The first question is whether the force balance Equation (3.10), which should in general be true for low Rossby numbers, holds in the Sun. The interior solar Rossby number is currently unknown, but recent helioseismic estimates (Hanasoge et al., 2012; Greer et al., 2015) give Ro $\lesssim 0.1$ in the deep interior. Thus, it is likely that Equation (3.10) (and the derivative thermal wind Equations (3.11) and (3.12)) apply in the solar CZ, except perhaps in the layers just below the photosphere. thermal wind balance in the Sun is also not prohibited by observational results. We can derive the temperature in the solar CZ from the rotation rate of Figure 3.1 assuming thermal wind balance holds, integrating Equations (3.11) and (3.12) to get $\hat{P}$ and $\hat{S}$ in the meridional plane and using Equation (1.2) to get $\hat{T}$. In this calculation, we set Ω_0 to the sidereal Carrington rate and use the same polytropic reference state employed in our models for the solar profiles. The result is shown in Figure 3.13. The equator-to-pole temperature contrast required to drive the solar-like differential rotation is $\sim$10 K (approximately uniform with radius), which is well below the detection limit of helioseismology (e.g., Brun et al. 2010).

The second question is whether the Sun's Busse columns send energy preferentially poleward. In general, stellar convection transitions through a series of convective regimes as the supercriticality (measured by the reduced Rayleigh number $\mathcal{R}$) increases (Hindman et al., 2020). Both the least supercritical case in our work (FE10-3, for which $\mathcal{R} \sim 2$) and the most supercritical cases (the pair FF2-2 and FE2-2, for which $\mathcal{R} \sim 50$) have a strong preference for poleward transport by Busse columns, suggesting that the poleward transport is a feature of the most unstable mode of convection that stays present as the flows get ever more complex.

Finally, it is an open question how the Sun might transport energy equatorward to maintain equilibrium. In our simulations, the net poleward transport of energy by Busse columns is, at its maximum, a few percent of the solar luminosity, which is counteracted almost entirely by conduction in the FF cases (Figure 3.12). In the Sun, the thermal diffusivity associated with radiative heating

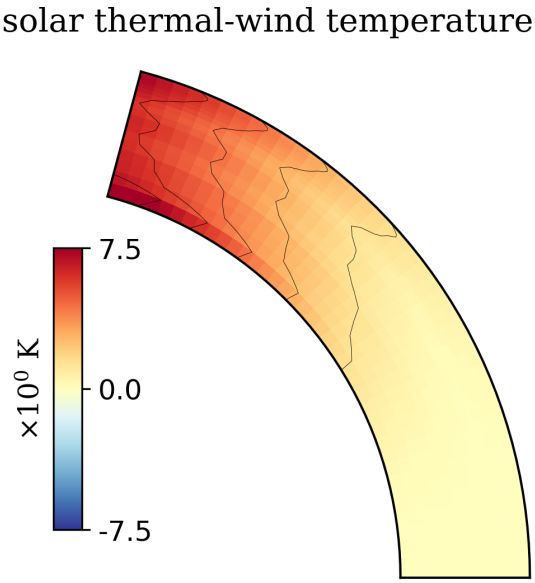

Figure 3.13: **The Sun's "Thermal Wind" Temperature Profile**. Temperature deviation from the spherical mean in the solar CZ, assuming thermal wind balance holds. The temperature has been calculated from the rotation rate inferred from helioseismology (Figure 3.1), using Equations (3.11), (3.12) and(1.2).

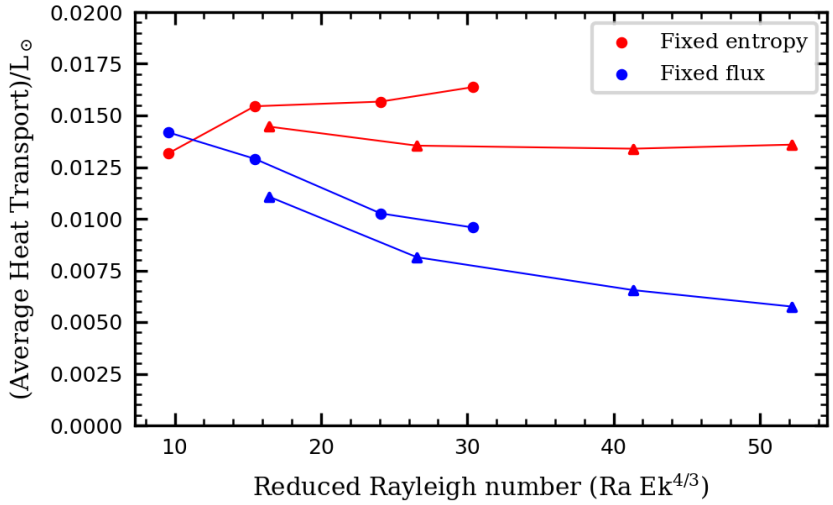

Figure 3.14: **Total Busse-Column Heat Transport for Each Thermal Boundary Condition**. Net poleward transport of heat from Busse columns for all simulations in the suite (except the barely supercritical cases FE10-3 and FF10-3) plotted versus the reduced Rayleigh number $\mathcal{R} \equiv \mathrm{Ra\ Ek}^{4/3}$. The poleward heat flux $|\mathscr{I}_{\theta,\,\mathrm{conv}}|$ has been averaged over latitude. Circles mark the $\Omega_0 = 3\Omega_\odot$ cases and triangles the $\Omega = 2\Omega_\odot$ cases.

is $\sim 10^7$ cm^2 s^{-1} at mid-CZ (e.g., Hindman et al. 2020), which (if a thermal wind were operating with a temperature contrast of $\sim$10 K) would correspond to a latitudinal energy flux of $\sim 10^{-7}\ L_\odot$. Figure 3.14 shows how the Busse-column heat flux scales with supercriticality. The trends are different between the FE and FF cases (and the $\Omega_0 = 3\Omega_\odot$ and $\Omega_0 = 2\Omega_\odot$ cases), but there is clearly a tendency for the net transport to go down for our more supercritical FF simulations (blue curves). This indicates that the balance between conductive and convective heat flux could hold in the Sun, just with much smaller flux magnitudes. We admit that these results are only suggestive, since the flux in all our models is still orders of magnitude higher than the presumed solar value of $10^{-7}\ L_\odot$.

On a more practical note, it is advantageous to use an FF outer boundary condition in solar simulations for two reasons. First, maintaining a strong differential rotation is particularly relevant for dynamo models, since the dynamo cannot be maintained without sufficient shear (e.g., Brown et al. 2010; Guerrero et al. 2016a; Matilsky & Toomre 2020a; Bice & Toomre 2020). Second, using an FE outer boundary condition leads to superluminous poles, which are directly at odds with solar observations. Figure 3.15 shows the conductive flux as a function of latitude at the top of the domain for the FE cases. For case FE2-3, the flux in the polar regions reaches a value in excess of the "solar-luminosity flux" ($L_\odot/4\pi R_\odot^2$) by about 20%. This is far greater than the observationally constrained value of $< 1\%$ for the Sun (Rast et al., 2008).

We very much view this paper as a complement to Miesch et al. (2006). In that work, a systematic tilt of the rotation contours was achieved by imposing a small latitudinal entropy gradient at the inner boundary, thereby ensuring that the entropy increased monotonically from equator to pole. And indeed, for all our FF cases, there is a similar monotonic equator-to-pole entropy gradient at the inner boundary. Monotonicity is *not* achieved in the FE cases. In other words, Miesch et al. (2006) showed that it is possible to tilt the rotation contours by imposing a preferred geostrophic balance, and here we have shown how this preferred balance is naturally established as the result of poleward energy transport by Busse columns and the FF outer boundary condition.

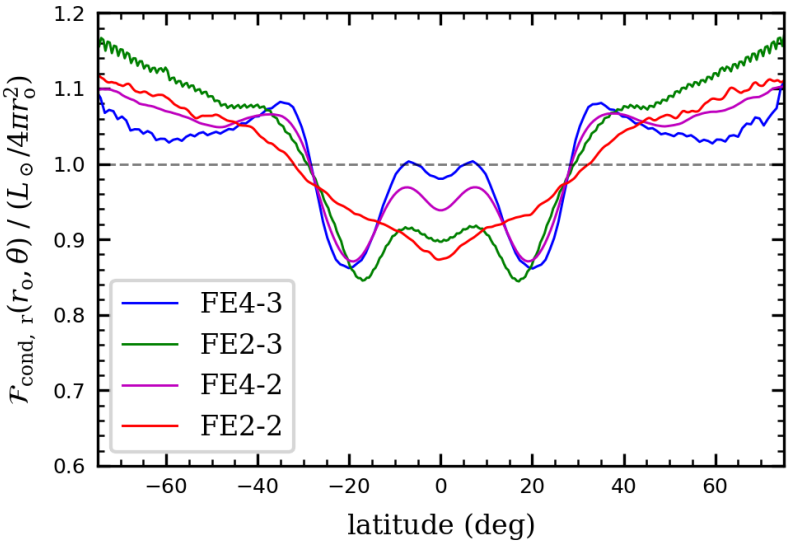

Figure 3.15: **The "Leaky Poles" of Fixed-Entropy Simulations**. Latitudinal profile of $\mathcal{F}_{\rm cond,\ r}$ at the outer boundary for several of the FE cases, normalized by the flux needed to carry out the solar luminosity equally at all latitudes (the "solar-luminosity flux," $L_\odot/4\pi R_\odot^2$). The flux has been averaged over time and longitude.

We conclude that any successful dynamical model of the Sun's convection zone must be consistent with three key observations: (1) The Sun possesses strong latitudinal differential rotation; (2) The isorotation contours are tilted positively in the sense of Figure 3.5; and (3) The emergent intensity is nearly spherically symmetric. We have demonstrated in this paper that the transport of angular momentum and heat by Busse columns can yield results consistent with observations (1) and (2). Busse columns transport angular momentum outward, away from the rotation axis, thus speeding up the equator. They simultaneously transport heat poleward via the enthalpy flux associated with pressure work. These two transports reach equilibrium once thermal wind balance is achieved.

While it is satisfying to address the observations (1) and (2) with a single mechanism (i.e., the action of Busse columns), observation (3) presents a theoretical problem. The thermal wind balance resulting from Busse columns requires that the solar poles be at a higher temperature than the equator, with a contrast of $\sim$10 K throughout the CZ. The emergent intensity at the solar surface, however, is nearly uniform in latitude, with less than $\sim$2.5 K variation in effective temperature (Rast et al., 2008). This suggests that the thermal wind balance must only be maintained in the deep CZ, and the surface layers (perhaps within the Near-Surface Shear Layer) may have different dynamics. Those dynamics must somehow screen the surface from the imposition of the latitudinal temperature gradient from below.

In our models, the proper proxy for the emergent intensity is the radial conductive flux at the outer surface. For the FF cases, we impose latitudinal independence of this flux as a boundary condition. Further, we have shown that this boundary condition is conducive to achieving strong differential rotation and properly tilted isorotation contours. However, a fully self-consistent model of the solar interior would reproduce the latitudinal independence at the outer boundary as a natural consequence of the near-surface convection and not as an enforced boundary condition.

Since the underlying dynamics giving rise to latitudinally independent emissivity in the Sun are not well understood, we cannot predict a priori whether that same mechnism would be sufficient to enforce latitudinally independent flux for other stars. It has long been postulated that oblateness

induced by rotation in high-mass stars (in which a radiation layer overlies an interior CZ) could result in superluminous poles (e.g., von Zeipel 1924; Collins 1963). Here, we have identified Busse columns as a possible mechanism for producing hot poles in low-mass stars (in which the CZ overlies the radiation layer) that does not depend on the star's distortion. Furthermore, Busse columns do not necessarily require rapid rotation—they simply require strong rotational constraint, or in other words, low Rossby number. Thus, small dim stars that are expected to have weak convection may have active Busse columns and hot poles, even with only moderate rotation. Finally, since the homogeneity (or lack thereof) of the stellar emissive flux may significantly affect the interior differential rotation, we should not assume that the positive tilts of the isorotation contours inferred for the Sun are a general feature of other low-mass stars.

3.8 Diagnostic Parameters for the Simulation Suite

Table 3.2 contains various input and diagnostic parameters for the entire simulation suite as defined in Section 3.3. Recall that for each simulation name, "FE" or "FF" refers to the type of outer thermal boundary condition employed, the first number gives the diffusion value $\nu = \kappa$ in units of 10^{12} cm^2 s^{-1}, and the second number after the dash gives the frame rotation rate Ω_0 in units of $\Omega_\odot \equiv 2.87 \times 10^{-6}$ rad s^{-1}, or $\Omega_\odot/2\pi = 456$ nHz. N_r, N_θ, and N_ϕ refer to the number of radial, colatitudinal, and longitudinal grid points, respectively. The run time is given in units of the thermal diffusion time, defined to be H^2/κ, with $H \equiv r_\mathrm{o} - r_\mathrm{i}$ the shell depth.

Table 3.2: **Diagnostic Parameters for Each Thermal Boundary Condition**. Fluid diagnostic parameters for the different simulations. The 18 simulations here are in four groupings according to FE or FF at two different rotation rates.

Name	(N_r, N_θ, N_ϕ)	$\mathrm{Ra_F}$	$\mathrm{Re} = \mathrm{Pe}$	Ek	Ro	$\mathcal{R} \equiv \mathrm{Ra\ Ek}^{4/3}$	$\Delta\Omega/\Omega_0$	Run time
FE2-3	(128, 384, 768)	8.52×10^5	63.2	4.62×10^{-4}	3.38×10^{-2}	30.4	0.097	23.6
FE2.3-3	(128, 384, 768)	5.60×10^5	51.8	5.31×10^{-4}	3.21×10^{-2}	24.1	0.092	7.77
FE3-3	(96, 384, 768)	2.52×10^5	35.2	6.93×10^{-4}	2.90×10^{-2}	15.5	0.078	59.6
FE4-3	(128, 192, 384)	1.07×10^5	21.9	9.23×10^{-4}	2.55×10^{-2}	9.62	0.062	33.4
FE10-3	(64, 96, 192)	6.82×10^3	2.54	2.31×10^{-3}	7.45×10^{-3}	2.08	0.0048	238.5
FE2-2	(128, 576, 1152)	8.52×10^5	75.6	6.93×10^{-4}	5.91×10^{-2}	52.2	0.082	7.78
FE2.3-2	(128, 576, 1152)	5.60×10^5	62.2	7.96×10^{-4}	5.61×10^{-2}	41.3	0.088	9.14
FE3-2	(96, 384, 768)	2.52×10^5	42.8	1.04×10^{-3}	5.09×10^{-2}	26.6	0.092	11.9
FE4-2	(64, 288, 576)	1.07×10^5	28.0	1.39×10^{-3}	4.51×10^{-2}	16.6	0.086	47.7
FF2-3	(128, 576, 1152)	8.52×10^5	64.5	4.62×10^{-4}	3.45×10^{-2}	30.4	0.140	14.7
FF2.3-3	(128, 384, 768)	5.60×10^5	52.9	5.31×10^{-4}	3.28×10^{-2}	24.1	0.131	7.90
FF3-3	(96, 384, 768)	2.52×10^5	35.8	6.93×10^{-4}	2.95×10^{-2}	15.5	0.108	14.4
FF4-3	(128, 192, 384)	1.07×10^5	22.4	9.23×10^{-4}	2.46×10^{-2}	9.62	0.080	25.5
FF10-3	(64, 96, 192)	6.82×10^3	2.89	2.31×10^{-3}	8.58×10^{-3}	2.08	0.0024	15.9
FF2-2	(128, 576, 1152)	8.52×10^5	81.2	6.93×10^{-4}	6.33×10^{-2}	52.2	0.110	6.68
FF2.3-2	(128, 576, 1152)	5.60×10^5	65.3	7.96×10^{-4}	5.89×10^{-2}	41.3	0.121	8.27
FF3-2	(96, 384, 768)	2.52×10^5	44.4	1.04×10^{-3}	5.30×10^{-2}	26.6	0.128	10.3
FF4-2	(128, 384, 768)	1.07×10^5	28.9	1.39×10^{-3}	4.66×10^{-2}	16.6	0.117	70.4

Chapter 4

Exploring Bistability in the Cycles of the Solar Dynamo through Global Simulations

The calling card of solar magnetism is the sunspot cycle, during which sunspots regularly reverse their polarity sense every 11 years. However, a number of more complicated time-dependent behaviors have also been identified. In particular, there are temporal modulations associated with active longitudes and hemispheric asymmetry, when sunspots appear at certain solar longitudes or else in one hemisphere preferentially. So far, a direct link between between this asymmetric temporal behavior and the underlying solar dynamo has remained elusive. In this work, we present results from global, 3-D magnetohydrodynamic (MHD) simulations, which display both behavior reminiscent of the sunspot cycle (regular polarity reversals and equatorward migration of internal magnetic field) and asymmetric, irregular behavior that in the simulations we interpret as active longitudes and hemispheric asymmetry. The simulations are thus bistable, in that the turbulent convection can stably support two distinct flavors of magnetism at different times, in superposition, or with smooth transitions from one state to the other. We discuss this new family of dynamo models in the context of the extensive space-telescope observations of the Sun's surface magnetic field with the Solar and Heliospheric Observatory (SOHO) and the Solar Dynamics Observatory (SDO), as well as earlier observations of sunspot number and synoptic maps. We suggest that the solar dynamo itself may be bistable in nature, exhibiting two types of temporal behavior in the magnetic field.

This Chapter is primarily a restatement of the work published in Matilsky & Toomre (2020a)

(also see the related conference proceedings paper, Matilsky & Toomre 2020b). As the primary author of the paper, I conducted the simulations, performed their analyses, created the Figures, and wrote the text. My coauthor Juri Toomre recognized the novelty of the simulations I had stumbled upon and encouraged me to pursue this remarkable phenomenon of bistability further. He additionally provided advice and guidance throughout the writing process, gave detailed text edits, and suggested schematic designs of some of the figures.

4.1 Introduction

Since the early observations of sunspot number, the Sun's magnetic field has been known to follow the fairly regular 11-year sunspot cycle. Sunspots appear at mid-latitudes at the beginning of the cycle, then at latitudes a bit higher during the peak of solar activity, and finally at sites progressively closer to the equator as the magnetic activity wanes (e.g., Hathaway 2011). Polarimetric observations from the NSO/Kitt Peak Observatory and magnetograms from the Michelson Doppler Imager (MDI) aboard SOHO and the Helioseismic and Magnetic Imager (HMI) aboard SDO have enabled the detailed and continuous study of sunspots for the last $\sim$50 years (recall Figure 1.2). Sunspots appear in pairs of opposite polarity sense (i.e., bipolar active regions) from one cycle to the next, making a 22-year cycle overall (e.g., Hathaway 2015). In addition, a number of other cycles (less obvious and regular than the 22-year cycle) have been identified, from a slow $\sim$100-year modulation of the peak cycle amplitudes called the Gleissberg Cycle (e.g., Gleissberg 1939; Ogurtsov et al. 2002), to a rapid $\sim$2-year periodicity in the global magnetic field (e.g., Ulrich & Tran 2013). On timescales in between, *active longitudes* (longitudes at which sunspots appear more frequently and with greater strength) persist for several decades (e.g., Henney & Harvey 2002). There are also periods (the longest being $\sim$50 yr) associated with *hemispheric asymmetry*, or times at which more sunspots conglomerate in either the Northern or Southern Hemispheres (e.g., Ballester et al. 2005). Finally, there are several recorded *grand minima*, or times throughout history when solar activity is substantially diminished over protracted intervals of several decades (e.g., Hoyt & Schatten 1998).

All of these complicated features of the solar cycle must have their roots in the global solar dynamo—the process by which the Sun's interior magnetic field regenerates through dynamical interactions between rotation and convection. Sunspots are believed to be the result of rising toroidal loops of magnetic field. That their sites of emergence migrate equatorward with the sunspot cycle and that their polarity senses flip every 11 years suggest an interior toroidal reservoir of magnetism that also migrates equatorward and flips polarity every 11 years. The additional cycles and behavior mentioned above could also be indicative of corresponding cycles in the interior magnetic field.

In the past decade or so, global, 3-D, MHD simulations of the solar convection zone have made significant headway in reproducing aspects of the solar cycle. Using the `Anelastic Spherical Harmonic` (`ASH`) code, Brown et al. (2010) and Brown et al. (2011) have shown that it is possible to build strong interior "wreaths" of magnetism amidst a chaotic, turbulent flow. These wreaths can be space-filling, with nearly 360°-connectivity throughout the spherical shell, and can exhibit regular polarity reversals, during which the longitudinal direction of magnetic field in the wreath flips every few years of simulation time. Also using `ASH`, Augustson et al. (2015) have achieved wreath-building dynamos which exhibit both equatorward propagation of wreaths at low latitudes and poleward propagation of wreaths at high latitudes—a signature feature of the SOHO/SDO observations (e.g., Hathaway 2015).

Perhaps one of the most significant issues facing global MHD simulations of solar convection is that the wide range of spatial and temporal scales relevant for the fluid makes a direct numerical simulation impossible. Researchers have attempted to address this problem by using various prescriptions for sub-grid-scale (SGS) turbulent effects or by restricting the global domain. Warnecke et al. (2014) used the `Pencil` code to solve the MHD equations in a spherical-wedge geometry, showing that global convection could yield $\alpha\Omega$-type dynamos with the direction of propagation of the interior magnetic field being set by the Parker-Yoshimura rule. Passos & Charbonneau (2014) used the `EULAG-MHD` code (which incorporates implicit dissipation on the smallest spatial scales to maintain numerical stability) to achieve regular, cyclic polarity reversals in their global

"Millennium Simulation." The cycles persisted over very long time-scales, with statistical features showing long-term trends reminiscent of the observed solar Gleissberg modulation. Hotta et al. (2016) have explored a large dynamical range for solar convection using their `Reduced Speed of Sound Technique` (`RSST`) code. They explored the coupling of a near-surface layer of small-scale (< 10 Mm) convection and deep, large-scale flows, finding that coherent magnetic structures could persist even in the presence of very small diffusivities.

Another important outstanding issue for solar MHD simulations is that most lack the eruption of interior magnetic flux and subsequent decay of active regions believed to play an essential role in the global dynamo. In the work of Nelson et al. (2013a,b), an extension of `ASH` incorporating a Dynamic Smagorinsky treatment of the sub-grid-scale (SGS) fluid motions achieved a dynamo in which small loops of magnetism detached from the interior wreaths and rose to the outer surface via magnetic buoyancy instabilities. The polarity, twist, and tilt of the loops displayed statistical properties reminiscent of Joy's law for sunspot emergence. Using a finite-difference spherical anelastic MHD code, Fan & Fang (2014) found that the convection gave rise to super-equipartition magnetic flux bundles that had similar characteristics to emerging active regions on the Sun. More recently, dynamos with wreaths that give rise to buoyant loops have been achieved with `Rayleigh` (the code used in this work) in modeling the intense magnetism exhibited by M-dwarf stars (Bice & Toomre, 2020). These simulations have thus shown it is possible to connect MHD simulations of the interior solar dynamo to the emergence of magnetic flux that is actually observed at the photosphere.

It has generally been difficult for simulations to reproduce equatorward propagation of magnetic field as seen in the solar butterfly diagram (although see Käpylä et al. 2012 and Augustson et al. 2015 for notable exceptions). Furthermore, two other prominent features of solar magnetic activity—active longitudes and hemispheric asymmetry—have not been systematically explored in global simulations. In this work, we report on a new class of dynamo simulations whose magnetism exhibits polarity-reversing cycles with equatorward propagation, as well as a quasi-regular, hemispherically asymmetric cycle, the features of which are suggestive of active longitudes and

hemispheric asymmetry. Both cycles are present simultaneously, although usually one cycle is more dominant than the other.

In Section 4.2 we discuss our numerical methods and the parameter space covered by our simulations, as well as the hydrodynamic (HD) progenitor common to each magnetic simulation. In Section 4.3 we discuss the bistable nature of the magnetism achieved in our dynamo cases. We discuss striking flux-transport-like behavior in Section 4.4. We examine each cycling mode individually in Sections 4.5 and 4.6. In Sections 4.3–4.6 we refer only to our primary lowest-magnetic-Prandtl-number case, and we return to the higher-magnetic-Prandtl-number cases in Section 4.7. In Section 4.8 we explore the dynamical origins of the two cycles in terms of the production of magnetic field. In Section 4.9 we discuss our bistable dynamo simulations in the context of solar observations and present our conclusions in Section 4.10.

4.2 Numerical Experiment

We consider time-dependent, 3-D simulations of a rotating, convecting shell of fluid modeled after the solar convection zone (CZ), again using `Rayleigh 0.9.1` (Featherstone & Hindman, 2016a; Matsui et al., 2016; Featherstone, 2018). We use notation identical to that of the previous two "HD" Chapters. However, we now consider a magnetized convection zone. `Rayleigh` thus solves the LBR Equations (1.1) in full MHD.[1] Recall that all simulations in this thesis have impenetrable, stress-free boundaries, a fixed-flux ($\partial\hat{S}/\partial r = 0$) bottom, and here, they have a fixed-flux top as well. For the magnetic field, we match to a potential field at both boundaries—see Equation (1.7)(d). Other magnetic lower boundary conditions, such as a perfect conductor or a purely radial field, could be considered, but there is no obvious choice from a physical point of view.

[1] We briefly note that the simulations presented in this Chapter used `Rayleigh 0.9.1`, which had a bug in its implementation of the magnetic induction equation. As noted in Section 1.3.3, `Rayleigh` evolves the induction equation (1.1c) by representing the magnetic field by flux functions: $\boldsymbol{B} = \nabla \times [A\hat{\boldsymbol{e}}_r + \nabla \times (C\hat{\boldsymbol{e}}_r)]$. In spectral space (and neglecting the nonlinear emf terms), the equation for the A flux function is $\partial A/\partial t = \eta(r)\{[\ell(\ell+1)/r^2][\partial^2/\partial r^2 + (d\ln\eta/dr)\partial/\partial r - [\ell(\ell+1)/r^2]\}A$. In `Rayleigh`, up through version `1.0.0` (Featherstone et al., 2021), the term in the A equation proportional to $(d\ln\eta/dr)\partial A/\partial r$ was not computed correctly in the Crank-Nicolson solve. This effectively resulted in that term being too small by a factor of $\sim$2 for all timesteps. Since $\eta(r)$ did not vary rapidly with radius, the error likely did not affect the core bistability results presented in this Chapter and in the publications, Matilsky & Toomre (2020a,b). However, for due diligence, we re-ran case D3-1 (from $t = 9610\ P_{\rm rot}$ to $t = 10350\ P_{\rm rot}$—an interval of about 700 $P_{\rm rot}$) using `Rayleigh 1.0.1` and the bistability behavior was largely identical.

Table 4.1: **Common Input Parameters for the Bistability Experiment**. Input parameter values common to all four cases (H3, D3-1, D3-2, and D3-4). See Section 4.11 for the definition of the flux Rayleigh number $\mathrm{Ra_F}$.

Parameter	Symbol	Value
Spherical-shell inner boundary	r_i	5.00×10^{10} cm
Spherical-shell outer boundary	r_o	6.59×10^{10} cm
Specific heat at constant pressure	c_p	3.50×10^{8} erg K^{-1} g^{-1}
Ratio of specific heats	γ	5/3
Density at the inner boundary	$\overline{\rho}_\mathrm{i}$	0.181 g cm^{-3}
Luminosity of the Sun	$L_\odot$	3.85×10^{33} erg s^{-1}
Mass of the Sun	$M_\odot$	1.99×10^{33} g
Frame rotation rate	Ω_0	8.61×10^{-6} rad s^{-1}
Frame rotation period	$P_\mathrm{rot} = 2\pi/\Omega_0$	8.45 days
Viscosity at the outer boundary	$\nu(r_\mathrm{o})$	3.00×10^{12} cm^2 s^{-1}
Flux Rayleigh number	$\mathrm{Ra_F}$	2.56×10^{6}
Thermal Prandtl number	$\mathrm{Pr} = \nu/\kappa$	1

Each case rotates at three times the solar Carrington rate, $3\Omega_\odot$, as discussed further below. The background thermodynamic state (adiabatically stratified polytrope with density contrast of $\sim$20 across the shell and a solar luminosity injected via internal heating) is identical to those of our previously discussed three-density-scale-height models (i.e., case N3 from Chapter 2 and all the cases from Chapter 3). One difference between the bistable dynamo simulations discussed here and the simulations from the HD Chapters is that the diffusivities $\nu(r)$, $\kappa(r)$, and $\eta(r)$ vary with radius like $\overline{\rho}(r)^{-1/2}$. In the HD simulations, all diffusivities were constant in space.

We discuss three dynamo simulations in the present study, which all start from the same hydrodynamic progenitor. We define $\Omega_\odot \equiv 2.87 \times 10^{-6}$ rad s^{-1} as the sidereal Carrington rotation rate, and all our models rotate at three times this rate to ensure a low Rossby number and thus a solar-like differential rotation, in which the equator rotates faster than the poles (e.g., Brown et al. 2010). The transition from solar to anti-solar differential rotation as simulations grow increasingly more turbulent has come to be called the "convective conundrum" (O'Mara et al., 2016). The anti-solar regime can be avoided by either rotating faster or lowering the luminosity, and we opt for the former. We refer to the hydrodynamic progenitor as case H3 ("H" for hydrodynamic, "3" for $\Omega_0 = 3\Omega_\odot$). Some input parameters common to case H3 and the three dynamo cases are shown

in Table 4.1.

The three dynamo simulations were initialized from the well-equilibrated hydrodynamic case H3 after about 6400 $P_{\rm rot}$, using the full MHD equations. These dynamo cases differ in the values of the magnetic Prandtl number $\mathrm{Pr_m} = \nu/\eta$, which takes on the values 1, 2, and 4. For all cases, the kinematic viscosity profile $\nu(r)$ is fixed, effectively keeping the Rayleigh number constant. We set the value of $\mathrm{Pr_m}$ by varying the value of the magnetic diffusivity at the top of the domain. We label the corresponding dynamo simulations as cases D3-1, D3-2, and D3-4, where the last number corresponds to the value of $\mathrm{Pr_m}$ being 1, 2, and 4, respectively. To resolve both the flow field and magnetic structures, we use a substantial resolution of at least $(N_r, N_\theta, N_\phi) = (96, 384, 768)$ for the number of radial, latitudinal, and longitudinal grid points, respectively (see Table 4.2).

Our dynamo cases expand the parameter space explored by Brown et al. (2010)—who examined the case $\mathrm{Pr_m} = 0.5$ while varying the rotation rate—to higher magnetic Prandtl numbers. In all cases discussed here, the magnetic field was initialized from a random seed field of amplitude $\sim$1 G ("random" in terms of the amplitude of each individual spectral component).

Solutions to the nonlinear MHD equations in rotating, convecting spherical shells involve highly time-dependent and intricate flow structures. Figure 4.1 shows a sample of the global flow structure achieved in the hydrodynamic progenitor H3. As seen in the orthographic and Mollweide projections of the radial velocity v_r, the flows at any given time consist of Taylor columns between about $\pm 20°$-latitude (also called Busse columns and banana cells in the literature) and a broken honeycomb network of upflows and downflows at higher latitudes. The Taylor columns transport angular momentum outward (Brun & Toomre, 2002; Busse, 2002; Matilsky et al., 2019) and drive a strong differential rotation ($\Omega - \Omega_0$), with an associated meridional circulation ($\langle \rho \boldsymbol{v}_{\rm m} \rangle_t$), as seen in Figures 4.1(c,d).[2]

[2] In this Chapter, we define the "meridional part" of a vector field $\boldsymbol{A}$ through $\boldsymbol{A}_{\rm m} \equiv A_r \hat{\boldsymbol{e}}_r + A_\theta \hat{\boldsymbol{e}}_\theta$. This is equivalent to the "poloidal component" of vector fields referred to elsewhere in this thesis (e.g., $\boldsymbol{B}_{\rm m}$ in this Chapter is equivalent to $\boldsymbol{B}_{\rm pol}$ in the next Chapter 5.) The terminology used here coheres with the notation of Matilsky & Toomre (2020a). Another taxonomic difference in this Chapter is that the angular brackets with the "t" subscript denote a combined temporal and longitudinal average, while angular brackets with no subscript denote a longitudinal average at a particular time.

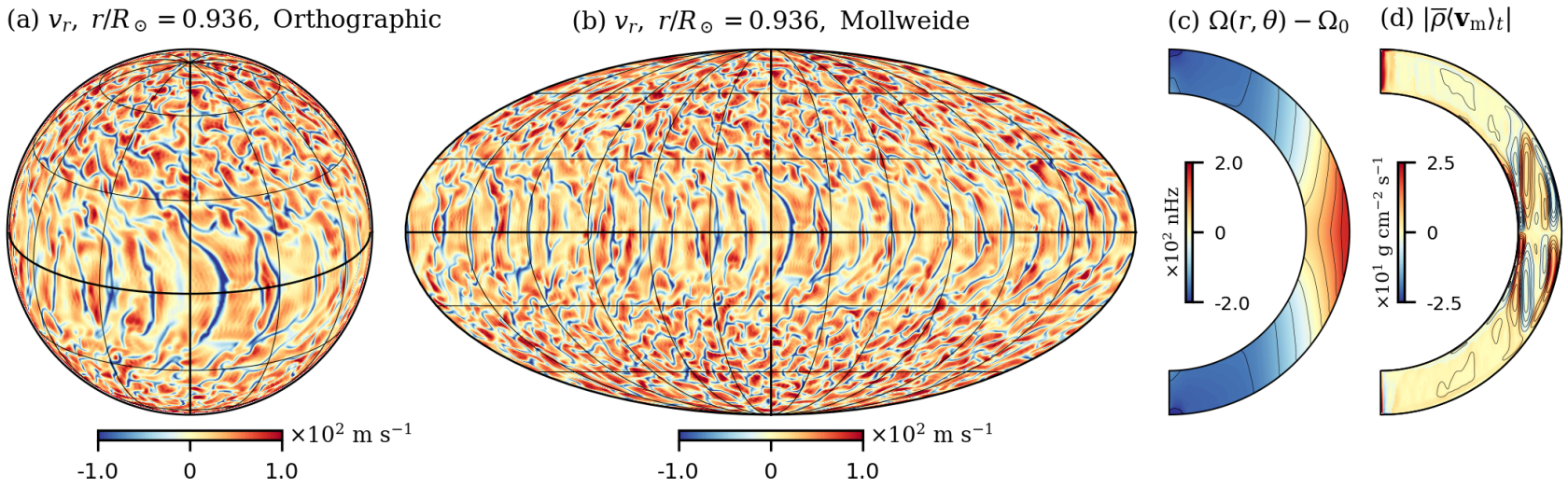

Figure 4.1: **Turbulent Flows in a Hydrodynamic Dynamo Progenitor**. Flow structures in the hydrodynamic case H3. (a) Snapshot of the convection (as traced by v_r) near the outer surface, shown in orthographic projection. (b) The same snapshot of v_r, shown in Mollweide projection. (c) Averaged fluid rotation rate ($\Omega(r,\theta) - \Omega_0 \equiv \langle v_\phi \rangle_t / r \sin\theta$) in the meridional plane. (d) Averaged meridional circulation, with the mass flux ($\langle \rho \boldsymbol{v}_m \rangle_t$) magnitude plotted in color, overlaid on circulation streamlines. In panel (d), red and blue tones correspond to clockwise and counterclockwise circulation, respectively.

4.3 Bistable Magnetic Cycles in the Dynamo Cases

The magnetism in our dynamo cases exhibits two striking (and distinct) cycling modes. Usually one is dominant, but they can also coexist simultaneously. The phenomenon of *bistability* in dynamical systems generally refers to the coexistence of two stable equilibrium states, and we use the term somewhat loosely to refer to the two different types of dynamo cycle. In this and the following sections, we discuss case D3-1, which exhibits bistable cycling in the cleanest manner. We return to the higher-$\mathrm{Pr_m}$ cases in Section 4.7.

Each cycle is associated with a unique morphology of the magnetic field, as seen in Figure 4.2. In roughly the lower half of the shell at an early time as in Figure 4.2(a), there is one pair of opposite-polarity wreaths in each hemisphere (a *fourfold-wreath* structure) confined to within $\sim$40°-latitude of the equator. At this instant, the polarity sense of the wreath structure is largely symmetric across the equator. Each wreath mostly has 360°-connectivity, linking the magnetic field in a large torus. The wreaths individually have rms field strengths of $\sim$5 kG and longitudinally averaged rms field strengths $\sim$2.5 kG.

Later in the simulation, near the middle of the CZ as in Figure 4.2(b), there is a strong, negative-B_ϕ *partial wreath* (wrapping $\sim$180° around the sphere), as well as a slightly less prominent positive-B_ϕ partial wreath on the opposite side of the sphere. The negative-B_ϕ partial wreath is dominant at this time, with a peak strength of $\sim$40 kG, compared to the positive-B_ϕ peak field strength of $\sim$20 kG. In the longitudinal average, there is a residual $\langle B_\phi \rangle$ that is negative and has a peak magnitude of $\sim$10 kG. The partial-wreath structure occupies most of the domain in radius, but is confined between the equator and 20°-south in latitude.

The temporal behavior of the magnetic field as a whole roughly consists of transitions between the two magnetic-field structures presented in Figure 4.2. Figure 4.3 shows the evolution in time-latitude space near mid-CZ for $\langle B_\phi \rangle$ (throughout this Chapter, angular brackets with no subscript denote a longitudinal average at a particular time, while angular brackets with a "t" subscript denote a combined longitudinal and temporal average), as well as the evolution of the toroidal

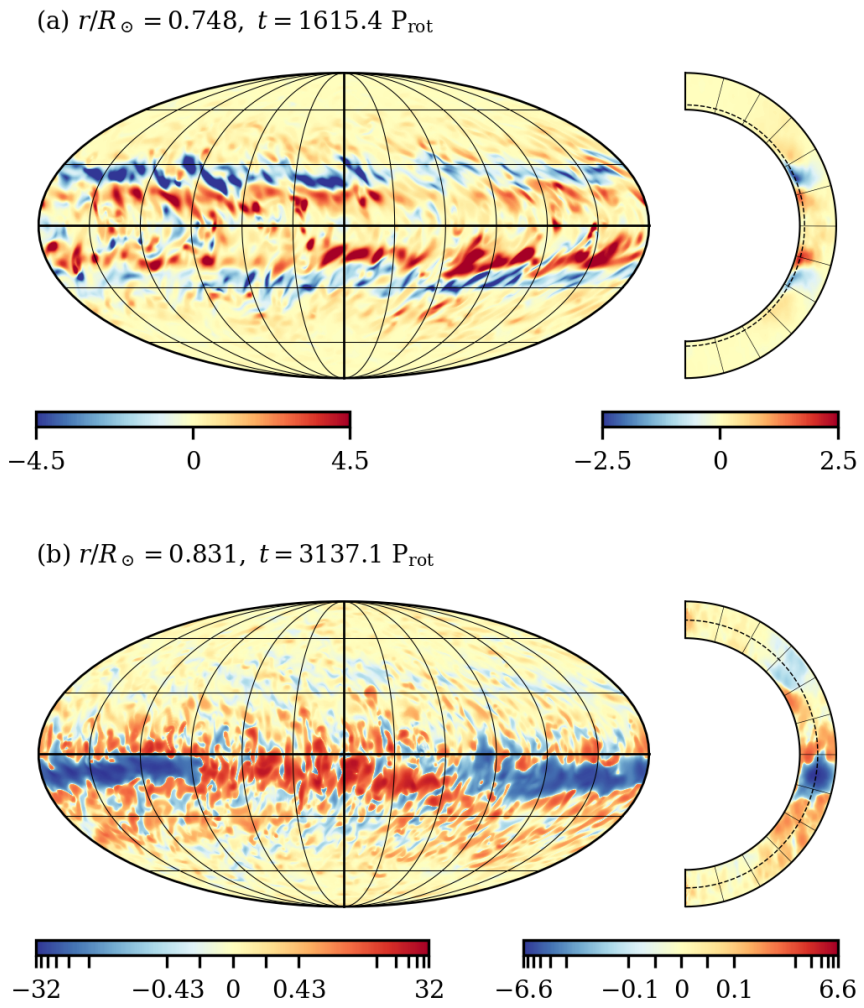

Figure 4.2: **Two Magnetic-Field Structures in a Bistable Dynamo**. Snapshots of the azimuthal magnetic field B_ϕ (in kG) for case D3-1 at two different depth/time pairs, shown in global Mollweide view on the left and accompanied by the longitudinal average in the meridional plane on the right. (a) The field deep in the shell at an early time in the simulation. (b) The field in the middle of the shell at a later time. In panel (b), the color maps are symmetric-logarithmic to capture both weak-amplitude and strong-amplitude magnetic structures. The colors in the interval around zero map linearly to field strength and the two intervals on either side (one positive and one negative) map logarithmically. An animated versions of each panel is available in the online version of Matilsky & Toomre (2020a).

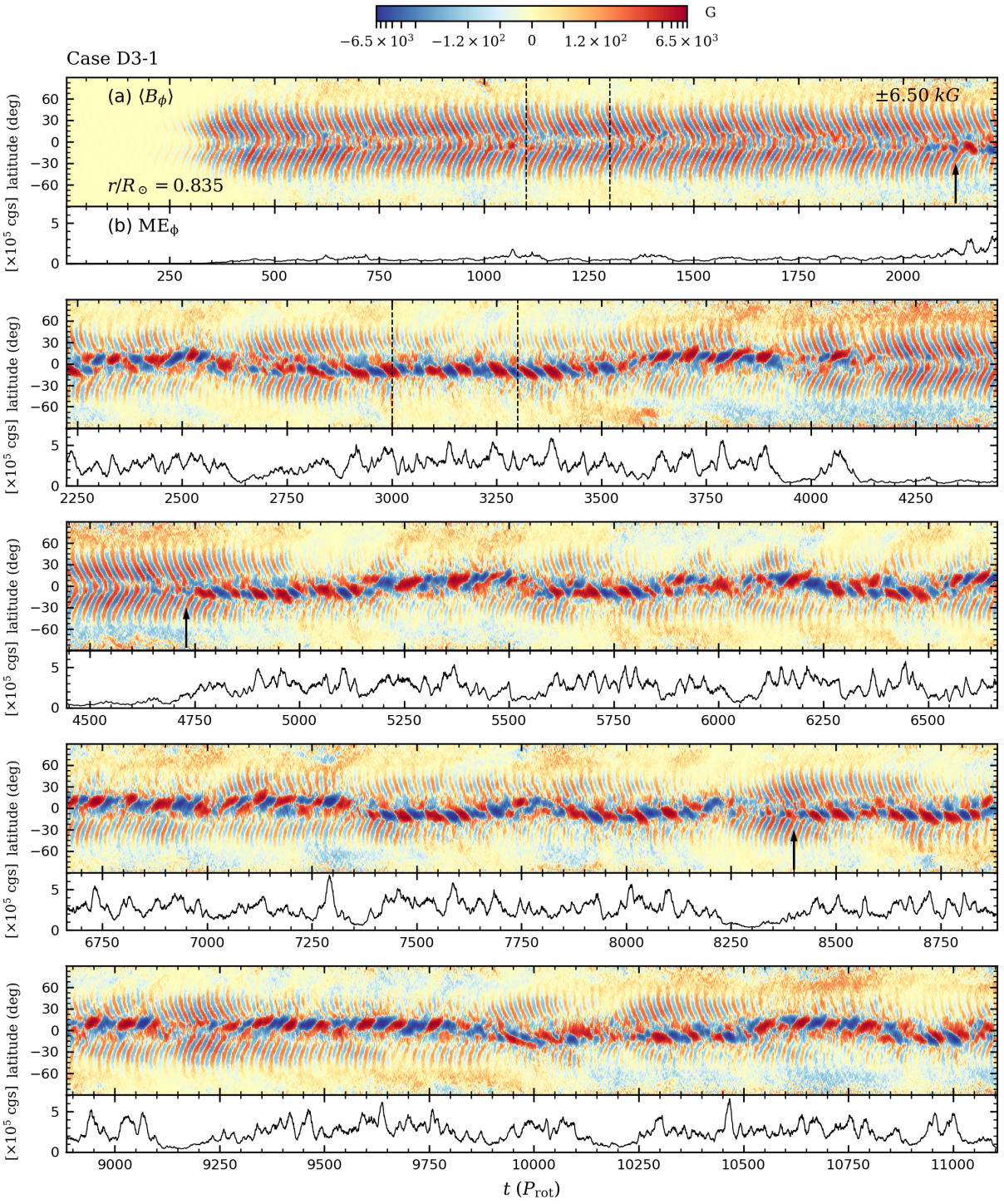

Figure 4.3: **Extended Evolution of Bistable Dynamo**. Extended time-latitude diagram of the azimuthal magnetic field $\langle B_\phi \rangle$ for case D3-1 at $r/R_\odot = 0.835$ (mid-CZ). Panels (a) (split across multiple rows) show the longitudinally averaged field $\langle B_\phi \rangle$ as a function of time and latitude. The saturation values of the color map are indicated in the top row, and the map is symmetric-logarithmic, as in Figure 4.2(b). Sharing the same time axis, panels (b) show the energy density in the azimuthal magnetic field, $\mathrm{ME}_\phi = B_\phi^2/8\pi$, averaged about $r/R_\odot = 0.835$ over 10% of the shell by radius. This caption is continued in the main text within quotation marks.

magnetic energy, $B_\phi^2/8\pi$. To maximize the size of this important Figure 4.3, we continue its large caption of here: "In panels (b), the y-axis is measured in the cgs units of energy density, erg cm^{-3}. The arrows mark wreaths in the fourfold-wreath cycle originating at mid-latitudes that appear to seed partial wreaths in the South. Time is measured from the instant when the seed magnetic field was introduced to the hydrodynamic progenitor (namely, 6400 $P_{\rm rot}$). The dashed lines mark the intervals shown in closeup view in Figures 4.7 and 4.10."

After the dynamo has established strong fields from the initial seed field (around $t = 300\ P_{\rm rot}$), the *fourfold-wreath cycle* dominates. Each wreath emerges at $\sim$40°–50°-latitude and then migrates steadily equatorward. The newly formed wreaths alternate between positive-$\langle B_\phi \rangle$ and negative-$\langle B_\phi \rangle$ being dominant, with the time between the appearance of two wreaths of the same polarity—the fourfold-wreath cycle period—equal to $\sim$25 $P_{\rm rot}$, or about six months. This is the same time it takes an individual wreath to migrate from its mid-latitude starting point to the equator. Effectively each hemisphere operates on its own (i.e., not necessarily in phase), producing wreaths of a given polarity at mid-latitudes that reappear once they reach the equator.

At around $t = 2100\ P_{\rm rot}$, the fourfold-wreath cycles are disturbed by the partial-wreath cycle, which starts in the South (first arrow in Figure 4.3(a)). The dominant polarity of the partial-wreath structure reverses quasi-periodically. We can estimate the period (time between two successive states of one dominant polarity) from a visual inspection of Figure 4.3(a): between $t = 2950\ P_{\rm rot}$ and $t = 3350\ P_{\rm rot}$ (an interval slightly larger than the one spanned by the second set of dashed lines), there are roughly five cycles, yielding a period of $\sim$80 $P_{\rm rot}$. We note that visual inspections of other intervals would yield slightly different cycle periods, making the period of $\sim$80 $P_{\rm rot}$ only approximate. Nevertheless, we thus identify a *partial-wreath cycle* with a period about three times as long as that of the fourfold-wreath cycle.

The partial-wreath pair wanders into the North around $t = 2250\ P_{\rm rot}$ and flips from North to South once more before the fourfold-wreath cycle becomes dominant for the second time around $t = 4150\ P_{\rm rot}$. The rest of the simulation displays a complex seesaw behavior between the two cycling states. The fourfold-wreath cycle never really disappears, but does significantly decrease in

amplitude when the partial-wreath cycle is dominant. Examining Figure 4.3(a) in detail, it seems that whenever the partial-wreath cycle starts, its field comes originally from the fourfold-wreath cycle. That is, a wreath of one polarity will migrate toward the equator and then significantly grow in amplitude, seeding the following partial-wreath cycle with that same polarity dominant. Three instances of this phenomenon are marked by the arrows in Figure 4.3(a) .

Along with the time-latitude panels in Figure 4.3(a), we show the temporal behavior of the energy in the azimuthal magnetic field in Figure 4.3(b), averaged over 10% of the shell (by radius) at mid-depth. The fourfold-wreath cycle is seen to correspond to a low-energy state of the magnetic field, with sporadic peaks in energy, but no discernible energy cycle associated with the polarity reversals. When the partial-wreath cycle first begins (around $t = 2100\ P_{\rm rot}$), the field jumps into a high-energy state, with local peaks spaced by roughly half the partial-wreath cycle period.

4.4 Polar Caps of Magnetism

Also visible in Figure 4.3(a) is a weak azimuthal magnetic field at high latitudes on the order of tens of Gauss (see, for example, the positive $\langle B_\phi \rangle$ in the North and the negative $\langle B_\phi \rangle$ in the South during the interval from 3500 to 5000 $P_{\rm rot}$). These polar caps of magnetism fluctuate in amplitude and occasionally reverse polarity, but not with any regularity and with no discernible relationship to the fourfold-wreath or partial-wreath cycles.

There is a significantly stronger polar cap associated with the meridional magnetic field $\boldsymbol{B}_{\rm m}$, with magnitude $\sim$1 kG. Figure 4.4 shows the radial magnetic field when there are intense polar caps of magnetism. Near the top of the domain (left-hand column), the local structure of B_r inherits the honeycomb network of downflows associated with the Taylor columns, while deeper down (right-hand column), the field is more homogeneous. At both depths shown, however, the complicated polar-cap structure on average resembles a dipolar field, with magnetic-north lining up with geometric-north. The instantaneous views of B_θ (not shown) similarly display a dipolar structure, with B_θ positive near the poles in both hemispheres.

Figure 4.5 provides the time-latitude diagram for $\langle B_r \rangle$ near the top of the domain during an

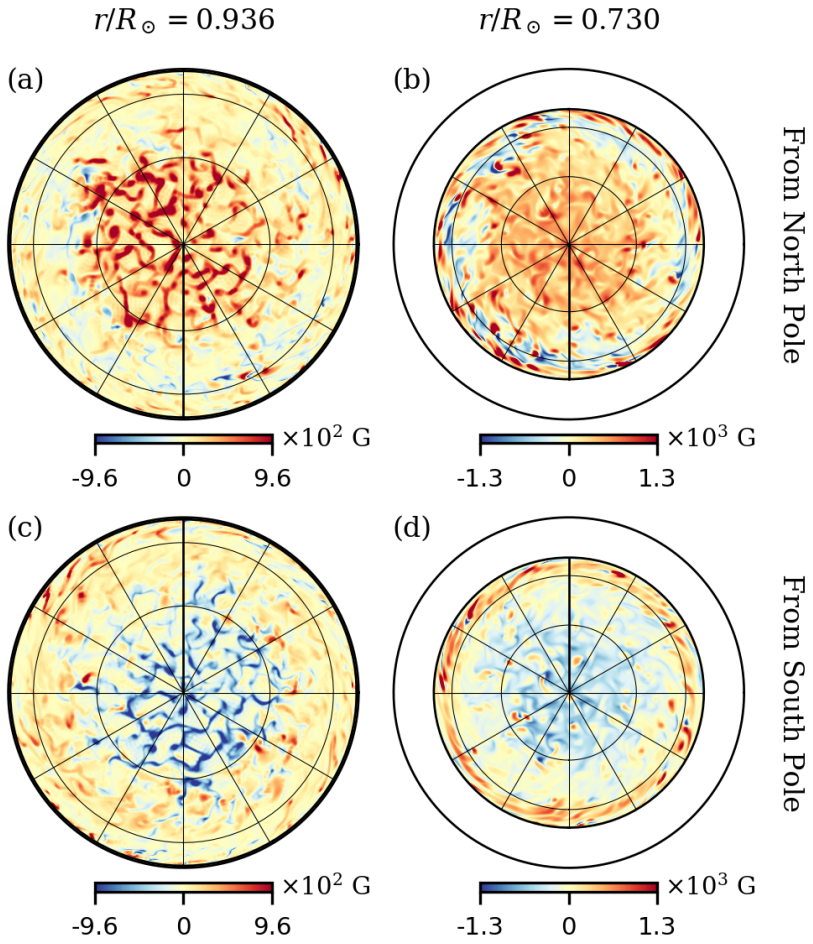

Figure 4.4: **Polar Caps of Magnetism**. Spherical cuts of the instantaneous radial magnetic field B_r, viewed from the North Pole (top row) and the South Pole (bottom row). The instant shown is $t \approx 4200\ P_{\rm rot}$, just after the first transition from partial-wreath to fourfold-wreath cycling, when there is intense meridional field at both the North and South Poles. Two depths are sampled: one near the top of the domain and one near the bottom.

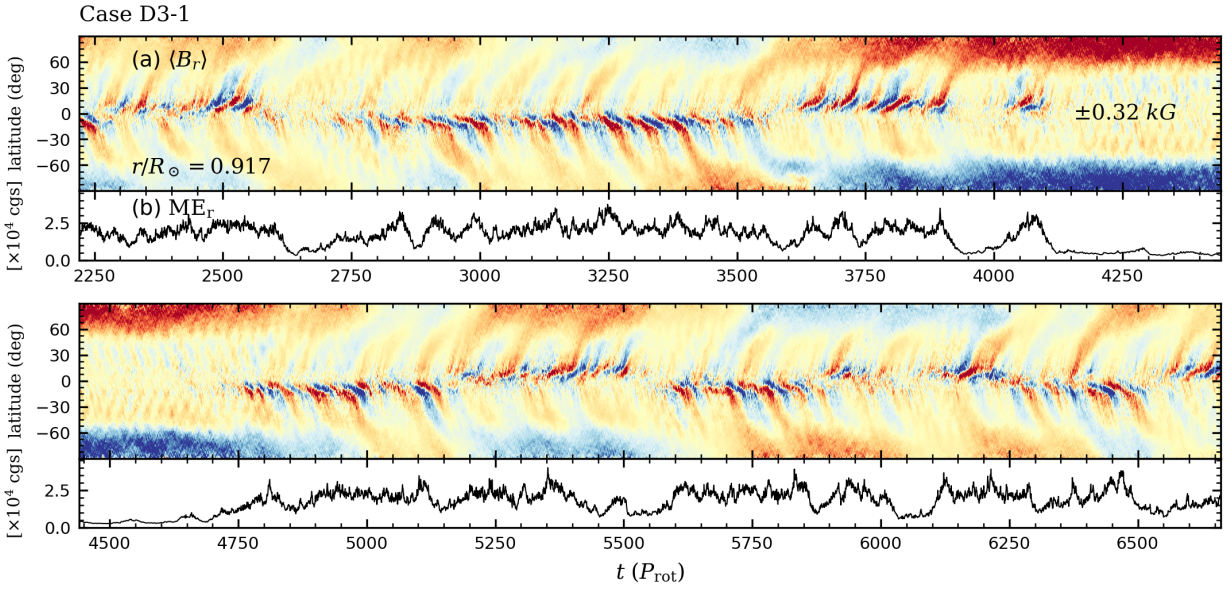

Figure 4.5: **Flux-Transport of Magnetic Field**. Time-latitude diagram of radial magnetic field $\langle B_r \rangle$ for case D3-1 at $r/R_\odot = 0.917$ (upper CZ), and associated energy density at the same depth. The time interval sampled corresponds to the second and third panels of the extended time trace in Figure 4.3.

interval in the middle of the simulation. There is clearly a strong dipolar component to the field at the poles. After a fairly quiescent initial interval, the dipolar field strengthens (at $t \approx 3750\ P_{\rm rot}$) a few hundred rotations before the fourfold-wreath cycle becomes dominant for the second time. The partial wreaths produce flux that is transported to the poles, seen in Figure 4.5 as intermittent large plumes of red and blue.

Not all the partial-wreath cycles produce field that propagates all the way to the poles, and there does not seem to be a one-to-one correspondence between polarity reversals of the partial wreaths and reversals in the polar caps. For nearly every partial-wreath cycle, however, the radial field propagates much further poleward than the $\pm 20^\circ$ latitude limits that are maintained fairly consistently for $\langle B_\phi \rangle$.

The poleward migration of $\langle B_r \rangle$ seen in Figure 4.5 bears a striking resemblance to the concept the meridional circulation acting as a "conveyor belt" of magnetism in the flux-transport (F-T) dynamo framework (e.g., Charbonneau 2014). In that picture, the meridional circulation advects the meridional component of magnetic field to the poles near the outer surface, where it accumulates and is eventually pumped back down to the equator in the deep CZ, also by the meridional circulation. This poloidal field is then sheared into toroidal field by the differential rotation, starting the cycle anew. In the F-T framework, the meridional circulation time thus sets the cycle period.

However, case D3-1 is more complicated than the simple F-T model for two reasons. Firstly, the meridional circulation time for case D3-1 is on the order of 400 $P_{\rm rot}$, which is substantially longer than either the partial-wreath or fourfold-wreath cycle periods. Secondly, although the poles occasionally flip polarity, there is no clean correspondence between the polarity of the field at the poles and the polarity of the field in the equatorial regions during subsequent cycles.

4.5 Evolution of the Fourfold-Wreath Cycle

Figure 4.6 shows the evolution of the azimuthal magnetic field B_ϕ during one reversal in the fourfold-wreath cycle. At any given time, each wreath has a complicated structure due to stretching and pummeling by the Taylor columns, but generally has the same sense for B_ϕ all the way around

the sphere, indicating field lines that connect in a large torus. The accompanying snapshots of $\langle B_\phi \rangle$ in the meridional plane indicate that the wreaths are strongest deep in the shell and are confined in radius to the lower half of the CZ and in latitude to within $\sim 40^\circ$ of the equator.

Each wreath marches steadily equatorward as the cycle progresses. As a wreath of one polarity reaches the equator, a new wreath of that same polarity appears at a higher latitude. In Figure 4.6(a), for example, there are two opposite-polarity wreaths in the Northern Hemisphere below $\sim 30^\circ$-latitude (roughly equal in amplitude) and a negative-$\langle B_\phi \rangle$ wreath that is just beginning to form above $\sim 30^\circ$-latitude. By the time a given wreath migrates from mid-latitudes to within $\sim 10^\circ$ of the equator, a new wreath of that same polarity has formed at mid-latitudes, completing the cycle. Therefore, the configuration in Figure 4.6(e) has essentially returned to that of Figure 4.6(a).

Figure 4.7 shows a close-up view (in time-latitude space) of a small time interval containing about eight fourfold-wreath cycles (marked by the first set of dashed lines in Figure 4.3(a)), including the instants sampled in Figure 4.6. Here the field is first seen to appear (at its weakest) at roughly 40°-latitude north and south and migrates steadily equatorward, attaining its maximum strength between 20°–30° north and south, while stopping short of the equator at about 10° north and south.

Interestingly, the Southern Hemisphere is often out of phase with the Northern Hemisphere and it is hard to pinpoint whether the fourfold-wreath structure is symmetric about the equator or antisymmetric. Indeed, the simulation exhibits both symmetric and antisymmetric tendencies at different times (for example, compare the symmetric configuration in Figure 4.2(a) to the antisymmetric configurations shown in Figure 4.6). At $t = 1200\ P_{\rm rot}$ (horizontal center of Figure 4.7), the wreath structure is clearly antisymmetric in the large.

The symmetry of dynamo states in mean-field dynamo theory is usually quantified by the prevalence of the dipole ($\ell = 1$) and quadrupole ($\ell = 2$). Our dynamo cases, by contrast, are dominated by higher-order modes that serve to localize each wreath in space, leaving the dipolar and quadrupolar contributions extremely weak. Figure 4.8 shows the magnetic-field power spectra,

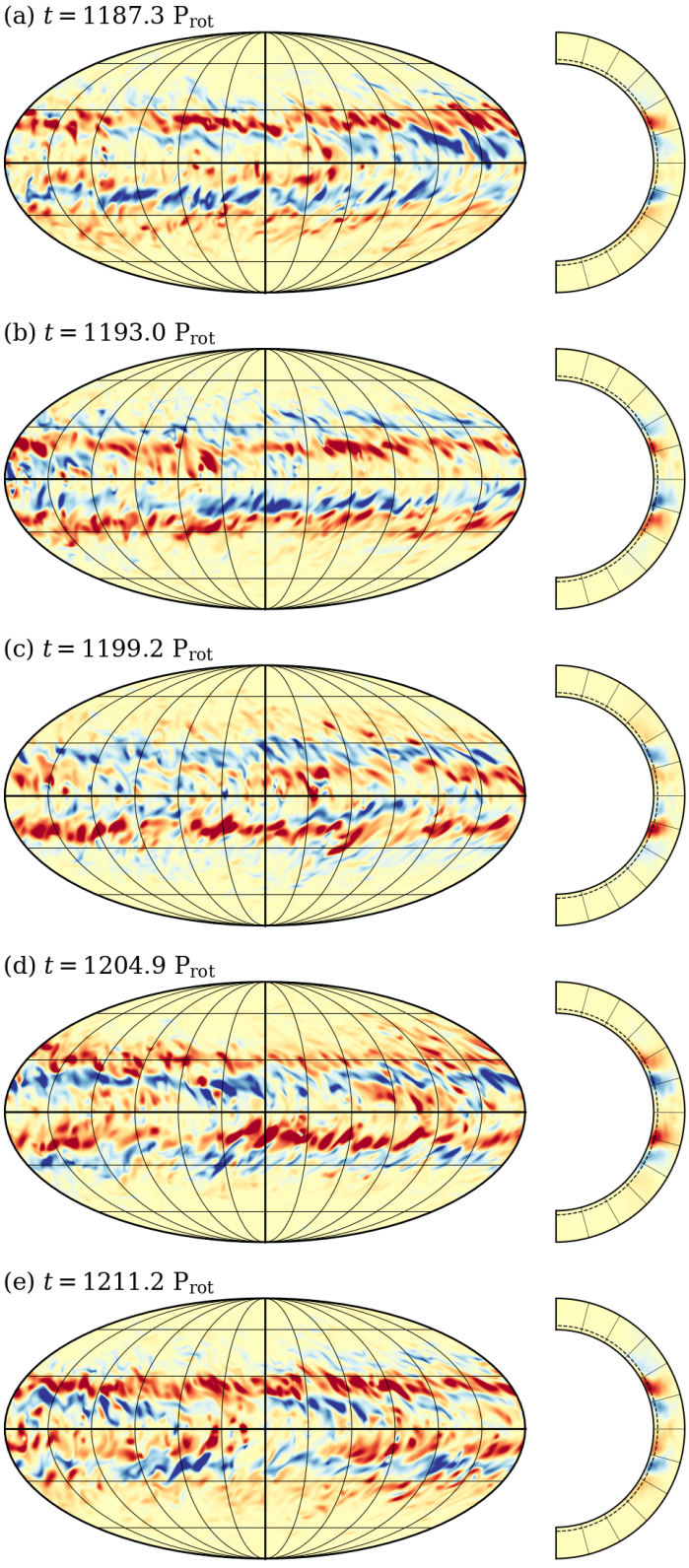

Figure 4.6: **Walking though a Regular Polarity Reversal**. Mollweide snapshots (at $r/R_\odot = 0.748$) of B_ϕ and meridional snapshots of $\langle B_\phi \rangle$ for one fourfold-wreath cycle. Snapshots are separated by about one-quarter of a cycle ($\sim$6 $P_{\rm rot}$). The color map is identical to that of Figure 4.2(a), with the Mollweide plots saturated at $\pm$4.5 kG and the longitude-average plots saturated at $\pm$2.5 kG.

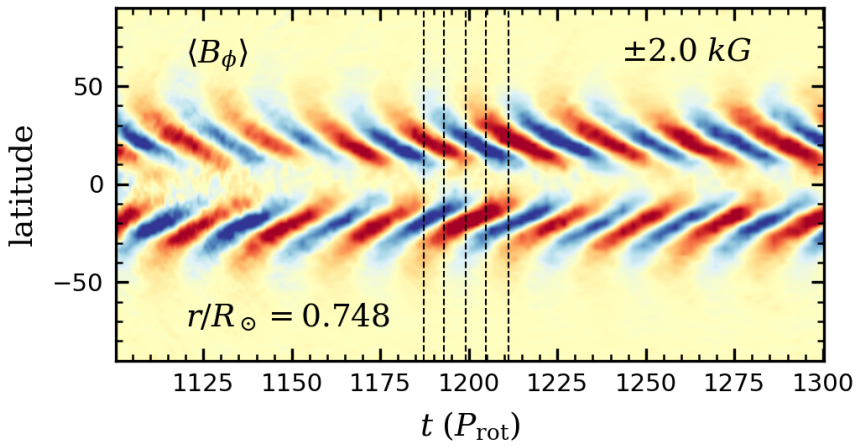

Figure 4.7: **Regular Fourfold-Wreath Cycles**. Close-up view of the time-latitude behavior of $\langle B_\phi \rangle$ near the bottom of the CZ ($r/R_\odot = 0.748$) during the interval marked by the vertical dashed lines in Figure 4.3(a). This interval (between 1100 and 1300 $P_{\rm rot}$), encompasses about eight fourfold-wreath cycles. The dashed lines indicate the times sampled by the series of Mollweide projections in Figure 4.6.

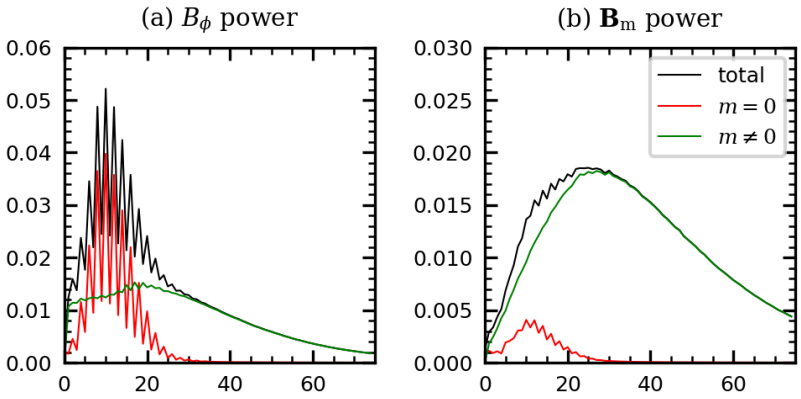

Figure 4.8: **Spatial Scales of the Toroidal and Poloidal Magnetic Fields**. Power spectra of the magnetic field at $r/R_\odot = 0.748$ during fourfold-wreath cycling, averaged between $t = 0$ and $t = 2200\ P_\mathrm{rot}$. Separate curves indicate contributions from all m, $m = 0$, and $|m| > 0$. The sum of the total power over all ℓ equals 1. (a) Spectrum of azimuthal magnetic field B_ϕ. (b) Spectrum of meridional magnetic field $\boldsymbol{B}_\mathrm{m} \equiv B_r \hat{\boldsymbol{e}}_r + B_\theta \hat{\boldsymbol{e}}_\theta$.

averaged over the initial interval during which the fourfold-wreath cycle dominates. The power in the longitudinally averaged magnetic fields (the $m = 0$ power) peaks around $\ell = 10$. The power in the fluctuating magnetic fields ($|m| > 0$) peaks at the smaller scales, around $\ell = 20$ for B'_ϕ and $\ell = 25$ for $\boldsymbol{B}'_\mathrm{m}$.

The peak around $\ell = 10$ is consistent with the fourfold-wreath structure as seen in Figures 4.2(a) and 4.6: each wreath in a given hemisphere has a latitudinal extent of about 15°, or roughly one-tenth of the 180° in latitude covered by the full sphere. We note that for the longitudinally averaged fields, the dipolar and quadrupolar modes ($\ell = 1$ and 2, respectively) are weaker by a factor of ∼10 compared to any of the modes near $\ell = 10$.

In Figure 4.9(a), we show the temporal behavior of the power in the longitudinally averaged ($m = 0$) field $\langle B_\phi \rangle$ around $\ell = 10$ deep in the shell during the fourfold-wreath cycle. Most of the time the fourfold-wreath structure is symmetric about the equator, with the even modes $\ell = 8, 10, 12$ containing up to 60% of the total power for $\langle B_\phi \rangle$. The two hemispheres are out of phase, however, and the symmetric (odd) and antisymmetric (even) modes can sometimes be roughly equal (e.g., near $t = 800\ P_\mathrm{rot}$). Near $t = 1200\ P_\mathrm{rot}$, the antisymmetric modes dominate, as we noted in discussing Figure 4.7.

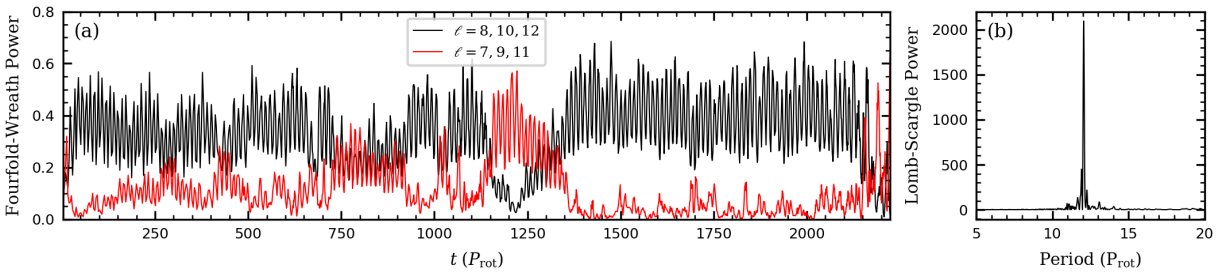

Figure 4.9: **Changing Symmetry of Magnetic Field about the Equator**. (a) Temporal evolution of the power for $\langle B_\phi \rangle$ at $r/R_\odot = 0.748$ in the modes $\ell = 8, 10, 12$ (black curve) and $\ell = 7, 9, 11$ (red curve). These are the even/odd modes near the peak of the spectrum at $\ell \approx 10$, which contain most of the power. Power is shown during the initial interval for which the fourfold-wreath cycle is dominant, coincident with the top panel in Figure 4.3. (b) Lomb-Scargle periodogram of the $\ell = 7$–12 contributions to $\langle B_\phi \rangle$ during the interval shown in panel (a). Normalized Lomb-Scargle power in each frequency component is shown versus period, with a clear peak occurring at $P_{\rm energy} \equiv 12.0\ P_{\rm rot}$.

The $m = 0$ power around $\ell = 10$ is is a proxy for the total energy contained in the fourfold-wreath structure. The oscillations in Figure 4.9(a) thus show that the fourfold-wreath energy oscillates periodically. In Figure 4.9(b), we decompose the time series for all the power contained around $\ell = 10$, both symmetric (even) and antisymmetric (odd) modes, into its frequency (or period) components. There is clearly one period that is dominant, which corresponds to an energy cycle of $\mathrm{P_{energy}} = 12.0\ \mathrm{P_{rot}}$. Since the polarity alternates between energy cycles, the fourfold-wreath cycle period is

$$\mathrm{P_{fourfold}} = 2\ \mathrm{P_{energy}} = 24.0\ \mathrm{P_{rot}}, \tag{4.1}$$

similar to the estimate of $\sim$25 P_{rot} mentioned previously.

4.6 Evolution of the Partial-Wreath Cycle

The partial-wreath component (when present) is strongest at mid-depth. From Figure 4.3(a), the partial-wreath structure first appears around $t = 2100\ P_{\mathrm{rot}}$ and cycles between positive-$\langle B_\phi \rangle$-dominant and negative-$\langle B_\phi \rangle$-dominant partial-wreath pairs. Unlike the fourfold-wreath structures (which cycle regularly even when the partial-wreath structure dominates), the partial-wreath structures cycle intermittently, turning off altogether at times, but always returning. There is some variation in the time-latitude behavior of $\langle B_\phi \rangle$ from cycle to cycle, but in general, $\langle B_\phi \rangle$ stays confined to within $\sim 20^\circ$ of the equator in a given hemisphere and shows a tendency to propagate toward higher latitudes with time.

Even when the partial-wreath cycle is dominant, the equatorward-propagating fourfold-wreath cycle still persists with its regular period of 24.0 P_{rot} unchanged. However, the fourfold-wreath structure is of much weaker amplitude and is less coherent in the hemisphere where the partial wreaths reside. There is thus a wide dynamical range in the amplitudes of the magnetic field overall. The partial-wreath cycle is associated with longitudinally averaged field strengths of $\sim$10 kG, and when the partial-wreath cycle is dominant, the fourfold-wreath cycle's longitudinally averaged field strengths are reduced to several hundred G from $\sim$2 kG.

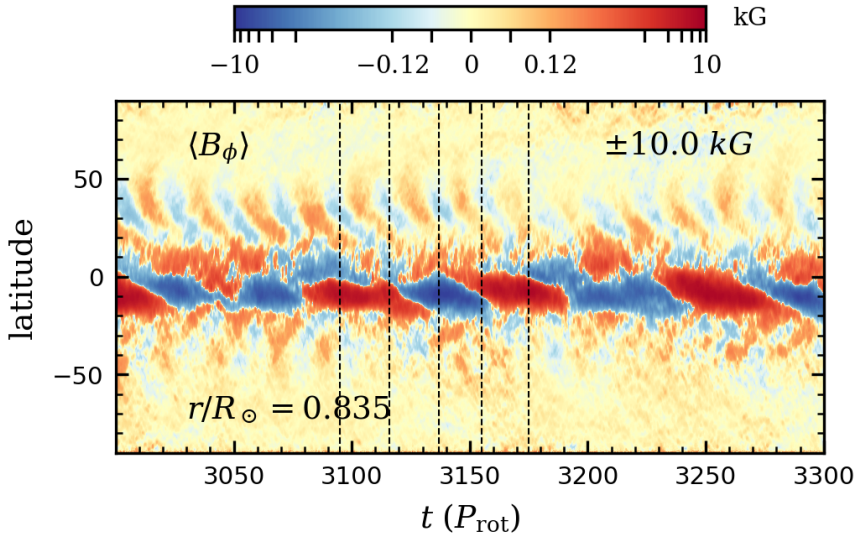

Figure 4.10: **Irregular Partial-Wreath Cycles**. Close-up view of the time-latitude behavior of $\langle B_\phi \rangle$ during the interval marked by the first set of vertical dashed lines in Figure 4.3(a). This interval (between 3000 and 3300 $P_{\rm rot}$), encompasses about four partial-wreath cycles. The vertical dashed lines denote the instances sampled by the volume-renderings of B_ϕ in Figure 4.11.

To determine in detail how the partial-wreath structure modulates over the course of a cycle, we show in Figure 4.11 a series of volume-renderings of the azimuthal field. In each snapshot, the positive-B_ϕ and negative-B_ϕ partial wreaths are centered roughly around $\phi = 210^\circ$ and $\phi = 30^\circ$ in longitude, respectively, although "islands" of magnetism associated with each wreath extend around the whole sphere. In the first snapshot (panel a), the positive-B_ϕ partial-wreath is dominant. Its amplitude and longitudinal extent then steadily decline over the next half-cycle while the negative-B_ϕ partial-wreath becomes dominant (panels b,c). In the second half of the cycle (panels d,e), the positive-B_ϕ wreath expands and strengthens until it is dominant again and the configuration is roughly the same it was at the beginning of the cycle. In the longitudinal average (e.g., Figure 4.3(a)), much cancellation occurs, but the sign of $\langle B_\phi \rangle$ still reflects which partial wreath is dominant.

In order to track the partial-wreath structure over multiple cycles, we trace B_ϕ with respect to time and longitude in a frame rotating at the same rate as in Figure 4.11. Figure 4.12 shows the time-longitude trace for B_ϕ at 10°-south latitude and at two depths, during an interval when the partial-wreath structure is stronger than the fourfold-wreath structure and cycling in the South. The choice of 10°-south latitude cuts the partial wreaths roughly in their core, where the field strengths are highest.

Approximately the same propagation pattern in time-longitude space occurs both at mid-depth and deep in the shell, despite the field being tracked at the same rate for both depths. This rate is close to the equatorial fluid rotation rate at mid-depth, suggesting that the whole asymmetric wreath structure is "anchored" in the middle of the shell and moves through the fluid as a single entity. At mid-depth, the field pattern is uniformly located at a higher longitude than the field pattern deep down. This displacement does not change with time, suggesting that it is due to the inherent geometry of the wreath rather than the shearing action of the flow.

In the rotating frame chosen, the field structure is approximately stationary. Each partial wreath (either positive-B_ϕ or negative-B_ϕ) is modulated in amplitude over a period of $\sim$80 $P_{\rm rot}$ (the same as the cycle period identified in the time-latitude trace of $\langle B_\phi \rangle$), but remains basically at a fixed longitude. Furthermore, the positive-B_ϕ and negative-B_ϕ wreaths are out of phase with

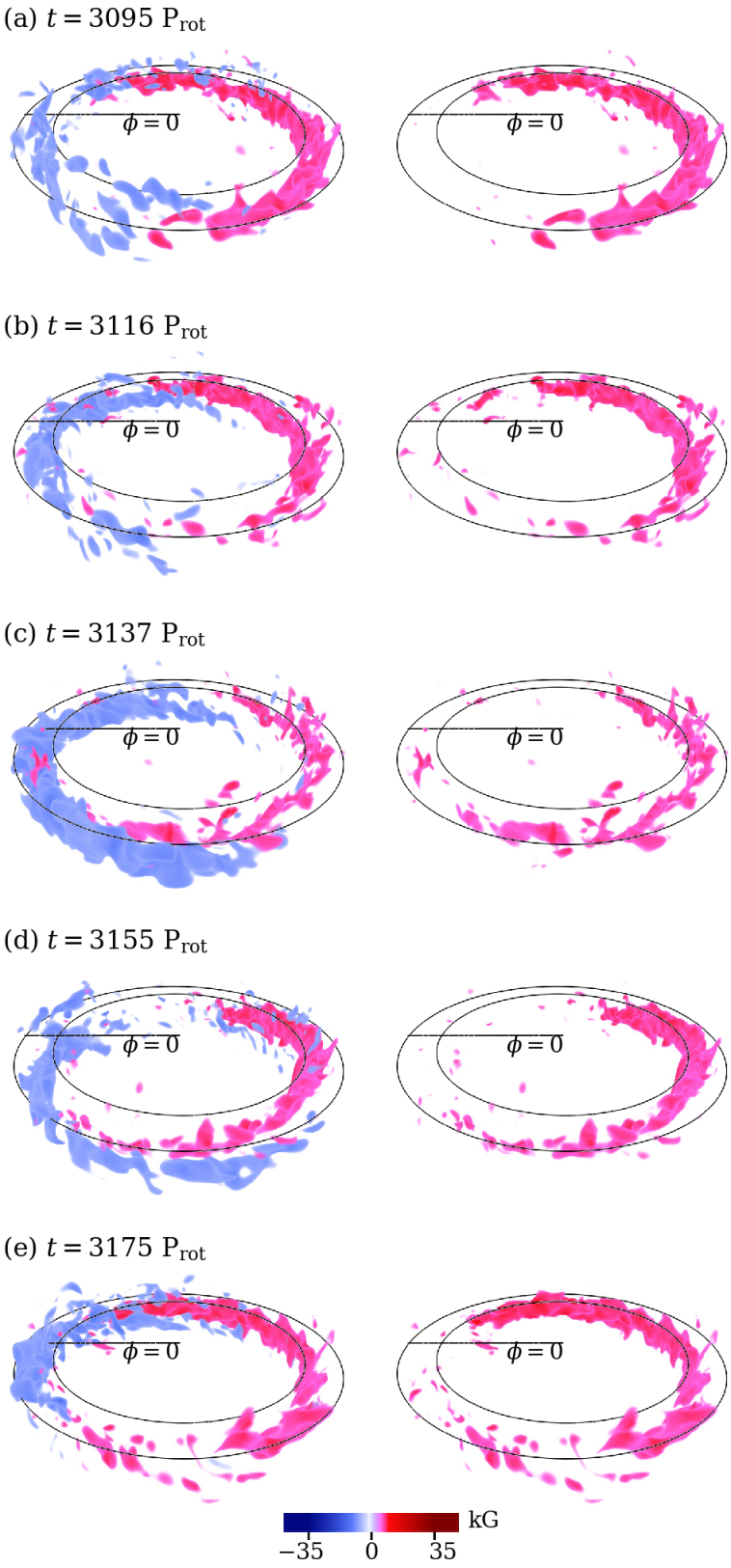

Figure 4.11: **Walking through a Partial-Wreath Cycle**. Volume-rendering of B_ϕ throughout one partial-wreath cycle. We track the partial wreaths in a frame rotating at 32 nHz faster than the frame rotation rate Ω_0, approximately equal to the equatorial rotation rate at mid-depth. Only strong fields ($|B_\phi| > 5$ kG) are depicted. To show the field everywhere in 3-D space and simultaneously emphasize the strong fields, transparency varies linearly with field strength, with structures for which $|B_\phi| \geq 35$ kG being completely opaque. The first row (panel a) samples the field when the red partial wreath is dominant, and subsequent samples (panels b–e) are separated by roughly one-quarter of the partial-wreath cycle period. The left-hand column shows the full B_ϕ profile and the right-hand column shows only positive B_ϕ. The view is from ∼30° north of the equator and 90° longitude. The spherical-shell boundaries in the equatorial plane and the location of 0°-longitude are marked by the black curves.

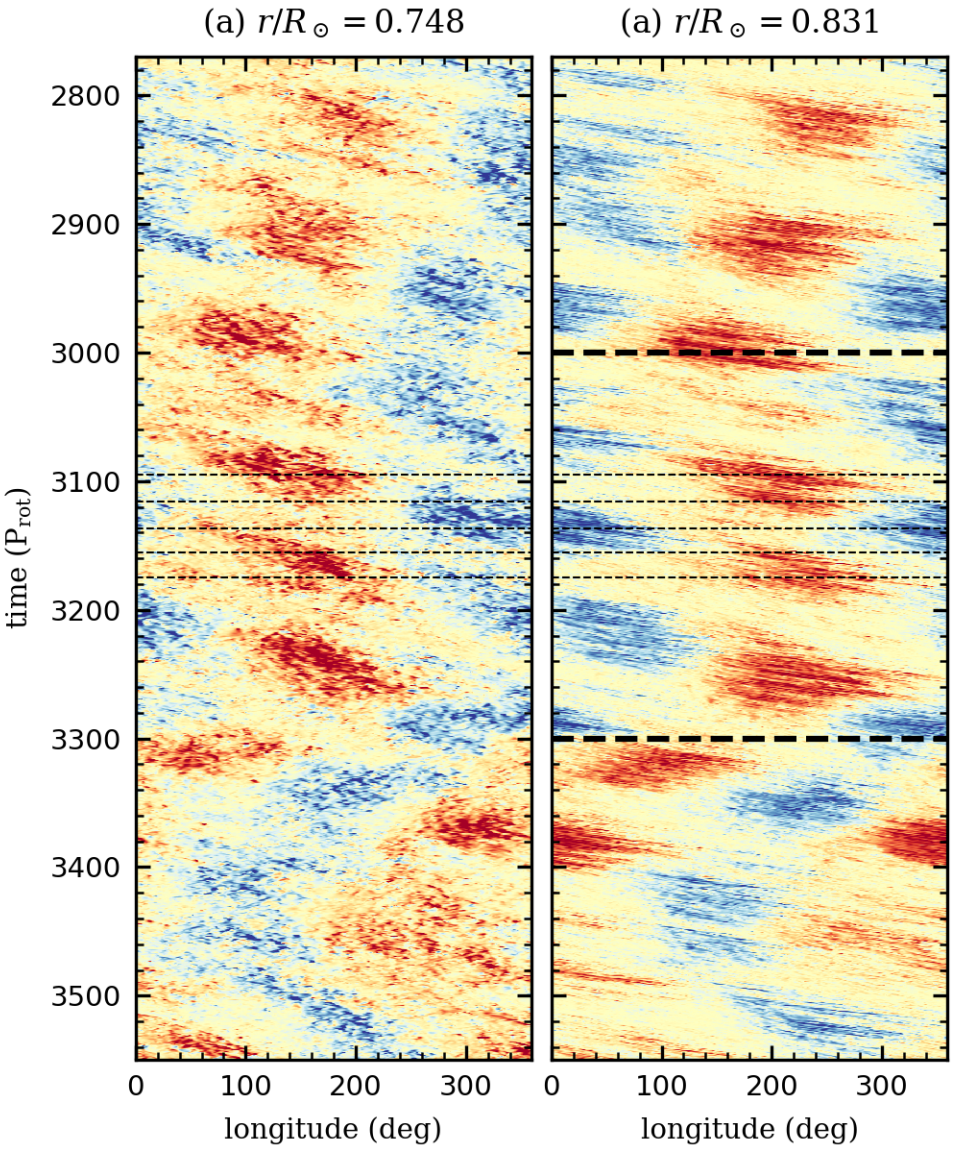

Figure 4.12: **Modulation of Active Longitudes during a Partial-Wreath Cycle**. Time-longitude trace of B_ϕ for 10°-south latitude (a) deep in the shell and (b) at mid-depth, tracked at the same rotation rate as in Figure 4.11. The color map saturation values are ±12 kG in panel (a) and ±25 kG in panel (b). The interval shown in close-up view in Figure 4.10 is marked by the thick horizontal dashed lines in panel (b). The instances sampled in Figure 4.11 are marked by the thinner dashed lines in both panels.

another. At any given time, there are thus two partial wreaths, but in general when the positive-B_ϕ wreath is strong, the negative-B_ϕ wreath is weak, and vice versa.

The partial-wreath structure is still not exactly stationary even when tracked in the chosen frame. Figure 4.12 shows a weak zigzag pattern for each the positive-B_ϕ and negative-B_ϕ partial wreaths, implying that the propagation rate of the wreath through the fluid is not constant with time, or that longitudinal extents of each partial wreath shrink and expand throughout the cycle.

In light of Figures 4.11 and 4.12, the "polarity reversals" in $\langle B_\phi \rangle$ during the partial-wreath cycle are in fact accomplished by each partial wreath weakening and strengthening mostly *in place*, with the positive-B_ϕ partial wreath oscillating in time roughly 180° out of phase with negative-B_ϕ one. This stands in contrast to the reversals of the fourfold-wreath cycles, which are achieved by full wreaths migrating equatorward from mid-latitudes and getting replaced by new wreaths of the opposite polarity.

4.6.1 Partial-Wreath Cycle Period and Hemispheric Asymmetry

The partial-wreath cycle period is roughly 80 $P_{\rm rot}$, as identified previously, but it is substantially irregular. We determine the period more formally by calculating the periodicities associated with the relative energy content in the two partial wreaths:

$$A_{\rm partial} \equiv \frac{B_\phi^+ - B_\phi^-}{B_\phi^+ + B_\phi^-}, \tag{4.2}$$

the "+" and "−" superscripts referring to instantaneous rms averages of the field strength over the regions where B_ϕ is positive and negative (respectively), thus measuring the energy content in the positive and negative partial wreaths separately. The mean in the rms is taken over longitude, low latitudes between ±25°, and all depths. Unlike the linear longitudinal average $\langle B_\phi \rangle$, the rms-average $A_{\rm partial}$ is more sensitive to the strongest fields, and thus better determines the relative amplitudes of the partial wreaths as visualized in Figure 4.11.

Figure 4.13(a) shows the relative energy content over an interval for which no period is easily identifiable in the time-latitude trace of $\langle B_\phi \rangle$ in Figure 4.3(a), but the partial-wreath cycle is still

visible in the well-defined peaks and troughs of $A_{\rm partial}$. In Figure 4.13(b), we show the periodogram associated with $A_{\rm partial}$. There is a distinctive peak in power at

$$\mathrm{P}_{\rm partial} \equiv 81.5\ \mathrm{P}_{\rm rot}, \tag{4.3}$$

which we define to be the (dominant) partial-wreath cycle period. Due to the irregularity of the partial-wreath cycle—caused by some cycles being longer or shorter than $\mathrm{P}_{\rm partial}$, as well as significant amplitude and phase modulation—there is a substantial spread in the periods for which the Lomb-Scargle power is large. The dominant period identified in Equation (4.3) is thus consistent with the previous estimate $\sim$80 $P_{\rm rot}$ from a visual examination of Figure 4.3(a).

The partial wreaths tend to reside predominantly in one hemisphere or the other, although they are not strictly confined and can in some instances cross the equator. Nonetheless, this phenomenon leads to a substantial *hemispheric asymmetry*, which we define for our dynamo models as

$$A_{\rm hem} \equiv \frac{B_\phi^{\rm N} - B_\phi^{\rm S}}{B_\phi^{\rm N} + B_\phi^{\rm S}}, \tag{4.4}$$

the "N" and "S" superscripts referring to instantaneous rms averages of the field strength over the Northern and Southern Hemispheres (respectively). The mean in the rms is taken over longitude, low latitudes (between the equator and 25°-latitude for the Northern Hemisphere and comparably for the Southern Hemisphere), and all depths.

Figure 4.14(a) shows the temporal behavior of the hemispheric asymmetry for case D3-1 during roughly the latter half of the simulation, when the partial-wreath cycle is usually substantially stronger than the fourfold-wreath cycle. The dominant hemisphere switches between North and South chaotically, with no single period easily seen. We have confirmed this aperiodic nature by computing the periodogram associated with $A_{\rm hem}$ shown in Figure 4.14(b): there are a wide range of periods that are relevant, with no obvious peak in the power spectrum. What is clear from the broad peak near 2000 $P_{\rm rot}$ in the periodogram (and from a visual inspection of Figure 4.14(a)) is that asymmetry of a single sign—corresponding to partial wreaths cycling in preferentially in a single hemisphere—can persist for long time-scales, up to $\sim$1000 $P_{\rm rot}$.

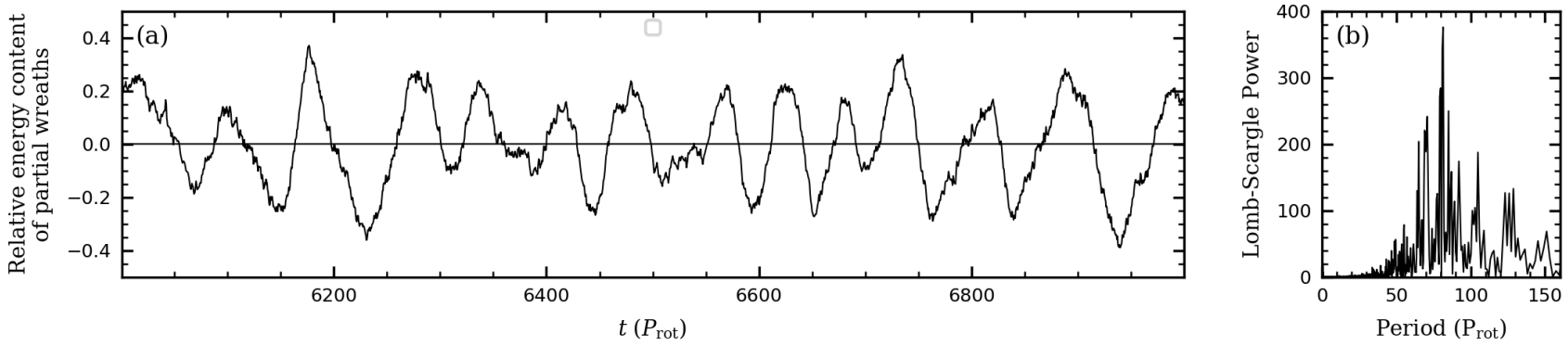

Figure 4.13: **Periodogram of the Fourfold-Wreath Cycle**. (a) Temporal evolution of $A_{\rm partial}$ (Equation (4.2)) during the interval between 6000 $P_{\rm rot}$ and 7000 $P_{\rm rot}$ in case D3-1. (b) Normalized Lomb-Scargle periodogram of $A_{\rm partial}$ for case D3-1 during the interval from 5100 $P_{\rm rot}$ until the end of the simulation, during which time the partial-wreath pair is consistently stronger than the fourfold-wreath structure.

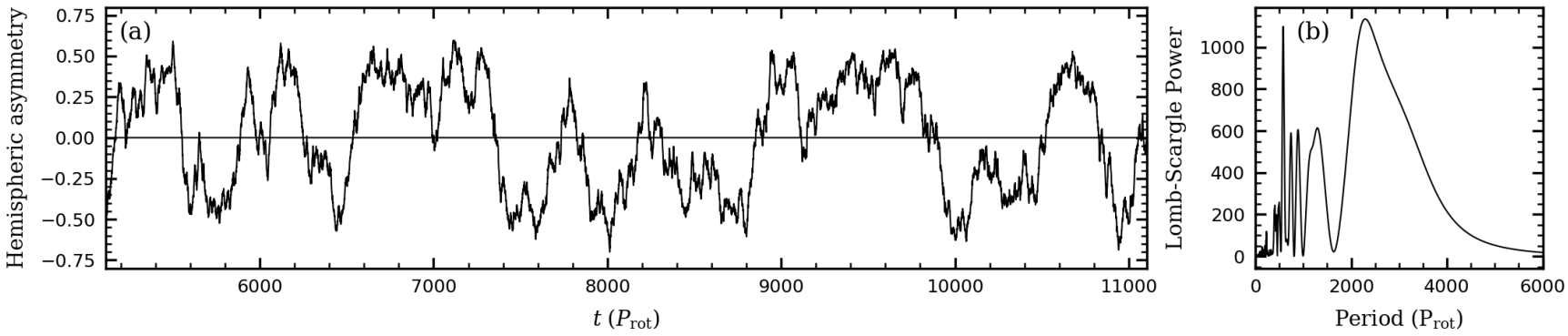

Figure 4.14: **Temporal Evolution of Hemispheric Asymmetry**. (a) Temporal evolution of $A_{\rm hem}$ (Equation (4.4)) during the interval between 5100 $P_{\rm rot}$ and the end of the simulation in case D3-1. (b) Normalized Lomb-Scargle periodogram of $A_{\rm hem}$ for case D3-1 during the same interval as in panel (a).

4.7 Bistability Trends with Higher Magnetic Prandtl Number ($\mathrm{Pr_m}$)

Because we keep the viscous diffusivity fixed while lowering the magnetic diffusivity, the magnetic structures grow increasingly more complex the higher the magnetic Prandtl number ($\mathrm{Pr_m}$). Figure 4.15 contains snapshots of the azimuthal magnetic field B_ϕ (in Mollweide projection) near the beginning of each of the three dynamo cases. At these early times, the structure of B_ϕ consists largely of the fourfold wreaths. As $\mathrm{Pr_m}$ is increased, the magnetic structures become more shredded and dominated by small-scale features. The local field strength increases, but the global coherence of the field decreases.

Although bistability (in the form of the fourfold and partial-wreath cycles) is most clearly evident in case D3-1, similar behavior can be seen in the higher-$\mathrm{Pr_m}$ cases D3-2 and D3-4. In Figure 4.16, we show extended time-latitude diagrams for case D3-2, with the time axes and color map scaled to be directly comparable to Figure 4.3. Case D3-2 exhibits bistability with largely the same characteristics as case D3-1, namely a fourfold-wreath cycle with regular polarity reversals and a single-hemisphere partial-wreath cycle with irregular polarity reversals. The fourfold-wreath cycle has a weaker signal, however, due to the finer-scale magnetic structures. The system destabilizes after only $\sim$250 P_{rot} to launch the partial-wreath cycle, which is less intermittent than in case D3-1, wandering between the Northern and Southern Hemispheres without ever fully shutting down.

From Figure 4.15(c), the fourfold-wreath structure in case D3-4 is less striking than for the lower-magnetic-Prandtl number cases. Each wreath is also significantly tilted in latitude and thus there is very little signal left after a longitudinal average. The partial wreaths, which appear later in the simulation, are also less coherent. Nonetheless, the fourfold-wreath and partial-wreath cycles in case D3-4 can still be detected in sequences of Mollweide projections.

Each of the higher-$\mathrm{Pr_m}$ cases has substantial polar caps of magnetism, which occasionally reverse polarity but are not clearly tied to either of the two cycles. In time-latitude diagrams for $\langle B_r \rangle$ and $\langle B_\theta \rangle$ (not shown), there is a clear tendency for the meridional field to break off from the partial wreaths and move to the poles, just as in Figure 4.5 for case D3-1.

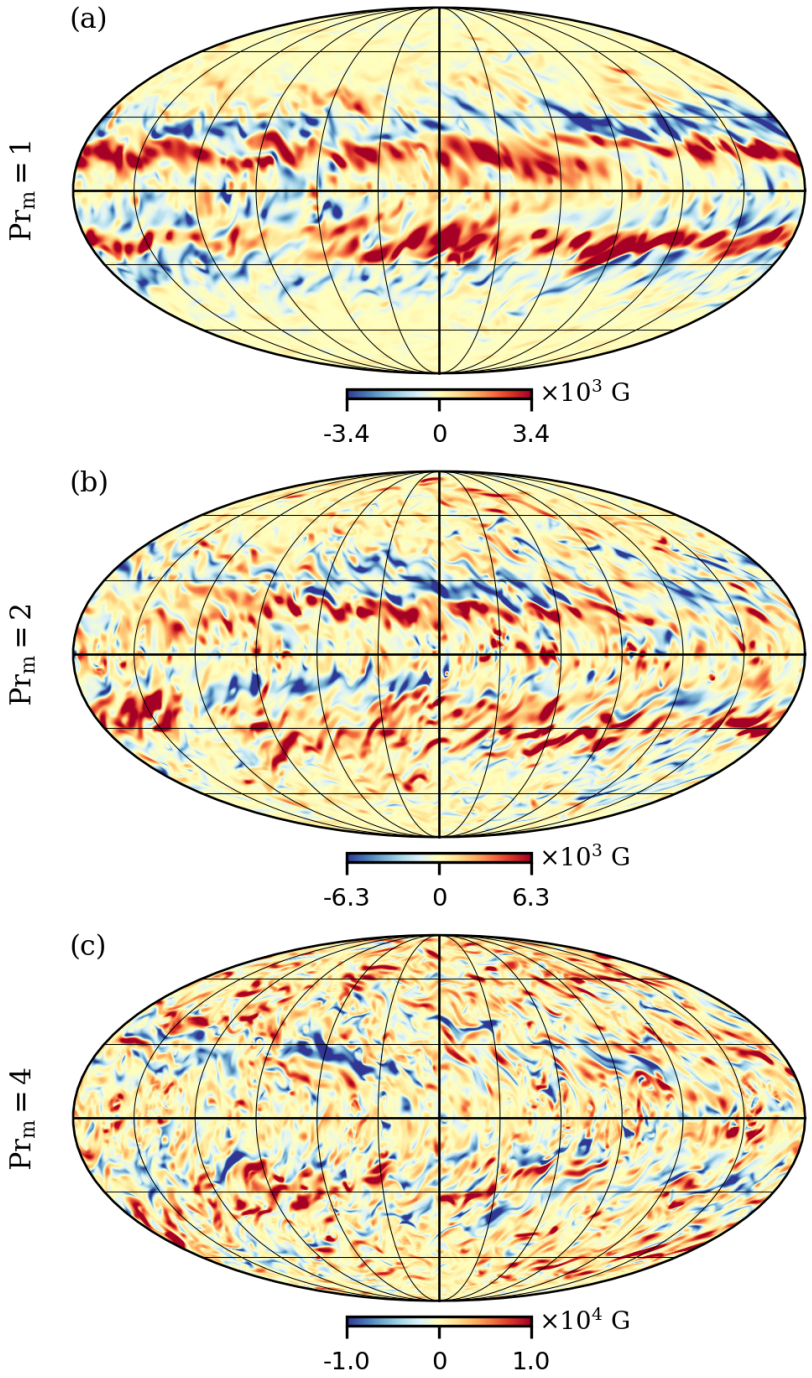

Figure 4.15: **Fourfold Wreaths at Different Levels of Turbulence**. Snapshots on spherical surfaces of the azimuthal magnetic field B_ϕ shown in global Mollweide projection for the three dynamo cases D3-1, D3-2, and D3-4 with increasing $\mathrm{Pr_m}$ from (a) to (c). Each model is sampled near the bottom of the shell ($r/R_\odot = 0.748$) at an early time within the dynamo simulation (less than 100 P_{rot} after appreciable magnetism develops).

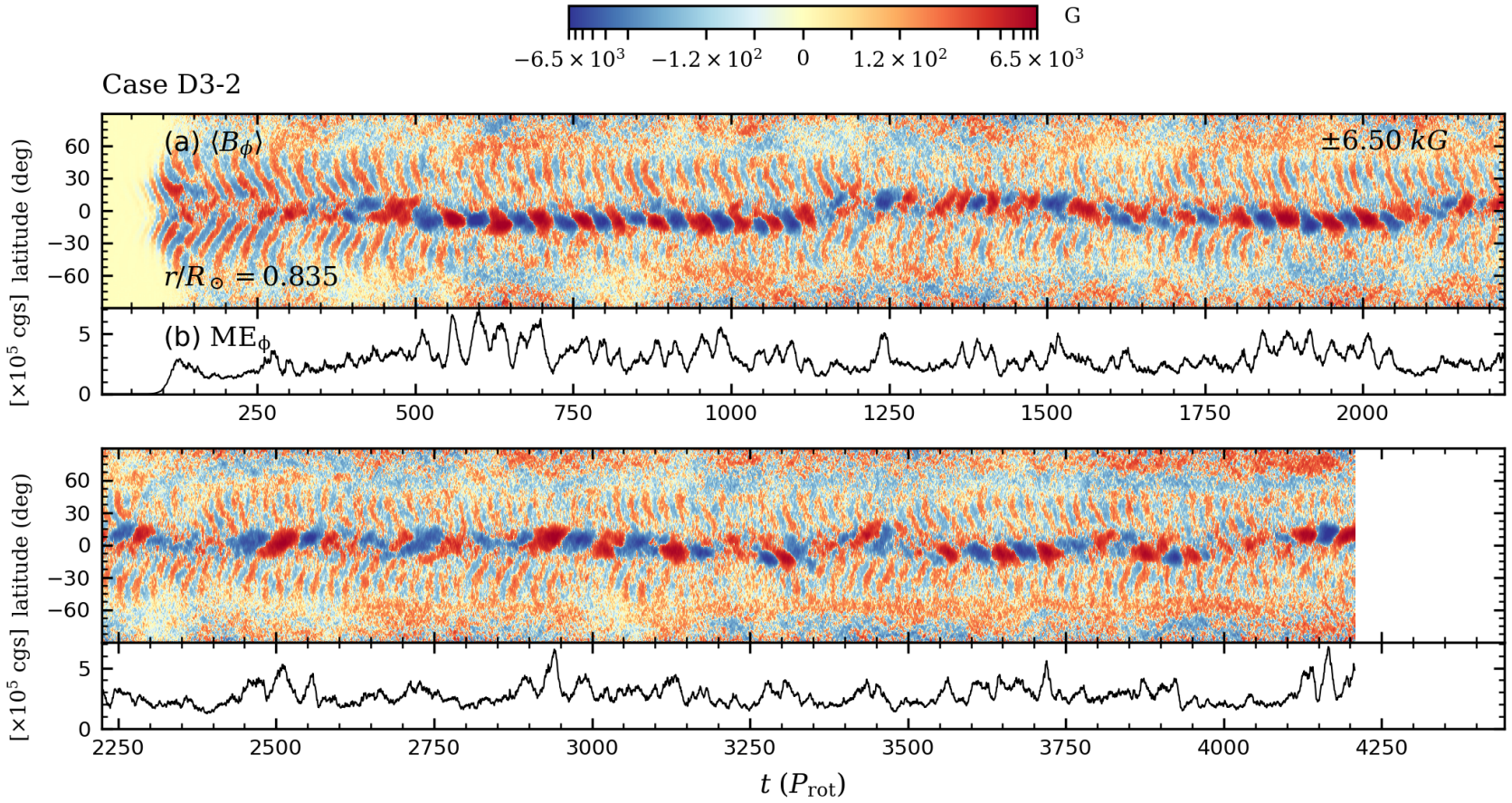

Figure 4.16: **Bistability in a More Turbulent Dynamo**. Extended time-latitude diagram of azimuthal magnetic field $\langle B_\phi \rangle$ and energy trace for ME_ϕ at mid-depth ($r/R_\odot = 0.835$) for case D3-2 (at $\mathrm{Pr_m} = 2$), similar to Figure 4.3. Here the fourfold-wreath and partial-wreath cycles are seen to coexist for most of the simulation, with the partial-wreath cycle in particular being less intermittent than in case D3-1.

Table 4.2: **Fluid Parameters for the Different Cases in the Bistability Experiment**. Diagnostic parameters, grid resolution, and simulation run times for all cases.

Case	$\mathrm{Pr_m}$	$\eta(r_\mathrm{o})$	Ro	Re	$\mathrm{Re_m}$	$\Delta\Omega/\Omega_0$	(N_r, N_θ, N_ϕ)	ℓ_max	Diffusion time	Run time	Run time
H3	-	-	0.0599	56.4	-	0.228	(96, 384, 768)	255	115 P_rot	6390 P_rot	55.6 TDT
D3-1	1	3.00×10^{12}	0.0609	58.3	76.5	0.183	(96, 384, 768)	255	115 P_rot	11100 P_rot	96.7 MDT
D3-2	2	1.50×10^{12}	0.0609	57.0	101	0.127	(96, 384, 768)	255	230 P_rot	4210 P_rot	18.3 MDT
D3-4	4	0.75×10^{12}	0.0599	53.0	131	0.063	(128, 576, 1152)	383	460 P_rot	2140 P_rot	4.65 MDT

Table 4.3: **Kinetic and Magnetic Energies in the Bistability Experiment**. Volume-averaged energy budgets for cases H3, D3-1, D3-2, and D3-4. "KE" and "ME" refer to the kinetic and magnetic energy densities, respectively. Units are cgs, with a common exponent divided out. The subscripts ϕ, m, and c refer the energy contributions from the mean azimuthal field components ($\langle v_\phi \rangle$ and $\langle B_\phi \rangle$), the mean meridional field components ($\langle \boldsymbol{v}_\mathrm{m} \rangle$ and $\langle \boldsymbol{B}_\mathrm{m} \rangle$), and the convective components ($\boldsymbol{v}'$ and $\boldsymbol{B}'$), respectively. The fraction of the total energy (no subscripts; magnetic and kinetic energies considered separately) from each contribution is shown as the percentage in parentheses.

Case	KE/10^6	KE$_\phi$/10^6	KE$_\mathrm{m}$/10^6	KE$_\mathrm{c}$/10^6	ME/10^5	ME$_\phi$/10^5	ME$_\mathrm{m}$/10^5	ME$_\mathrm{c}$/10^5
H3	19.3	17.5 (91.1%)	0.0053 (0.027%)	1.70 (8.83%)	-	-	-	-
D3-1	13.5	11.7 (86.7%)	0.0053 (0.039%)	1.79 (13.2%)	2.15	0.161 (7.50%)	0.015 (0.69%)	1.98 (91.8%)
D3-2	7.89	6.12 (77.6%)	0.0048 (0.061%)	1.76 (22.3%)	3.79	0.162 (4.26%)	0.029 (0.77%)	3.60 (95.0%)
D3-4	3.52	1.88 (53.4%)	0.0038 (0.11%)	1.64 (46.5%)	6.15	0.051 (0.82%)	0.031 (0.50%)	6.07 (98.7%)

The biggest global effect of increasing the magnetic Prandtl number is to lower the overall differential rotation, while keeping the shape of the rotation profile in the meridional plane largely fixed. Table 4.2 contains the values of some of the diagnostic non-dimensional parameters (as well as the grid resolution and various timescales) characterizing each system. We quantify the strength of the differential rotation as the difference at the outer surface of the rotation rate between the equator and 60°-latitude, normalized by the frame rotation rate: $\Delta\Omega/\Omega_0 \equiv [\Omega(r_o, \pi/2) - \Omega(r_o, \pi/6)]/\Omega_0$. For comparison, for the solar rotation rate determined through helioseismology, $\Delta\Omega/\Omega_0 = 0.197$, if we take $\Omega_0 = \Omega_\odot$ and r_o to be the radius just below near-surface shear layer (Howe et al., 2000). The magnitude of the differential rotation in case H3 is quite strong at 0.228—even greater than the solar value. As $\mathrm{Pr_m}$ increases, $\Delta\Omega/\Omega_0$ is steadily weakened by the presence of small-scale magnetic structures. These counteract the Reynolds stress produced by the Taylor columns (which tend to drive a strong differential rotation) through feedbacks from the non-axisymmetric Maxwell stress.

From Table 4.2, modifying the magnetic Prandtl number has little effect on the resulting level of rotational constraint (parameterized by the Rossby number) or the level of turbulence (parameterized by the Reynolds number). This agrees with the fact that the hydrodynamic structures (in terms of their distribution of length-scales and amplitudes) in the dynamo cases are largely similar to those of the hydrodynamic case H3. The main effect of modifying $\mathrm{Pr_m}$ comes from the degree of complexity in the magnetic structures, as seen by the steady increase of $\mathrm{Re_m}$ with $\mathrm{Pr_m}$.

The bulk energy budget for the simulation suite is shown in Table 4.3. Case H3 has both the highest kinetic energy from the differential rotation (KE_ϕ) and the highest kinetic energy overall. For the dynamo cases, as the magnetic Prandtl number is increased, the energy in the meridional circulation ($\mathrm{KE_m}$) and convection ($\mathrm{KE_c}$) stays roughly the same as in case H3, while the energy in the differential rotation (KE_ϕ) sharply decreases.

The magnetic energy density (which is dominated by the fluctuating contribution $\mathrm{ME_c}$ for all three dynamo cases) steadily increases with increasing $\mathrm{Pr_m}$, at the expense of the energy in the differential rotation. The energy in the mean magnetic fields ME_ϕ and $\mathrm{ME_m}$ seems to vary in no clear way with $\mathrm{Pr_m}$, although the mean energy in the azimuthal field (ME_ϕ) is significantly less in

case D3-4, consistent with the shredded profile of B_ϕ seen in Figure 4.15(c).

4.8 The Dynamical Origins of Each Cycling Mode

The real 22-year sunspot cycle must be the result of a complex interaction between turbulent convection, rotation, and magnetism. Our simulations, although far less turbulent than the Sun, have the advantage that the dynamical origins of each of the two cycling modes identified can be explored in a fair amount of detail. This is because we can probe each term in the dynamical equations with high spatio-temporal resolution and accuracy, something we are unable to do for the Sun. We devote this section to describing the dynamics that lead to the partial-wreath and fourfold-wreath cycles in case D3-1. We focus the discussion on the dominant terms in the induction Equation (1.1c) and their physical origins.

We note at the outset that for both cycles, there is very little temporal modulation in either the differential rotation (DR; the main driver of the dynamo through the Ω-effect) or the meridional circulation (MC). This stands in contrast to the dynamos of Augustson et al. (2015) and Guerrero et al. (2016a,b), in which significant modulation of the DR (10–20%) played a significant role. For the fourfold-wreath cycle, modulation of mean flows is undetectable. For the partial-wreath cycle, there is a $\sim$5% weaker DR when compared to the fourfold-wreath cycle (due to the stronger magnetic fields), and a $\sim$1% modulation of the DR from cycle to cycle. The MC develops significant equatorial asymmetry during partial-wreath cycling, but this appears to be mostly a response to the magnetic field and has little effect on the dynamics.

4.8.1 Dynamics of the Fourfold-Wreath Cycle

The magnetic field in our simulations is dominated by the azimuthal component B_ϕ. We therefore first turn our attention to the ϕ-component of the longitudinally averaged Equation

(1.1c), i.e.,

$$\frac{\partial \langle B_\phi \rangle}{\partial t} \approx \underbrace{(\langle \boldsymbol{B} \rangle \cdot \nabla \langle \boldsymbol{v} \rangle)_\phi}_{\mathrm{MS}_\phi} + \underbrace{\langle \boldsymbol{B}' \cdot \nabla \boldsymbol{v}' \rangle_\phi}_{\mathrm{FS}_\phi}$$
$$\underbrace{- \langle \boldsymbol{v} \cdot \nabla \boldsymbol{B} \rangle_\phi}_{\mathrm{TA}_\phi} \underbrace{- \langle \nabla \times [\eta(r) \nabla \times \boldsymbol{B}] \rangle_\phi}_{\mathrm{RD}_\phi}, \tag{4.5}$$

where "MS," "FS," "TA," and "RD" refer to mean shear, fluctuating shear, total advection, and resistive dissipation, respectively. The generation due to fluid compression, $-\langle B_\phi \nabla \cdot \boldsymbol{v} \rangle$, is very weak and we neglect it throughout.

Figure 4.17 shows profiles of the terms in Equation (4.5) averaged over a short time interval during fourfold-wreath cycling. The time interval chosen is not unique and the profiles in Figure 4.17 are representative of the generation terms at any time the fourfold-wreath cycle is dominant. The governing term is clearly the mean-shear, or Ω-effect (MS_ϕ). The fluctuating shear (FS_ϕ) is the weakest term overall and has no obvious pattern in its spatial distribution. The total advection (TA_ϕ) is weak and also has no cellular structure (compare to Figure 4.1(d)), suggesting that transport of B_ϕ by the meridional circulation is negligible. The resistive dissipation (RD_ϕ) plays some role (especially near the inner boundary) and has a sign structure opposite to that of $\langle B_\phi \rangle$, acting to destroy whatever field is already present.

The mean-shear production of $\langle B_\phi \rangle$ has a similar pattern to $\langle B_\phi \rangle$ itself, but with the four wreaths displaced closer to the equator, which tends to drive the $\langle B_\phi \rangle$ wreath structure equatorward. Furthermore, like the fourfold wreaths themselves, the wreaths of MS_ϕ reappear at mid-latitudes after they disappear near the equator. In Figure 4.17(a), for example, the negative-MS_ϕ wreath straddling (-15°)-latitude in the Southern Hemisphere is associated with a weak negative-MS_ϕ wreath forming at (-40°)-latitude. Positive B_ϕ thus forms at high latitudes where originally there was negative B_ϕ, creating a polarity reversal.

It is unclear exactly what stops the equatorward migration—i.e., why the wreaths have significantly reduced amplitude in the $\pm 10^\circ$-latitude band straddling the equator. In the Sun, there is presumably only one wreath per hemisphere, each with opposite polarity (as inferred from

the solar butterfly diagram). When the two wreaths meet at the equator, they annihilate, as in magnetic reconnection. The same process cannot occur in the fourfold-wreath cycle because the wreaths are often equatorially symmetric.

We now investigate the origins of the displacement of the shear-production pattern relative to the azimuthal magnetic field. The mean shear is (neglecting curvature terms)

$$\mathrm{MS}_\phi \approx \langle \boldsymbol{B}_\mathrm{m} \rangle \cdot \nabla \langle v_\phi \rangle \,. \tag{4.6}$$

The magnetic field components $\langle \boldsymbol{B}_\mathrm{m} \rangle$ and $\langle B_\phi \rangle$, the azimuthal velocity field $\langle v_\phi \rangle$, and the shear production MS_ϕ are shown as a set of snapshots in Figure 4.18. The meridional magnetic field has a fourfold structure and is roughly coincident spatially with the $\langle B_\phi \rangle$ wreaths. From Figure 4.18(a), the streamlines of $\boldsymbol{B}_\mathrm{m}$ are roughly counterclockwise for positive $\langle B_\phi \rangle$ and clockwise for negative $\langle B_\phi \rangle$.

The profile of $\langle v_\phi \rangle$ comes from a differential rotation (at least during the fourfold-wreath cycle) nearly identical to that of the hydrodynamic progenitor, case H3 (compare to Figure 4.1(c)). The direction field of $\langle \nabla v_\phi \rangle$ (perpendicular to the contours in Figure 4.18(b)) is thus cylindrically outward and slightly tilted toward the equator. The combination of $\langle \boldsymbol{B}_\mathrm{m} \rangle$ and $\langle \nabla v_\phi \rangle$ creates the pattern of MS_ϕ shown in Figure 4.18(c).

The overall geometry depicted in Figure 4.18 thus explains the displacement of the term MS_ϕ relative to $\langle B_\phi \rangle$. In the positive-$\langle B_\phi \rangle$ wreath in the Northern Hemisphere, for example, the field lines wind so that $\langle \boldsymbol{B}_\mathrm{m} \rangle$ points outward in the lower-latitude part of the wreath (corresponding to positive MS_ϕ via Equation (4.6)) and inward in the higher-latitude part of the wreath (corresponding to negative MS_ϕ). With time, the positive-$\langle B_\phi \rangle$ wreath is thus strengthened at lower latitudes and weakened at higher latitudes, sending the whole structure south toward the equator so that the positive-$\langle B_\phi \rangle$ wreath is eventually replaced with a negative-$\langle B_\phi \rangle$ wreath.

The nature of the Ω-effect can also be used to estimate the fourfold-wreath cycle period. Since the mean-shear term is responsible for the cycling of $\langle B_\phi \rangle$, the cycle period should be given

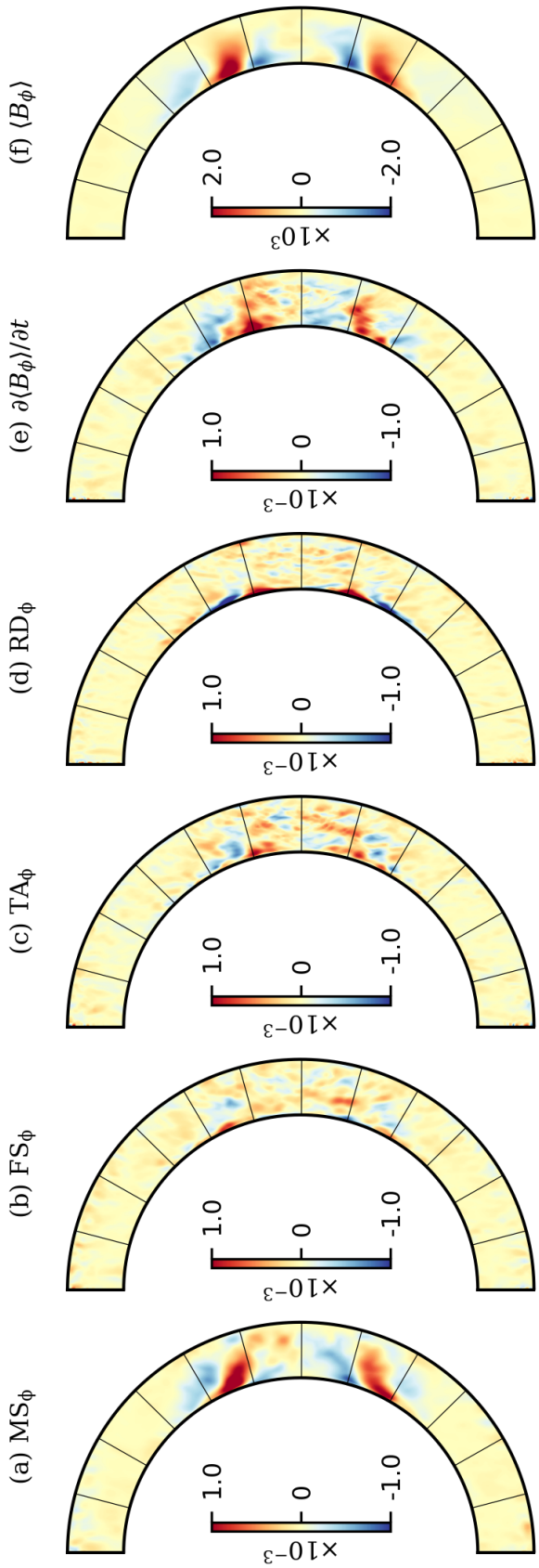

Figure 4.17: **Inductive Generation of the Fourfold Wreaths**. Generation terms in the azimuthal component of the longitudinally averaged induction Equation (4.5) for case D3-1, averaged over an interval of one rotation period centered at 660 $P_{\rm rot}$. The terms are (a) mean shear, (b) fluctuating shear, (c) total advection, (d) resistive dissipation, (e) sum of all terms (approximately equal to the time-derivative of $\langle B_\phi \rangle$), and (f) $\langle B_\phi \rangle$ itself. The units are cgs (G s^{-1} in panels a–e and G in panel f).

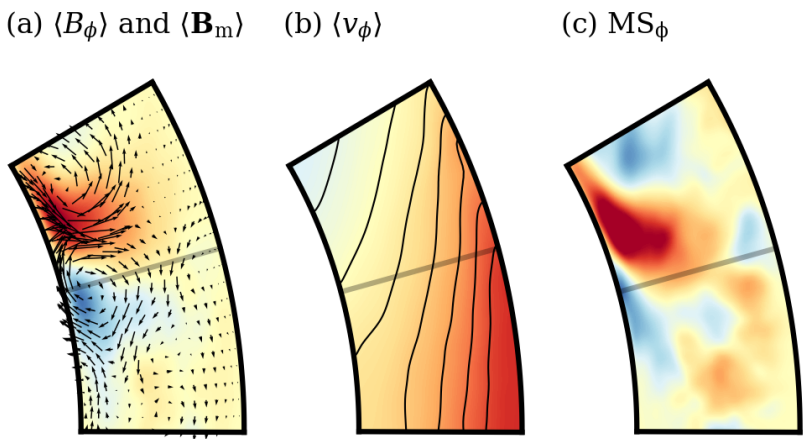

Figure 4.18: **Mean-Shear Production of the Fourfold Wreaths**. Instantaneous profiles (at $t = 660\ P_\mathrm{rot}$) of (a) the longitudinally averaged magnetic field, (b) the longitudinally averaged azimuthal velocity, and (c) the mean-shear production MS_ϕ between the equator and 30°-north for case D3-1. In panel (a), $\langle B_\phi \rangle$ is plotted in color (with saturation values ±2.5 kG) and $\langle \boldsymbol{B}_\mathrm{m} \rangle$ is plotted as a vector field (with the longest arrows corresponding to ∼750 G). In panels (b,c), $\langle v_\phi \rangle$ and MS_ϕ are shown in color with saturation values of ±750 m s^{-1} and ±0.001 G s^{-1}, respectively.

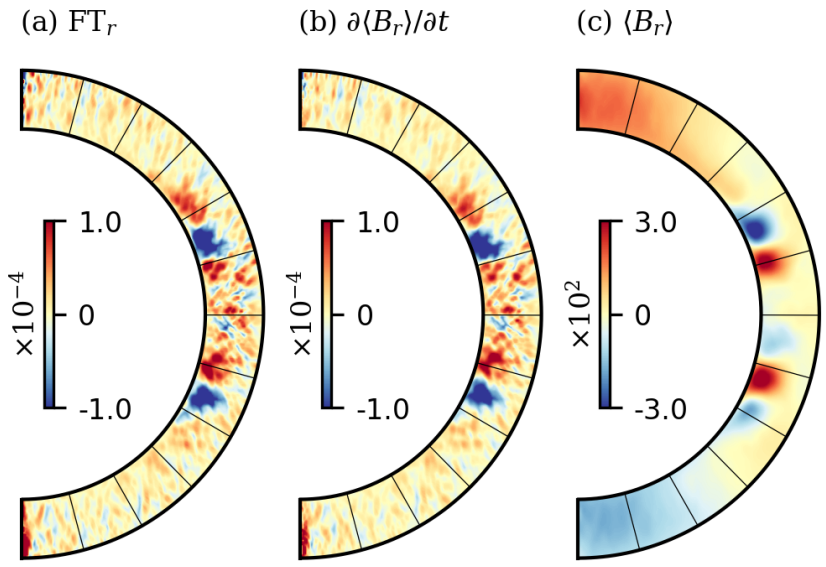

Figure 4.19: **Inductive Generation of the Poloidal Magnetic Field**. Generation terms appearing in Equation (4.9), averaged from snapshots taken at the beginning of 57 successive fourfold-wreath cycles. (a) Fluctuating transport, (b) sum of all terms (equal to the time-derivative of $\langle B_r \rangle$), and (c) $\langle B_r \rangle$ itself. The units are cgs (G s^{-1} in panels a–b and G in panel c).

roughly by

$$P_{\text{fourfold}} \sim \frac{4\left\langle B_\phi \right\rangle_{\max}}{(\text{MS}_\phi)_{\text{rms}}} \sim \frac{4\left\langle B_\phi \right\rangle_{\max}}{\left\langle \boldsymbol{B}_{\text{m}} \right\rangle_{\text{rms}} \left\langle \nabla v_\phi \right\rangle_{\text{rms}}}, \tag{4.7}$$

where $\left\langle B_\phi \right\rangle_{\max}$ is the typical azimuthal magnetic field's maximum amplitude in the wreath's core and the "rms" subscripts refer to rms magnitudes taken over the whole wreath. For the wreath pair in Figure 4.18 (taking the mean between the equator and 30°-north in lower half of the CZ), we compute $\left\langle B_\phi \right\rangle_{\max} = 2.63$ kG, $\left\langle \boldsymbol{B}_{\text{m}} \right\rangle_{\text{rms}} = 302$ G, and $\left\langle \nabla v_\phi \right\rangle_{\text{rms}} = 2.17 \times 10^{-6}$ s^{-1}, yielding

$$P_{\text{fourfold}} \sim 22.0\ P_{\text{rot}}, \tag{4.8}$$

in good agreement with the actual cycle period of Equation (4.1).

To investigate the source of the meridional field $\boldsymbol{B}_{\text{m}}$, we turn to the radial component of the longitudinally averaged Equation (1.1c), which we write as

$$\begin{aligned} \frac{\partial \left\langle B_r \right\rangle}{\partial t} = &\underbrace{\left[\nabla \times \left(\left\langle \boldsymbol{v} \right\rangle \times \left\langle \boldsymbol{B} \right\rangle\right)\right]_r}_{\text{MT}_r} + \underbrace{\left[\nabla \times \left(\left\langle \boldsymbol{v}' \times \boldsymbol{B}' \right\rangle\right)\right]_r}_{\text{FT}_r} \\ &\underbrace{- \left\langle \nabla \times \left[\eta(r) \nabla \times \boldsymbol{B}\right] \right\rangle_r}_{\text{RD}_r}. \end{aligned} \tag{4.9}$$

Here "MT" and "FT" refer to the mean transport (magnetic field generation from the mean electromotive force—or emf—$\left\langle \boldsymbol{v} \right\rangle \times \left\langle \boldsymbol{B} \right\rangle$) and the fluctuating transport (or generation from the fluctuating emf $\left\langle \boldsymbol{v}' \times \boldsymbol{B}' \right\rangle$), respectively.

Figure 4.19 shows the dominant generation terms for $\left\langle B_r \right\rangle$ alongside $\left\langle B_r \right\rangle$ itself. We only show the fluctuating transport FT_r, which is an order of magnitude larger than both MT_r and RD_r. Similar to the generation of $\left\langle B_\phi \right\rangle$ shown in Figure 4.6, the profile for $\partial \left\langle B_r \right\rangle / \partial t$ is displaced equatorward relative to $\left\langle B_r \right\rangle$, leading to the equatorward propagation of $\left\langle B_r \right\rangle$ as well as $\left\langle B_\phi \right\rangle$. The generation terms for $\left\langle B_\theta \right\rangle$ (not shown) possess a similar structure, with FT_θ dominating the other terms by a factor of $\sim$5.

The fluctuating transport is similar in spirit to the α-effect from mean-field theory, which represents the emf caused by the helical action of convection on the magnetic field. In this respect, the fourfold-wreath cycle is characteristic of an $\alpha\Omega$ dynamo. However, our simulations are distinct

from most mean-field dynamo models in that the generation of both meridional field and azimuthal field occurs in the same location in the CZ, with the meridional circulation playing essentially no role. This stands in contrast to the flux-transport paradigm, in which the α-effect creates meridional field at high latitudes that is then pumped deep into the CZ by the meridional circulation to seed the Ω-effect in the following cycle.

4.8.2 Dynamics of the Partial-Wreath Cycle

The physical mechanisms responsible for the system transitioning between the fourfold-wreath and partial-wreath states remain unclear. Nevertheless, we can understand the maintenance of the dynamo during the partial-wreath state in terms of the dominant induction terms. Furthermore, even though the partial-wreath structure is inherently non-axisymmetric, it is sufficient to perform a mean-field analysis—i.e., identify the dominant longitudinally averaged induction terms of Equations (4.5) and (4.9). Since the longitudinally averaged field $\langle B_\phi \rangle$ has the same polarity as the dominant partial wreath, there is a one-to-one correspondence between cycles in $\langle B_\phi \rangle$ and partial-wreath cycles.

The mean-field generation terms during the partial-wreath cycle vary rapidly in space and time. Therefore, significant spatial and temporal averaging must be performed to extract a meaningful signal. Figure 4.20 shows the spatially-averaged contributions to the production of $\langle B_\phi \rangle$ in case D3-1 from the mean shear (which is clearly dominant) and the other terms, as well as $\langle B_\phi \rangle$ itself, during the interval of partial-wreath cycling depicted in Figure 4.10. All three profiles are roughly sinusoidal. The profile of mean-shear production slightly leads the profile of $\langle B_\phi \rangle$ in time, indicating that the rise and fall of $\langle B_\phi \rangle$ is directly caused by the mean-shear production. The contribution from the other induction terms (which are dominated by the resistive dissipation) is $\sim 180^\circ$ out-of-phase with $\langle B_\phi \rangle$, meaning the magnetic diffusion attempts to destroy whatever field is already there.

The production of $\langle \boldsymbol{B}_\mathrm{m} \rangle$ (which in turn affects the production of $\langle B_\phi \rangle$ through mean-shear) is highly chaotic in time during the partial-wreath cycle, and so instead of plotting the production

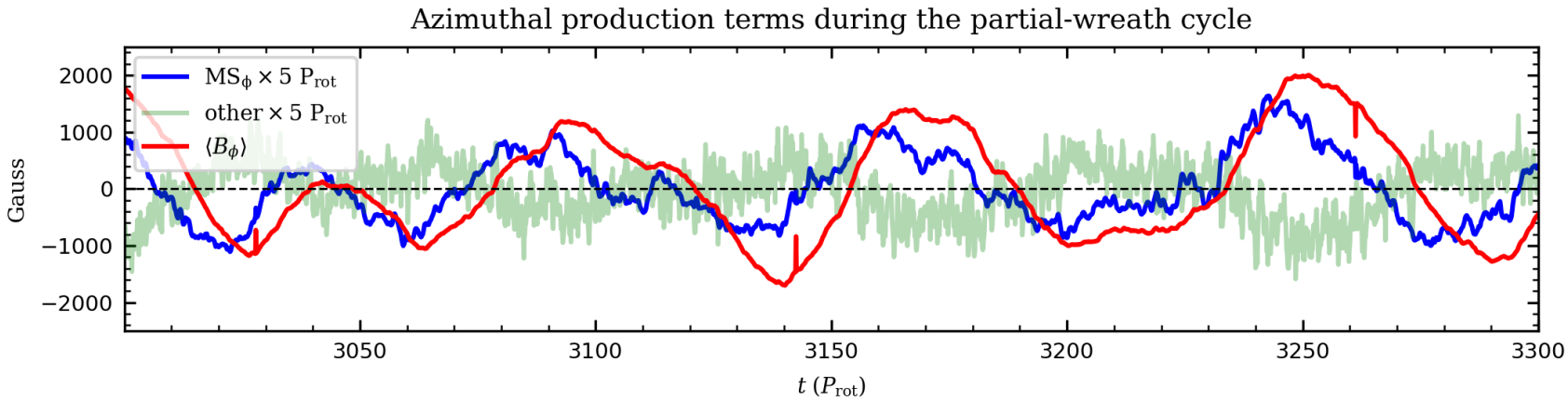

Figure 4.20: **Inductive Generation of Partial Wreaths during a Cycle**. The dominant generation terms appearing in Equation (4.9), as well as $\langle B_\phi \rangle$, when the partial-wreath structure is cycling in the South, during the same interval shown in Figure 4.10). Quantities are averaged over radius and between 0° and 20°-south in latitude. The generation terms are broken up into mean-shear and "other" (i.e., $\partial \langle B_\phi \rangle / \partial t - \mathrm{MS}_\phi$) and multiplied by 5 $P_{\rm rot}$ to put them on the same scale as $\langle B_\phi \rangle$. The contribution to "other" dominated by the resistive dissipation.

terms in Equation (4.9) as functions of time, we simply quote their temporally-averaged magnitudes below. Just as in the fourfold-wreath cycle, the dominant term producing $\langle \boldsymbol{B}_{\rm m} \rangle$ is the fluctuating emf:

$$(\mathrm{FT_r})_{\rm rms} = 9.3\ (\mathrm{MT_r})_{\rm rms} \tag{4.10}$$

$$(\mathrm{FT_r})_{\rm rms} = 2.6\ (\mathrm{RD_r})_{\rm rms} \tag{4.11}$$

at mid-depth, where the mean is taken over the time interval (3000, 3300) $P_{\rm rot}$ and the latitude band between 0° and 20°-south. Similar relationships hold for the production of $\langle B_\theta \rangle$, which is also dominated by the fluctuating emf

4.9 Bistability in the Context of Solar Observations

Continuous, full-disc observations of the photospheric magnetic field, produced by MDI/SOHO and HMI/SDO, have greatly constrained certain features of the solar dynamo and have yielded a number of surprises. Stenflo & Kosovichev (2012) analyzed a large set of MDI magnetograms from 1995–2011 and found that Joy's law (which states that emerging sunspot pairs are tilted on average such that the leading spot is closer to the equator, and that the tilt is proportional to heliographic latitude) holds for active regions both large and small. Furthermore, there was no observed dependence of tilt angle on total active-region flux (or region area), implying that the tilts were inherent to buoyant flux ropes in the solar interior. This stands in contrast to the argument that the tilts are established by the Coriolis force as the flux ropes rise through the CZ (e.g., D'Silva & Choudhuri 1993; Fan et al. 1994).

The view that the interior flux ropes are associated with a preferred sense of tilt is interesting in light of the fourfold-wreath cycle. Each of the fourfold wreaths possesses a particular sense of twist as in Figure 4.18(a). If loops were to spontaneously break off from the wreaths (this does not occur in our simulations because the magnetic diffusivity is too high), they would be endowed with a tilt from the twisting magnetic field lines in the wreath. Nelson et al. (2013b) achieved the separation of magnetic loops from interior wreaths and found that the sample of loops reaching the

surface made contact with Joy's law. This supports the idea that a fourfold-wreath-like structure in the Sun could establish systematic tilts associated with flux ropes in the deep interior.

Stenflo & Kosovichev (2012) further reported that a statistically significant fraction of active regions (5%–25%, depending on the region's size) violate Hale's polarity law, strongly suggesting that there must be multiple reservoirs of interior magnetism from which buoyant flux ropes originate. Additionally, the "anti-Hale" active regions could appear in the same latitude band as "Hale" active regions, suggesting close proximity in latitude for the reservoirs. This result agrees with the geometry of both the fourfold-wreath structure (whose wreaths come in opposite-polarity pairs with wreaths in a pair separated in latitude by $\sim 15^\circ$) and the partial-wreath structure (with opposite-polarity partial wreaths at approximately the same latitude).

Li (2018) performed another extensive analysis of sunspot groups from 1996–2018 using both the MDI and HMI magnetograms, also reporting that a sizeable fraction ($\sim 8\%$) of sunspot pairs violate Hale's polarity law and confirming the result obtained by Stenflo & Kosovichev (2012). In addition, Li (2018) found that the anti-Hale sunspots had different properties than Hale sunspots, namely, smaller bipole separation and weaker total magnetic flux. These results further support the idea that the Hale and anti-Hale sunspots may come from different interior reservoirs.

It is also possible that the anti-Hale active regions form an essential part of the solar dynamo. Hathaway & Upton (2016) find that modeling the flux transport of active regions observed by SDO during the current solar cycle can be used to predict the amplitude and hemispheric asymmetry of the following cycle. Central to such predictions is the initial distribution of active-region tilts, which would be significantly modified by the presence of anti-Hale active regions. Although it is unlikely that the real interior solar magnetic field matches the fourfold-wreath and partial-wreath structures in detail, such configurations offer two ways in which violations of Hale's polarity law could occur.

We now discuss the asymmetric features of solar activity, many of which are captured by the partial-wreath cycle. For well over a century, sunspots have been observed to emerge preferentially at particular solar longitudes (e.g., Maunder 1905; Svalgaard & Wilcox 1975; Bogart 1982; Henney

& Harvey 2002). This phenomenon, referred to as *active longitudes*, remains poorly understood.

It is common for active longitudes to come in pairs, separated by about 180° in longitude (e.g., Bai 2003). The pairs are also usually found in a single hemisphere and are part of the global *hemispheric asymmetry* in magnetic activity. Finally, the pairs may be associated with opposite polarity of the azimuthal magnetic field on opposite sides of the Sun, as suggested by synoptic maps from the Wilcox Solar Observatory (Mordvinov & Kitchatinov, 2004). Thus, it is possible that the pairs are associated with nests of Hale and anti-Hale active regions on opposite sides of the Sun, although a systematic study of the MDI/HMI magnetograms would be needed to confirm this result.

Active longitudes and their associated hemispheric asymmetry bear a striking resemblance to the partial-wreath structure in our simulated dynamos. The partial wreaths preferentially occupy one hemisphere at a time. They come in opposite-polarity pairs, with the strongest magnetism on opposite sides of the sphere (see the Mollweide projection in Figure 4.2(b) and the 3-D volume-renderings in Figure 4.11). The time-longitude diagrams for the partial wreaths in case D3-1 (Figure 4.12) show that each wreath is roughly stationary once an appropriate rotating frame is chosen, similar to the quasi-rigid structure formed by active-longitude pairs in the Carrington reference frame (Berdyugina & Usoskin, 2003).

Figures 4.11 and 4.12 would also indicate cyclic behavior, in which the strongest active longitude flips by about 180° over the partial-wreath cycle period. Berdyugina & Usoskin (2003) reported such behavior in observations of solar sunspot number, wherein the active longitudes appeared to flip between opposite sides of the Sun every ∼3.7 years, or every ∼53 solar Carrington rotations. Our simulation suite displays similar properties in the relative energy content of the partial wreaths (Figure 4.13), showing that the dominant partial wreath switches with a quasi-regular period of 81.5 $P_{\rm rot}$.

The hemispheric asymmetry in solar activity can be seen in a wide variety of activity indicators, such as number of flares, sunspot number, sunspot area, and photospheric magnetic flux (e.g., Schüssler & Cameron 2018 and references therein). Many studies have been performed on

the periodic behavior of the asymmetry, with most agreeing on a long-term period of ∼50 years and a short-term period of ∼10 years (see Hathaway 2015 and reference therein). Our simulations each possess a significant hemispheric asymmetry (Figure 4.14(a)), although there is no obvious associated cycle (Figure 4.14(b)). Nevertheless, our simulations make contact with observations in that the hemispheric asymmetry occurs as a long-term modulation of another cycle, which in our simulations is that of the partial wreaths.

In summary, the dynamo cases presented here show similarities to several features of solar activity, namely, the sunspot cycle, opposite-polarity magnetic regions in close proximity, active longitudes, and hemispheric asymmetry. We do not suggest that all these observed features of the Sun's activity are a result of fourfold-wreath and partial-wreath structures existing in the solar CZ. Rather, our simulations provide insights as to how a solar-like convection zone can support dynamos exhibiting a wide range of cyclic behavior.

4.10 Conclusions

We have explored three dynamo simulations of a 3-D, solar-like convection zone at varying magnetic Prandtl number. These dynamo cases display clear signs of bistability. In particular, there is a fourfold-wreath structure that exhibits equatorward propagation and regular polarity reversals. There is also a single-hemisphere partial-wreath pair that is roughly stationary and whose whose dominant polarity changes cyclically, but with an irregular period. The fourfold-wreath cycle captures aspects of the 22-year sunspot cycle (namely, the solar butterfly diagram), whereas the partial-wreath cycle is reminiscent of several of the observed features of active longitudes and hemispheric asymmetry.

We have examined the dynamics of the fourfold-wreath cycle in detail, and find they are approximately described by an $\alpha\Omega$ dynamo. The mean shear, or Ω-effect, is responsible for the generating the wreaths. The regular polarity reversals and equatorward propagation are caused by the inherent geometry of the wreaths (namely the meridional field winding counterclockwise for positive B_ϕ and clockwise for negative B_ϕ) coupled to a solar-like differential rotation. Generation

of the meridional field occurs through the fluctuating emf, which is similar to an α-effect, but fully nonlinear. Both effects occur in the same localized region of the CZ (with the meridional circulation playing basically no role), unlike in the flux-transport dynamo framework. As a whole, the production terms for the fourfold-wreath cycle are similar to those of model "K3S" of Augustson et al. (2015), although in that work, significant modulation of the differential rotation played a large role, whereas in our dynamo cases, the differential rotation stays mostly constant with time.

The partial-wreath cycle has longitudinally averaged dynamics similar to an $\alpha\Omega$ dynamo as well, but it is not fully clear how the system transitions between the regularly cycling fourfold-wreaths and the single-hemispheric partial-wreath pair. It is possible that the transition is governed by the fourfold-wreath structure changing between equatorially symmetric and antisymmetric states, but more work needs to be done to assess in detail how such a mechanism operates. Equatorial parity also played a key role in model K3S, wherein atypical dominance of the radial magnetic field by the even-ℓ modes acted as a precursor to the cycling dynamo entering a "grand minimum." Similarly, in the global convective dynamo simulation of Raynaud & Tobias (2016), the interaction of hydromagnetic modes with different symmetries led to transitions between distinct cycling dynamo states. The magnetic Prandtl number also may be significant in determining whether the system is unstable to the partial-wreath state; Nelson et al. (2013a) found magnetic structures resembling single-hemisphere partial-wreaths in their high-$\mathrm{Pr_m}$ simulations but not low-$\mathrm{Pr_m}$.

Our work suggests that spherical-shell convection can support complex dynamos capable of exhibiting vastly different global structures for the magnetism simultaneously. In particular, the bistable properties of our dynamo cases are consistent with a solar dynamo containing two cycles at once: one associated with the observed butterfly diagram and one associated with active longitudes and hemispheric asymmetry. We recognize that our simulations here are just beginning to explore the complexities that might be at work in the highly nonlinear and turbulent dynamics of the Sun. The range of scales that we can capture and the diffusivities we use are still far removed from the solar regime. However, we have found that some reasonable large-scale behavior emerges from our dynamo models, and these may broaden our insights into the physical processes occurring deep

within the interior of the Sun.

4.11 Definitions of Non-Dimensional Numbers and Diffusion Times

After the example of Featherstone & Hindman (2016b), we parameterize the strength of the imposed driving through a bulk "flux Rayleigh number,"

$$\mathrm{Ra_F} \equiv \frac{\tilde{g}\tilde{F}H^4}{c_\mathrm{p}\tilde{\rho}\tilde{T}\nu^3}, \tag{4.12}$$

where H is the shell depth and F is the energy flux associated with the combined conduction and convection in a statistically steady state. The tildes refer to volume-averages over the full spherical shell.

We parameterize the degree of rotational constraint through a bulk Rossby number,

$$\mathrm{Ro} \equiv \left(\widetilde{\frac{v'}{2\Omega_0 H_v}} \right), \tag{4.13}$$

where the typical velocity $v'(r)$ refers to the rms of the convective ($|m| > 0$) velocity over a sphere of radius r. The typical length-scale of the flow structure $H_v(r)$ is not well-represented by either the scale height or the shell depth. Instead, we choose $H_v(r)$ based on the power spectrum of the convective velocity. Specifically, $H_v(r) \equiv 2\pi r/\ell_v(r)$, where $\ell_v(r) \equiv \sum_{|m|>0} \ell |\hat{\boldsymbol{v}}_{\ell m}|^2$ and $|\hat{\boldsymbol{v}}_{\ell m}|^2$ refers to the normalized (ℓ, m)-power associated with $\boldsymbol{v}$ at radius r. We similarly define a spectral length-scale $H_B(r)$ associated with the convective magnetic-field structures.

We assess the level of turbulence through a volume-averaged Reynolds number,

$$\mathrm{Re} \equiv \left(\widetilde{\frac{v' H_v}{\nu}} \right) \tag{4.14}$$

and a volume-averaged magnetic Reynolds number,

$$\mathrm{Re_m} \equiv \left(\widetilde{\frac{v' H_B}{\eta}} \right), \tag{4.15}$$

We define the thermal diffusion time (which is equal to the viscous diffusion, time since Pr = 1) as

$$\mathrm{TDT} = \frac{(r_\mathrm{o} - r_\mathrm{i})^2}{\kappa(r_\mathrm{o})} = 115\ P_\mathrm{rot}, \tag{4.16}$$

which is the same for all four cases.

We define the magnetic diffusion time as

$$\mathrm{MDT} = \frac{(r_\mathrm{o} - r_\mathrm{i})^2}{\eta(r_\mathrm{o})} = 115,\ 230,\ 460\ P_\mathrm{rot} \tag{4.17}$$

for cases D3-1, D3-2, and D3-4, respectively.

Chapter 5

Confinement of the Solar Tachocline by Dynamo Action in the Radiative Interior

The helioseismically inferred tachocline (why it is observed to be so thin, at $\sim 0.05 R_\odot$) is an outstanding fundamental mystery of solar physics. Spiegel & Zahn (1992) (hereafter SZ92) first recognized that the tachocline should have "radiatively spread" to a thickness of (at minimum) ~ 0.4 $R_\odot$ by the current age of the Sun (see Section 5.1). To remain consistent with the helioseismic deductions, there must be a torque that forces the radiative interior to remain in solid-body rotation and prevents radiative spread. Various tachocline confinement scenarios postulate the origin of this torque (for reviews, see, e.g., Gilman 2000a; Miesch 2005; Brun & Strugarek 2019; and references therein). The two most commonly invoked confinement mechanisms are the "fast HD scenario" of SZ92 (the confining torque is caused by HD instabilities and operates on the fast dynamical time-scale; see Section 5.2) and the "slow MHD scenario" of Gough & McIntyre (1998) (the confining torque is caused by a primordial magnetic field and operates on the slow meridional-circulation time-scale; see Section 5.3). As described in the following Sections, much work has been done to assess the validity of each of these confinement scenarios. Significant progress has been made in identifying many of the waves, instabilities, and dynamo processes present in the tachocline, but the origin of the confining torque is still an open question.

The parameter space in which radiative spread occurs is not currently accessible by global simulations (e.g., Brun et al. 2011; Wood & Brummell 2012, 2018; and references therein; also see Table 5.1). Because global simulations have greatly enhanced turbulent diffusions, however, the

tachocline still spreads viscously. As described in Chapter 1, most prior work employing global simulations has focused on the influence of an imposed or transient tachocline on the dynamo, generally by artificially lowering the viscosity below the convection zone. No global model we are aware of has been demonstrated to achieve tachocline confinement against the inevitable viscous spread by a self-consistently generated torque. In this Chapter (Sections 5.4–5.10), we present a global `Rayleigh` simulation that achieves differential rotation in the convection zone coexisting with solid-body rotation in the radiative interior. This shear layer, which we call a "tachocline," remains in a statistically steady state for many viscous diffusion times. The magnetic torque from a self-excited dynamo forces the radiative interior into solid-body rotation and prevents the viscous imprinting of the convection zone's differential rotation.

Our work supports the hypothesis that magnetism is responsible for solid-body rotation in the solar radiative interior, but postulates a very new form and origin of this magnetism. In contrast to the primordial magnetic-field remnant originally envisioned in the slow scenario, the confining magnetic fields in our simulation are primarily non-axisymmetric (similar to the partial-wreath structures just encountered in Chapter 4), and are also oscillating in time. The more fundamental difference, however, is that the magnetism in our MHD case is maintained *inductively*, even below the layer of convective overshoot. The induction is caused by strong horizontal motions, which we argue represent inertial oscillations, and are likely excited by the pummeling of convective downflows from above. This work thus hints that the Sun's "stable" radiative interior may be a dynamically active region that can amplify magnetic field and significantly affect the operation of the global dynamo.

The MHD case presented in this Chapter is the first fully 3-D, nonlinear, global simulation that has been shown to achieve dynamics similar to a magnetic confinement scenario. Aspects of our MHD case—namely, strong horizontal velocities and magnetic fields below the overshoot layer—have been frequently encountered in prior simulations, but have not been recognized to be the result of an active dynamo, and have not been shown to confine a tachocline. In Section 5.9.,We discuss these similarities between our MHD case and prior work. In Section 5.10, we discuss how

our work offers a new perspective on the solar tachocline. We assess the likelihood that the solar dynamo penetrates deep into the radiative interior and whether it might confine the tachocline against radiative spread. We conclude by offering some future directions global simulations might take to fully address the solar tachocline confinement problem.

This Chapter is based on work currently being prepared for an upcoming publication, Matilsky et al. (2022) and was briefly described in the conference proceedings paper, Matilsky & Toomre (2021). As the primary author of the paper, I conducted the simulations, performed their analyses, created most of the Figures (with the exception of the two final Figures by Catherine Blume), and wrote the text. My coauthors Juri Toomre, Bradley Hindman, Nicholas Featherstone, and Catherine Blume provided (and likely will continue to provide) advice and guidance throughout the process, gave detailed text edits, and suggested schematic designs of some of the figures. Special thanks is owed to Mark Miesch for his explanation of the Gough-and-McIntyre model (slow confinement scenario) and to Nicholas Brummell and Pascale Garaud for their explanation of the phenomenon of radiative spread.

5.1 Radiative Spread of the Solar Tachocline

SZ92 imagine the solar radiative interior as a non-magnetic (HD) ball of ideal gas, with the convection zone at the top imposing its differential rotation as a boundary condition. Initially, the radiative interior is assumed to rotate like a solid body (at rate $\Omega_{\rm RI}$), except for a thin boundary layer of shear at the top, which represents the tachocline. The tachocline has initial thickness h_0 and radial location r_0 (helioseismically, $h_0 \approx 0.05 R_\odot$ and $r_0 \approx 0.72 R_\odot$; see Section 1.1.2). SZ92 assume a thin tachocline, or $h_0/r_0 \ll 1$. They also consider a laminar fluid, hydrostatic and geostrophic thermodynamic perturbations (here we call this "thermal wind balance," following the terminology of Chapter 3), strong rotational constraint (as defined in this thesis, low Ekman and Rossby numbers), weak differential rotation, axisymmetry, and the Boussinesq approximation (specifically, the Boussinesq equations in the form of Spiegel & Veronis 1960). Under these assumptions, SZ92 argue that the tachocline naturally spreads via two distinct processes: viscous diffusion and radiative

thermal diffusion. SZ92 note that in the Sun, the molecular thermal conductivity can be neglected compared to the radiative thermal conductivity. SZ92 ultimately find that radiative spread should dominate viscous spread in the solar tachocline, and furthermore, that unless radiative spread were prevented, the tachocline would be much thicker than is helioseismically observed.

Viscous tachocline spread is simple to understand. The convection zone above drags the radiative interior with it via viscous forces, and the convection zone's differential rotation thus imprints downward. Through viscous spread, the tachocline boundary layer should grow like $t^{1/2}$, where t is the time since the tachocline was initially confined. Furthermore, viscous spread should take place on the viscous diffusion time-scale.

Radiative spread is conceptually more complicated. Unlike viscosity, thermal diffusion does not directly torque the radiative interior; instead, it induces a meridional circulation that transports angular momentum via advection. In brief, thermal wind balance implies that the differential rotation is always coupled to the horizontal pressure gradient (through geostrophic balance), which in turn is coupled to the horizontal temperature gradient (through hydrostatic balance). There is thus an equator-to-pole temperature contrast in the top layers of the radiative interior, which rotate differentially, and no such temperature contrast in the deeper layers, which rotate like a solid body. The equator-to-pole temperature contrast must then spread inward via radiative diffusion. As the temperature in the radiative interior changes, buoyancy forces will drive a meridional circulation that ultimately stops the diffusive spread and establishes an advection-diffusion balance of heat. This circulation also advects angular momentum in a manner that imprints the differential rotation inward. Because the meridional circulation always closely balances radiative diffusion, the spreading process is *not* diffusive and does not occur on the thermal diffusion time-scale. Spiegel & Zahn (1992) instead find that radiative spread occurs on the Eddington-Sweet time-scale $t_{\rm ES}$ and is "hyperdiffusive:" The temperature gradient, meridional circulation, and differential rotation are expected to burrow inward like $t^{1/4}$.

The two diffusive spreading processes can be summarized by the following angular-momentum

equation, paraphrased from Spiegel & Zahn (1992):

$$\frac{\partial \Omega'}{\partial t} \approx -\left(\frac{r_0^4}{t_{\rm ES}}\right)\frac{\partial^4 \Omega'}{\partial r^4} + \left(\frac{r_0^2}{t_{\rm visc}}\right)\frac{\partial^2 \Omega'}{\partial r^2}, \tag{5.1a}$$

$$\text{where} \qquad t_{\rm ES} \equiv \frac{N^2}{4\Omega_{\rm RI}^2}\left(\frac{r_0^2}{\kappa}\right) \qquad \text{and} \qquad t_{\rm visc} \equiv \frac{r_0^2}{\nu} \tag{5.1b}$$

are the Eddington-Sweet and viscous diffusion times across the radiative interior, respectively. Here κ and ν denote the radiative diffusivity and molecular viscosity of the Sun, respectively. The buoyancy frequency is defined through $N^2 = (g/c_{\rm p})d\overline{S}/dr$ and Ω' denotes the deviation of the angular velocity from the solid-body rate $\Omega_{\rm RI}$. The first term on the right-hand side of Equation (5.1a) represents the radiative spread of the tachocline and the second term represents the viscous spread. Note that the radiative diffusivity κ acts on the temperature gradient, not the entropy gradient. Otherwise, the notation in Equations (5.1) is identical to that of the rest of this thesis (compare to Equations (1.1)).

We note that although the time-scale $t_{\rm ES}$ shows up in the phenomenon of radiative-spread, the meridional circulation invoked is *not* the classical Eddington-Sweet (or Eddington-Vogt-Sweet) circulation (Vogt, 1924; Eddington, 1925; Sweet, 1950). The Eddington-Sweet circulation arises in rotating stellar radiative interiors because even small oblateness causes heating of gas by photons to depend slightly on latitude (von Zeipel, 1924). Because the equatorial regions are "puffed out" in a rotating star, the radial temperature gradient and absorbed radiative flux are smaller, and the equator is heated less rapidly than the poles. The only way the star can maintain thermodynamic equilibrium is if a weak meridional circulation transports heat from pole to equator. Simple considerations reveal that the required circulation overturns on a time-scale of $\sim t_{\rm ES}$. In the solar tachocline, the meridional circulation is also generated by a pole-to-equator temperature contrast, but this contrast comes from the convection zone's thermal wind, not the oblateness. The circulation cells are highly elongated in latitude (they occupy the thin tachocline in SZ92's theory) and have a circulation time of $\sim (h_0/r_0)^4 t_{\rm ES}$. In the context of the tachocline, $t_{\rm ES}$ thus does not represent a circulation time, but rather the time it takes the circulation itself to burrow all the way to the solar core via radiative spread.

Clark (1973) was the first to note the competition between viscosity and meridional circulation in transporting angular momentum. He considered a cylinder of initially uniformly rotating stably stratified fluid subject to a time-varying rotation rate applied at the outer boundary. In the linear calculations, the changing boundary condition induced a meridional circulation in a thermal boundary layer whose thickness grew hyperdiffusively as $t^{1/4}$. Advection of angular momentum by this circulation caused the rotation rate imposed at the outer boundary to burrow inward at the same hyperdiffusive rate. Overall, these results were remarkably similar to SZ92's theory of radiative spread. Haynes et al. (1991) obtained similar results on fast (though not strictly hyperdiffusive) downward burrowing of circulations in the Earth's middle atmosphere. Since these initial theoretical calculations, the burrowing of meridional circulation has been identified as a robust phenomenon in simulations of rotating, stably stratified convection (e.g., Elliott 1997; Garaud & Brummell 2008; Garaud & Acevedo-Arreguin 2009; Wood & Brummell 2012, 2018).

We list the Sun's diffusions at the base of the convection zone (including the magnetic diffusivity η, for completeness) in Table 5.1. We also list other relevant solar parameters (most importantly, the diffusive time-scales) and the corresponding parameters in the MHD case (with a tachocline) that we discuss in the following sections. We note the parameters chosen for our MHD case, although they are unique, are typical of all global simulations we are aware of. In particular, global simulations have Prandtl numbers of order unity and diffusivities (explicit in the case of, e.g., `Rayleigh` and `ASH`, and implicit in, e.g., the `EULAG-MHD` cases) many orders of magnitude higher than in the Sun. From Table 5.1, the time-scale $t_{\rm visc}$ for viscous spread of the solar tachocline is greater than the Eddington-Sweet time-scale $t_{\rm ES}$ for radiative spread. Both time-scales are much longer than the age of the Sun (4.6 billion years), but radiative spread is still significant because the meridional circulation burrows faster than the diffusive rate. In the MHD case, the viscous time-scale is significantly shorter than the Eddington-Sweet time-scale. The viscous spread thus dominates and the computations cannot be run long enough for radiative spread to be significant.

Because of the competition between viscous and radiative tachocline spread, the defining parameter of a given star or simulation measures the ratio of the Eddington-Sweet time to the

Table 5.1: **Diffusive Time-Scales in the Radiative Interior of the Sun and Our MHD Case**. Here we list the numerical values associated with the diffusive processes (viscous, radiative, and magnetic) relevant for the Sun and our MHD case (with a tachocline) discussed in this Chapter. The quoted values are at the base of the convection zone (or equivalently, the top of the radiative interior). Note that since the MHD case covers only a spherical shell (not the whole Sun) the depth of its radiative interior ($H \equiv r_{\rm ov} - r_{\rm i}$, where $r_{\rm ov}$ is the base of the convective overshoot layer and $r_{\rm i}$ is the inner boundary of the simulated shell) is smaller than the solar value, r_0. The molecular diffusivity values for the base of the solar convection zone are quoted from Brandenburg & Subramanian (2005) (ν and η) and Hindman et al. (2020) (κ), who in turn derived them from the statistical physics considerations of Landau et al. (1998) and Spitzer (1962), respectively. All quantities are considered to have two significant figures.

Parameter	**Solar Value**	**MHD Case Value**
Depth of radiative interior (H)	5.0×10^{10} cm (also r_0)	1.6×10^{10} cm
Rotation frequency $\left(\frac{\Omega_{\rm RI}}{2\pi}\right)$	430 nHz	1400 nHz
Buoyancy frequency $\left(\frac{N}{2\pi}\right)$	0.19 mHz	0.19 mHz
Viscosity (ν)	10 cm^2 s^{-1}	1.1×10^{12} cm^2 s^{-1}
Viscous diffusion time $\left(t_{\rm visc} \equiv \frac{H^2}{\nu}\right)$	7.9×10^{12} years	7.4 years
Thermal conductivity (κ)	10^7 cm^2 s^{-1}	1.1×10^{12} cm^2 s^{-1}
Eddington-Sweet time $\left(t_{\rm ES} \equiv \left[\frac{N}{2\Omega_{\rm RI}}\right]^2 \frac{H^2}{\kappa}\right)$	3.9×10^{11} years	3.4×10^4 years
Magnetic diffusivity (η)	10^4 cm^2 s^{-1}	2.8×10^{11} cm^2 s^{-1}
Magnetic diffusion time $\left(t_{\rm mag} \equiv \frac{H^2}{\eta}\right)$	7.9×10^9 years	29 years
Prandtl number ${\rm Pr} \equiv \frac{\nu}{\kappa}$	10^{-6}	1
Magnetic Prandtl number ${\rm Pr_m} \equiv \frac{\nu}{\eta}$	10^{-4}	4
$\sigma \equiv \sqrt{\frac{t_{\rm ES}}{t_{\rm visc}}} = \frac{N}{2\Omega_{\rm RI}}\sqrt{\rm Pr}$	0.22	68

viscous diffusion time. This quantity, first identified in Garaud & Brummell (2008) and Garaud & Acevedo-Arreguin (2009), is defined through

$$\sigma \equiv \sqrt{\frac{t_{\rm ES}}{t_{\rm visc}}} = \frac{N}{2\Omega_{\rm RI}}\sqrt{\frac{\nu}{\kappa}} = \frac{N}{2\Omega_{\rm RI}}\sqrt{\rm Pr}. \tag{5.2}$$

As would be intuitively expected, Garaud & Brummell (2008) and Garaud & Acevedo-Arreguin (2009) found that radiative spread is significant only for $\sigma < 1$. Prior global simulations had $\sigma = O(100)$ (e.g., Brun & Zahn 2006; Rogers 2011; Strugarek et al. 2011a,b) and so could not assess radiative spread. These results were further supported by the 2-D global models of Acevedo-Arreguin et al. (2013) (including both a radiative interior and simplified convection zone) and the fully 3-D, fairly turbulent local simulations of Wood & Brummell (2012, 2018).

The low-σ regime is currently rather difficult for global simulations to achieve. The ratio $N/2\Omega_{\rm RI} = 200$ in the Sun, and so simulations could either lower the level of stable stratification in the radiative interior (since $N \sim \sqrt{d\overline{S}/dr}$) or run at low Prandtl number, say, Pr $\sim 10^{-5}$. [1] The stable entropy gradient should not be lowered too far below the solar value, since the overshoot layer would grow unrealistically large, and the mixing properties of the overshoot would be unrealistic (e.g., Hurlburt et al. 1986, 1994; Brummell et al. 2002; Korre et al. 2019; Korre & Featherstone 2021). Very low Prandtl number achieved by very low viscosity is difficult because of the fine spatial resolution it would require. Finally, there is not much leeway to lower the Prandtl number by increasing the thermal diffusion; the sub-grid-scale thermal diffusion is usually already quite high, and if raised by a factor of 10 or so, it would prevent convection entirely.

5.2 Tachocline Instabilities and the Fast Confinement Scenario

SZ92 proposed a tachocline confinement scenario in the form of strongly anisotropic turbulence in the radiative interior. The very stable stratification implies effectively 2-D motions, which, if turbulent, could mix fluid in the horizontal directions much more efficiently than the vertical

[1] The other option—greatly increase the rotation rate—is generally undesirable since it would cause unrealistic levels of rotational constraint. It also causes numerical problems due to the small scales introduced—see, e.g., Featherstone & Hindman 2016b; Hindman et al. 2020.

(Zahn, 1974, 1992). SZ92 thus proposed that anisotropic turbulence could homogenize angular velocity in latitude below the convection zone, keeping the radiative interior rotating like a solid body and maintaining the tachocline. The homogenization would occur on the fast dynamical time-scale of the instabilities (hence, "fast" confinement scenario; see, e.g., Gilman 2000a for the origin of the "slow" and "fast" terminology). Anisotropic transport was nominally expected from the theory of geostrophic turbulence (e.g., Rhines 1979) and might be produced by shear instabilities in the tachocline due to the high Reynolds number of the horizontal shear (Zahn, 1975). Other than these speculations, however, SZ92 did not identify the instabilities that might lead to turbulence.

Since SZ92, substantial work has been done to characterize the instabilities that may occur in the tachocline. Charbonneau et al. (1999a) analyzed the linear shear instability of an inviscid, incompressible fluid on a 2-D spherical surface. They performed analysis following the instability criteria for rotating stars laid out in Watson (1981) and Dziembowski & Kosovichev (1987), finding that the tachocline's shear was stable to any perturbation. However, the shear was very close to the marginal value required for instability onset and it was argued that small differences in the helioseismic inversions of the tachocline's radial location were consistent with instability. For example, the horizontal shear at $r/R_\odot = 0.75$ (only slightly higher than the nominal location of the tachocline, $r/R_\odot = 0.72$) was shown to induce the instability of low-azimuthal-order modes ($m = 1, 2, 3$), with growth rates on the order of years.

Charbonneau et al. (1999a) also noted that there were marginally stable solutions (neither growing nor decaying) with oscillation periods varying continuously between the equatorial and polar rotation rates. These solutions could be interpreted as Rossby waves (waves with a Coriolis restoring force) in critical layers.[2] Critical layers are regions bounded by turning points in latitude where the Rossby-wave frequency equals the background rotation frequency. Nonlinear behavior of critical-layer Rossby waves has been studied extensively for shear flows in the context of meteorology (e.g., Killworth & McIntyre 1985; Haynes 1989) and stellar astrophysics (e.g., Watson

[2] These critical-layer Rossby waves have also been described as "baroclinic" waves and instabilities (e.g., Gilman 1967a,b,c,d; Braginsky & Roberts 1975; McIntyre 1970, 1998; Gilman & Dikpati 2014).

1981). Usually it is found that the waves become unstable in the presence of maxima in potential vorticity (potential vorticity is the dot product of vorticity and the background stratification; in our notation, it would be $\omega_r d\overline{S}/dr$, where ω_r is the radial vorticity $(\nabla \times \boldsymbol{v})_r$; see, e.g. Gilman & Dikpati 2014). The waves then nonlinearly evolve into strong spiral structures that eventually break within the critical layer and locally smooth out the potential vorticity, driving the system back toward marginal stability.

Garaud (2001) considered the weakly nonlinear regime of the tachocline's shear instability explored by Charbonneau et al. (1999a). She found that once again the $m = 1, 2, 3$ modes were the only unstable ones, and also confirmed the interpretation of the unstable perturbations as breaking critical-layer Rossby waves. The system ultimately reached a state of marginal instability that depended slightly on the chosen initial rotation profiles and relative amplitudes of the initial $m = 1, 2, 3$ perturbations. In general, however, the final state had an angular momentum profile deviating by no more than $\sim$0.2% from the initial state. Garaud (2001) thus concluded that the tachocline was effectively in a state of marginal stability with respect to shear, and that shear instabilities were unlikely to cause significant angular momentum transport.

Dikpati & Gilman (2001a,b) analyzed the tachocline's shear instability using a "shallow-water" formalism (e.g., Pedlosky 1987; Gilman 2000b), in which weak vertical motions are allowed so long as they conserve mass. They found that in the upper part of the tachocline (the overshoot layer, where the stable stratification is weakest), shear instabilities could lead to significant angular momentum transport. Furthermore, the instabilities were associated with a net pattern of kinetic helicity. Dikpati (2012) continued this analysis in the fully nonlinear regime, largely confirming the linear results and showing that the lowest-order ($m = 1, 2$) modes were the most unstable. She also confirmed the presence of net kinetic helicity and proposed that the upper layers of the tachocline could generate an α-effect, thereby driving the solar dynamo entirely from within the tachocline.

Garaud (2020) and Cope et al. (2020) presented the first investigations of 3-D shear instabilities and their mixing properties in non-rotating, non-magnetic Cartesian-box simulations representing a local region of the tachocline. They found that in the regime appropriate for the

Sun (low Prandtl number and high Péclet number—where the advection of heat dominates the diffusion of heat), shear instabilities induced substantial vertical mixing in addition to horizontal mixing. The results were thus incompatible with SZ92's strongly anisotropic mixing. However, Garaud (2020) noted that the presence of rotation, magnetism, and compositional stratification would probably alter the character of the identified shear instabilities, including their mixing properties.

Significant work has also been done to characterize the tachocline's magneto-shear, or magneto-rotational, instability (e.g., Gilman & Fox 1997; Dikpati & Gilman 1999; Gilman 2000b; Dikpati et al. 2003; Dikpati & Gilman 2005; Miesch 2007; Gilman & Dikpati 2014; Lawson et al. 2015; Gilman 2018a,b). These investigations suggested that the presence of toroidal fields in the tachocline can destabilize latitudinal shear that would otherwise be stable in a purely hydrodynamic system. Long-wavelength (low m) disturbances were once again identified as the most unstable, with $m = 1, 2$ modes resulting from broad toroidal wreaths (wide in latitude and radius) and modes with m as high as 7 resulting from narrow toroidal wreaths. The $m = 1, 2$ modes in particular were argued by Dikpati & Gilman (2005) to be a potential origin of the observed active longitudes discussed in Chapter 4.

Lawson et al. (2015) argued for the presence of magneto-shear instabilities occurring in their global, 3-D `EULAG-MHD` simulations. They further proposed that these instabilities "pumped" magnetic field downward and may have influenced the global dynamo cycle. Notably, Lawson et al. (2015) attributed strong horizontal velocities to magneto-shear instabilities, which may have supported the anisotropic turbulence required by the fast confinement scenario. Gilman (2018a,b) examined joint magnetic buoyancy and magneto-shear instability in the solar tachocline with values of the horizontal and vertical shear taken from helioseismology. He found that vigorous instabilities induced by weak toroidal fields in high-m modes would mostly prevent the storage of toroidal wreaths at high latitudes. Low latitudes, by contrast, were found to not only be stable to shear, but also be stable to the magnetic buoyancy instability until the field strengths rose to very high amplitudes ($\sim$10 kG). He thus argued that the shear profile of the tachocline may yield a new explanation for the appearance of sunspots at low latitudes.

We finally note that Zahn et al. (1997) and Kumar & Quataert (1997) proposed a fast confinement scenario by the breaking of prograde and retrograde gravity waves. These waves would have their frequencies, and thus dissipation rates, shifted due to differential rotation near the base of the convection zone. There could thus be a latitudinal gradient in the wave-field's local dissipation rate, which could redistribute angular momentum to maintain solid-body rotation on the time-scale of $\sim 10^7$ years (still "fast" compared to the Eddington-Sweet time-scale of $\sim 10^{12}$ years). Talon et al. (2002) carried this analysis further, finding that gravity-wave breaking could extract angular momentum from the deep radiative interiors of low-mass stars and could possibly lead to a slowly rotating core. As of now, however, the angular-momentum transport properties of gravity waves in a 3-D, nonlinear context are unknown. The only global simulations dedicated to characterizing stellar gravity waves in detail were the `ASH` models of Alvan et al. (2014, 2015). They found that a rich spectrum of gravity modes was excited by overshooting convection. They identified the driving mechanism of the waves, computed their eigenspectra in the context of theoretical ray-tracing formalism (e.g., Gough 1993), and examined other properties like mode lifetimes and nonlinear propagation patterns. Although angular momentum transport was not computed explicitly, this work highlighted the need to study gravity waves in 3-D spherical geometry using global simulations.

5.3 The Slow MHD Tachocline Confinement Scenario

Gough & McIntyre (1998) (hereafter GM98) argued that the fast tachocline scenarios were unlikely to hold up in the solar interior. They agreed that instabilities in the presence of strong stable stratification may induce essentially 2-D geostrophic turbulence. However, they noted that geostrophic turbulence in the Earth's atmosphere was known to drive the system away from uniform rotation, not toward it (McIntyre, 1994). In the atmospheric sciences, this effect had been called "negative viscosity" and was well documented (e.g., Starr 1968 and references therein). Similarly, GM98 argued that the torques from dissipating gravity waves were not known to suppress shear (Gough, 1977) and should (like geostrophic turbulence) enhance it (Plumb & McEwan, 1978; Andrews et al., 1987; McIntyre, 1994).

GM98 thus proposed a confinement scenario wherein a tachocline-confining torque could be generated by an axisymmetric poloidal magnetic field in the radiative interior, presumed to be a primordial remnant from the Sun's birth. As the differential rotation burrowed inward, the poloidal field (which was assumed to be stationary, confined from above by the meridional circulation) would create a toroidal field. According to Ferraro's law of isorotation (Ferraro, 1937), the associated magnetic-tension torque would force isorotation contours to fall on poloidal field lines (with solid-body rotation as a special case) and could stop the burrowing. The magnetic torque would react on the long time-scale associated with radiative spread, namely, the Eddington-Sweet time (hence, "slow" confinement scenario),

The idea that a large-scale magnetic field could significantly affect the differential rotation in stellar radiative interiors was not new (e.g., Ferraro 1937; Alfvén 1943; Cowling 1957). After the work of Ferraro (1937), there was much debate on whether radiative interiors might rotate like solid bodies if magnetism were present. This debate began well before the discovery of the tachocline (e.g., Chandrasekhar 1956; Tassoul & Tassoul 1986; Mestel & Weiss 1987; Mestel et al. 1988). In presenting the slow confinement scenario, however, GM98 were unique in making the strong (paraphrased) statement: "To reconcile the thin tachocline revealed by helioseismology with the theory of radiative spread, there *must* be a primordial magnetic field in the radiative interior."

GM98 derived the linear magnetic-boundary-layer equations for solar tachocline confinement, including the proposed poloidal magnetic field in the angular-momentum equation as a Lorentz torque. The toroidal field was assumed to arise from a balance between mean shear (the Ω-effect mentioned in Chapter 1) and magnetic diffusion. In the slow confinement theory, the amplitude of the poloidal field set the thickness of the tachocline. From the helioseismic constraints, GM98 estimated a fairly weak field ($\sim$1 G) would be enough to produce a tachocline width of $\sim 0.02 R_\odot$. This result largely agreed with the earlier work of Mestel & Weiss (1987), who proposed that differential rotation in the radiative interior was possible only if the magnetic field did not exceed $\sim$0.03 G. Mestel & Weiss (1987)'s value of the field could be so small (and still induce solid-body rotation) because it was not required to confine the shear to a thin layer.

Since these boundary-layer calculations, much work has been done to assess the slow scenario under more realistic conditions. Garaud (2002) and Garaud & Garaud (2008) presented axisymmetric (2-D), nonlinear models of an isolated radiative interior (with the convection zone's differential rotation applied as a top boundary condition) containing a primordial magnetic field. Garaud (2002) found that the slow scenario was achieved only for a narrow range of poloidal field amplitudes and Garaud & Garaud (2008) showed that prior assessments of the slow scenario (e.g., Brun & Zahn 2006) did not reproduce the dynamics of a slow confinement scenario likely because of inappropriate boundary conditions applied at the top of the radiative interior. Acevedo-Arreguin et al. (2013) presented the first global numerical simulation of a slow scenario in 2-D, including the full radiative interior and convection zone with simplified nonlinear convective dynamics. They found that the slow scenario could at least be qualitatively reproduced, but only for the correct parameter space ($\sigma \ll 1$, and also small absolute magnitudes of the diffusive coefficients). Other global attempts to model the slow scenario in 3-D (Brun & Zahn, 2006; Strugarek et al., 2011a,b) had likely yielded null results because of the sampled parameter regime (e.g., $\sigma > 1$), not the failure of the slow scenario.

Finally, Wood & Brummell (2018) presented the first 3-D, fully nonlinear, moderately turbulent, self-consistent simulation of tachocline confinement in a local Cartesian box. They ensured the correct ordering of time-scales: even though the simulation was far from an astrophysical parameter regime, the Eddington-Sweet time was significantly shorter than the viscous diffusion time ($\sigma < 1$) and radiative spread was clearly shown to occur. Wood & Brummell (2018) largely confirmed the results of Acevedo-Arreguin et al. (2013) in showing that a 3-D version of the slow scenario was possible in the right parameter regime. Furthermore, they found that the meridional flow could confine the primordial magnetic field to the stable layer, even amidst 3-D turbulence. This was interesting in light of the 3-D global simulations of Brun & Zahn (2006) and Strugarek et al. (2011a,b), in which the primordial field would not stay confined to the radiative interior.

We briefly remark that in addition to the slow confinement scenario, Forgács-Dajka & Petrovay (2001) proposed a "fast magnetic scenario." Similar to GM98, the tachocline confine-

ment was imagined to occur via a magnetic torque. The requisite poloidal field, however, diffused inward from the cycling dynamo in the convection zone above. This torque would thus respond to the burrowing meridional circulation on the time-scale of the solar cycle, i.e., ∼22 years. As long as a large magnetic diffusivity was assumed (turbulently enhanced, presumably by MHD instabilities), an oscillating poloidal field imposed at the top of the radiative interior could confine the tachocline against radiative spread (for more details, see Forgács-Dajka & Petrovay 2001, 2002; Forgács-Dajka 2004; Barnabé et al. 2017).

5.4 Numerical Experiment

We consider 3-D, global, nonlinear `Rayleigh` simulations of a solar-like star that includes a convection zone coupled to a radiative interior. We simulate both a hydrodynamic (HD) case and a magnetohydrodynamic (MHD) case using `Rayleigh 1.0.1` (Featherstone & Hindman, 2016a; Matsui et al., 2016; Featherstone et al., 2021).[3] This shell captures most of the solar convection zone ($0.72R_\odot$ to $r_\mathrm{o} \equiv 0.95R_\odot$ by radius) and part of the underlying radiative interior ($r_\mathrm{i} \equiv 0.49R_\odot$ to $0.72R_\odot$ by radius). As in our other models, each case has a solar luminosity driven through the layer via internal heating in the convection zone only. Each model rotates at three times the solar Carrington rate, $3\Omega_\odot$, where $\Omega_\odot = 2.87 \times 10^{-6}$ rad s^{-1}. Each model has stress-free, impenetrable, and fixed-flux boundary conditions, and the MHD case has potential-field-matching boundary conditions.

As in Chapter 4, the diffusivities $\nu(r)$, $\kappa(r)$, and $\eta(r)$ vary with radius like $\overline{\rho}(r)^{-1/2}$. They do not approach very low values in the radiative interior, as has usually been implemented in previous work for the purpose of delaying tachocline spread. The thermal Prandtl number ($\mathrm{Pr} \equiv \nu/\kappa$) is unity (as always), and in the MHD case, the magnetic Prandtl number ($\mathrm{Pr_m} \equiv \nu/\eta$) is 4. At the top of the domain, $\nu(r_\mathrm{o}) = \kappa(r_\mathrm{o}) = 5 \times 10^{12}$ cm^2 s^{-1} and $\eta(r_\mathrm{o}) = 1.25 \times 10^{12}$ cm^2 s^{-1}. Except for the addition of the stable layer and slightly higher diffusions, the HD and MHD cases are identical

[3] In this version of `Rayleigh`, the bug mentioned in Chapter 4 that affected simulations with radially varying $\eta(r)$ was fixed.

to cases H3 and D3-4 (respectively) discussed in Chapter 4. Both our Prandtl numbers are of order unity, in contrast to the very low Prandtl numbers in the solar interior (Table 5.1). We choose $\mathrm{Pr} = 1$ largely to remain consistent with our earlier work. We do note that lower thermal Prandtl numbers (e.g., $\mathrm{Pr} = 1/4$) in early `ASH` and recent `Rayleigh` models seem to produce more turbulent and vortical convective structures (e.g., Brun & Toomre 2002; Miesch et al. 2006; Brown et al. 2008, 2010, 2011; Orvedahl et al. 2018; Bice & Toomre 2020) and more recently have been shown to yield "patchy" active nests of convection that significantly affect the global dynamo cycles and may produce active longitudes (Bice & Toomre, 2022). Higher magnetic Prandtl number is more conducive to dynamo action since large-scale vortical motions can induct strong magnetic fields that take a long time to diffuse away. We explored a range of magnetic Prandtl numbers ($\mathrm{Pr_m} =$ 1/2, 1, 2, 4, and 8) and found that all cases with $\mathrm{Pr_m} \geq 2$ led to magnetic tachocline confinement. The confinement was most pronounced for $\mathrm{Pr_m} = 4$.

We simulate a combined stable radiative interior and unstable convection zone by choosing the appropriate background entropy gradient. In the convection zone, this background gradient is set to zero, as in the models from all previous Chapters. The combined effects of internal heating near the bottom and conductive cooling near the top force convection, which establishes a slightly superadiabatic entropy gradient in the perturbations. In the radiative interior, the background entropy gradient, which is constant in space, is strongly subadiabatic: $d\overline{S}/dr \equiv \beta = 0.01$ erg g^{-1} K^{-1} cm^{-1}. The "stiffness" β is thus roughly the same as the solar stiffness at the base of the convection zone.[4] We match the entropy gradient from its convection-zone value (0) to its radiative-interior value (β) over a transition width of $\sim 0.05 R_\odot$. A detailed description of the models, including the background state, is given in the supplementary Section 5.11. Also see Table 5.1 for the diffusive time-scales.

The HD case is initialized from a small thermal field ($\hat{S} \sim 10$ erg g^{-1} K^{-1}) randomly distributed throughout the whole shell) and run to an equilibrated state, which we define as the time

[4] The solar entropy gradient, of course, varies with radius (see Brun et al. 2011; his Figure 3) and is concave-down, which yields a resonant cavity for trapped gravity modes. One consequence of choosing constant $d\overline{S}/dr$ in our simulations' radiative interiors is that our gravity-mode cavities have the wrong lower turning point; i.e., the waves reflect off the impenetrable inner boundary, instead of becoming evanescent when the buoyancy frequency becomes low enough. Our gravity-wave spectrum for the MHD case is shown in Figure 5.12.

interval following the volume-integrated kinetic energy reaching statistically steady values in the radiative interior. We define "equilibrated" in this way because it takes longer to achieve a steady state in the radiative interior than in the convection zone. The MHD case is initialized identically to the HD case, but with a small magnetic field (amplitude ∼1 G; randomly distributed throughout the *convection zone only*) in addition to the thermal field. In the MHD case, the magnetic field exponentially grows through dynamo action to amplitudes of ∼10 kG (in the radiative interior, the seed field first spreads downward diffusively, but is amplified there by dynamo action as well). We define the MHD case's equilibrated state as the time interval following the volume-integrated magnetic energy reaching statistically steady values in the radiative interior. Note that the MHD case (since it operates a dynamo) is not really in *equilibrium* per se. Rather, the magnetic field fluctuates significantly (both in topology and amplitude) about a stationary mean state.

We run the HD case in its equilibrated state for 26.5 viscous diffusion times across the radiative interior (equivalently, 8200 rotations). This ensures that the viscosity has ample time to imprint the differential rotation all the way through the shell. We run the MHD case for 10.6 magnetic diffusion times across the radiative interior (equivalently, 13100 rotations, or 42.4 viscous diffusion times). This ensures that the tachocline achieved in the MHD case is in good torque balance (magnetic torque fighting viscous torque) and furthermore, that the MHD case's dynamo becomes fully saturated. The MHD simulation covers ∼25 dynamo cycles, as discussed in Section 5.7. The diffusion times are defined and evaluated in Table 5.1.

To distinguish between different parts of the spherical shell, we define two critical radii, which we mark in all applicable figures: the base of the convection zone ($r_{\rm bcz} = 0.73 R_\odot$; solid black curves in the figures) and the base of the overshoot layer ($r_{\rm ov} = 0.71\ R_\odot$; dashed green curves in the figures). Following Brun et al. (2011), we define the convection zone as the region in which the convective heat flux (enthalpy flux; $\mathcal{F}_{\rm enth}$) is positive (i.e., outward). We thus define the two critical radii such that below $r_{\rm bcz}$, $\mathcal{F}_{\rm enth}$ becomes negative (i.e., inward) and below $r_{\rm ov}$, $\mathcal{F}_{\rm enth}$ approaches zero. Specifically, the base of the overshoot layer is defined to be where $\mathcal{F}_{\rm enth}$ becomes 5% of its minimum value achieved in the overshoot layer; this also corresponds to the location where the

vertical convective velocities drop by $\sim 10^2$. We call $r > r_{\rm bcz}$ the "convection zone," $r < r_{\rm ov}$ the "radiative interior," and $r_{\rm ov} < r < r_{\rm bcz}$ the "overshoot layer." Under the same definitions, the HD case's overshoot layer is slightly deeper than the MHD case's, extending from $0.70 R_\odot$ to $0.73 R_\odot$; the vertical convective velocities drop by $\sim 10^3$ in the HD case's overshoot layer.

5.5 Solid-Body Rotation in the MHD Case's Radiative Interior

Figures 5.1(a,b) show the rotation-frequency profiles for the HD and MHD cases (respectively), plotted in the (r, θ)-plane. The rotation frequency has been averaged in longitude and in time over each case's equilibrated state. In the HD case, the differential rotation in the convection zone has diffusively imprinted onto the entire radiative interior, as should be expected from prior work in the high-σ regime (e.g., Miesch 2005; Garaud & Acevedo-Arreguin 2009; Brun et al. 2011; Acevedo-Arreguin et al. 2013; Brun et al. 2017; Guerrero et al. 2019).

In the MHD case, however, the radiative interior sustains near-solid-body rotation, while the convection zone rotates differentially. We call the shear layer between the convection zone and radiative interior in the MHD case a "tachocline." However, we emphasize that in the convection zone, the differential rotation in our MHD case differs from the solar differential rotation (and from the differential rotation in the HD case, which is quite solar-like) in several ways. First, the rotation contrast is too small by a factor of ~ 5 compared to the observed solar value. Second, most of the MHD case's differential rotation is at low latitudes, unlike the Sun, which has strong shear at high latitudes as well. Third, the MHD case has a noticeably banded average rotation profile, which is non-monotonic in latitude.[5] Overall, the tachocline achieved in our MHD case is quite similar to that of the `EULAG-MHD` "millennium simulation" (Passos & Charbonneau, 2014; Lawson et al., 2015) and that of the `EULAG-MHD` "case RC01" (Guerrero et al., 2016a, 2019). This Chapter is

[5] The Sun technically has a banded differential rotation during any given sunspot cycle due to the torsional oscillations. This effect comes in the form of a $\sim$3–4 nHz "fast band" in each hemisphere that migrates equatorward with the solar cycle (e.g., Howe 2009). Relative to the solar differential rotation contrast ($\sim$80 nHz between equator and 60°), this is a $\sim$5% effect, which is actually the same order of magnitude as in our MHD case (from Figure 5.1(c), we can estimate a fast band of $\sim$5 nHz, which is a $\sim$10% effect compared to the differential rotation contrast). Our MHD case is still different than the Sun, however, because the *temporally averaged* differential rotation is banded, whereas the Sun's is latitudinally monotonic.

focused on understanding the mechanism by which solid-body rotation is maintained in our MHD case and confined to the radiative interior. We leave the full tachocline confinement problem (i.e., how solid-body rotation could be maintained alongside a solar-like differential rotation profile in the convection zone) to future work.

Figure 5.1(c) shows the rotation profile in the MHD case as a function of radius for different latitudes. To quantify the thickness of the tachocline, we define the radially varying latitudinal rotation contrast $\Delta\Omega(r)$ as the difference in rotation rate between the equator and 60° latitude at the fixed radius r. In the HD case, $\Delta\Omega(r)/\Omega_0 \sim 0.2$ throughout the whole shell (similar in magnitude to the solar value). By contrast, $\Delta\Omega(r)$ for the MHD case is drastically lower in the radiative interior than in the convection zone. Explicitly, the MHD case has $\Delta\Omega(r)/\Omega_0 = 4 \times 10^{-2} \equiv \Delta\Omega_{\rm CZ}/\Omega_0$ at the top of the convection zone and $\Delta\Omega(r)/\Omega_0 = 7 \times 10^{-4} \equiv \Delta\Omega_{\rm RI}/\Omega_0$ at the bottom of the radiative interior. In describing the MHD case, we arbitrarily define the base of the tachocline ($r_{\rm tach} = 0.64\ R_\odot$; dotted red curves in the figures) as the location where $\Delta\Omega(r)$ has dropped by a factor of 20 from its value at the top of the convection zone. We define the top of the tachocline as $r_{\rm ov}$, so the tachocline occupies $(r_{\rm tach},\, r_{\rm ov}) \equiv (0.64R_\odot,\, 0.71R_\odot)$ by radius.

The convective-velocity and magnetic-field amplitudes for the equilibrated MHD case are shown in Figure 5.2. Below the overshoot layer, the vertical components of $\boldsymbol{v}'$ and $\boldsymbol{B}'$ are dwarfed by the horizontal components. The plunge in vertical velocity (Figure 5.2(a)) is a consequence of the stable stratification. Specifically, v_r' falls by ∼2 orders of magnitude across the overshoot layer and by ∼5 orders of magnitude across the whole radiative interior. Because of the anelastic approximation, this means that the flows are not only horizontal, but almost completely divergenceless (i.e., incompressible). The convective horizontal velocity field is thus determined almost entirely by the convective radial vorticity ω_r', which acts essentially like a streamfunction for the horizontal flow. As was discussed in Sections 5.1–5.3, such purely vortical flows have been expected from early theoretical considerations (e.g., Charbonneau et al. 1999b; Garaud 2001; Dikpati & Gilman 2001a,b) and have likely been present in global numerical simulations as well (e.g., Brun et al. 2011; Lawson et al. 2015; Guerrero et al. 2016a; Bice & Toomre 2020).

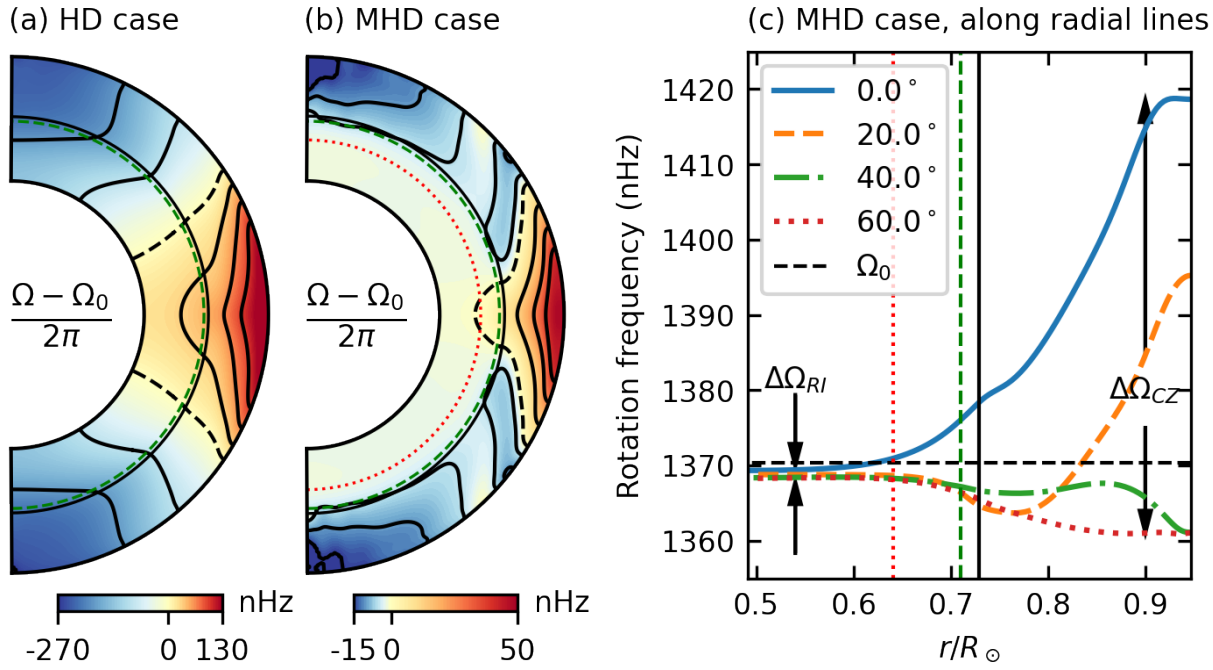

Figure 5.1: **A Simulated Radiative Interior Magnetically Forced into Solid-Body Rotation.** (a) Level surfaces (contours) of $(\Omega - \Omega_0)/2\pi$ in the HD case, plotted in the meridional plane. Negative values are normalized separately from positive values, so that there are three equally spaced positive and negative contours each (solid contours). The zero contour $\Omega = \Omega_0$ is dashed. (b) Like (a), but for the MHD case. (c) Rotation frequency $\Omega/2\pi$ at different latitudes along radial lines in the MHD case. The rotation contrasts in the convection zone and radiative interior are marked by vertical arrows; the frame rotation frequency $\Omega_0/2\pi$ is marked by the horizontal dashed line. In all panels, the solid black, dashed green, and dotted red curves (vertical lines in panel (c)) refer to $r_{\rm bcz}$, $r_{\rm ov}$, and $r_{\rm tach}$, respectively.

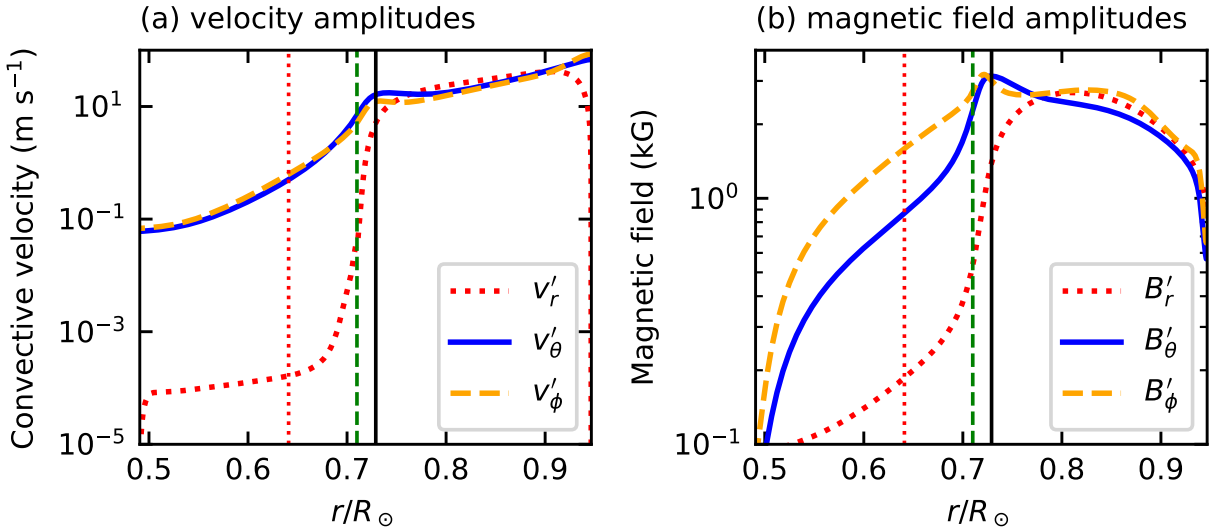

Figure 5.2: **Flow and Field Strengths in the MHD case.** (a) Rms of the convective velocity (full velocity with the longitudinal mean subtracted). The mean is taken in time over the equilibrated state and over spheres of radius r. Each component (r, θ, and ϕ) is plotted separately, as shown in the legend. (b) Same as (a), but for the convective magnetic field. In both panels, the locations $r_{\rm bcz}$, $r_{\rm ov}$, and $r_{\rm tach}$, are marked by vertical lines as in Figure 5.1.

From Figure 5.2(b), the vertical component of the magnetic field B_r' also declines in the radiative interior, but more gradually than v_r'. It falls by a factor of $\sim$50 from mid-convection zone ($\sim 0.84 R_\odot$) to the base of the overshoot layer. In the very deep radiative interior, though not quite in the overshoot layer or tachocline, B_r' can be neglected and the magnetic field is well characterized by its horizontal components. Figure 5.3 shows this horizontal field at the base of the overshoot layer at an instant during the equilibrated state (specifically, the very end of the simulation run, $t = 16050$ rotations). We note that both field components are largely non-axisymmetric, mainly composed of spherical-harmonic orders $m = 1, 2$. At the particular instant sampled by Figure 5.3, $m = 1$ dominates. After the explorations of Chapter 4, we call these structures partial wreaths, although we note that here $m = 2$ structures are present in addition to $m = 1$.

In general, B_ϕ is slightly stronger than B_θ and more concentrated near the equator. There is clearly some correlation between the two horizontal field components within the partial wreaths. As shown in Figure 5.3(c), the product $B_\theta B_\phi$ is mostly positive in the North and negative in the South. This correlation (as discussed in the next Section 5.6) indicates that (1) the toroidal field B_ϕ is generated primarily from the poloidal field B_θ via mean shear and (2) the resulting Lorentz force from bent poloidal field lines sends angular momentum poleward (which shows up in Figure 5.3 as the preferred sign structure of the product $B_\theta B_\phi$). The poleward angular-momentum transport tends to eliminate the latitudinal shear.

5.6 Dynamical Maintenance of the MHD Case's Tachocline

As mentioned in Section 5.4, the solid-body rotation in the MHD case's radiative interior has been sustained for over 10 magnetic diffusion times (40 viscous diffusion times) across the radiative interior. This means that the system, on average, must be in dynamical torque balance, with zero net torque on the system. We note that the torque balance (and the inductive balance we discuss next) only applies to the system over a long temporal average that encompasses multiple dynamo cycles. As shown in the following Section 5.7, this system is running a cycling dynamo with period of a few hundred rotations. The magnetic fields and differential rotation thus change slowly in time;

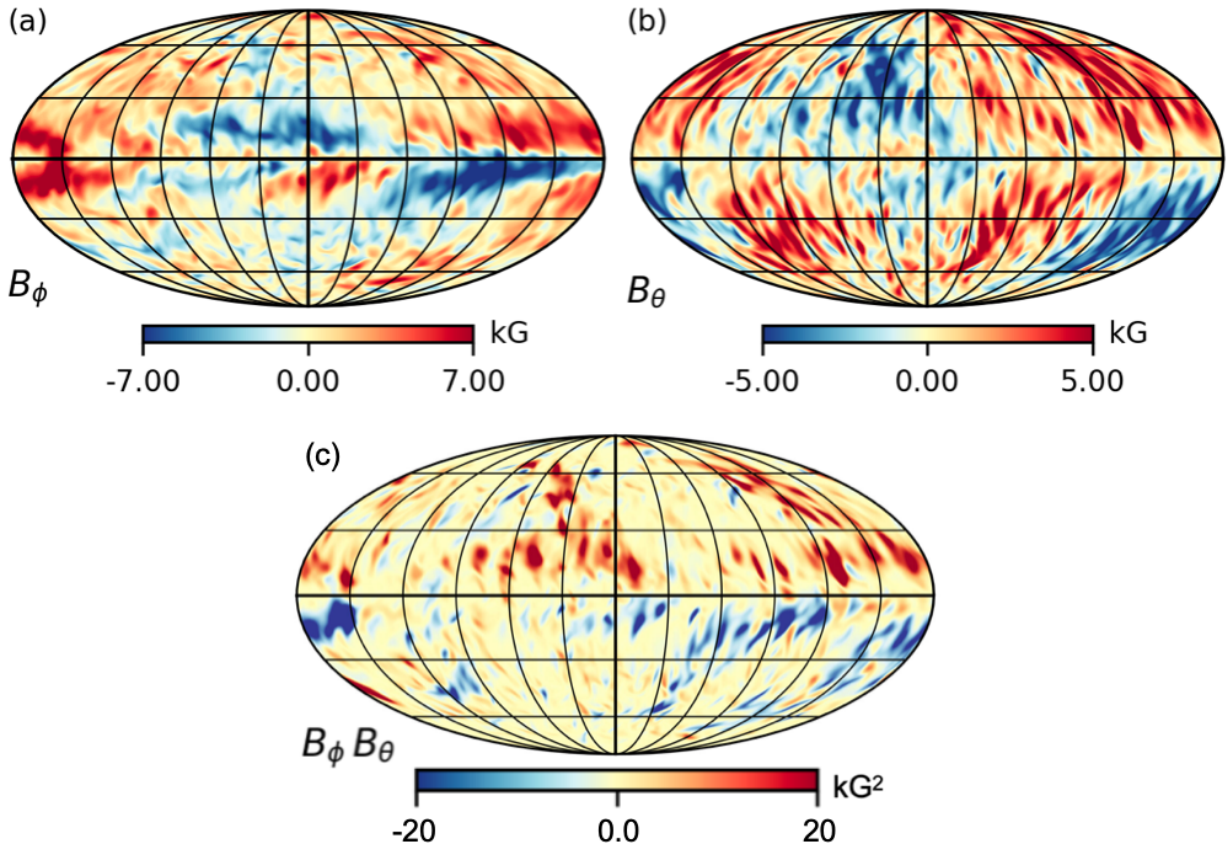

Figure 5.3: **Non-Axisymmetric Partial Wreaths Forcing Solid-Body Rotation.** Snapshots during the MHD case's equilibrated state of (a) B_ϕ, (b) B_θ, and (c) their product, $B_\phi B_\theta$. Each snapshot is plotted in full Mollweide view on a spherical surface at the base of the overshoot layer, $r_{\rm ov}/R_\odot = 0.71$. The snapshot is taken at the end of the simulation run, namely, $t = 16050$ rotations.

during a particular dynamo cycle, there may be a net torque, but the average torque approaches zero after several dynamo cycles.

In the MHD case's tachocline, the torques are primarily viscous and magnetic:

$$\tau_{\rm v} + \tau_{\rm mag} \equiv \underbrace{\nabla \cdot [\overline{\rho}\nu r^2 \sin^2\theta \nabla\Omega]}_{\text{viscous torque } (\tau_{\rm v})} + \underbrace{\frac{1}{4\pi}\nabla \cdot [r\sin\theta \langle B_\phi \boldsymbol{B}_{\rm pol}\rangle]}_{\text{magnetic torque } (\tau_{\rm mag})} \approx 0, \tag{5.3}$$

where $\boldsymbol{B}_{\rm pol} \equiv B_r\hat{\boldsymbol{e}}_r + B_\theta\hat{\boldsymbol{e}}_\theta$ is the poloidal magnetic field and the form of each torque is derived in Miesch & Hindman (2011). Also recall Chapter 2, Equation (2.4). The angular brackets denote a combined longitudinal and temporal average (this combined average is also implied by Ω, which is defined as $\langle v_\phi\rangle / r\sin\theta + \Omega_0$). In the `Rayleigh` code, longitudinal averages are calculated by taking the full 3-D snapshot of the flows in the spherical shell and averaging over all longitudinal collocation points (or equivalently, by taking the $m = 0$ component of the discrete Fourier transform of the field in ϕ). In general, we output these longitudinal-average snapshots every $\sim$1 rotation (although the sampling is non-uniform due to the variable time-step). The temporal averages are then computed by averaging together the ten thousand or so longitudinal-average snapshots. The system is run in its "equilibrated state" for $\sim$25 dynamo cycles; as more and more cycles are included in the average, the total torque approaches zero.

We note that the magnetic torque can be interpreted as the tension force associated the poloidal magnetic field lines bent in the toroidal direction. Since we employ this result frequently in the following discussion, we derive it here. The magnetic torque is obtained simply by multiplying the toroidal Lorentz force (longitudinally and temporally averaged) by the moment arm $r\sin\theta$:

$$\tau_{\rm mag} = \frac{r\sin\theta}{4\pi}\langle[\underbrace{(\nabla\times\boldsymbol{B})\times\boldsymbol{B}}_{\text{MHD Lorentz force}}]_\phi\rangle \tag{5.4a}$$

$$= \frac{r\sin\theta}{4\pi}\langle(\underbrace{\boldsymbol{B}\cdot\nabla\boldsymbol{B}}_{\text{toroidal magnetic tension force}})_\phi\rangle \tag{5.4b}$$

$$= \frac{1}{4\pi}\langle\underbrace{\boldsymbol{B}_{\rm pol}\cdot\nabla(r\sin\theta B_\phi)}_{\text{tension torque from bent poloidal field lines}}\rangle \tag{5.4c}$$

$$= \underbrace{\frac{1}{4\pi}\nabla\cdot[r\sin\theta\langle B_\phi\boldsymbol{B}_{\rm pol}\rangle]}_{\text{magnetic torque from Equation (5.3)}} \tag{5.4d}$$

In deriving these expressions, we have used (in order) the identity $(\nabla\times\boldsymbol{B})\times\boldsymbol{B} = \boldsymbol{B}\cdot\nabla\boldsymbol{B} - (1/2)\nabla B^2$, the expression for $\boldsymbol{B}\cdot\nabla\boldsymbol{B}$ in spherical coordinates, and the solenoidal field condition $\nabla\cdot\boldsymbol{B} = 0$. Throughout these manipulations, we have dropped terms that do not survive a longitudinal average, like $(\nabla B^2)_\phi$, which is a perfect derivative with respect to ϕ. The magnetic torque is thus interpreted as either the torque from the magnetic-tension force, $\langle(\boldsymbol{B}\cdot\nabla\boldsymbol{B})_\phi\rangle$, or equivalently (as derived in Miesch & Hindman 2011 and presented in Equation (5.3)), as the divergence of the angular momentum flux, $(r\sin\theta/4\pi)\langle B_\phi\boldsymbol{B}_{\rm pol}\rangle$.

The torque balance in the MHD case is shown in Figure 5.4. See Equation (2.4) for the definitions of the three non-magnetic torques (in our MHD case, the meridional-circulation torque plays very little role all throughout the shell). This balance is dominated by the torques from the Reynolds stress (defined and discussed at length in Chapter 2), magnetic tension, and viscosity, which we show in the meridional plane in Figures 5.4(a,b,c), respectively. In the convection zone, the torque balance is similar to previous HD simulations (e.g., Hotta et al. 2015; Matilsky et al. 2019; see Chapters 2 and 3). The Reynolds stress maintains a solar-like differential rotation outside the tangent cylinder (cylinder circumscribing the radiative interior) by spinning up the fluid far from the rotation axis and slowing down the fluid close to the rotation axis. The convection zone's viscous and magnetic torques both work to counter the Reynolds stress. Magnetic torque in simulated convection zones quenching the differential rotation is a common occurrence and why it happens is still an open question (e.g., Browning 2008; Yadav et al. 2015; Lawson et al. 2015; Yadav et al. 2016; Guerrero et al. 2016a; Bice & Toomre 2020, 2022). As was discussed in Chapter 4, the differential-rotation quenching is most pronounced at higher magnetic Prandtl number, which may be due to the growing dominance of small-scale magnetism over convection (Bice & Toomre, 2022).

In the tachocline (Figure 5.4(d)), viscosity works to imprint the differential rotation from above by spinning up the equator and slowing down the mid-latitude regions. However, the imprinting is almost completely halted by the magnetic torque. The same viscous imprinting occurs in the HD case, but because there is no other substantial torque on the system, the differential rotation in the convection zone successfully drags the radiative interior along with it (Figure 5.1a).

We have separately confirmed that the magnetic torque in the MHD case's tachocline is primarily due to the correlation between horizontal field components $B_\phi B_\theta$ (see Figure 5.3), with the other correlation $B_\phi B_r$ playing a lesser role.

As discussed in Section 5.3, magnetic confinement scenarios for the solar tachocline follow arguments similar to those invoked in Ferraro's law of isorotation. Here we illustrate how Ferraro's law extends to our MHD case, which is dominated by non-axisymmetric partial wreaths. We closely follow the arguments laid out in Mestel & Weiss (1987). Differential rotation (nonzero $\nabla\Omega$) will bend poloidal magnetic field lines to produce a toroidal field through mean shear. This is expressed through the toroidal component of the magnetic induction equation, which, if mean shear dominates the other induction terms, takes the form

$$\frac{\partial B_\phi}{\partial t} \approx \underbrace{r\sin\theta \boldsymbol{B}_{\rm pol}\cdot\nabla\Omega}_{\text{mean shear}} \underbrace{-\{\nabla\times[\eta(r)\nabla\times\boldsymbol{B}]\}_\phi}_{\text{toroidal diffusion}}. \tag{5.5}$$

See Section 5.11.2, Equation (5.15a) for a full derivation. Here we define the mean-shear term (the Ω-effect) as the axisymmetric differential rotation bending the *non-axisymmetric* poloidal magnetic field. Equation (5.5) yields $B_\phi \approx (r\sin\theta \boldsymbol{B}_{\rm pol}\cdot\nabla\Omega)t_{\rm bend}$ (we ignore the diffusion in this illustration), where $t_{\rm bend}$ is the time-scale over which the bending occurs. From Equation (5.3), the associated torque due to magnetic tension is $\nabla\cdot[r^2\sin^2\theta\langle\hat{\boldsymbol{e}}_{\rm pol}B_{\rm pol}^2\nabla_{\rm pol}\Omega\rangle]t_{\rm bend}$, which tends to eliminate gradients in Ω parallel to $\boldsymbol{B}_{\rm pol}$. Here, $\hat{\boldsymbol{e}}_{\rm pol}\equiv\boldsymbol{B}_{\rm pol}/|\boldsymbol{B}_{\rm pol}|$ is the unit vector in the direction of $\boldsymbol{B}_{\rm pol}$ and $\nabla_{\rm pol}\equiv\hat{\boldsymbol{e}}_{\rm pol}\cdot\nabla$ is the derivative in the direction of $\boldsymbol{B}_{\rm pol}$. When magnetic tension is dominant, the equilibrium state will require $\langle\hat{\boldsymbol{e}}_{\rm pol}\nabla_{\rm pol}\Omega\rangle = 0$. For an axisymmetric poloidal magnetic field, this reduces to $\langle\boldsymbol{B}_{\rm pol}\rangle\cdot\nabla\Omega = 0$, which is the original Ferraro's law. However, a non-axisymmetric field is more restrictive, since the direction $\hat{\boldsymbol{e}}_{\rm pol}$ changes with longitude. For $\hat{\boldsymbol{e}}_{\rm pol}\nabla_{\rm pol}\Omega$ to average to zero, the most likely solution is $\nabla_{\rm pol}\Omega = 0$ everywhere—i.e., solid-body rotation.[6]

Figure 5.5(a) shows the production toroidal magnetic energy in the MHD case's radiative

[6] More specifically, the bending time-scale $t_{\rm bend}$ is the time it takes an Alfvén wave—with speed v_A determined by the *poloidal* magnetic field, i.e., $v_A^2 = |\boldsymbol{B}_{\rm pol}|^2/4\pi\overline{\rho}$—to traverse a distance long enough that Ω changes substantially. Mestel & Weiss (1987) showed that when these Alfvén waves dissipate, gradients in Ω will ultimately be eliminated (in the absence of non-magnetic forces) if the field is non-axisymmetric.

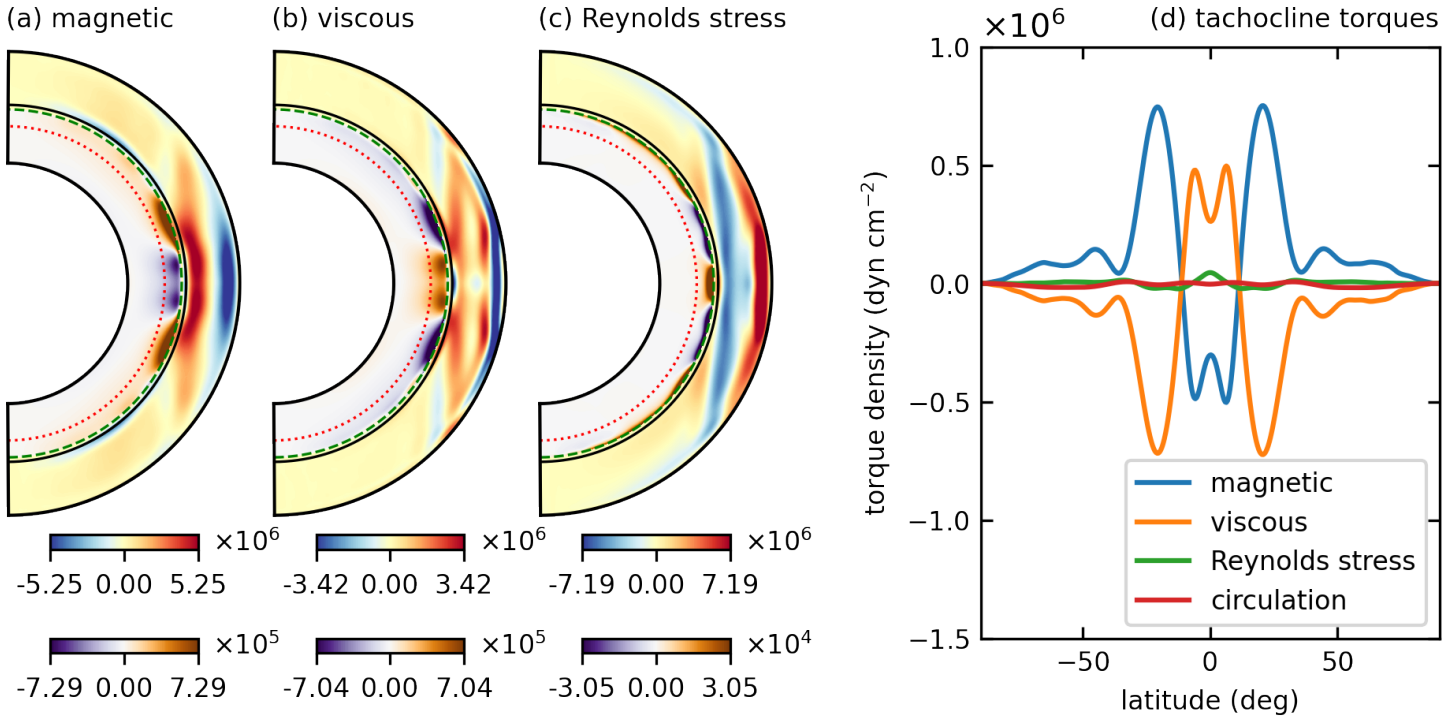

Figure 5.4: **Magnetic Torque Maintaining the MHD Case's Tachocline.** (a)–(c) The dominant torque balance (from left to right: magnetic, viscous, and Reynolds stress) in the full meridional plane for the MHD case. Two separate color tables are used for the convection zone (top colorbar) and radiative interior (bottom colorbar). The torque densities are plotted in the cgs units of pressure (dyn cm^{-2}). (d) Latitudinal profiles of the torque balance (also including the meridional circulation), averaged in radius over the tachocline.

interior, i.e., Equation (5.5)—strictly, the full Equation (5.15a)—multiplied by $B_\phi/4\pi$. The resulting magnetic-energy production equation is then averaged over spheres and in time. Similar to the torque Equation (5.3), `Rayleigh` outputs spherical-average snapshots of the simulation by averaging the full 3-D profiles over longitude and colatitude. These snapshots are output at the same ∼1-rotation cadence as the longitude-average snapshots (but non-uniformly sampled due to the varying time-step), and then averaged over the equilibrated state to form the temporal average. Similar to the torque balance, the magnetic-energy balance can be nonzero for a given dynamo cycle, but becomes zero when averaged over many dynamo cycles.

Figure 5.5(a) shows that, on average, the toroidal magnetic field is produced predominantly by mean shear and is destroyed by magnetic diffusion. Because B_r is so weak in the radiative interior (Figure 5.2), it is the horizontal shear that dominates the production of toroidal field. This shows that Ferraro's law (as applied to non-axisymmetric fields after Mestel & Weiss 1987) is responsible for the torque forcing solid-body rotation. The generation of B_ϕ by mean shear acting on B_θ also coheres with the correlation between B_θ and B_ϕ pointed out in Figure 5.3.

Toroidal field produced by the Ω-effect is a common feature of most global dynamo simulations (e.g., Brown et al. 2010, 2011; Lawson et al. 2015; Matilsky & Toomre 2020a; Bice & Toomre 2020; Brun et al. 2022) and is the central torque-producing mechanism invoked by the fast and slow magnetic tachocline confinement scenarios. The ultimate question for our work is thus, "How does a poloidal magnetic field permeate the MHD case's radiative interior and maintain large amplitudes for over 10 magnetic diffusion times?" In the slow magnetic confinement scenario (GM98), the interior poloidal magnetic field is a primordial remnant. It is supposedly prevented from diffusing away (the Sun has already made it through ∼1 magnetic diffusion time; see Table 5.1) by the vertical component of the meridional circulation. In the fast magnetic confinement scenario (Forgács-Dajka & Petrovay, 2001), the poloidal field is cyclically pumped downward from the convection zone above via turbulent diffusion. There is clearly vigorous dynamo action in the MHD case's convection zone; fields of amplitude ∼10 kG are amplified and then sustained for many magnetic diffusion times. Additionally, our sub-grid-scale magnetic diffusivity is quite high at all radii. We thus might suspect

that the radiative interior's magnetic field is simply diffusing down from the convection zone above, as in the fast confinement scenario. This is not the case, however, as we now show.

Since the magnetic field is primarily horizontal, the production of poloidal magnetic energy is dominated by the θ-component of the MHD induction equation,

$$\frac{\partial B_\theta}{\partial t} \approx \underbrace{-B_\theta \left(\frac{1}{r \sin\theta} \frac{\partial v_\phi}{\partial \phi} + \frac{\cot\theta}{r} v_\theta \right)}_{\theta \text{ compression}} + \underbrace{r(B_r \hat{\boldsymbol{e}}_r + B_\phi \hat{\boldsymbol{e}}_\phi) \cdot \nabla \left(\frac{v_\theta}{r} \right)}_{\theta \text{ shear}} - \underbrace{\nabla \times [\eta(r) \nabla \times \boldsymbol{B}]_\theta}_{\theta \text{ diffusion}}, \qquad (5.6)$$

multiplied by $B_\theta / 4\pi$. See Section 5.11.2, Equation (5.15b) for a full derivation. This production, temporally and spherically averaged, is shown in Figure 5.5(b). Clearly the poloidal magnetic field is not pumped in via diffusion, but instead is amplified inductively (and destroyed diffusively) at all radii, just like the toroidal field. The induction comes from two mechanisms: compression (the longitudinal squeezing of field lines) and fluctuating shear (the tilting of radial and longitudinal field into colatitudinal field by the convective—non-circulatory—meridional flow). Note that in the tachocline, the compression and shear contribute roughly equally to poloidal magnetic energy production, but below the tachocline, production is almost exclusively by compression.

The results encapsulated in Figure 5.5(b) may prove to be profound. They imply that strong magnetism could be maintained by dynamo action, *even below the convective overshoot layer*. This picture is quite different from the mechanisms usually invoked to explain how magnetism might enter the radiative interior—e.g., magnetic "pumping," magnetic diffusion, and primordial remnants. Furthermore, in the interface-dynamo paradigm, it is often argued that the radiative interior basically acts as an "abyssal deep" (to borrow a term from oceanography)—a passive storage reservoir for magnetic field produced in the tachocline. The "quiescent" stable layer accepts field pumped in from above, until the magnetism grows strong enough to form buoyant loops that then rise through the convection zone to form sunspots (e.g., Spruit & van Ballegooijen 1982; van Ballegooijen 1982; Moreno-Insertis et al. 1992; Parker 1993; Ferriz-Mas & Schuessler 1994). If our results extend to the Sun, the solar radiative interior may be a site of induction that contributes significantly to driving the global dynamo.

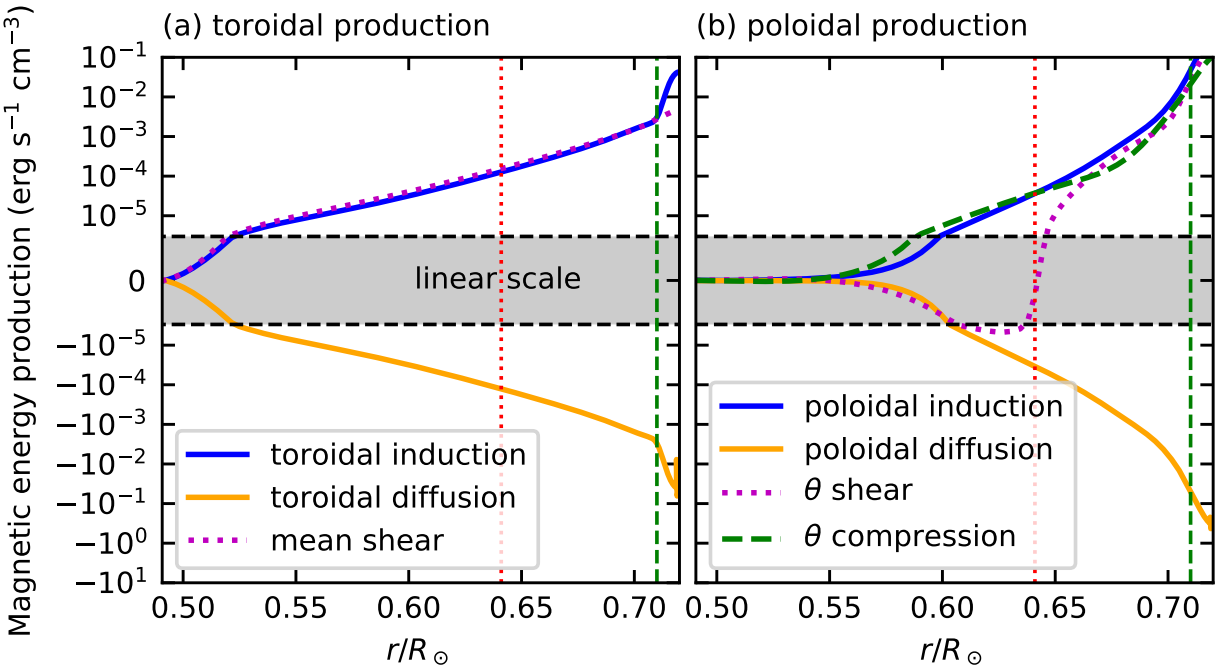

Figure 5.5: **Dynamo Action in the MHD Case's Radiative Interior.** The steady-state productions of (a) toroidal magnetic energy and (b) poloidal magnetic energy are plotted as functions of radius below the overshoot layer. The different production rates are defined explicitly in the supplementary Section 5.11 in Equations (5.15a) and (5.15b). These equations have been averaged in time over the equilibrated state and over spheres of radius r. Each panel shares the same x- and y-axes. The y-axis is scaled logarithmically (unshaded region) for absolute values $> 3 \times 10^{-6}$ erg s^{-1} cm^{-3} and linearly (shaded region) otherwise. In both panels, the locations $r_{\rm ov}$ and $r_{\rm tach}$ are marked by vertical lines, as in previous Figures.

5.7 Tachocline Confinement by Cycling Partial Wreaths

The tachocline in our MHD case is clearly confined by the magnetic torque (Figure 5.4). We have further shown that this torque is generated by the bending of poloidal field lines by the mean shear (which, although very weak, is nonzero in the radiative interior). This process is well represented by the typical partial-wreath structure shown in Figure 5.3. Here, we investigate how the partial wreaths vary throughout the shell, and how they cycle in time. We show that in addition to the stationary component, the cycling components of the wreaths give rise to the confining torque.

Figure 5.6 shows the full morphology of the horizontal magnetic fields and fluid flows throughout the shell, at the end of the simulation (same instant sampled by Figure 5.3). The magnetic field in the radiative interior (top row) is quite smooth and mostly consists of an $m = 1$ partial wreath in the North and an $m = 2$ partial wreath in the South. The horizontal flows, represented by the convective radial vorticity ω_r', are at smaller scales ($m \sim 10$) and have less clear symmetry about the equator. Higher up in the shell (bottom two rows) the magnetic fields develop more fine structure, but the imprint of the large-scale partial wreaths remains. The horizontal flows also become finer-scale in the convection zone, with no obvious imprint from the motions in the radiative interior.

Figure 5.6 suggests that the radiative interior and convection zone have essentially distinct flow and field properties, except for the large-scale ($m = 1, 2$) magnetic fields. To investigate further, we show the time-radius diagrams of the longitudinally averaged ($m = 0$) horizontal magnetic fields in Figure 5.7. Although our MHD case's magnetic field is dominated by the non-axisymmetric components, we speculate that we can use the longitudinal average $\langle B_\phi \rangle$ (this time with the angular brackets *not* implying a temporal average as well) to trace the dynamo cycle and polarity reversals, as we did in Chapter 4. Figure 5.7 shows that the partial wreaths in the overshoot layer lead the system, and the fields in the deep radiative interior follow. Any pattern realized in the overshoot layer appears near the base of the radiative interior $\sim$250 rotations later, which also seems to be

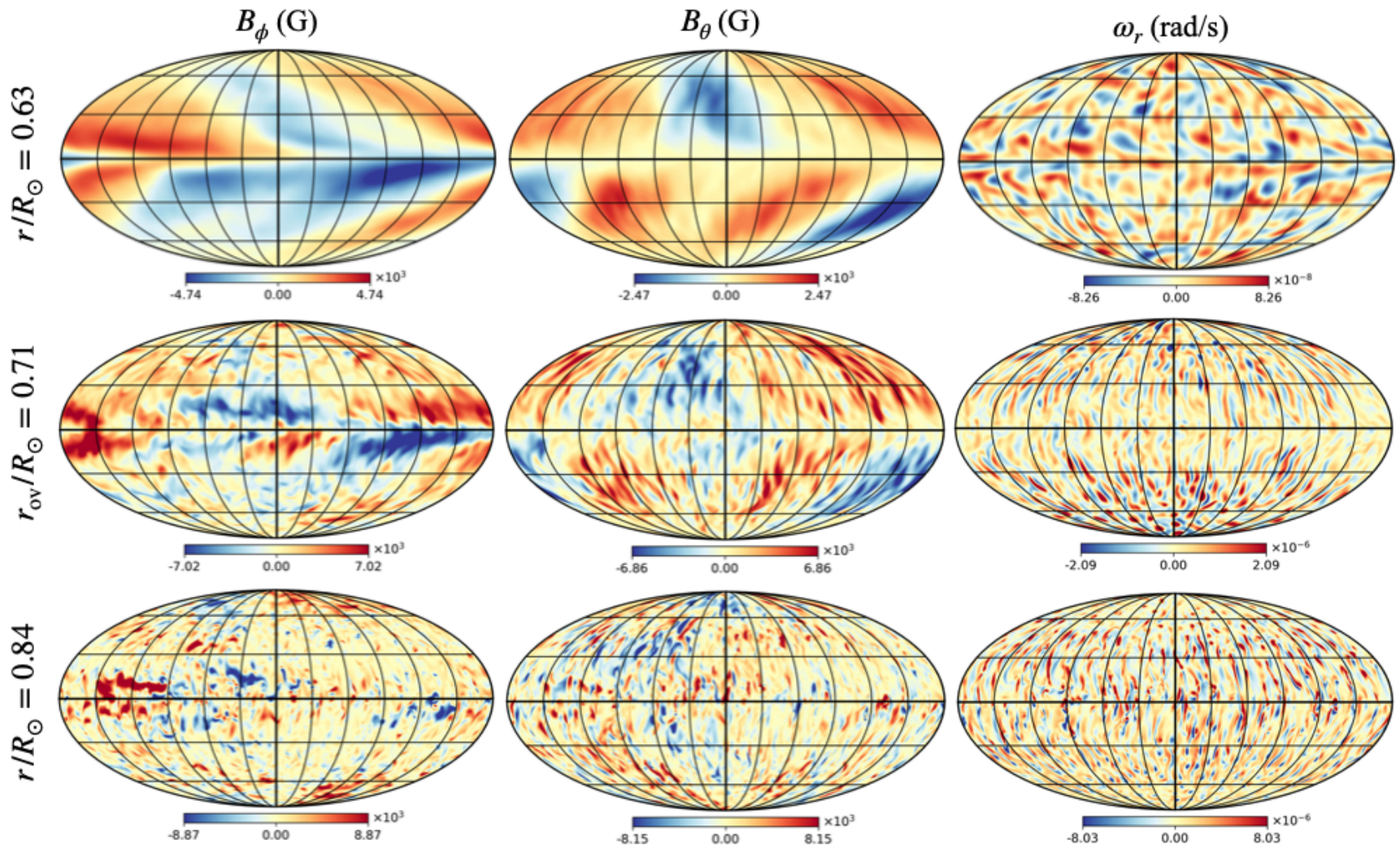

Figure 5.6: **Full Morphology of the MHD Case's Dynamo.** Full spherical Mollweide snapshot views of the MHD case's dynamo. The snapshots are taken at the end of the simulation run ($t = 16050$ rotations; same as Figure 5.3). Different fluid variables are shown in each column. From left to right: toroidal magnetic field B_ϕ, poloidal magnetic field B_θ, and convective horizontal flows (convective radial vorticity ω_r'). Different depths are shown in each row. From top to bottom: just below the tachocline ($r/R_\odot = 0.63$), the base of the overshoot layer ($r_{ov}/R_\odot = 0.71$), and mid-convection-zone ($r/R_\odot = 0.84$).

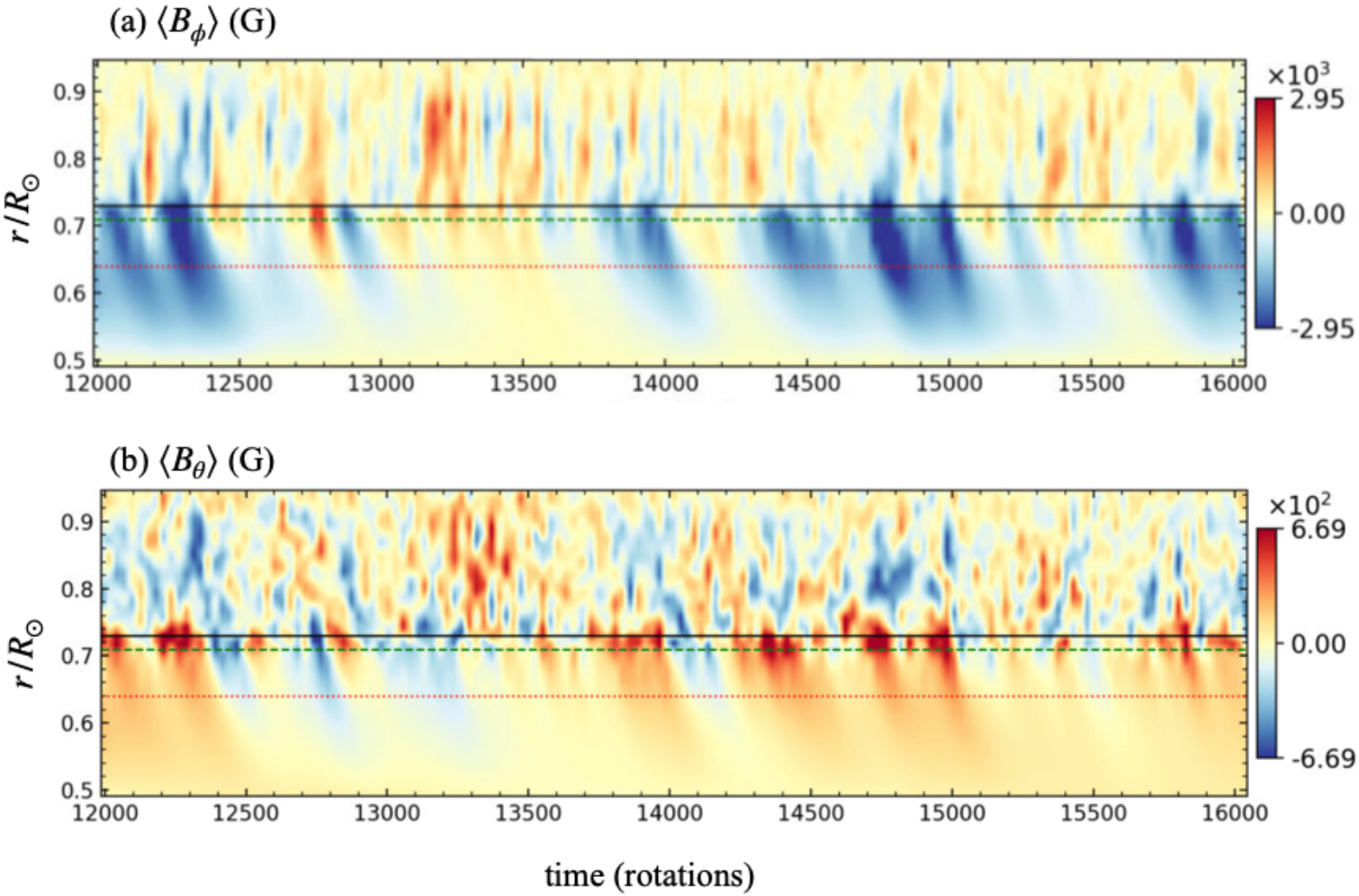

Figure 5.7: **Time-Radius Diagram of the Confining Dynamo.** The longitudinally averaged magnetic field is shown as a function of time and radius for (a) $\langle B_\phi \rangle$ and (b) $\langle B_\theta \rangle$. The three critical radii are marked by their usual lines. The field is sampled over the last ∼4000 rotations at a latitude of 10 degrees in the Northern Hemisphere.

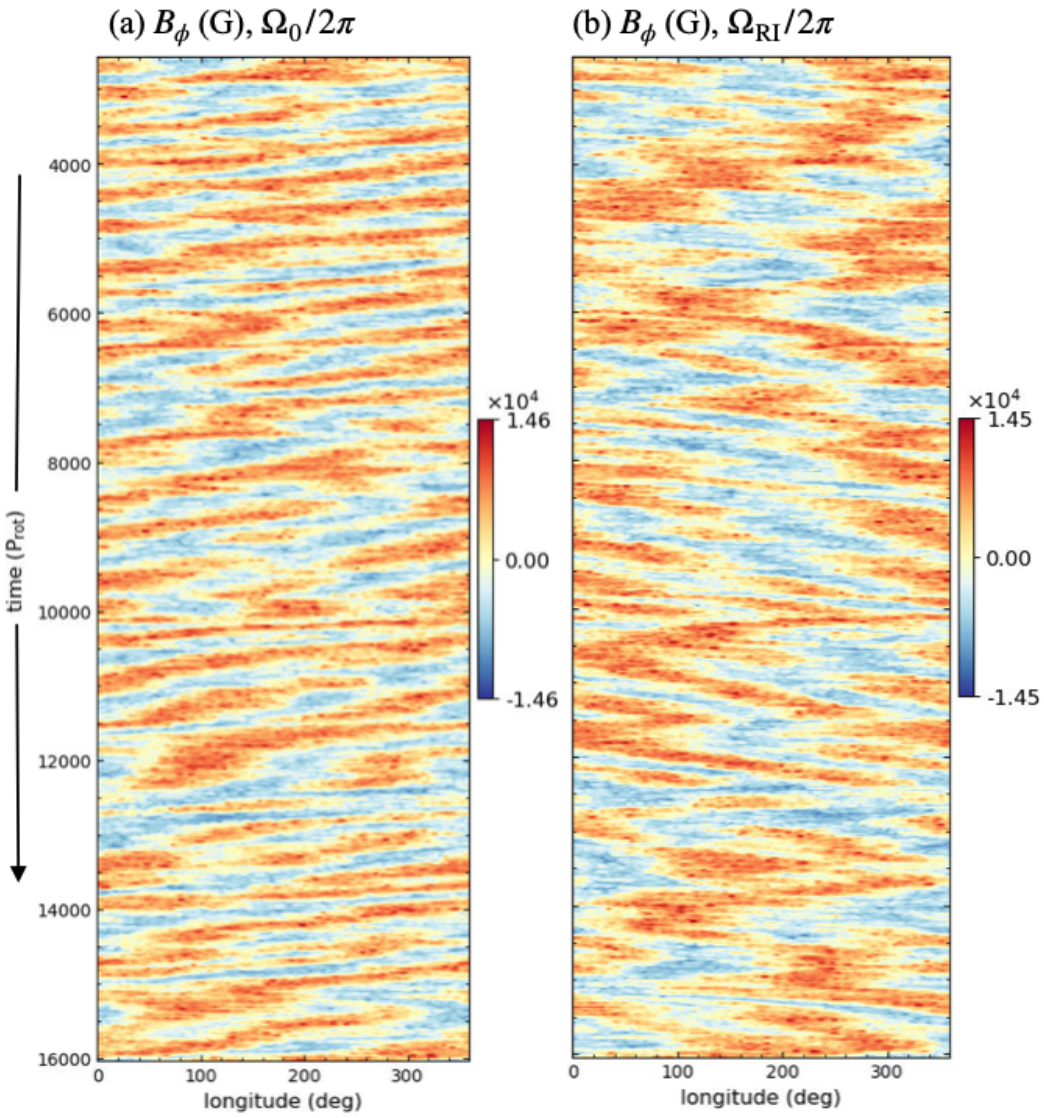

Figure 5.8: **Confining Magnetism as Partial Wreaths.** The full non-axisymmetric toroidal magnetic field B_ϕ is shown as "partial wreaths," similar to the structures encountered in Chapter 4. The time-longitude plots (longitude on the x-axis, time running *vertically downward* on the y-axis) are shown in (a) the rotating-frame frequency $\Omega_0/2\pi$ and (b) a frame rotating slightly slower, at the background rotation rate, $\Omega_{\rm RI}/2\pi \equiv \Omega_0/2\pi - 2.3$ nHz. The field is sampled over the whole equilibrated state at $r = r_{\rm ov}$ at a latitude of 10 degrees in the Northern Hemisphere.

about the time for a polarity reversal of the partial-wreath pair at a fixed radius. As in Chapter 4, we define the partial-wreath polarity via the longitudinal average, i.e., the sign of $\langle B_\phi \rangle$ or $\langle B_\theta \rangle$. This yields a rough dynamo cycle period of $\sim$500 rotations, though we note that the reversals are not regular. The magnetic diffusion time across the radiative interior is substantially longer, $\sim$1300 rotations, suggesting once again that the magnetic field does not spread inward diffusively. In the convection zone, there is possibly some radial propagation of the fields upward from the overshoot layer, although this is less clear. The polarity reversals are more rapid in the convection zone, occurring every $\sim$100 rotations, for a dynamo cycle of $\sim$200 rotations.

Following the methods of Section 4.6, we examine the toroidal field in time-longitude space (Figure 5.8), choosing a radial level of $r_{\rm ov}$ and a latitude of 10 degrees, which from Figures 5.2 and 5.3 is also approximately the region of strongest magnetic-field amplitude. If we rotate with the frame (Figure 5.8(a)), the non-axisymmetric field structure is seen to travel a full 360° backward in longitude over the previously identified cycle period of $\sim$500 rotations. This suggests that the field structure rotates slower than the frame rate, likely at the radiative interior's rotation rate $\Omega_{\rm RI}$. If we co-rotate with the radiative interior at frequency $\Omega_{\rm RI}/2\pi \equiv \Omega_0/2\pi - 2.3$ nHz (Figure 5.8(b)), the toroidal field is approximately stationary, staying roughly localized at the same longitudes.[7] The polarity reversal is the flip-flop back and forth between the dominant partial wreath. Note, however, that even co-rotating with the radiative interior, a given partial wreath zigzags in longitude, sometimes moving $\sim$2.5 nHz faster or slower than the background rotation frequency. This zigzag effect was also mentioned in Chapter 4 (Matilsky & Toomre, 2020a).

Partial-wreath cycles are fairly difficult to visualize, and so far we have described them largely from a phenomenological perspective. To be more precise, we now analyze the MHD case's $m = 1, 2$ magnetic-field components in frequency space. We Fourier-transform each field component and their derivatives in both longitude and time. We consider an equally spaced time series of length T, yielding frequencies $f_n \equiv n/T$ equally spaced by the frequency resolution, $1/T$ (the number

[7] Note that we *define* $\Omega_{\rm RI}$ arbitrarily to force the time-longitude behavior of the partial wreaths to appear as stationary as possible. This is justified by the field structures largely being advected by the background flow; from Figure 5.1(c), $\Omega_{\rm RI}$ chosen in this way is clearly close to the background rotation rate of the radiative interior.

of frequencies N_f equals the number of samples N_t, and n runs from $-N_f/2$ to $N_f/2+1$). In our convention, positive frequency indicates a *retrograde*-traveling wave. We denote the doubly-transformed quantities with tildes and normalize them so that Parseval's theorem takes the form (e.g., for the toroidal field B_ϕ):

$$\left\langle B_\phi^2 \right\rangle = \sum_m \sum_n \widetilde{B_\phi}^*(m, f_n)\widetilde{B_\phi}(m, f_n), \tag{5.7}$$

where the angular brackets here denote a combined longitudinal and temporal average, and the asterisk denotes the complex conjugate. This makes the spectral coefficients (e.g., $\widetilde{B_\phi}(m, f_n)$) represent the "amount" of field (e.g., B_ϕ) present at a given wavenumber m and frequency f_n. When added in quadrature, these amounts give the total magnetic-field amplitude $\left\langle B_\phi^2 \right\rangle^{1/2}$.

Figure 5.9 shows distribution of the horizontal-field components in latitude-frequency space for $m = 1$. Clearly the fields are localized near a central frequency of $\sim$2.5 nHz (consistent, within our frequency resolution, with the $(\Omega_0 - \Omega_{\rm RI})/2\pi = 2.3$ nHz identified from the time-longitude diagram), but have substantial components in a surrounding interval $\sim$5 nHz wide. This is basically consistent with the zigzag pattern in Figure 5.8). The fields are primarily at positive frequencies; thus, the whole structure moves primarily retrograde in the rotating frame. The dispersion in frequency indicates that the partial wreaths are not stationary, however, but change their longitudinal position even in their "home" frame.

Because the expressions for magnetic torque in Equation (5.4) are quadratic in the magnetic field, each wavenumber-frequency pair is associated with a contribution to the torque. These contributions can be defined (using, e.g., Expression (5.4c)) as:

$$\tau_{\rm mag}(m, f_n) \equiv \frac{1}{4\pi}[\widetilde{\boldsymbol{B}_{\rm pol}}(m, f_n)]^* \cdot \nabla \left[r \sin\theta \widetilde{B_\phi}(m, f_n) \right] \tag{5.8}$$

$$\text{with} \qquad \sum_m \sum_n \tau_{\rm mag}(m, f_n) = \tau_{\rm mag}.$$

Because the magnetic field is a real quantity, each "mixed" product $\tau_{\rm mag}(m, f_n)$ is purely real.

In Figure 5.10, we plot the torque contributions as a function of latitude and frequency at the base of the overshoot layer. As in Figure 5.4(d), the total torque at this depth (Figure 5.10(a))

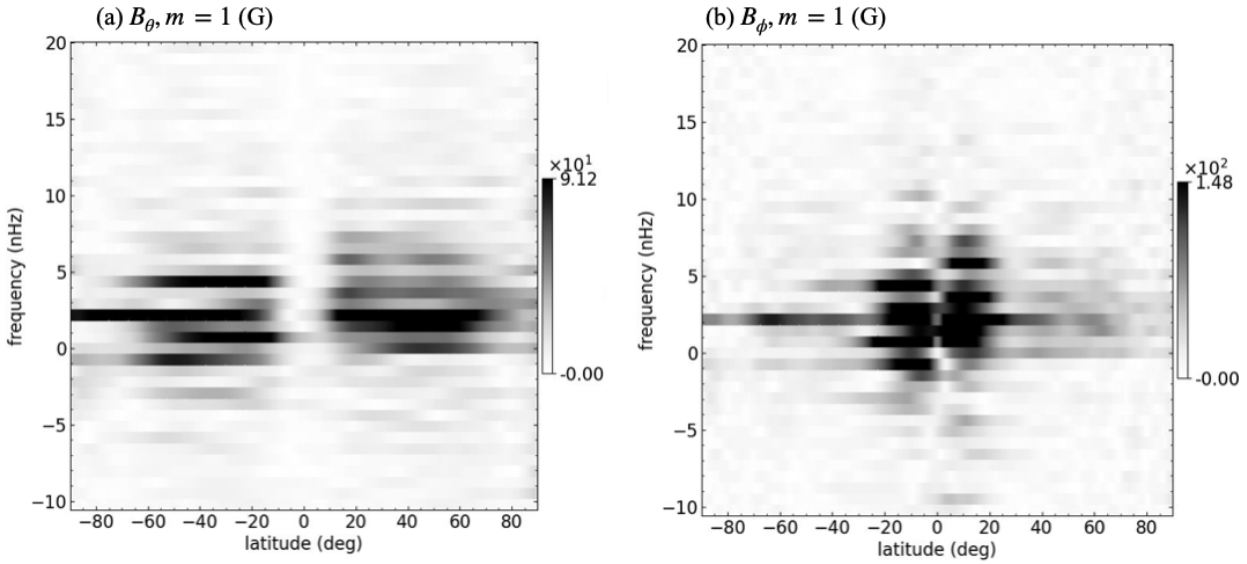

Figure 5.9: **Cycling Frequencies of the Partial Wreaths.** The absolute values of the $m = 1$ spectral coefficients for the horizontal magnetic fields are shown at the base of the overshoot layer for (a) $|\widetilde{B_\phi}|$ and (b) $|\widetilde{B_\theta}|$. The coefficient values are plotted in gray-scale with respect to latitude and frequency. For this time series, the sampling interval is $T = 1880$ rotations, the frequency resolution is $\sim$0.7 nHz, and the Nyquist frequency is 5000 nHz. The interval starts and ends at $t = 4420$ rotations and $t = 6300$ rotations, respectively.

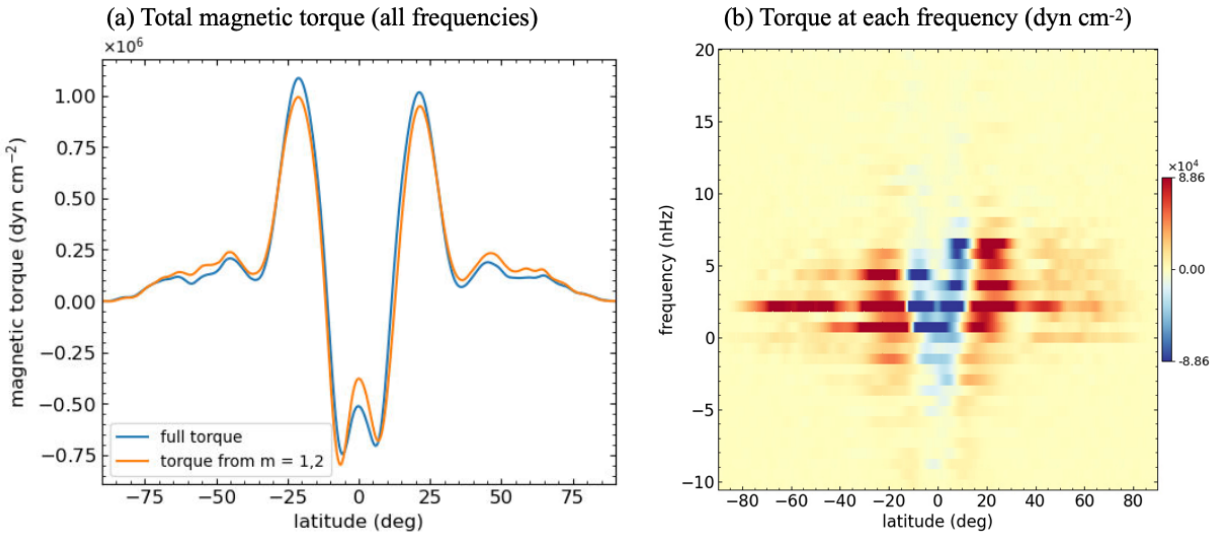

Figure 5.10: **Magnetic Torque from Each Cycling Frequency.** The magnetic torque from the two wavenumbers $m = 1, 2$ is shown as a function of latitude at the base of the overshoot layer. The time series is the same as in Figure 5.9. (a) The torque contributions, defined in Equation (5.8), summed over $m = 1, 2$ and all frequencies, along with the torque directly computed from the longitudinal-average data (or equivalently, the mode contributions summed over all m). Compare to Figure 5.4. (b) The $m = 1, 2$ torque contributions, each frequency considered separately as a function of latitude.

is concentrated at low latitudes, spinning the equator down and the higher-latitude regions up. We sum over $m = 1, 2$ only, and these two modes contain nearly all the torque. Broken up by frequency (Figure 5.10(b)), the components of magnetism producing the torque are seen to roughly follow the distribution of the toroidal field (Figure 5.9(a)). *It is thus the cycling partial-wreath dynamo that produces the magnetic torque confining the tachocline against viscosity.* Furthermore, each latitudinal strip at a fixed frequency in Figure 5.10(b) roughly matches the full latitudinal profile of Figure 5.10(a). This simply emphasizes the fact that the bending of poloidal field lines by the shear (and subsequent tension force tending to eliminate the shear) is a local process. However complicated the $m = 1, 2$ magnetic field structures behave in space and time, each part of the structure (which may cycle at its own distinct frequency), produces torque to counter the viscously imposed differential rotation.

The results of this Section offer a new possibility for magnetic confinement scenarios. Gough & McIntyre (1998) imagined the confining poloidal magnetic field to be an axisymmetric and stationary primordial remnant, entirely separate from the convection zone above. Forgács-Dajka & Petrovay (2001) imagined the poloidal field to be axisymmetric and cycling, brought in from the convection zone via diffusion (and not allowed to react back on the convection zone), and considered only one frequency component corresponding to a period of 22 years. Here we have identified a new confining structure, which is non-axisymmetric (composed mostly of $m = 1, 2$ partial wreaths), cycles at multiple frequencies, and is fully coupled to the convection zone above.

5.8 Inertial Modes and Dynamo Action in the Radiative Interior

Figure 5.5 shows that both horizontal components of the magnetic field are produced inductively in the radiative interior by horizontal motions. Here, we clearly show that the frequencies of these motions occur primarily in the "inertial band"—i.e., the frequency interval $\pm 2\Omega_0/2\pi = \pm 2700$ nHz. We thus loosely refer to the horizontal motions as inertial oscillations and describe them using the terminology presented in, e.g., Gizon et al. (2020b, 2021) and Zaqarashvili et al. (2021). We clearly identify the higher-frequency modes as classical equatorially confined (or "equatorial")

Rossby waves, recently identified at the solar surface by Löptien et al. (2018). There are also low-frequency oscillations that we argue represent MHD Rossby waves, possibly in critical layers (bands in latitude bounded by "critical points," where the Rossby-mode frequency equals the background rotation frequency). The horizontal power is dominated by the equatorial Rossby waves, but the low-frequency modes, whose energy is in equipartition with the poloidal magnetic-field energy, appear to cause the induction of poloidal field inferred from Figure 5.5(b).

Strong horizontal motions in the radiative interior are expected from the many investigations of shear and magnetic instabilities (Section 5.2). They have also been encountered frequently in prior global simulations. For example, in the middle of the MHD case's radiative interior, the horizontal velocity amplitude (on the order of $\sim$1–10 m s^{-1}; see Figure 5.2) is similar to the amplitudes reported in work utilizing the `ASH` code (e.g., Alvan et al. 2015), as well as the `EULAG-MHD` code (e.g., Lawson et al. 2015). They have likely been present in other global simulations as well, though not explicitly reported. Racine et al. (2011), Augustson et al. (2013), and Guerrero et al. (2016a), for example, all describe sizable α-effects, with α-tensor components $\sim$1–10 m s^{-1}, operating in their radiative interiors. Large α-effects would, in turn, require strong horizontal motions.[8]

As mentioned in Section 5.2, Alvan et al. (2014, 2015) investigated in detail the rich gravity-wave-field associated with the vertical motions in global simulations. The character and source of the horizontal motions, however, has yet to be systematically explored. Lawson et al. (2015) claimed that the horizontal motions were partly due to magneto-shear and Tayler instabilities, but this was not explicitly shown. The uncertainty as to where the horizontal velocities come from highlights the difficulty in identifying wave and instability properties of turbulent 3-D simulations.

As discussed in Section 5.5, the horizontal motions are nearly incompressible and are essentially described by the convective radial vorticity $\omega_r' \equiv (\nabla \times \boldsymbol{v}')_r$. The longitudinally averaged

[8] According to classical mean-field analysis, toroidal field produces poloidal field through an emf according to $\partial \langle \boldsymbol{B}_{\rm pol} \rangle / \partial t = \nabla \times \langle \boldsymbol{v}' \times \boldsymbol{B}' \rangle$, with $\langle \boldsymbol{v}' \times \boldsymbol{B}' \rangle \approx \boldsymbol{\alpha} \cdot \langle \boldsymbol{B} \rangle$, where $\boldsymbol{\alpha}$ is a second-rank tensor related to the kinetic and/or current helicities of the flow (e.g., Brandenburg & Subramanian 2005 and references therein). The α-tensor values reported in global simulations can thus be interpreted roughly as convective velocities, which must be purely horizontal in the radiative interior because of the stable stratification.

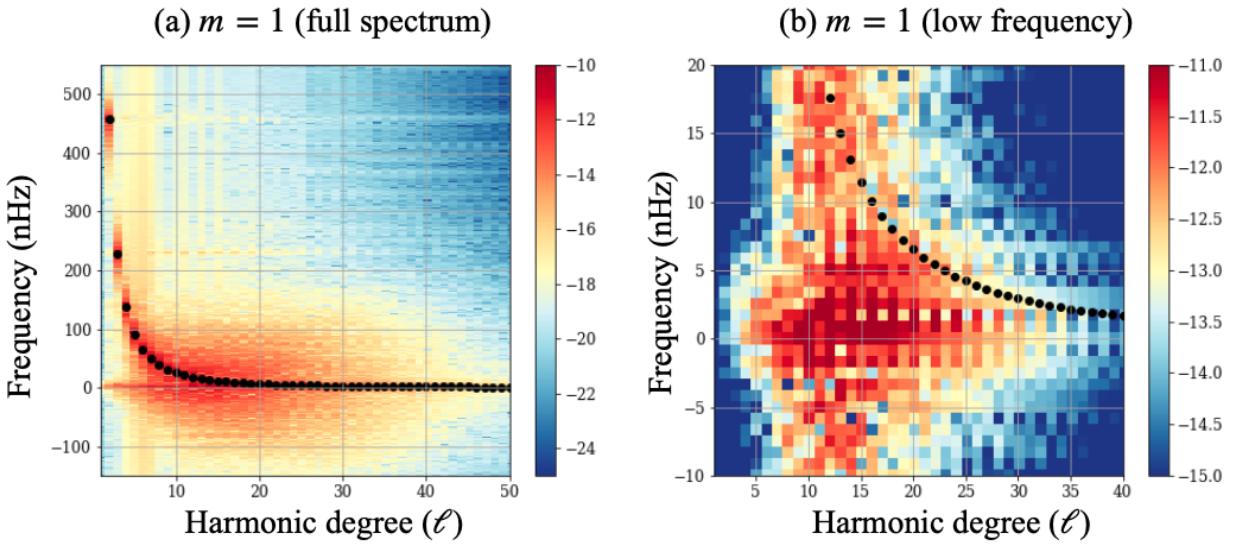

Figure 5.11: **Rossby Waves and Other Low-Frequency Inertial Oscillations.** The dispersion relation of the horizontal motions is shown deep in the radiative interior ($r/R_\odot = 0.55$) for the $m = 1$ power in the inertial band. The full inertial band is $\pm 2\Omega_0/2\pi = \pm 2700$ nHz, but we here plot a smaller sub-interval of frequencies that contains most of the power. We plot $|\widetilde{\omega_r}(r = 0.55R_\odot, \ell, m = 1, f_n)|^2$ on a log-10 scale (indicated by the colorbar) as a function of ℓ and f_n for (a) the full inertial-mode spectrum and (b) the low-frequency region. In both panels, we denote the results from the classical dispersion relation (5.10), $f_{\ell 1} = 2\Omega_0/[2\pi\ell(\ell+1)]$, by black dots. We note that although the radiative interior rotates at a rate $\Omega_{\rm RI}$, which is slightly slower than Ω_0, this difference would be negligible on the scale of the above plots. In this case, the sampling interval is 1650 rotations, the frequency resolution is 0.8 nHz, and the Nyquist frequency is 5000 nHz. Figure credit: Catherine Blume.

component $\langle\omega_r\rangle$ is nonzero, but simply represents the differential rotation, which cannot induct poloidal magnetic field. An equatorial Rossby mode in a sphere *rigidly rotating* with frequency $\Omega_{\rm RI}/2\pi$ is described by its spherical-harmonic degree ℓ, azimuthal order $m \neq 0$, and radial eigenfunction $A_{\ell m}(r)$. The horizontal eigenfunction of the mode is the spherical harmonic $Y_{\ell m}(\theta, \phi)$. The full mode is a global oscillation in the radial vorticity of the form:

$$\omega_{r;\ell m}(r, \theta, \phi, t) = A_{\ell m}(r) Y_{\ell m}(\theta, \phi) \exp\left(-i 2\pi f_{\ell m} t\right), \tag{5.9}$$

whose frequency follows the dispersion relation:

$$f_{\ell m} = \frac{2m\Omega_{\rm RI}}{2\pi\ell(\ell+1)}. \tag{5.10}$$

Here, $f_{\ell m}$ is the mode frequency, t is the time, and the real part of $\omega_{r;\ell m}$ gives the convective radial vorticity due to the mode. Rossby waves in the Earth's atmosphere and oceans were described in Rossby (1939) and Rossby (1945), and extended to rotating spheres by Haurwitz (1940) and Longuet-Higgins (1964). In stars, Rossby waves are often called r-modes (e.g., Unno et al. 1989). Good reviews of Rossby waves in the astrophysical context (including the equatorial modes) are given by Zaqarashvili et al. (2021) and Gizon et al. (2021).

To identify waves in our MHD case, we analyze the temporal power spectra of the spherical-harmonic components of ω_r (ignoring $m = 0$). As in discussing the magnetic field, we denote the spectral coefficients of the horizontal motions by $\widetilde{\omega_r}(r, \ell, m, f_n)$. Here, we have transformed in colatitude (i.e., $\theta \to \ell$) in addition to longitude and time. Recall that $f_n \equiv n/T$, with T the length of the uniformly sampled time series.

Figure 5.11 shows the $m = 1$ horizontal power as a function of harmonic degree. In Figure 5.11(a), the power closely follows the classical Rossby-wave dispersion relation (for a fixed m, frequency is proportional to $1/[\ell(\ell+1)]$) for low ℓ, but gets fairly muddy for high ℓ. We zoom in on the low-frequency region in Figure 5.11(b). The dominant flows at low frequencies are concentrated in the $\sim$[0, 5] nHz region, just like the partial-wreath dynamo cycle, and they are clearly separate from the expected Rossby-wave frequencies. We thus refer to the horizontal motions in the band ±5

nHz as low-frequency inertial oscillations and motions outside this interval (but still in the inertial band) as equatorial Rossby waves.

We believe that the low-frequency oscillations produce the induction of poloidal field of Figure 5.5(b) for two reasons. First, the magnetic field "lives" in the low-frequency region, according to Figure 5.9. For the Rossby waves to induct the magnetic field, there would have to be at least some magnetism oscillating at high frequency, shifted by a small amount from the Rossby waves. The beating between $\boldsymbol{v}'$ and $\boldsymbol{B}'$ could then cause an emf at the right frequencies to account for the induction. In the deep radiative interior ($r/R_\odot = 0.60$), the magnetic-field amplitude at the equatorial Rossby-wave frequencies is $B_\theta \sim 5$ G and the horizontal power of the Rossby waves is $\omega_r' \sim 2\times10^{-8}$ rad s^{-1}, so the production of poloidal magnetic is $(B_\theta^2/4\pi)\omega_r' \sim 4\times10^{-8}$ erg s^{-1} cm^{-3}. Even if all the high-frequency magnetic power were organized into ridges like the Rossby waves, but shifted by a few nHz (which we do not observe), there would thus not be enough magnetic field to yield the induction shown in Figure 5.5(b).

Second, the low-frequency inertial oscillations *do* have enough amplitude to account for the observed induction. For example, at the same $r/R_\odot = 0.60$ depth for low frequencies, we can estimate $B_\theta \sim 500$ G, $\omega_r' \sim 5\times10^{-10}$ rad s^{-1}, and thus $(B_\theta^2/4\pi)\omega_r' \sim\ 10^{-5}$ erg s^{-1} cm^{-3}. Furthermore, the low-frequency inertial oscillations seem to be clustered exactly around the frequencies associated with the cycling partial-wreath dynamo. It thus seems very likely that the induction is due to the flows within the identified ±5 nHz low-frequency band (although we have not yet explicitly demonstrated this).

We speculate that these inertial oscillations are similar to the critical-layer Rossby waves described in Section 5.2 (e.g., Braginsky & Roberts 1975; Watson 1981; Charbonneau et al. 1999a; Garaud 2001). These waves have horizontal eigenfunctions with amplitude highest between two critical points in latitude, which are located where the mode frequency equals the background rotation frequency. In the MHD case, the radiative interior rotates ∼2.3 nHz (or more conveniently here, ∼2.5 nHz) slower than the frame rate. Furthermore, the background rotation frequency varies over the partial-wreath cycles (like a torsional oscillation) by an amplitude of ∼2.5 nHz. At any

given time, the background rotation rate can thus be anywhere in the $\sim$[0, 5] nHz range. There could then be critical-layer Rossby waves, having a continuous spectrum of frequencies also in the $\sim$[0, 5] nHz range. Finally, because the low-frequency inertial oscillations appear with roughly the same energy as the poloidal magnetic field, they may well be "MHD" Rossby waves (a hybrid between equatorial Rossby waves and Alfvén waves). We discuss the possibility of MHD Rossby waves more in Section 5.10.

We briefly note that the power in the *vertical* velocity consists of a rich spectrum of gravity waves, which we show in Figure 5.12. Vertical power is clearly concentrated in ridges that correspond to the gravity-wave dispersion relation. Furthermore, the gravity and inertial waves appear to live in distinct frequency intervals, with the gravity-mode frequencies well outside the inertial band. Hence, the influence of "gravito-inertial" modes (e.g., Rieutord et al. 2001; Baruteau & Rieutord 2013; Mirouh et al. 2016) is likely small in our MHD case. Figure 5.12 clearly shows that the horizontal motions are *not* due to gravity waves, as may have been suspected from the initial investigations of Alvan et al. (2014) and Alvan et al. (2015). The same frequency separation likely holds in the Sun. The solar gravity modes are not anelastic and the resonant cavity is quite different than in our simulations.[9] However, the range of frequencies in the excited solar gravity modes should still roughly fill the space between very low frequency and the buoyancy frequency (which is on par with that of our simulations). Thus, unless the very-low-frequency (very-high-radial-order) gravity modes are for some reason preferentially excited in the Sun, most of the gravity modes will lie well outside the inertial band.

5.9 Magnetic Tachocline Confinement in Global Simulations

We first note that most, if not all, MHD simulations including stable layers also have strong poloidal magnetic fields in their radiative interiors (e.g., Ghizaru et al. 2010; Racine et al. 2011; Passos & Charbonneau 2014; Lawson et al. 2015; Guerrero et al. 2016a,b, 2019; Bice & Toomre

[9] In our models, the gravity waves reflect off an unphysical rigid boundary at $r = r_{\rm i}$, whereas in the Sun, they have a lower turning point where the mode frequency becomes greater than the local buoyancy frequency.

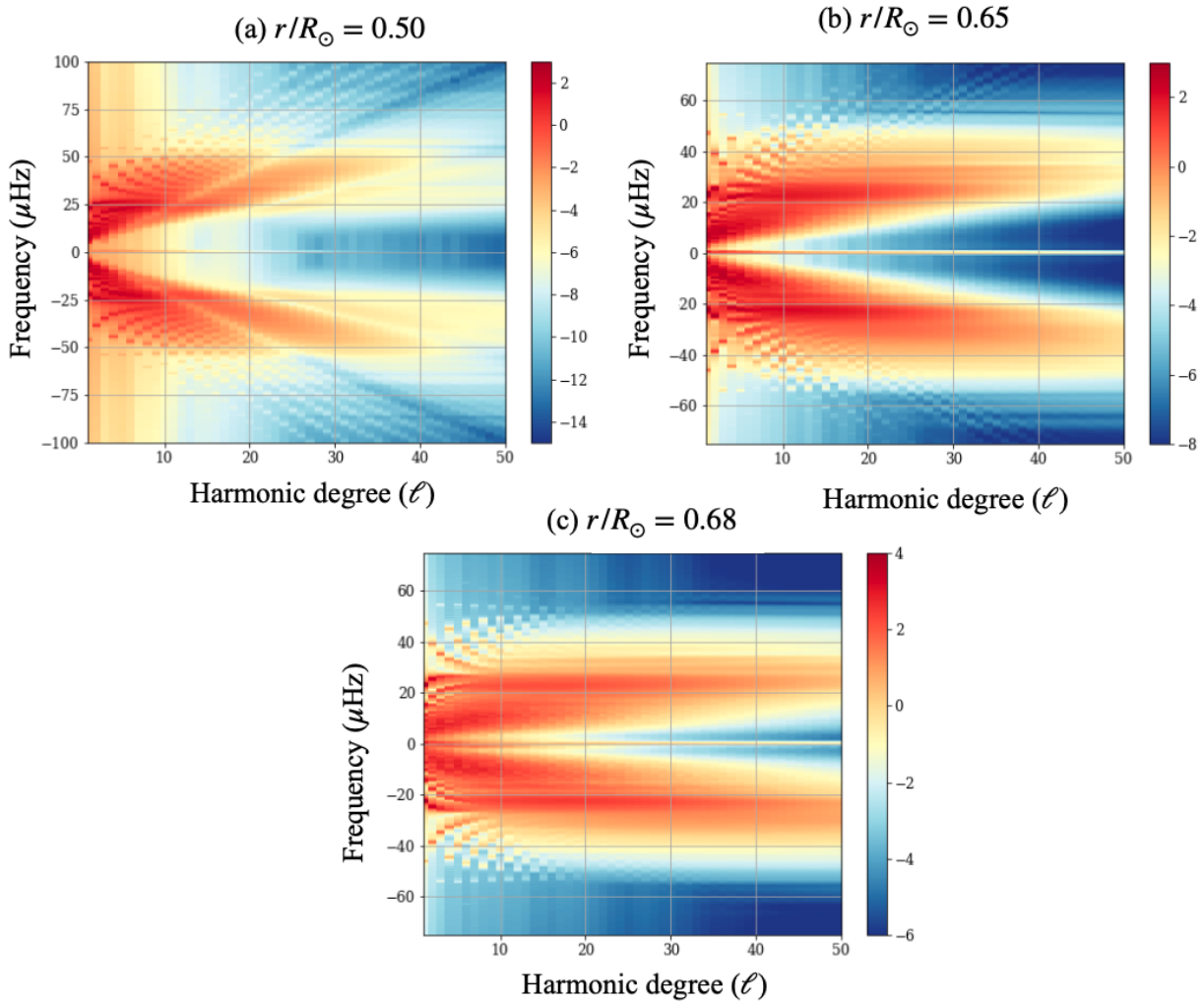

Figure 5.12: **Gravity Waves Below the Tachocline.** The gravity-wave dispersion relation in the MHD case is shown at three different depths in the radiative interior. The full gravity-wave band is approximately $\pm N/2\pi = \pm 190$ μHz (see Table 5.1; note that the gravitational acceleration, and thus N, varies slightly throughout the radiative interior), but we here plot a smaller sub-interval of frequencies that contains most of the power. The temporal power spectra of the radial velocity summed over all m, $\sum_m |\widetilde{v_r}(r, \ell, m, f_n)|^2$, is plotted on a log-10 scale (indicated by the colorbar) as functions of spherical-harmonic degree ℓ and frequency f_n for three different radial levels, radius increasing from (a)–(c). In this case, the sampling interval is ∼2.75 rotations, the frequency resolution is 0.5 μHz, and the Nyquist frequency is 500 μHz. Figure credit: Catherine Blume.

2020, 2022; Brun et al. 2022). These examples all have tachoclines implemented by enforcing very low diffusions throughout the radiative interior. There is thus ostensibly negligible diffusive imprinting of magnetic field from above, and we can similarly rule out "downward pumping" of magnetic field by downflow plumes because of the stable stratification. The likely conclusion is that the fields come locally from induction. The possibility of induction in these low-diffusion models is also supported by the presence of strong horizontal motions within the stable layer.

We thus speculate that many prior simulations may have contained dynamo action in their stable layers, though it was not recognized as such. However, it is difficult to know if the magnetism could have been confining the tachocline in the low-diffusion models. The main goal of lowering the diffusions is to slow down the eventual tachocline spread. If this technique is successful, the differential rotation never enters the radiative interior during the course of the simulation, and the process by which Ferraro's law enforces solid-body rotation cannot take place.

However, even substantially lowering the radiative interior's diffusions often does not successfully confine the tachocline (e.g., all the `ASH` simulations of F-type stars in Augustson et al. 2012, 2013; about half the `EULAG-MHD` simulations in Guerrero et al. 2019; and the "M07R01m" and "M09Sm" `ASH` simulations of Brun et al. 2022). It is a puzzle why this happens, especially in the `EULAG-MHD` code where diffusion is implicit and reportedly too low to be measured (e.g., Lawson et al. 2015; Guerrero et al. 2016a,b). In any case, it would be hard to explicitly demonstrate magnetic confinement in a model with low diffusions. The torque balance could not be assessed until after the simulation had been run past the very long viscous diffusion time across the radiative interior (which is designed at the outset to be much longer than the intended run time of the simulation). Furthermore, in the `EULAG-MHD` simulations, there does not seem to be a method available to compute the torque associated with the implicit diffusive operator in the first place. We thus argue that keeping the diffusions relatively high everywhere in the shell has the advantage of making a thorough dynamical analysis possible. In future global simulations assessing the tachocline-confinement problem, we strongly support explicit diffusions and running the simulation for multiple diffusion times.

5.10 Revisiting Magnetic Tachocline Confinement in the Sun

We have presented the first 3-D gobal simulation to evince a mechanism similar to one of the magnetic confinement scenarios proposed for the Sun. Here, we speculate whether the rather specific form of the confining magnetism we have identified (non-axisymmetric, cycling partial wreaths induced locally by dynamo action all throughout the radiative interior) could be playing out in the Sun. To that end, we briefly discuss three issues that will have to clarified in future work. (1) Could there be strong horizontal motions, in the form of vortical Rossby waves and other low-frequency inertial oscillations, in the solar radiative interior? (2) Could such horizontal motions induce dynamo action, with non-axisymmetric fields that are consistent with the observed 22-year cycle? (3) Do the answers to the two prior questions change between the parameter space of simulations (in which the tachocline spreads viscously) and that of the Sun (in which the tachocline spreads radiatively)?

(1) As discussed in 5.2, horizontal motions have long been thought to occur in the solar radiative interior via shear instabilities (e.g., Zahn 1974, 1992; Charbonneau et al. 1999a; Garaud 2020; Cope et al. 2020. More recently, there has been much work to characterize magneto-shear instabilities in the form of MHD Rossby waves (a hybrid between equatorial Rossby waves and Alfvén waves) in the solar tachocline (Zaqarashvili et al., 2021)). Specifically, it seems likely that there is an exchange of energy between differential rotation, unstable MHD Rossby waves, and the magnetic fields in the tachocline (e.g., Dikpati 2012; Dikpati et al. 2017, 2018a,b). These nonlinear energy exchanges, also called Tachocline Nonlinear Oscillations (TNOs), have been postulated to cause the observed "seasons" in space weather (bursts of solar flares and coronal mass ejections every 6–18 months; e.g., McIntosh et al. 2015). TNOs have been simulated using the shallow-water formalism (Dikpati et al., 2017, 2018a,b) and reveal tilted flow and field patterns remarkably reminiscent of Figures 5.3 and 5.6). Finally, Zaqarashvili (2018) and Zaqarashvili & Gurgenashvili (2018) have shown that MHD Rossby waves in the solar tachocline could yield oscillation periods on the order of $\sim$10 years (i.e., close to the sunspot cycle period), as well as $\sim$100 years (i.e., close

to the Gleissberg cycle period).

(2) Whether the horizontal motions could induce dynamo action is an open question. The results of Dikpati et al. (2017, 2018b); Zaqarashvili (2018); Zaqarashvili & Gurgenashvili (2018) are highly suggestive, showing that unstable MHD Rossby waves are likely to at least be strongly correlated with observed dynamo variations, and may even drive them. Additionally, recall from Section 5.2 that some of the work on magneto-shear instabilities (e.g., Dikpati & Gilman 2001a; Dikpati 2012; etc.) postulated that Rossby waves could induce an α-effect through their net helicity. Furthermore, MHD Rossby waves in the convection zone have been invoked as a potential driver of the solar dynamo (Gilman, 1969a,b). Finally, MHD Rossby waves in the stably stratified Earth's core (in the form of "baroclinic instabilities," as described by Braginsky & Roberts 1975) have been explicitly shown to be capable of sustained dynamo action. In future work, we must assess exactly what type of wave or instability the low-frequency oscillations of Figure 5.11 represent. If they are MHD Rossby waves, our MHD case would be good evidence that such waves in the solar tachocline could help drive a dynamo.

One feature of the MHD case's dynamo (which was also a feature of many instability analyses) is the dominance of *non-axisymmetric* (specifically, $m = 1, 2$) magnetic fields. Whether such a field in the radiative interior would be consistent with Hale's polarity law, which would seem to indicate one largely axisymmetric reservoir of toroidal field in each hemisphere, is unclear. As discussed in Chapter 4, there are a significant number of "anti-Hale" bipolar active regions (Stenflo & Kosovichev, 2012; Li, 2018), which might be consistent with some amount of non-axisymmetry. Also, the magnetic field's geometry and amplitude in the deep radiative interior are almost entirely unconstrained by helioseismology. The path forward thus seems best suited to global modeling. To verify whether a confining dynamo would be consistent with solar-cycle observations, future global simulations must better assess the magnetic coupling (or lack thereof) between convection zone and radiative interior.

(3) It is a tantalizing possibility that a dynamo driven by inertial oscillations maintains the solar tachocline. But could the process we have identified operate in the solar parameter regime?

Apart from the MHD case being much more laminar than the Sun, the essential difference lies in the mechanism of tachocline spread: viscous versus radiative. In the Sun, the meridional circulation should burrow inward and also play a dominant role in the torque balance (e.g., Spiegel & Zahn 1992; Garaud & Brummell 2008; Garaud & Garaud 2008; Wood & Brummell 2012; Acevedo-Arreguin et al. 2013; Wood & Brummell 2018). In current global simulations (and for the foreseeable future), this burrowing does not occur. Empirically, we cannot say if circulation-burrowing (or its absence) should strongly affect the system's dynamics, aside from changing the form of the torque that imprints the differential rotation. The only 3-D (local) simulations to clearly display radiative spread (Wood & Brummell, 2012, 2018) indicate that the imprinting of differential rotation is largely uniform (i.e., the shear profile simply grows vertically in time with little horizontal dependence). This would seem to be quite similar to viscous spread. Wood & Brummell (2018) further found that radiative spread could be prevented by magnetic field in a process like Ferraro's law; however, they considered a primordial field as in Gough & McIntyre (1998). It is thus too soon to say definitively whether these results would extend to a global dynamo in a solar-like parameter space.

In summary, the MHD case presented here offers a strong piece of evidence that magnetic tachocline confinement is possible in a fully 3-D, global geometry with fairly turbulent motions. It also clearly shows the presence of classical equatorial Rossby waves, which make up most of the horizontal motion, as well as low-frequency inertial oscillations, which may represent MHD and/or critical-layer Rossby waves. The low-frequency modes appear to induce dynamo action even below the convective-overshoot layer. These results suggest that the radiative interior of the Sun is not an "abyssal deep" at all, but rather is filled with strong horizontal motions, and that dynamo action may extend beneath the convection zone. In future work, we will assess the detailed origin of the low frequency modes and how they cohere with our current understanding of Rossby waves in the Sun.

5.11 Supplement: Numerical Specifics and Equation Identities

Our HD and MHD cases are simulations of spherical shells spanning $(r_\mathrm{i},\ r_\mathrm{o}) \equiv (0.49R_\odot,\ 0.95R_\odot)$, where $R_\odot \approx 700{,}000$ km is the solar radius. The base of the convection zone occurs near $0.72R_\odot$, so our shell covers about 160,000 km (by radius) in both the convection and radiative interior. In the convection zone, this translates to a density contrast of $\sim$20, or about three density scale heights (to borrow our notation from Chapter 2, $N_\rho = 3$). Our grid resolution is $N_\theta = 384$ and $N_\phi = 768$ in the horizontal directions (the maximum spherical harmonic degree after de-aliasing is $\ell_\mathrm{max} = 255$) and $N_r = (64, 64, 64)$ in the vertical direction. We use three stacked Chebyshev domains in radius (each with 64 grid points) with boundaries (r_i, $0.67R_\odot$, $0.72R_\odot$, r_o). The use of three radial domains and two internal boundaries maximizes the grid resolution in the overshoot layer (the Chebyshev collocation points cluster near the ends of each domain). We define the viscous and magnetic diffusion times across the radiative interior as $[r_\mathrm{ov} - r_\mathrm{i}]^2/\nu(r_\mathrm{ov})$ (this translates to 295 rotations) and $[r_\mathrm{ov} - r_\mathrm{i}]^2/\eta(r_\mathrm{ov})$ (this translates to 1180 rotations), respectively. The HD case was run in its equilibrated state for 7810 rotations (26.5 viscous diffusion times) and the MHD case for 12500 rotations (10.6 magnetic diffusion times).

5.11.1 Background Thermodynamic State

We treat the thermodynamic profiles of the stable-to-unstable transition in the Sun (which occurs at $r \equiv r_\mathrm{bcz}$) slightly differently than past work has. We choose a simplified entropy-gradient profile, which is zero in the convection zone, achieves a constant positive value in the stable layer, and has smooth matching in between. As mentioned in Chapter 1 (and now proven), the background state is fully specified by the entropy gradient and gravitational-acceleration profile. We begin by

assuming that the solar interior is a spherically symmetric ideal gas in hydrostatic balance:

$$\frac{d\overline{P}}{dr} = -\overline{\rho} g(r), \tag{5.11a}$$

$$\overline{P}(r) = \overline{\rho}(r)\mathcal{R}\overline{T}(r), \tag{5.11b}$$

$$\text{and} \qquad \frac{d\ln\overline{T}}{dr} - (\gamma-1)\frac{d\ln\overline{\rho}}{dr} = \frac{1}{c_{\rm v}}\frac{d\overline{S}}{dr}. \tag{5.11c}$$

Here, $c_{\rm v}$ ($c_{\rm p}$) is the specific heat at constant volume (pressure), $\mathcal{R} = k_B/\mu m_p$ is the gas constant (with k_B Boltzmann's constant, m_p the proton mass, and μ the mean molecular weight), and $\gamma = c_{\rm p}/c_{\rm v}$.

Equations (5.11) can be combined to yield an ordinary first-order differential equation for the temperature:

$$\frac{d\overline{T}}{dr} - \left[\frac{1}{c_{\rm p}}\frac{d\overline{S}}{dr}\right]\overline{T}(r) = -\frac{g(r)}{c_{\rm p}},$$

which has the analytic solution

$$\begin{aligned}\overline{T}(r) = &-\frac{e^{\overline{S}(r)/c_{\rm p}}}{c_{\rm p}}\int_{r_1}^{r} g(\widetilde{r}) e^{-\overline{S}(\widetilde{r})/c_{\rm p}} d\widetilde{r} \\ &+ \overline{T}(r_1) e^{[\overline{S}(r)-\overline{S}(r_1)]/c_{\rm p}},\end{aligned} \tag{5.12}$$

where r_1 is an arbitrary radius from which to start the integration. We choose $r_0 = r_{\rm tach} \equiv 5\times10^{10}$ cm $\approx 0.72 R_\odot$, $\overline{\rho}(r_{\rm tach}) = 0.18$ g cm^{-3}, and $\overline{T}(r_{\rm tach}) = 2.6\times10^6$ K. The thermodynamic variables at the base of the convection zone are thus pinned to the same values as in Featherstone & Hindman (2016a); Matilsky et al. (2020); Hindman et al. (2020); and the other simulations described in this thesis. We integrate numerically on a fine grid (5,000 uniformly spaced radial points) and then interpolate onto the simulation grid.

Equation (5.12), combined with Equations (5.11) and the boundary conditions, gives the temperature, density, and pressure in terms of the entropy gradient and gravitational acceleration, which is $g(r) = GM_\odot/r^2$. We choose a quartic matching between $d\overline{S}/dr = 0$ in the convection zone

and $d\overline{S}/dr = \beta \equiv 0.01$ erg g^{-1} K^{-1} cm^{-1} in the radiative interior:

$$\frac{d\overline{S}}{dr} = \begin{cases} \beta & r \leq r_{\rm tach} - \delta \\ \beta\left\{1 - \left[1 - \left(\frac{r - r_{\rm tach}}{\delta}\right)^2\right]^2\right\} & r_{\rm tach} - \delta < r < r_{\rm tach} \\ 0 & r \geq r_{\rm tach} \end{cases} \tag{5.13}$$

The quartic matching (instead of the tanh or erf profile employed in (for example) Guerrero et al. 2016a) ensures that none of the stable gradient in the radiative interior "leaks" into the convection zone. The solar stiffness β is (for example) $\sim 10^4$–10^5 times higher than the entropy gradients in `EULAG-MHD` needed to drive the convection (or in `Rayleigh`, $\sim 10^4$–10^5 times higher than the entropy gradients *driven by* the convection). A tanh matching (e.g., $d\overline{S}/dr = (\beta/2)\{1 - \tanh[(r - r_{\rm tach})/\delta]\}$) thus results in convective stability all the way up to about $r_{\rm tach} + 5\delta$, since $[1 - \tanh(5)]/2 \approx 5 \times 10^{-5}$. In the two cases presented here, we choose $\delta/R_\odot = 0.05$.

We do use a tanh profile to put the internal heating $Q(r)$ almost completely in the convection zone: $Q(r) = \alpha \tanh[(r - r_{\rm tach})/\delta_{\rm heat}][\overline{P}(r) - \overline{P}(r_{\rm o})]$, where $\delta_{\rm heat}/R_\odot = 0.03$. The constant α is chosen so the volume integral of $Q(r)$ over the whole shell is the solar luminosity. In the convection zones of our two models, the reference state is thus nearly identical the three-scale-height models in our prior work (Featherstone & Hindman, 2016a,b; Matilsky et al., 2018, 2019; Matilsky & Toomre, 2020a; Matilsky et al., 2020; Hindman et al., 2020; Matilsky & Toomre, 2021; Korre & Featherstone, 2021).

5.11.2 Induction Equation in Spherical Coordinates

We write the MHD induction equation as

$$\frac{\partial \boldsymbol{B}}{\partial t} = \nabla \times [\boldsymbol{v} \times \boldsymbol{B}] - \nabla \times [\eta(r) \nabla \times \boldsymbol{B}] \tag{5.14a}$$

$$\text{or} \quad \frac{\partial \boldsymbol{B}}{\partial t} = -\boldsymbol{B}(\nabla \cdot \boldsymbol{v}) + \boldsymbol{B} \cdot \nabla \boldsymbol{v} - \boldsymbol{v} \cdot \nabla \boldsymbol{B} + \mathbf{D}, \tag{5.14b}$$

where $\mathbf{D} \equiv -\nabla \times [\eta(r) \nabla \times \boldsymbol{B}]$. We refer to the first and second terms on the right-hand side of Equation (5.14a) as the "induction" and "diffusion," respectively. The three induction terms on

the right-hand side of Equation (5.14b) are traditionally interpreted as "compression," "shear," and "advection," respectively (recall the inductive analyses of the bistable dynamos in Chapter 4). This interpretation is problematic, however, because only compression and shear *perpendicular* to magnetic field lines can cause induction, and furthermore, only gradients in the local rate of strain (not the velocity) can cause shear. For example, $[\boldsymbol{B}\cdot\nabla\boldsymbol{v}]_\phi = r\sin\theta\boldsymbol{B}_{\rm pol}\cdot\nabla(v_\phi/r\sin\theta) + (1/r\sin\theta)B_\phi\partial v_\phi/\partial\phi$. Only the first term can shear poloidal field (via gradients not in the velocity v_ϕ but in the rate of strain $v_\phi/r\sin\theta$) to produce toroidal field; the second term cancels with a term in $-B_\phi(\nabla\cdot\boldsymbol{v})$. We thus rewrite Equation (5.14b) for the horizontal directions as follows:

$$\frac{\partial B_\phi}{\partial t} = \underbrace{-B_\phi\left[\left(\frac{\partial v_r}{\partial r}\right)+\left(\frac{1}{r}\frac{\partial v_\theta}{\partial\theta}+\frac{v_r}{r}\right)\right]}_{\text{“perpendicular” toroidal compression}} + \underbrace{r\sin\theta\boldsymbol{B}_{\rm pol}\cdot\nabla\left(\frac{v_\phi}{r\sin\theta}\right)}_{\text{“perpendicular” toroidal shear}} - \boldsymbol{v}\cdot\nabla B_\phi + D_\phi \tag{5.15a}$$

and

$$\frac{\partial B_\theta}{\partial t} = \underbrace{-B_\theta\left[\left(\frac{\partial v_r}{\partial r}\right)+\left(\frac{1}{r\sin\theta}\frac{\partial v_\phi}{\partial\phi}+\frac{\cot\theta v_\theta}{r}+\frac{v_r}{r}\right)\right]}_{\text{“perpendicular” }\theta\text{ compression}} + \underbrace{r(B_r\hat{\boldsymbol{e}}_r+B_\phi\hat{\boldsymbol{e}}_\phi)\cdot\nabla\left(\frac{v_\theta}{r}\right)}_{\text{“perpendicular” }\theta\text{ shear}} - \boldsymbol{v}\cdot\nabla B_\theta + D_\theta, \tag{5.15b}$$

where the third term on the right-hand side of each equation is the advection. These Equations follow straightforwardly from Equation (5.14b) by canceling and rearranging terms. However, the "perpendicularity" of the shear and compression may be seen by considering, at a given point (r,θ,ϕ), planes perpendicular to the directions $(\hat{\boldsymbol{e}}_r,\hat{\boldsymbol{e}}_\theta,\hat{\boldsymbol{e}}_\phi)$ and then computing $\nabla\cdot\boldsymbol{v}$ and $\boldsymbol{B}\cdot\nabla$ while keeping the gradient operator restricted to these planes and expressing the result in spherical coordinates. We will present the details in future work.

When the azimuthal flow is dominated by the mean rotation rate, it makes sense to define

$$\text{mean shear} \equiv r\sin\theta\boldsymbol{B}_{\rm pol}\cdot\nabla\Omega. \tag{5.16}$$

Note that our mean-shear term uses the *full* $\boldsymbol{B}_{\rm pol}$, not the temporally and longitudinally averaged $\langle\boldsymbol{B}_{\rm pol}\rangle$ that is used in the original Ferraro's law. When the advection terms can be neglected, when

mean shear dominates the other induction terms in Equation (5.15a), and when the velocities are largely horizontal (all conditions well satisfied in the MHD case's radiative interior), Equations (5.15) reduce to Equations (5.5) and (5.6).

Because our fields are non-axisymmetric, we consider the evolution of the magnetic energy density $B^2/8\pi$, which is obtained from taking the dot product of the induction equation with $\boldsymbol{B}/4\pi$. As in Figure 5.4, we analyze the production of toroidal and poloidal magnetic energy ($B_\phi^2/8\pi$ and $B_{\rm pol}^2/8\pi$, respectively) separately. In the legend of Figure 5.4, we thus refer to the magnetic energy production terms due to "mean shear"—$(B_\phi/4\pi) \times$ (mean shear); "poloidal induction" $\boldsymbol{B}_{\rm pol} \cdot \nabla \times [\boldsymbol{v} \times \boldsymbol{B}]$; "$\theta$ compression"—$(B_\theta/4\pi) \times$ (θ compression); and so on.

Chapter 6

Concluding Remarks

In this thesis, we have explored the dynamics of the solar interior using the advanced machinery of fully 3-D, global, nonlinear, magnetic convection simulations. We sought to understand how convection under the influence of rotation and magnetism could explain some of the most striking aspects of the observed solar dynamo and helioseismically inferred differential rotation.

We began by discussing the hydrodynamic (HD) Sun, assessing the dynamics of the helioseismically inferred Near-Surface Shear Layer (NSSL) and the tilts of the solar isorotation contours. We found that the solar NSSL—which may play a prominent role in the global dynamo as a site of strong shear in close proximity to sunspots—is still essentially an unsolved problem. This is likely because of our inability to understand the dynamics of the Sun's meridional circulation, and possibly its near-surface magnetism. In addressing the tilts of the isorotation contours, we found that a fixed-flux outer thermal boundary condition—which was inspired by the observed invariance of the Sun's emissive flux with latitude—led to solar-like contour tilts. By contrast, the commonly employed fixed-entropy (in other work, fixed-temperature) thermal boundary condition led to the opposite sense of tilt. We identified for the first time a purely HD mechanism (namely, heat transport by Busse columns, or convective Rossby waves) by which the Sun might move thermal energy from equator to pole. In combination with a fixed-flux boundary condition (which prohibits "leaks" of energy out through the poles), the Busse columns could thus maintain the thermal wind that has long been invoked to explain the helioeseismically observed contour tilts.

In future work, there is much to be done regarding the HD Sun. First, the "convective

conundrum" is still a major problem for simulations. Restated here, the issue is that simulated convection pushed closer to the turbulent solar parameter regime seems unable to maintain a solar-like differential rotation. Specifically, simulations must rotate more rapidly than the solar rate, carry less luminosity than the Sun, or a combination thereof. Otherwise, they risk falling into "anti-solar" states, with polar regions rotating faster than the equator. One approach to addressing the convective conundrum would be to remove the simulation's luminosity via a cooling layer (with amplitude and thickness controlled a priori), in place of the traditionally employed outer thermal boundary layer. This could potentially separate the spatial scales of the thermal driving from those of the angular momentum transport, thereby assessing whether the large-scale motions in current simulations are being driven too hard. Simulated convective velocities being too high at the large scales is the often-invoked, though still untested, reason for the convective conundrum (recall our detailed discussion of this scale-separation issue in the Introduction, Section 1.2.3). Our work on the NSSL and outer thermal boundary condition shows that the near-surface dynamics may significantly affect the global properties of simulations, and the most obvious step forward is the demolition of our rather unrealistic outer thermal boundary layer.

Second, future work may address the NSSL by way of a systematic investigation of the dynamics of meridional circulation. We recall that our models did not reproduce the NSSL because the meridional circulation developed in a thin band to eliminate any shear (and earlier global models of the NSSL likely suffered from the same issue). How meridional circulation develops, in global convection simulations or in a real star, is a difficult problem. The circulation is at a higher order than the dominant flows (convection and differential rotation) and responds to residual force balances that usually require very long integration times to assess in the presence of high-amplitude convective "noise." The approach in past work has generally been to assume that changes to the differential rotation (i.e., torques) drive the meridional circulation. Invoking this phenomenon, so-called gyroscopic pumping (e.g., Haynes et al. 1991; McIntyre 1998, 2002; Miesch & Hindman 2011), may cause issues in our understanding, since it does not treat the meridional force balance directly. Global simulations are in a privileged position to address the meridional-circulation problem, since

the flows, while more laminar than in a star, are fully self-consistent and the meridional force balance can be directly assessed.

Third, the tilted solar isorotation contours were a striking surprise revealed by helioseismology and remain largely an outstanding problem. We have made substantial progress in this area by identifying poleward heat transport by Busse columns as a natural driver of the solar thermal wind. However, our results relied on an artificially imposed fixed-flux outer thermal boundary condition. How the Sun actually achieves latitudinally independent emissive flux (if there is indeed a thermal wind in the interior) is a non-trivial question. No doubt the convective flows at small scales (granulation, which is absent in most global simulations) may play an important role, as may the degree of turbulence, the small-scale magnetism, and the properties of the near-surface meridional circulation. Further inroads into addressing the convective conundrum and meridional circulation may thus also make progress in solving the problem of constant emissive flux (and the related problem of contour tilt).

In our explorations of the magnetohydrodynamic (MHD) Sun, we found a remarkable phenomenon of bistability. Here, our global dynamo simulations exhibited two distinct cycles simultaneously. One cycle involved a set of four "magnetic wreaths," similar to the structures encountered in past simulations, that in our case displayed a cycle reminiscent of the magnetic butterfly diagram. The other cycle involved our newly identified "partial wreaths," possibly similar to the non-axisymmetric single-hemisphere toroidal structures encountered in past dynamo simulations, that in our case displayed temporal behavior similar to the Sun's active longitudes and hemispheric asymmetry. The bistable system began with only the fourfold-wreath cycle operating, but eventually reached a state wherein both cycles operated more or less superimposed. Looked at another way, two basins of attraction were available to the dynamo, which could fall into one basin or both basins in a chaotic manner. Furthermore, small changes to the initial conditions resulted in vastly different states after a long time interval, also consistent with dynamical chaos. This work highlighted the richness of the nonlinear, chaotic dynamics present in stellar interiors, and also offered the practical possibility that solar and stellar dynamos observed in one state may exist in

quite different states at other points of their evolution.

We ended this thesis by discussing our extension of the bistable dynamos to include a stably stratified radiative layer below the convection zone. In this MHD case, the partial-wreath cycle was dominant. The magnetism extended all the way into the radiative interior and produced a torque that forced the background fluid into solid-body rotation. Meanwhile, Reynolds stresses in the convection zone forced a weak solar-like differential rotation. The resulting shear layer bore resemblance to the solar tachocline and was maintained against viscous spread for many diffusion times. This was the first time a 3-D global simulation was shown capable of self-consistently confining a tachocline magnetically. The MHD case was similar in some ways to the early slow and fast magnetic confinement scenarios, but implied a form for the confining magnetism that was distinct from the axisymmetric primordial-field remnant (Gough-and-McIntyre slow scenario) or the "turbulently pumped" axisymmetric magnetism from the 22-year cycle (Forgács-Dajka-and-Petrovay fast scenario). In particular, our confining magnetic torque came from the non-axisymmetric, irregularly cycling partial wreaths. Furthermore, we showed that the partial wreaths were inductively produced, likely by low-frequency inertial oscillations, even below the convective overshoot layer. These results may profoundly challenge the idea that stellar radiative interiors are passive reservoirs or "abyssal deeps," simply accepting whatever magnetism the convection zone pumps in and storing it until it grows strong enough to buoyantly rise to the surface. Instead, our calculations were consistent with a dynamically active radiative interior, in which dynamo amplification can occur locally via the strong horizontal motions associated with inertial oscillations.

In future work, the sensitivities of bistable dynamos—and the apparently related problem of magnetic tachocline confinement—must be more systematically explored. Due to inherent computational constraints, we so far have only sampled a small portion of parameter space, and the richness of magnetism achieved even in this limited regime was still quite impressive. Pinpointing how fourfold and partial wreaths may operate in the solar interior (which, of course, rotates at the solar rate and is highly turbulent—a parameter space that is still inaccessible to global models because of the convective conundrum) may yield significant insights into the solar dynamo. More

specifically, the Sun's striking 22-year cycle, long-period modulations, active longitudes, and hemispheric asymmetry are the results of complex nonlinear dynamics in the interior. Future global simulations will be powerful tools to reproduce some of the Sun's behaviors and understand them from a fundamental dynamical perspective.

If partial wreaths are indeed a possible magnetic phenomenon capable of confining the solar tachocline, future global models must assess the inductive properties of the radiative interior. We plan specifically to classify the low-frequency inertial oscillations that gave rise to dynamo action in our MHD case. We will assess how these magnetically important oscillations may be related to the large body of prior work on MHD Rossby waves and tachocline magneto-shear instabilities. If inertial oscillations really can drive a dynamo, our work hints at a profoundly different view of stellar radiative interiors. Instead of being a passive reservoir, or "abyssal deep," the stable layer may need to be treated as a dynamically active region fully coupled to its neighboring convection zone. The interplay of convective overshoot, inertial oscillations, and magnetic induction may then significantly affect our understanding of stellar dynamos.

In conclusion, it is our view that the field of solar and stellar interiors—although one of the oldest and most well-studied branches of astrophysics—still contains many mysteries. Observations of the solar magnetic field, as well as the internal rotation profile deduced by helioseismology, show that stars can exhibit remarkably well-ordered behavior. Even more striking, this behavior arises from the nonlinear dynamics of highly turbulent convection under the influence of rotation and magnetism. In this thesis, we have only begun to scratch the surface of some of the major observed phenomena—the NSSL, the isorotation contour tilts, the 22-year cycle, and the solar tachocline. Our work has shown that global simulations present a unique window into the dynamics of stellar interiors and may provide many more insights going forward. We hope that this thesis may serve to highlight what is possible using global modeling and that it may potentially inspire future research in solar and stellar dynamics.

Bibliography

Acevedo-Arreguin, L. A., Garaud, P., & Wood, T. S. 2013, "Dynamics of the solar tachocline – III. Numerical solutions of the Gough and McIntyre model", Mon. Not. R. Astron. Soc., 434, 720, doi: 10.1093/mnras/stt1065

Alfvén, H. 1943, "On the effect of a vertical magnetic field in a conducting atmosphere", Ark. Mat. Astro. Fysik, 29A, 11

Alvan, L., Brun, A. S., & Mathis, S. 2014, "Theoretical seismology in 3D: Nonlinear simulations of internal gravity waves in solar-like stars", Astron. Astrophys., 565, A42, doi: 10.1051/0004-6361/201323253

Alvan, L., Strugarek, A., Brun, A. S., Mathis, S., & Garcia, R. A. 2015, "Characterizing the propagation of gravity waves in 3D nonlinear simulations of solar-like stars", Astron. Astrophys., 581, A112, doi: 10.1051/0004-6361/201526250

Anders, E. H., Vasil, G. M., Brown, B. P., & Korre, L. 2020, "Convective dynamics with mixed temperature boundary conditions: Why thermal relaxation matters and how to accelerate it", Phys. Rev. Fluids, 5, doi: 10.1103/physrevfluids.5.083501

Andrews, D. G., Holton, J. R., & Leovy, C. B. 1987, Middle atmosphere dynamics (New York: Academic Press). https://www.osti.gov/biblio/5936274

Anselmann, P., Hampel, W., Heusser, G., Kiko, J., Kirsten, T., Laubenstein, M., Pernicka, E., Pezzoni, S., Rönn, U., Sann, M., Schlosser, C., Wink, R., Wójcik, M., Ammon, R., Ebert, K., Fritsch, T., Heidt, D., Henrich, E., Stieglitz, L., Weirich, F., Balata, M., Lalla, H., Bellotti, E., Cattadori, C., Cremonesi, O., Ferrari, N., Fiorini, E., Zanotti, L., Altmann, M., Feilitzsch, F., Mößbauer, R., Schanda, U., Berthomieu, G., Schatzman, E., Carmi, I., Dostrovsky, I., Bacci, C., Belli, P., Bernabei, R., d'Angelo, S., Paoluzi, L., Bevilacqua, A., Charbit, S., Cribier, M., Gosset, L., Rich, J., Spiro, M., Stolarczyk, T., Tao, C., Vignaud, D., Boger, J., Hahn, R., Hartmann, F., Rowley, J., Stoenner, R., & Weneser, J. 1995, "GALLEX solar neutrino observations: Complete results for GALLEX II", Phys. Lett. B, 357, 237, doi: 10.1016/0370-2693(95)00897-t

Antia, H. M., & Basu, S. 2001, "Temporal variations of the solar rotation rate at high latitudes", Astrophys. J., 559, L67, doi: 10.1086/323701

Antonucci, E., Hoeksema, J. T., & Scherrer, P. H. 1990, "Rotation of the photospheric magnetic fields: A North-South asymmetry", Astrophys. J., 360, 296, doi: 10.1086/169120

Asplund, M., Amarsi, A. M., & Grevesse, N. 2021, "The chemical make-up of the Sun: A 2020 vision", Astron. Astrophys., 653, A141, doi: 10.1051/0004-6361/202140445

Asplund, M., Grevesse, N., Sauval, A. J., & Scott, P. 2009, "The chemical composition of the Sun", Ann. Rev. Astron. Astrophys., 47, 481, doi: 10.1146/annurev.astro.46.060407.145222

Augustson, K., Brun, A. S., Miesch, M., & Toomre, J. 2015, "Grand minima and equatorward propagation in a cycling stellar convective dynamo", Astrophys. J., 809, 149, doi: 10.1088/0004-637x/809/2/149

Augustson, K. C., Brown, B. P., Brun, A. S., Miesch, M. S., & Toomre, J. 2012, "Convection and differential rotation in F-type stars", Astrophys. J., 756, 169, doi: 10.1088/0004-637x/756/2/169

Augustson, K. C., Brun, A. S., & Toomre, J. 2013, "Dynamo action and magnetic cycles in F-type stars", Astrophys. J., 777, 153, doi: 10.1088/0004-637x/777/2/153

Babcock, H. W. 1961, "The topology of the Sun's magnetic field and the 22-year cycle", Astrophys. J., 133, 572, doi: 10.1086/147060

Bahcall, J. N. 1964, "Solar neutrinos. I. Theoretical", Phys. Rev. Lett., 12, 300, doi: 10.1103/physrevlett.12.300

Bahcall, J. N., Bahcall, N. A., & Ulrich, R. K. 1968, "Mixing in the Sun and neutrino fluxes", Astrophys. J. Lett., 2, L91

Bahcall, J. N., Pinsonneault, M. H., & Basu, S. 2001, "Solar models: Current epoch and time dependences, neutrinos, and helioseismological properties", Astrophys. J., 555, 990, doi: 10.1086/321493

Bahcall, J. N., & Shaviv, G. 1968, "Solar models and neutrino fluxes", Astrophys. J., 153, 113, doi: 10.1086/149641

Bai, T. 1990, "Solar 'hot spots' are still hot", Astrophys. J. Lett., 364, L17, doi: 10.1086/185864

Bai, T. 2003, "Hot spots for solar flares persisting for decades: Longitude distributions of flares of cycles 19–23", Astrophys. J., 585, 1114, doi: 10.1086/346152

Bai, T., & Sturrock, P. A. 1987, "The 152-day periodicity of the solar flare occurrence rate", Nat., 327, 601, doi: 10.1038/327601a0

Balbus, S. A. 2009a, "A simple model for solar isorotational contours", Mon. Not. R. Astron. Soc., 395, 2056, doi: 10.1111/j.1365-2966.2009.14469.x

Balbus, S. A., Bonart, J., Latter, H. N., & Weiss, N. O. 2009, "Differential rotation and convection in the Sun", Mon. Not. R. Astron. Soc., 400, 176, doi: 10.1111/j.1365-2966.2009.15464.x

Balbus, S. A., & Hawley, J. F. 1991, "A powerful local shear instability in weakly magnetized disks. I. Linear analysis. II. Nonlinear evolution", Astrophys. J., 376, 214, doi: 10.1086/170270

Ballester, J. L., Oliver, R., & Carbonell, M. 2005, "The periodic behaviour of the North-South asymmetry of sunspot areas revisited", Astron. Astrophys., 431, L5, doi: 10.1051/0004-6361:200400135

Balthasar, H., & Schussler, M. 1983, "Preferred longitudes of sunspot groups and high-speed solar wind streams: Evidence for a 'solar memory' ", Sol. Phys., 87, 23, doi: 10.1007/bf00151156

Barnabé, R., Strugarek, A., Charbonneau, P., Brun, A. S., & Zahn, J.-P. 2017, "Confinement of the solar tachocline by a cyclic dynamo magnetic field", Astron. Astrophys., 601, A47, doi: 10.1051/0004-6361/201630178

Bartenwerfer, D. 1973, "Differential rotation, magnetic fields and the solar neutrino flux", Astron. Astrophys., 25, 455

Baruteau, C., & Rieutord, M. 2013, "Inertial waves in a differentially rotating spherical shell", J. Fluid Mech., 719, 47, doi: 10.1017/jfm.2012.605

Basu, S. 2016, "Global seismology of the Sun", Liv. Rev. Sol. Phys., 13, doi: 10.1007/s41116-016-0003-4

Basu, S., & Antia, H. 2008, "Helioseismology and solar abundances", Phys. Rep., 457, 217, doi: 10.1016/j.physrep.2007.12.002

Basu, S., & Antia, H. M. 2003, "Changes in solar dynamics from 1995 to 2002", Astrophys. J., 585, 553, doi: 10.1086/346020

Basu, S., Chaplin, W. J., Elsworth, Y., New, R., & Serenelli, A. M. 2009, "Fresh insights on the structure of the solar core", Astrophys. J., 699, 1403, doi: 10.1088/0004-637x/699/2/1403

Basu, S., Pinsonneault, M. H., & Bahcall, J. N. 2000, "How much do helioseismological inferences depend on the assumed reference model?", Astrophys. J., 529, 1084, doi: 10.1086/308302

Beaudoin, P., Strugarek, A., & Charbonneau, P. 2018, "Differential rotation in solar-like convective envelopes: Influence of overshoot and magnetism", Astrophys. J., 859, 61, doi: 10.3847/1538-4357/aabfef

Beeck, B., Collet, R., Steffen, M., Asplund, M., Cameron, R. H., Freytag, B., Hayek, W., Ludwig, H.-G., & Schüssler, M. 2012, "Simulations of the solar near-surface layers with the CO5bold, MURaM, and Stagger codes", Astron. Astrophys., 539, A121, doi: 10.1051/0004-6361/201118252

Belucz, B., & Dikpati, M. 2013, "Role of asymmetric meridional circulation in producing North-South asymmetry in a solar cycle dynamo model", Astrophys. J., 779, 4, doi: 10.1088/0004-637x/779/1/4

Benz, A. O. 2016, "Flare observations", Liv. Rev. Sol. Phys., 14, doi: 10.1007/s41116-016-0004-3

Berdyugina, S. V., & Usoskin, I. G. 2003, "Active longitudes in sunspot activity: Century scale persistence", Astron. Astrophys., 405, 1121, doi: 10.1051/0004-6361:20030748

Berrington, K. 1995, "Summary of the iron and opacity projects", in Astronomical Society of the Pacific Conference Series, Vol. 78, Astrophysical Applications of Powerful New Databases, ed. S. J. Adelman & W. L. Wiese, 19

Bice, C. P., & Toomre, J. 2020, "Probing the influence of a tachocline in simulated M-dwarf dynamos", Astrophys. J., 893, 107, doi: 10.3847/1538-4357/ab8190

Bice, C. P., & Toomre, J. 2022, "Longitudinally modulated dynamo action in simulated M-dwarf stars", Astrophys. J., in press

Bogart, R. S. 1982, "Recurrence of solar activity: Evidence for active longitudes", Sol. Phys., 76, 155, doi: 10.1007/bf00214137

Böhm-Vitense, E. 2007, "Chromospheric activity in g and k main-sequence stars, and what it tells us about stellar dynamos", Astrophys. J., 657, 486, doi: 10.1086/510482

Braginsky, S. I., & Roberts, P. H. 1975, "Magnetic field generation by baroclinic waves", Proc. Roy. Soc. A., 347, 125, doi: 10.1098/rspa.1975.0201

Braginsky, S. I., & Roberts, P. H. 1995, "Equations governing convection in Earth's core and the geodynamo", Geophys. Astrophys. Fluid Dyn., 79, 1, doi: 10.1080/03091929508228992

Brandenburg, A. 2005, "The case for a distributed solar dynamo shaped by near-surface shear", Astrophys. J., 625, 539, doi: 10.1086/429584

Brandenburg, A. 2007, "Near-surface shear layer dynamics", Proc. Int. Astron. U., 2, 457, doi: 10.1017/s1743921307000919

Brandenburg, A. 2016, "Stellar mixing length theory with entropy rain", Astrophys. J., 832, 6, doi: 10.3847/0004-637x/832/1/6

Brandenburg, A. 2018, "Advances in mean-field dynamo theory and applications to astrophysical turbulence", J. Plasma Phys., 84, doi: 10.1017/s0022377818000806

Brandenburg, A., & Dobler, W. 2002, "Hydromagnetic turbulence in computer simulations", Comp. Phys. Comm., 147, 471, doi: 10.1016/s0010-4655(02)00334-x

Brandenburg, A., & Subramanian, K. 2005, "Astrophysical magnetic fields and nonlinear dynamo theory", Phys. Rep., 417, 1, doi: 10.1016/j.physrep.2005.06.005

Braun, D. C., & Birch, A. C. 2008, "Surface-focused seismic holography of sunspots: I. Observations", Sol. Phys., 251, 267, doi: 10.1007/s11207-008-9152-5

Braun, D. C., Birch, A. C., & Fan, Y. 2021, "Probing the solar meridional circulation using Fourier Legendre decomposition", Astrophys. J., 911, 54, doi: 10.3847/1538-4357/abe7e4

Braun, D. C., Fan, Y., Lindsey, C., & Jefferies, S. M. 1996, "Helioseismic measurements of subsurface outflows from sunspots", in Bull. Amer. Astron. Soc., Vol. 188, 69.11

Brown, B. P., Browning, M. K., Brun, A. S., Miesch, M. S., & Toomre, J. 2008, "Rapidly rotating Suns and active nests of convection", Astrophys. J., 689, 1354, doi: 10.1086/592397

Brown, B. P., Browning, M. K., Brun, A. S., Miesch, M. S., & Toomre, J. 2010, "Persistent magnetic wreaths in a rapidly rotating Sun", Astrophys. J., 711, 424, doi: 10.1088/0004-637x/711/1/424

Brown, B. P., Miesch, M. S., Browning, M. K., Brun, A. S., & Toomre, J. 2011, "Magnetic cycles in a convective dynamo simulation of a young solar-type star", Astrophys. J., 731, 69, doi: 10.1088/0004-637x/731/1/69

Brown, B. P., Vasil, G. M., & Zweibel, E. G. 2012, "Energy conservation and gravity waves in sound-proof treatments of stellar interiors. Part I. Anelastic approximations", Astrophys. J., 756, 109, doi: 10.1088/0004-637x/756/2/109

Brown, T. M., Christensen-Dalsgaard, J., Dziembowski, W. A., Goode, P., Gough, D. O., & Morrow, C. A. 1989, "Inferring the Sun's internal angular velocity from observed p-mode frequency splittings", Astrophys. J., 343, 526, doi: 10.1086/167727

Browning, M. K. 2008, "Simulations of dynamo action in fully convective stars", Astrophys. J., 676, 1262, doi: 10.1086/527432

Browning, M. K., Miesch, M. S., Brun, A. S., & Toomre, J. 2006, "Dynamo action in the solar convection zone and tachocline: Pumping and organization of toroidal fields", Astrophys. J., 648, L157, doi: 10.1086/507869

Brummell, N. H., Clune, T. L., & Toomre, J. 2002, "Penetration and overshooting in turbulent compressible convection", Astrophys. J., 570, 825, doi: 10.1086/339626

Brun, A., & Strugarek, A. 2019, "Turbulence, magnetism, and transport inside stars", EAS Pub. Series, 82, 311, doi: 10.1051/eas/1982029

Brun, A. S., Antia, H. M., & Chitre, S. M. 2010, "Is the solar convection zone in strict thermal wind balance?", Astron. Astrophys., 510, A33, doi: 10.1051/0004-6361/200913166

Brun, A. S., Browning, M. K., Dikpati, M., Hotta, H., & Strugarek, A. 2015, "Recent advances on solar global magnetism and variability", Space Sci. Rev., 196, 101, doi: 10.1007/s11214-013-0028-0

Brun, A. S., Miesch, M. S., & Toomre, J. 2004, "Global-scale turbulent convection and magnetic dynamo action in the solar envelope", Astrophys. J., 614, 1073, doi: 10.1086/423835

Brun, A. S., Miesch, M. S., & Toomre, J. 2011, "Modeling the dynamical coupling of solar convection with the radiative interior", Astrophys. J., 742, 79, doi: 10.1088/0004-637x/742/2/79

Brun, A. S., Strugarek, A., Noraz, Q., Perri, B., Varela, J., Augustson, K., Charbonneau, P., & Toomre, J. 2022, "Powering stellar magnetism: Energy transfers in cyclic dynamos of Sun-like stars", Astrophys. J., 926, 21, doi: 10.3847/1538-4357/ac469b

Brun, A. S., & Toomre, J. 2002, "Turbulent convection under the influence of rotation: Sustaining a strong differential rotation", Astrophys. J., 570, 865, doi: 10.1086/339228

Brun, A. S., & Zahn, J.-P. 2006, "Magnetic confinement of the solar tachocline", Astron. Astrophys., 457, 665, doi: 10.1051/0004-6361:20053908

Brun, A. S., Strugarek, A., Varela, J., Matt, S. P., Augustson, K. C., Emeriau, C., DoCao, O. L., Brown, B., & Toomre, J. 2017, "On differential rotation and overshooting in solar-like stars", Astrophys. J., 836, 192, doi: 10.3847/1538-4357/aa5c40

Buldgen, G., Salmon, S., & Noels, A. 2019, "Progress in global helioseismology: A new light on the solar modeling problem and its implications for solar-like stars", Front. Astron. Space Sci., 6, doi: 10.3389/fspas.2019.00042

Busse, F. H. 1970a, "Differential rotation in stellar convection zones", Astrophys. J., 159, 629, doi: 10.1086/150337

Busse, F. H. 1970b, "Thermal instabilities in rapidly rotating systems", J. Fluid Mech., 44, 441, doi: 10.1017/s0022112070001921

Busse, F. H. 1973, "Differential rotation in stellar convection zones. II", Astron. Astrophys., 28, 27

Busse, F. H. 2002, "Convective flows in rapidly rotating spheres and their dynamo action", Phys. Fluids, 14, 1301, doi: 10.1063/1.1455626

Carlsson, M., Pontieu, B. D., & Hansteen, V. H. 2019, "New view of the solar chromosphere", Ann. Rev. Astron. Astrophys., 57, 189, doi: 10.1146/annurev-astro-081817-052044

Chandrasekhar, S. 1956, "Axisymmetric magnetic fields and fluid motions.", Astrophys. J., 124, 232, doi: 10.1086/146217

Chandrasekhar, S. 1961, Hydrodynamic and hydromagnetic stability (New York: Dover Publications)

Chang, H.-Y. 2009, "Periodicity of north–south asymmetry of sunspot area revisited: Cepstrum analysis", New Astron., 14, 133, doi: 10.1016/j.newast.2008.07.001

Charbonneau, P. 2007, "Cross-hemispheric coupling in a Babcock-Leighton model of the solar cycle", Adv. Space Res., 40, 899, doi: 10.1016/j.asr.2006.12.046

Charbonneau, P. 2014, "Solar dynamo theory", Ann. Rev. Astron. Astrophys., 52, 251, doi: 10.1146/annurev-astro-081913-040012

Charbonneau, P. 2020, "Dynamo models of the solar cycle", Liv. Rev. Sol. Phys., 17, doi: 10.1007/s41116-020-00025-6

Charbonneau, P., Christensen-Dalsgaard, J., Henning, R., Larsen, R. M., Schou, J., Thompson, M. J., & Tomczyk, S. 1999a, "Helioseismic constraints on the structure of the solar tachocline", Astrophys. J., 527, 445, doi: 10.1086/308050

Charbonneau, P., Dikpati, M., & Gilman, P. A. 1999b, "Stability of the solar latitudinal differential rotation inferred from helioseismic data", Astrophys. J., 526, 523, doi: 10.1086/307989

Charbonneau, P., & MacGregor, K. B. 1997, "Solar interface dynamos. II. Linear, kinematic models in spherical geometry", Astrophys. J., 486, 502, doi: 10.1086/304485

Chen, F., Rempel, M., & Fan, Y. 2017, "Emergence of magnetic flux generated in a solar convective dynamo. I. The formation of sunspots and active regions, and the origin of their asymmetries", Astrophys. J., 846, 149, doi: 10.3847/1538-4357/aa85a0

Chen, R., & Zhao, J. 2017, "A comprehensive method to measure solar meridional circulation and the center-to-limb effect using time–distance helioseismology", Astrophys. J., 849, 144, doi: 10.3847/1538-4357/aa8eec

Cheung, M. C. M., Rempel, M., Title, A. M., & Schüssler, M. 2010, "Simulation of the formation of a solar active region", Astrophys. J., 720, 233, doi: 10.1088/0004-637x/720/1/233

Chou, D.-Y., & Dai, D.-C. 2001, "Solar cycle variations of subsurface meridional flows in the Sun", Astrophys. J., 559, L175, doi: 10.1086/323724

Choudhuri, A. R. 2021, "A theoretical estimate of the pole-equator temperature difference and a possible origin of the near-surface shear layer", Sol. Phys., 296, doi: 10.1007/s11207-021-01784-7

Christensen-Dalsgaard, J. 1991, "Some aspects of the theory of solar oscillations", Geophys. Astrophys. Fluid Dyn., 62, 123, doi: 10.1080/03091929108229129

Christensen-Dalsgaard, J. 2002, "Helioseismology", Rev. Mod. Phys., 74, 1073, doi: 10.1103/revmodphys.74.1073

Christensen-Dalsgaard, J. 2021, "Solar structure and evolution", Liv. Rev. Sol. Phys., 18, doi: 10.1007/s41116-020-00028-3

Christensen-Dalsgaard, J., Däppen, W., Ajukov, S. V., Anderson, E. R., Antia, H. M., Basu, S., Baturin, V. A., Berthomieu, G., Chaboyer, B., Chitre, S. M., Cox, A. N., Demarque, P., Donatowicz, J., Dziembowski, W. A., Gabriel, M., Gough, D. O., Guenther, D. B., Guzik, J. A., Harvey, J. W., Hill, F., Houdek, G., Iglesias, C. A., Kosovichev, A. G., Leibacher, J. W., Morel, P., Proffitt, C. R., Provost, J., Reiter, J., Rhodes, E. J., Rogers, F. J., Roxburgh, I. W., Thompson, M. J., & Ulrich, R. K. 1996, "The current state of solar modeling", Sci., 272, 1286, doi: 10.1126/science.272.5266.1286

Clark, A. 1973, "The linear spin-up of a strongly stratified fluid of small Prandtl number", J. Fluid Mech., 60, 561, doi: 10.1017/s0022112073000340

Claverie, A., Isaak, G. R., McLeod, C. P., van der Raay, H. B., & Cortes, T. R. 1979, "Solar structure from global studies of the 5-minute oscillation", Nat., 282, 591, doi: 10.1038/282591a0

Cleveland, B. T., Daily, T., Davis, R., Distel, J. R., Lande, K., Lee, C. K., Wildenhain, P. S., & Ullman, J. 1998, "Measurement of the solar electron neutrino flux with the Homestake chlorine detector", Astrophys. J., 496, 505, doi: 10.1086/305343

Cline, K. S., Brummell, N. H., & Cattaneo, F. 2003, "On the formation of magnetic structures by the combined action of velocity shear and magnetic buoyancy", Astrophys. J., 588, 630, doi: 10.1086/373894

Clune, T., Elliott, J., Miesch, M., Toomre, J., & Glatzmaier, G. 1999, "Computational aspects of a code to study rotating turbulent convection in spherical shells", Parallel Comp., 25, 361, doi: 10.1016/s0167-8191(99)00009-5

Collins, G. W. 1963, "Continuum emission from a rapidly rotating stellar atmosphere.", Astrophys. J., 138, 1134, doi: 10.1086/147712

Collins, George W., I. 1989, The fundamentals of stellar astrophysics II.

Cope, L., Garaud, P., & Caulfield, C. P. 2020, "The dynamics of stratified horizontal shear flows at low Péclet number", J. Fluid Mech., 903, doi: 10.1017/jfm.2020.600

Cowling, T. G. 1957, Magnetohydrodynamics (New York: Interscience Publishers)

Cox, J. P. 1980, Theory of stellar pulsation (Princeton: Princeton University Press)

Cranmer, S. R., & Winebarger, A. R. 2019, "The properties of the solar corona and its connection to the solar wind", Ann. Rev. Astron. Astrophys., 57, 157, doi: 10.1146/annurev-astro-091918-104416

Damiani, C., Rozelot, J., Lefebvre, S., Kilcik, A., & Kosovichev, A. 2011, "A brief history of the solar oblateness. A review", J. Atm. Sol.-Terr. Phys., 73, 241, doi: 10.1016/j.jastp.2010.02.021

Däppen, W., Gough, D. O., Kosovichev, A. G., & Thompson, M. J. 1991, "A new inversion for the hydrostatic stratification of the sun", in Challenges to Theories of the Structure of Moderate-Mass Stars (Berlin: Springer Berlin Heidelberg), 111–120, doi: 10.1007/3-540-54420-8_57

Däppen, W., Mihalas, D., Hummer, D. G., & Mihalas, B. W. 1988, "The equation of state for stellar envelopes. III. Thermodynamic quantities", Astrophys. J., 332, 261, doi: 10.1086/166650

Davis, R. 1964, "Solar neutrinos. II. Experimental", Phys. Rev. Lett., 12, 303, doi: 10.1103/physrevlett.12.303

Davis, R. 2003, "Nobel lecture: A half-century with solar neutrinos", Rev. Mod. Phys., 75, 985, doi: 10.1103/revmodphys.75.985

Davis, R., Harmer, D. S., & Hoffman, K. C. 1968, "Search for neutrinos from the Sun", Phys. Rev. Lett., 20, 1205, doi: 10.1103/physrevlett.20.1205

Demarque, P., Mengel, J. G., & Sweigart, A. V. 1973, "Rotating solar models with low neutrino flux", Astrophys. J., 183, 997, doi: 10.1086/152286

Deng, L. H., Xiang, Y. Y., Qu, Z. N., & An, J. M. 2016, "Systematic regularity of hemispheric sunspot areas over the past 140 years", Astron. J., 151, 70, doi: 10.3847/0004-6256/151/3/70

Deubner, F. L. 1975, "Observations of low wavenumber nonradial eigenmodes of the Sun", Astron. Astrophys., 44, 371

Dicke, R. H. 1964, "The Sun's rotation and relativity", Nat., 202, 432, doi: 10.1038/202432a0

Dicke, R. H., & Goldenberg, H. M. 1967, "Solar oblateness and general relativity", Phys. Rev. Lett., 18, 313, doi: 10.1103/physrevlett.18.313

Dicke, R. H., Kuhn, J. R., & Libbrecht, K. G. 1986, "The variable oblateness of the Sun: Measurements of 1984", Astrophys. J., 311, 1025, doi: 10.1086/164839

Dicke, R. H., Kuhn, J. R., & Libbrecht, K. G. 1987, "Is the solar oblateness variable? Measurements of 1985", Astrophys. J., 318, 451, doi: 10.1086/165382

Dikpati, M. 2012, "Nonlinear evolution of global hydrodynamic shallow-water instability in the solar tachocline", Astrophys. J., 745, 128, doi: 10.1088/0004-637x/745/2/128

Dikpati, M., Belucz, B., Gilman, P. A., & McIntosh, S. W. 2018a, "Phase speed of magnetized Rossby waves that cause solar seasons", Astrophys. J., 862, 159, doi: 10.3847/1538-4357/aacefa

Dikpati, M., Cally, P. S., McIntosh, S. W., & Heifetz, E. 2017, "The origin of the 'seasons' in space weather", Sci. Rep., 7, doi: 10.1038/s41598-017-14957-x

Dikpati, M., & Gilman, P. A. 1999, "Joint instability of latitudinal differential rotation and concentrated toroidal fields below the solar convection zone", Astrophys. J., 512, 417, doi: 10.1086/306748

Dikpati, M., & Gilman, P. A. 2001a, "Analysis of hydrodynamic stability of solar tachocline latitudinal differential rotation using a shallow-water model", Astrophys. J., 551, 536, doi: 10.1086/320080

Dikpati, M., & Gilman, P. A. 2001b, "Flux-transport dynamos with α-effect from global instability of tachocline differential rotation: A solution for magnetic parity selection in the Sun", Astrophys. J., 559, 428, doi: 10.1086/322410

Dikpati, M., & Gilman, P. A. 2005, "A shallow-water theory for the Sun's active longitudes", Astrophys. J., 635, L193, doi: 10.1086/499626

Dikpati, M., & Gilman, P. A. 2009, "Flux-transport solar dynamos", Space Sci. Rev., 144, 67, doi: 10.1007/s11214-008-9484-3

Dikpati, M., Gilman, P. A., & Rempel, M. 2003, "Stability analysis of tachocline latitudinal differential rotation and coexisting toroidal band using a shallow-water model", Astrophys. J., 596, 680, doi: 10.1086/377708

Dikpati, M., McIntosh, S. W., Bothun, G., Cally, P. S., Ghosh, S. S., Gilman, P. A., & Umurhan, O. M. 2018b, "Role of interaction between magnetic Rossby waves and tachocline differential rotation in producing solar seasons", Astrophys. J., 853, 144, doi: 10.3847/1538-4357/aaa70d

Dilke, F. W. W., & Gough, D. O. 1972, "The solar spoon", Nat., 240, 262, doi: 10.1038/240262a0

Domingo, V., Fleck, B., & Poland, A. I. 1995, "The SOHO mission: An overview", Sol. Phys., 162, 1, doi: 10.1007/bf00733425

D'Silva, S., & Choudhuri, A. R. 1993, "A theoretical model for tilts of bipolar magnetic regions", Astron. Astrophys., 272, 621

Duchlev, P. I., & Dermendjiev, V. N. 1996, "Periodicities in the N-S asymmetry of long-lived solar filaments", Sol. Phys., 168, 205, doi: 10.1007/bf00145836

Durney, B. R. 1999, "The Taylor-Proudman balance and the solar rotational data", Astrophys. J., 511, 945, doi: 10.1086/306696

Duvall, T. L., J. 1998, "Recent results and theoretical advances in local helioseismology", in ESA Special Publication, Vol. 418, Structure and Dynamics of the Interior of the Sun and Sun-like Stars, ed. S. Korzennik, 581

Duvall, T. L., & Harvey, J. W. 1983, "Observations of solar oscillations of low and intermediate degree", Nat., 302, 24, doi: 10.1038/302024a0

Duvall, T. L., Jeffferies, S. M., Harvey, J. W., & Pomerantz, M. A. 1993, "Time–distance helioseismology", Nat., 362, 430, doi: 10.1038/362430a0

Dziembowski, W., & Kosovichev, A. 1987, "Low frequency oscillations in slowly rotating stars. III. Kelvin-Helmholtz instability", Acta Astron., 37, 341

Dziembowski, W. A., Pamyatnykh, A. A., & Sienkiewicz, R. 1990, "Solar model from helioseismology and the neutrino flux problem", Mon. Not. R. Astron. Soc., 244, 542

Eddington, A. S. 1916, "On the radiative equilibrium of the stars", Mon. Not. R. Astron. Soc., 77, 16, doi: 10.1093/mnras/77.1.16

Eddington, A. S. 1925, "Circulating currents in rotating stars", The Observatory, 48, 73

Eddy, J. A. 1976, "The Maunder minimum", Sci., 192, 1189, doi: 10.1126/science.192.4245.1189

Edwards, J. M. 1990, "On the influence of the thermal and magnetic boundary conditions on the linear theory of magnetoconvection", Geophys. Astrophys. Fluid Dyn., 55, 1, doi: 10.1080/03091929008208942

Elliott, J. R. 1997, "Aspects of the solar tachocline", Astron. Astrophys., 327, 1222

Elliott, J. R., & Gough, D. O. 1999, "Calibration of the thickness of the solar tachocline", Astrophys. J., 516, 475, doi: 10.1086/307092

Elliott, J. R., Miesch, M. S., & Toomre, J. 2000, "Turbulent solar convection and its coupling with rotation: The effect of Prandtl number and thermal boundary conditions on the resulting differential rotation", Astrophys. J., 533, 546, doi: 10.1086/308643

Elsworth, Y., Howe, R., Isaak, G. R., McLeod, C. P., & New, R. 1990, "Evidence from solar seismology against non-standard solar-core models", Nat., 347, 536, doi: 10.1038/347536a0

Ezer, D., & Cameron, A. G. W. 1968, "Solar spin-down and neutrino fluxes", Astrophys. J. Lett., 1, L177

Fan, Y., & Fang, F. 2014, "A simulation of convective dynamo in the solar convective envelope: Maintenance of the solar-like differential rotation and emerging flux", Astrophys. J., 789, 35, doi: 10.1088/0004-637x/789/1/35

Fan, Y., Fisher, G. H., & McClymont, A. N. 1994, "Dynamics of emerging active region flux loops", Astrophys. J., 436, 907, doi: 10.1086/174967

Faulkner, J., & Gilliland, R. L. 1985, "Weakly interacting, massive particles and the solar neutrino flux", Astrophys. J., 299, 994, doi: 10.1086/163766

Featherstone, N. 2018, "Geodynamics/Rayleigh: Bug-Fix-Release: 0.9.1", Zenodo, doi: 10.5281/ZENODO.1236565

Featherstone, N. A., Edelmann, P. V. F., Gassmoeller, R., Matilsky, L. I., Orvedahl, R. J., & Wilson, C. R. 2021, "Rayleigh 1.0.1", doi: http://doi.org/10.5281/zenodo.5774039

Featherstone, N. A., & Hindman, B. W. 2016a, "The spectral amplitude of stellar convection and its scaling in the high-Rayleigh-number regime", Astrophys. J., 818, 32, doi: 10.3847/0004-637x/818/1/32

Featherstone, N. A., & Hindman, B. W. 2016b, "The emergence of solar supergranulation as a natural consequence of rotationally constrained interior convection", Astrophys. J., 830, L15, doi: 10.3847/2041-8205/830/1/l15

Featherstone, N. A., & Miesch, M. S. 2015, "Meridional circulation in solar and stellar convection zones", Astrophys. J., 804, 67, doi: 10.1088/0004-637x/804/1/67

Ferraro, V. C. A. 1937, "The non-uniform rotation of the Sun and its magnetic field", Mon. Not. R. Astron. Soc., 97, 458, doi: 10.1093/mnras/97.6.458

Ferriz-Mas, A., & Schuessler, M. 1994, "Waves and instabilities of a toroidal magnetic flux tube in a rotating star", Astrophys. J., 433, 852, doi: 10.1086/174694

Fivian, M. D., Hudson, H. S., Lin, R. P., & Zahid, H. J. 2008, "A large excess in apparent solar oblateness due to surface magnetism", Sci., 322, 560, doi: 10.1126/science.1160863

Forgács-Dajka, E. 2004, "Dynamics of the fast solar tachocline. II. Migrating field", Astron. Astrophys., 413, 1143, doi: 10.1051/0004-6361:20031569

Forgács-Dajka, E., & Petrovay, K. 2001, "Tachocline confinement by an oscillatory magnetic field", Sol. Phys., 203, 195, doi: 10.1023/a:1013389631585

Forgács-Dajka, E., & Petrovay, K. 2002, "Dynamics of the fast solar tachocline. I. Dipolar field", Astron. Astrophys., 389, 629, doi: 10.1051/0004-6361:20020586

Foukal, P. 1972, "Magnetic coupling of the active chromosphere to the solar interior", Astrophys. J., 173, 439, doi: 10.1086/151435

Foukal, P., & Jokipii, J. R. 1975, "On the rotation of gas and magnetic fields at the solar photosphere", Astrophys. J. Lett., 199, L71, doi: 10.1086/181851

Frazier, E. N. 1968, "A spatio-temporal analysis of velocity fields in the solar photosphere", Zeit. Astrophys., 68, 345

Garaud, P. 2001, "Latitudinal shear instability in the solar tachocline", Mon. Not. R. Astron. Soc., 324, 68, doi: 10.1046/j.1365-8711.2001.04245.x

Garaud, P. 2002, "Dynamics of the solar tachocline. I. An incompressible study", Mon. Not. R. Astron. Soc., 329, 1, doi: 10.1046/j.1365-8711.2002.04961.x

Garaud, P. 2020, "Horizontal shear instabilities at low Prandtl number", Astrophys. J., 901, 146, doi: 10.3847/1538-4357/ab9c99

Garaud, P., & Acevedo-Arreguin, L. A. 2009, "On the penetration of meridional circulation below the solar convection zone. II. Models with convection zone, the Taylor-Proudman constraint, and applications to other stars", Astrophys. J., 704, 1, doi: 10.1088/0004-637x/704/1/1

Garaud, P., & Brummell, N. H. 2008, "On the penetration of meridional circulation below the solar convection zone", Astrophys. J., 674, 498, doi: 10.1086/524837

Garaud, P., & Garaud, J.-D. 2008, "Dynamics of the solar tachocline. II. The stratified case", Mon. Not. R. Astron. Soc., 391, 1239, doi: 10.1111/j.1365-2966.2008.13930.x

Gastine, T., Wicht, J., & Aurnou, J. 2013, "Zonal flow regimes in rotating anelastic spherical shells: An application to giant planets", Icar., 225, 156, doi: 10.1016/j.icarus.2013.02.031

Ghizaru, M., Charbonneau, P., & Smolarkiewicz, P. K. 2010, "Magnetic cycles in global large-eddy simulations of solar convection", Astrophys. J., 715, L133, doi: 10.1088/2041-8205/715/2/l133

Giles, P. M., Duvall, T. L., Scherrer, P. H., & Bogart, R. S. 1997, "A subsurface flow of material from the Sun's equator to its poles", Nat., 390, 52, doi: 10.1038/36294

Gilman, P., & Dikpati, M. 2014, "Baroclinic instability in the solar tachocline", Astrophys. J., 787, 60, doi: 10.1088/0004-637x/787/1/60

Gilman, P. A. 1967a, "Stability of baroclinic flows in a zonal magnetic field: Part I", J. Atm. Sci., 24, 101, doi: 10.1175/1520-0469(1967)024<0101:sobfia>2.0.co;2

Gilman, P. A. 1967b, "Stability of baroclinic flows in a zonal magnetic field: Part II", J. Atm. Sci., 24, 119, doi: 10.1175/1520-0469(1967)024<0119:sobfia>2.0.co;2

Gilman, P. A. 1967c, "Stability of baroclinic flows in a zonal magnetic field: Part III", J. Atm. Sci., 24, 130, doi: 10.1175/1520-0469(1967)024<0130:sobfia>2.0.co;2

Gilman, P. A. 1967d, "Stability of a continuous baroclinic flow in a zonal magnetic field", J. Atm. Sci., 24, 333, doi: 10.1175/1520-0469(1967)024<0333:soacbf>2.0.co;2

Gilman, P. A. 1969a, "A Rossby-wave dynamo for the Sun, I", Sol. Phys., 8, 316, doi: 10.1007/bf00155379

Gilman, P. A. 1969b, "A Rossby-wave dynamo for the Sun, II", Sol. Phys., 9, 3, doi: 10.1007/bf00145722

Gilman, P. A. 1972, "Nonlinear Boussinesq convective model for large scale solar circulations", Sol. Phys., 27, 3, doi: 10.1007/bf00151765

Gilman, P. A. 1977, "Nonlinear dynamics of Boussinesq convection in a deep rotating spherical shell. I", Geophys. Astrophys. Fluid Dyn., 8, 93, doi: 10.1080/03091927708240373

Gilman, P. A. 1983, "Dynamically consistent nonlinear dynamos driven by convection in a rotating spherical shell. II. Dynamos with cycles and strong feedbacks", Astrophys. J. Supp., 53, 243, doi: 10.1086/190891

Gilman, P. A. 2000a, "Fluid dynamics and mhd of the solar convection zoneand tachocline: current understanding and unsolvedproblems", Sol. Phys., 192, 27, doi: 10.1023/a:1005280502744

Gilman, P. A. 2000b, "Magnetohydrodynamic 'shallow water' equations for the solar tachocline", Astrophys. J. Lett., 544, L79, doi: 10.1086/317291

Gilman, P. A. 2018a, "Magnetic buoyancy and rotational instabilities in the tachocline", Astrophys. J., 853, 65, doi: 10.3847/1538-4357/aaa4f4

Gilman, P. A. 2018b, "Magnetic buoyancy and magnetorotational instabilities in stellar tachoclines for solar- and antisolar-type differential rotation", Astrophys. J., 867, 45, doi: 10.3847/1538-4357/aae08e

Gilman, P. A., & Fox, P. A. 1997, "Joint instability of latitudinal differential rotation and toroidal magnetic fields below the solar convection zone", Astrophys. J., 484, 439, doi: 10.1086/304330

Gilman, P. A., & Miller, J. 1986, "Nonlinear convection of a compressible fluid in a rotating spherical shell", Astrophys. J. Supp., 61, 585, doi: 10.1086/191125

Gizon, L., & Birch, A. C. 2005, "Local helioseismology", Liv. Rev. Sol. Phys., 2, doi: 10.12942/lrsp-2005-6

Gizon, L., Cameron, R. H., Pourabdian, M., Liang, Z.-C., Fournier, D., Birch, A. C., & Hanson, C. S. 2020a, "Meridional flow in the Sun's convection zone is a single cell in each hemisphere", Sci., 368, 1469, doi: 10.1126/science.aaz7119

Gizon, L., Fournier, D., & Albekioni, M. 2020b, "Effect of latitudinal differential rotation on solar Rossby waves: Critical layers, eigenfunctions, and momentum fluxes in the equatorial β plane", Astron. Astrophys., 642, A178, doi: 10.1051/0004-6361/202038525

Gizon, L., Cameron, R. H., Bekki, Y., Birch, A. C., Bogart, R. S., Brun, A. S., Damiani, C., Fournier, D., Hyest, L., Jain, K., Lekshmi, B., Liang, Z.-C., & Proxauf, B. 2021, "Solar inertial modes: Observations, identification, and diagnostic promise", Astron. Astrophys., 652, L6, doi: 10.1051/0004-6361/202141462

Glatzmaier, G. A. 1984, "Numerical simulations of stellar convective dynamos. I. The model and method", J. Comp. Phys., 55, 461, doi: 10.1016/0021-9991(84)90033-0

Gleissberg, W. 1939, "A long-periodic fluctuation of the sunspot numbers", The Observatory, 62, 158

Gnevyshev, M. N., & Ohl, A. I. 1948, "On the 22-year cycle of solar activity", Astron. Zh., 25, 18

Goldreich, P., & Keeley, D. A. 1977, "Solar seismology. II. The stochastic excitation of the solar p-modes by turbulent convection", Astrophys. J., 212, 243, doi: 10.1086/155043

Goldreich, P., & Schubert, G. 1968, "A theoretical upper bound to the solar oblateness", Astrophys. J., 154, 1005, doi: 10.1086/149821

Gough, D. 1977, "Random remarks on solar hydrodynamics", in Int. Astron. U. Colloq. 36: The Energy Balance and Hydrodynamics of the Solar Chromosphere and Corona, 3–36

Gough, D. 1985, "Inverting helioseismic data", Sol. Phys., 100, 65, doi: 10.1007/bf00158422

Gough, D. O. 1969, "The anelastic approximation for thermal convection", J. Atmos. Soc., 26, 448, doi: 10.1175/1520-0469(1969)026<0448:taaftc>2.0.co;2

Gough, D. O. 1993, "Linear adiabatic stellar pulsation.", in Astrophysical Fluid Dynamics - Les Houches 1987, 399–560

Gough, D. O., & Kosovichev, A. G. 1993, "The influence of low-degree p-mode frequencies on the determination of the structure of the solar interior", Mon. Not. R. Astron. Soc., 264, 522, doi: 10.1093/mnras/264.2.522

Gough, D. O., & McIntyre, M. E. 1998, "Inevitability of a magnetic field in the Sun's radiative interior", Nat., 394, 755, doi: 10.1038/29472

Greer, B. J., Hindman, B. W., Featherstone, N. A., & Toomre, J. 2015, "Helioseismic imaging of fast convective flows throughout the near-surface shear layer", Astrophys. J., 803, L17, doi: 10.1088/2041-8205/803/2/l17

Greer, B. J., Hindman, B. W., & Toomre, J. 2014, "Multi-ridge fitting for ring-diagram helioseismology", Sol. Phys., 289, 2823, doi: 10.1007/s11207-014-0514-x

Greer, B. J., Hindman, B. W., & Toomre, J. 2016, "Helioseismic measurements of the Rossby number in the Sun's near-surface shear layer", Astrophys. J., 824, 4, doi: 10.3847/0004-637x/824/1/4

Guerrero, G., Smolarkiewicz, P. K., de Gouveia Dal Pino, E. M., Kosovichev, A. G., & Mansour, N. N. 2016a, "On the role of tachoclines in solar and stellar dynamos", Astrophys. J., 819, 104, doi: 10.3847/0004-637x/819/2/104

Guerrero, G., Smolarkiewicz, P. K., de Gouveia Dal Pino, E. M., Kosovichev, A. G., & Mansour, N. N. 2016b, "Understanding solar torsional oscillations from global dynamo models", Astrophys. J., 828, L3, doi: 10.3847/2041-8205/828/1/l3

Guerrero, G., Smolarkiewicz, P. K., Kosovichev, A. G., & Mansour, N. N. 2013, "Differential rotation in solar-like stars from global simulations", Astrophys. J., 779, 176, doi: 10.1088/0004-637x/779/2/176

Guerrero, G., Zaire, B., Smolarkiewicz, P. K., de Gouveia Dal Pino, E. M., Kosovichev, A. G., & Mansour, N. N. 2019, "What sets the magnetic field strength and cycle period in solar-type stars?", Astrophys. J., 880, 6, doi: 10.3847/1538-4357/ab224a

Guzik, J. A., & Swenson, F. J. 1997, "Seismological comparisons of solar models with element diffusion using the MHD, Opal, and Sireff equations of state", Astrophys. J., 491, 967, doi: 10.1086/304988

Gyenge, N., Ludmány, A., & Baranyi, T. 2016, "Active longitude and solar flare occurrences", Astrophys. J., 818, 127, doi: 10.3847/0004-637x/818/2/127

Haber, D., Hindman, B., Toomre, J., Bogart, R., Thompson, M., & Hill, F. 2000, "Solar shear flows deduced from helioseismic dense-pack samplings of ring diagrams", Sol. Phys., 192, 335, doi: 10.1023/a:1005235610132

Haber, D., Hindman, B., Toomre, J., & Thompson, M. 2004, "Organized subsurface flows near active regions", Sol. Phys., 220, 371, doi: 10.1023/b:sola.0000031405.52911.08

Haber, D. A., Hindman, B. W., Toomre, J., Bogart, R. S., Larsen, R. M., & Hill, F. 2002, "Evolving submerged meridional circulation cells within the upper convection zone revealed by ring-diagram analysis", Astrophys. J., 570, 855, doi: 10.1086/339631

Hanasoge, S. M., Duvall, T. L., & Sreenivasan, K. R. 2012, "Anomalously weak solar convection", Proc. Nat. Acad. Sci., 109, 11928, doi: 10.1073/pnas.1206570109

Harvey, J. W., Hill, F., Hubbard, R. P., Kennedy, J. R., Leibacher, J. W., Pintar, J. A., Gilman, P. A., Noyes, R. W., Title, A. M., Toomre, J., Ulrich, R. K., Bhatnagar, A., Kennewell, J. A., Marquette, W., Patrón, J., Saá, O., & Yasukawa, E. 1996, "The Global Oscillation Network Group (GONG) project", Sci., 272, 1284, doi: 10.1126/science.272.5266.1284

Hathaway, D. H. 2011, "A standard law for the equatorward drift of the sunspot zones", Sol. Phys., 273, 221, doi: 10.1007/s11207-011-9837-z

Hathaway, D. H. 2012, "Supergranules as probes of the Sun's meridional circulation", Astrophys. J., 760, 84, doi: 10.1088/0004-637x/760/1/84

Hathaway, D. H. 2015, "The solar cycle", Liv. Rev. Sol. Phys., 7, doi: 10.12942/lrsp-2010-1

Hathaway, D. H., & Choudhary, D. P. 2008, "Sunspot group decay", Sol. Phys., 250, 269, doi: 10.1007/s11207-008-9226-4

Hathaway, D. H., & Upton, L. A. 2016, "Predicting the amplitude and hemispheric asymmetry of solar cycle 25 with surface flux transport", J. Geophys. Res., 121, 10,744, doi: 10.1002/2016JA023190

Hathaway, D. H., Wilson, R. M., & Reichmann, E. J. 1999, "A synthesis of solar cycle prediction techniques", J. Geophys. Res., 104, 22375, doi: 10.1029/1999ja900313

Haurwitz, B. 1940, "The motion of atmospheric disturbances on the spherical Earth", J. Mar. Res., 3, 254–267

Haxton, W., Robertson, R. H., & Serenelli, A. M. 2013, "Solar neutrinos: Status and prospects", Ann. Rev. Astron. Astrophys., 51, 21, doi: 10.1146/annurev-astro-081811-125539

Haynes, P. H. 1989, "The effect of barotropic instability on the nonlinear evolution of a Rossby-wave critical layer", J. Fluid Mech., 207, 231, doi: 10.1017/s0022112089002569

Haynes, P. H., McIntyre, M. E., Shepherd, T. G., Marks, C. J., & Shine, K. P. 1991, "On the 'downward control' of extratropical diabatic circulations by eddy-induced mean zonal forces", J. Atm. Sci., 48, 651, doi: 10.1175/1520-0469(1991)048<0651:otcoed>2.0.co;2

Henney, C. J., & Harvey, J. W. 2002, "Phase coherence analysis of solar magnetic activity", Sol. Phys., 207, 199, doi: 10.1023/a:1016265629455

Hill, F. 1988, "Rings and trumpets: Three-dimensional power spectra of solar oscillations", Astrophys. J., 333, 996, doi: 10.1086/166807

Hindman, B. W., Featherstone, N. A., & Julien, K. 2020, "Morphological classification of the convective regimes in rotating stars", Astrophys. J., 898, 120, doi: 10.3847/1538-4357/ab9ec2

Hindman, B. W., Gizon, L., Duvall, T. L., Haber, D. A., & Toomre, J. 2004, "Comparison of solar subsurface flows assessed by ring and time-distance analyses", Astrophys. J., 613, 1253, doi: 10.1086/423263

Hotta, H., & Iijima, H. 2020, "On rising magnetic flux tube and formation of sunspots in a deep domain", Mon. Not. R. Astron. Soc., 494, 2523, doi: 10.1093/mnras/staa844

Hotta, H., Iijima, H., & Kusano, K. 2019, "Weak influence of near-surface layer on solar deep convection zone revealed by comprehensive simulation from base to surface", Sci. Adv., 5, doi: 10.1126/sciadv.aau2307

Hotta, H., & Kusano, K. 2021, "Solar differential rotation reproduced with high-resolution simulation", Nat. Astron., 5, 1100, doi: 10.1038/s41550-021-01459-0

Hotta, H., Rempel, M., & Yokoyama, T. 2015, "High-resolution calculation of the solar global convection with the reduced speed of sound technique. II. Near surface shear layer with the rotation", Astrophys. J., 798, 51, doi: 10.1088/0004-637x/798/1/51

Hotta, H., Rempel, M., & Yokoyama, T. 2016, "Large-scale magnetic fields at high Reynolds numbers in magnetohydrodynamic simulations", Sci., 351, 1427, doi: 10.1126/science.aad1893

Hotta, H., & Yokoyama, T. 2010, "Solar parity issue with flux-transport dynamo", Astrophys. J., 714, L308, doi: 10.1088/2041-8205/714/2/l308

Howard, R. 1967, "Velocity fields in the solar atmosphere", Sol. Phys., 2, 3, doi: 10.1007/bf00155889

Howard, R., & Harvey, J. 1970, "Spectroscopic determinations of solar rotation", Sol. Phys., 12, 23, doi: 10.1007/bf02276562

Howard, R., & Labonte, B. J. 1980, "The Sun is observed to be a torsional oscillator with a period of 11 years", Astrophys. J., 239, L33, doi: 10.1086/183286

Howe, R. 2009, "Solar interior rotation and its variation", Living Review of Solar Physics, 6, doi: 10.12942/lrsp-2009-1

Howe, R., Baker, D., Harra, L., van Driel-Gesztelyi, L., Komm, R., Hill, F., & González Hernández, I. 2013, "Magnetic polarity streams and subsurface flows", in Astronomical Society of the Pacific Conference Series, Vol. 478, Fifty Years of Seismology of the Sun and Stars, ed. K. Jain, S. C. Tripathy, F. Hill, J. W. Leibacher, & A. A. Pevtsov, 291

Howe, R., Christensen-Dalsgaard, J., Hill, F., Komm, R., Schou, J., & Thompson, M. J. 2005, "Solar convection-zone dynamics, 1995–2004", Astrophys. J., 634, 1405, doi: 10.1086/497107

Howe, R., Christensen-Dalsgaard, J., Hill, F., Komm, R. W., Larsen, R. M., Schou, J., Thompson, M. J., & Toomre, J. 2000, "Dynamic variations at the base of the solar convection zone", Sci., 287, 2456, doi: 10.1126/science.287.5462.2456

Hoyt, D. V., & Schatten, K. H. 1998, "Group sunspot numbers: A new solar activity reconstruction", Sol. Phys., 181, 491, doi: 10.1023/a:1005056326158

Hummer, D. G., & Mihalas, D. 1988, "The equation of state for stellar envelopes. I. An occupation probability formalism for the truncation of internal partition functions", Astrophys. J., 331, 794, doi: 10.1086/166600

Hurlburt, N. E., Toomre, J., & Massaguer, J. M. 1986, "Nonlinear compressible convection penetrating into stable layers and producing internal gravity waves", Astrophys. J., 311, 563, doi: 10.1086/164796

Hurlburt, N. E., Toomre, J., Massaguer, J. M., & Zahn, J.-P. 1994, "Penetration below a convective zone", Astrophys. J., 421, 245, doi: 10.1086/173642

Hurle, D. T. J., Jakeman, E., & Pike, E. R. 1967, "On the solution of the Bénard problem with boundaries of finite conductivity", Proc. Royal Soc. London. Series A. Math. Phys. Sci., 296, 469, doi: 10.1098/rspa.1967.0039

Iijima, H., Hotta, H., & Imada, S. 2019, "Semiconservative reduced speed of sound technique for low Mach number flows with large density variations", Astron. Astrophys., 622, A157, doi: 10.1051/0004-6361/201834031

Ivanov, E. 2007, "Active longitudes: Structure, dynamics, and rotation", Adv. Space Res., 40, 959, doi: 10.1016/j.asr.2007.02.093

Jefferies, S. M., Pomerantz, M. A., Duvall, T. L., J., Harvey, J. W., & Jaksha, D. B. 1988, "Helioseismology from the South Pole: Comparison of 1987 and 1981 results", in ESA Special Publication, Vol. 286, Seismology of the Sun and Sun-Like Stars, ed. E. J. Rolfe, 279–284

Jensen, J. M., & Pijpers, F. P. 2003, "Sensitivity kernels for time-distance inversion based on the Rytov approximation", Astron. Astrophys., 412, 257, doi: 10.1051/0004-6361:20031361

Jha, B. K., & Choudhuri, A. R. 2021, "A theoretical model of the near-surface shear layer of the Sun", Mon. Not. R. Astron. Soc., 506, 2189, doi: 10.1093/mnras/stab1717

Jones, C., Boronski, P., Brun, A., Glatzmaier, G., Gastine, T., Miesch, M., & Wicht, J. 2011, "Anelastic convection-driven dynamo benchmarks", Icar., 216, 120, doi: 10.1016/j.icarus.2011.08.014

Jones, C. A., Kuzanyan, K. M., & Mitchell, R. H. 2009, "Linear theory of compressible convection in rapidly rotating spherical shells, using the anelastic approximation", J. Fluid Mech., 634, 291, doi: 10.1017/s0022112009007253

Jouve, L., & Brun, A. S. 2009, "Three-dimensional nonlinear evolution of a magnetic flux tube in a spherical shell: Influence of turbulent convection and associated mean flows", Astrophys. J., 701, 1300, doi: 10.1088/0004-637x/701/2/1300

Kajita, T. 2016, "Nobel lecture: Discovery of atmospheric neutrino oscillations", Rev. Mod. Phys., 88, doi: 10.1103/revmodphys.88.030501

Käpylä, P. J., Mantere, M. J., & Brandenburg, A. 2012, "Cyclic magnetic activity due to turbulent convection in spherical wedge geometry", Astrophys. J., 755, L22, doi: 10.1088/2041-8205/755/1/l22

Käpylä, P. J., Rheinhardt, M., Brandenburg, A., Arlt, R., Käpylä, M. J., Lagg, A., Olspert, N., & Warnecke, J. 2017, "Extended subadiabatic layer in simulations of overshooting convection", Astrophys. J., 845, L23, doi: 10.3847/2041-8213/aa83ab

Karak, B. B., Rheinhardt, M., Brandenburg, A., Käpylä, P. J., & Käpylä, M. J. 2014, "Quenching and anisotropy of hydromagnetic turbulent transport", Astrophys. J., 795, 16, doi: 10.1088/0004-637x/795/1/16

Killworth, P. D., & McIntyre, M. E. 1985, "Do Rossby-wave critical layers absorb, reflect, or over-reflect?", J. Fluid Mech., 161, 449, doi: 10.1017/s0022112085003019

Kitchatinov, L. L., & Olemskoi, S. V. 2005, "Active longitudes of the Sun: The rotation period and statistical significance", Astronomy Letters, 31, 280, doi: 10.1134/1.1896072

Kitchatinov, L. L., & Ruediger, G. 1995, "Differential rotation in solar-type stars: Revisiting the Taylor-number puzzle", Astron. Astrophys., 299, 446

Kleeorin, N. I., & Ruzmaikin, A. A. 1984, "Mean-field dynamo with cubic non-linearity", Astron. Nach., 305, 265, doi: 10.1002/asna.2113050513

Komm, R., Hernández, I. G., Howe, R., & Hill, F. 2015, "Solar-cycle variation of subsurface meridional flow derived with ring-diagram analysis", Sol. Phys., 290, 3113, doi: 10.1007/s11207-015-0729-5

Korre, L., & Featherstone, N. A. 2021, "On the dynamics of overshooting convection in spherical shells: Effect of density stratification and rotation", Astrophys. J., 923, 52, doi: 10.3847/1538-4357/ac2dea

Korre, L., Garaud, P., & Brummell, N. H. 2019, "Convective overshooting and penetration in a Boussinesq spherical shell", Mon. Not. R. Astron. Soc., 484, 1220, doi: 10.1093/mnras/stz047

Koshiba, M. 2003, "Nobel lecture: Birth of neutrino astrophysics", Rev. Mod. Phys., 75, 1011, doi: 10.1103/revmodphys.75.1011

Kraft, R. P. 1967, "Studies of stellar rotation. V. The dependence of rotation on age among solar-type stars", Astrophys. J., 150, 551, doi: 10.1086/149359

Kumar, P., & Quataert, E. J. 1997, "Angular momentum transport by gravity waves and its effect on the rotation of the solar interior", Astrophys. J., 475, L143, doi: 10.1086/310477

Landau, L., Lifshitz, E., & Pitaevskii, L. 1998, Electrodynamics of Continuous Media: Landau and Lifshitz Course of Theoretical Physics, vol. 8 (Oxford: Pergamon Press)

Lantz, S. R. 1992, "Dynamical behavior of magnetic fields in a stratified, convecting fluid layer", PhD thesis, Cornell University, United States

Lawson, N., Strugarek, A., & Charbonneau, P. 2015, "Evidence of active MHD instability in EULAG-MHD simulations of solar convection", Astrophys. J., 813, 95, doi: 10.1088/0004-637x/813/2/95

Leibacher, J. W., & Stein, R. F. 1971, "A new description of the solar five-minute oscillation", Astrophys. Lett., 7, 191

Leighton, R. B. 1969, "A magneto-kinematic model of the solar cycle", Astrophys. J., 156, 1, doi: 10.1086/149943

Leighton, R. B., Noyes, R. W., & Simon, G. W. 1962, "Velocity fields in the solar atmosphere. I. Preliminary report.", Astrophys. J., 135, 474, doi: 10.1086/147285

Li, J. 2018, "A systematic study of Hale and anti-Hale sunspot physical parameters", Astrophys. J., 867, 89, doi: 10.3847/1538-4357/aae31a

Libbrecht, K. G., Woodard, M. F., & Kaufman, J. M. 1990, "Frequencies of solar oscillations", Astrophys. J. Supp., 74, 1129, doi: 10.1086/191528

Longuet-Higgins, M. 1964, "Planetary waves on a rotating sphere", Proc. Roy. Soc. A., 279, 446, doi: 10.1098/rspa.1964.0116

Löptien, B., Gizon, L., Birch, A. C., Schou, J., Proxauf, B., Duvall, T. L., Bogart, R. S., & Christensen, U. R. 2018, "Global-scale equatorial Rossby waves as an essential component of solar internal dynamics", Nat. Astron., 2, 568, doi: 10.1038/s41550-018-0460-x

Mandal, K., Hanasoge, S. M., Rajaguru, S. P., & Antia, H. M. 2018, "Helioseismic inversion to infer the depth profile of solar meridional flow using spherical Born kernels", Astrophys. J., 863, 39, doi: 10.3847/1538-4357/aacea2

Matilsky, L. I., Hindman, B. W., Featherstone, N., Blume, C., & Toomre, J. 2022, "Solar tachocline confinement by dynamo action in the radiative interior", Sci., To be submitted to Sci., doi: 10.3847/1538-4357/ab9ca0

Matilsky, L. I., Hindman, B. W., & Toomre, J. 2018, "Exploring the influence of density contrast on solar near-surface shear", in 20th Cambridge Workshop on Cool Stars, Stellar Systems, and the Sun, ed. S. J. Wolk (Zenodo), doi: 10.5281/ZENODO.1476707

Matilsky, L. I., Hindman, B. W., & Toomre, J. 2019, "The role of downflows in establishing solar near-surface shear", Astrophys. J., 871, 217, doi: 10.3847/1538-4357/aaf647

Matilsky, L. I., Hindman, B. W., & Toomre, J. 2020, "Revisiting the Sun's strong differential rotation along radial lines", Astrophys. J., 898, 111, doi: 10.3847/1538-4357/ab9ca0

Matilsky, L. I., & Toomre, J. 2020a, "Exploring bistability in the cycles of the solar dynamo through global simulations", Astrophys. J., 892, 106, doi: 10.3847/1538-4357/ab791c

Matilsky, L. I., & Toomre, J. 2020b, "Dynamo states with strikingly different symmetries coexisting in global solar simulations", in Astrophysics and Space Science Proceedings (Springer International Publishing), 197–199, doi: 10.1007/978-3-030-55336-4_27

Matilsky, L. I., & Toomre, J. 2021, "Building and maintaining a solar tachocline through convective dynamo action", in 20.5th Cambridge Workshop on Cool Stars, Stellar Systems, and the Sun, ed. S. J. Wolk (Zenodo), doi: 10.5281/ZENODO.4750777

Matsui, H., Heien, E., Aubert, J., Aurnou, J. M., Avery, M., Brown, B., Buffett, B. A., Busse, F., Christensen, U. R., Davies, C. J., Featherstone, N., Gastine, T., Glatzmaier, G. A., Gubbins, D., Guermond, J.-L., Hayashi, Y.-Y., Hollerbach, R., Hwang, L. J., Jackson, A., Jones, C. A., Jiang, W., Kellogg, L. H., Kuang, W., Landeau, M., Marti, P., Olson, P., Ribeiro, A., Sasaki, Y., Schaeffer, N., Simitev, R. D., Sheyko, A., Silva, L., Stanley, S., Takahashi, F., ichi Takehiro, S., Wicht, J., & Willis, A. P. 2016, "Performance benchmarks for a next generation numerical dynamo model", Geochem., Geophys., Geosys., 17, 1586, doi: 10.1002/2015gc006159

Maunder, E. 1905, "Magnetic disturbances, 1848 to 1881", Mon. Not. R. Astron. Soc., 65, 538

Maunder, E. W. 1890, "Professor Spoerer's researches on sunspots", Mon. Not. R. Astron. Soc., 50, 251

McDonald, A. B. 2016, "Nobel lecture: The Sudbury neutrino observatory: Observation of flavor change for solar neutrinos", Rev. Mod. Phys., 88, doi: 10.1103/revmodphys.88.030502

McIntosh, P. S. 1981, "The birth and evolution of sunspots: Observations", in The Physics of Sunspots, ed. L. E. Cram & J. H. Thomas, 7–54

McIntosh, S. W., Leamon, R. J., Krista, L. D., Title, A. M., Hudson, H. S., Riley, P., Harder, J. W., Kopp, G., Snow, M., Woods, T. N., Kasper, J. C., Stevens, M. L., & Ulrich, R. K. 2015, "The solar magnetic activity band interaction and instabilities that shape quasi-periodic variability", Nat. Comm., 6, doi: 10.1038/ncomms7491

McIntyre, M. 1994, "The quasi-biennial oscillation (QBO): Some points about the terrestrial QBO and the possibility of related phenomena in the solar interior", in The Solar Engine and its Influence on Terrestrial Atmosphere and Climate, ed. E. Nesme-Ribes, 293

McIntyre, M. E. 1970, "On the non-separable baroclinic parallel flow instability problem", J. Fluid Mech., 40, 273, doi: 10.1017/s0022112070000174

McIntyre, M. E. 1998, "Breaking waves and global-scale chemical transport in the Earth's atmosphere, with spinoffs for the Sun's interior", Prog. Theor. Phys. Supp., 130, 137, doi: 10.1143/ptps.130.137

McIntyre, M. E. 2002, "Some fundamental aspects of atmospheric dynamics, with a solar spinoff", in Meteorology and the Millennium, ed. R. P. Pearce, 283

Mestel, L., Moss, D. L., & Tayler, R. J. 1988, "The mutual interaction of magnetism, rotation and meridian circulation in stellar radiative zones", Mon. Not. R. Astron. Soc., 231, 873, doi: 10.1093/mnras/231.4.873

Mestel, L., & Weiss, N. O. 1987, "Magnetic fields and non-uniform rotation in stellar radiative zones", Mon. Not. R. Astron. Soc., 226, 123, doi: 10.1093/mnras/226.1.123

Miesch, M. S. 2005, "Large-scale dynamics of the convection zone and tachocline", Living Review of Solar Physics, 2, doi: 10.12942/lrsp-2005-1

Miesch, M. S. 2007, "Sustained magnetoshear instabilities in the solar tachocline", Astrophys. J., 658, L131, doi: 10.1086/515571

Miesch, M. S., Brun, A. S., & Toomre, J. 2006, "Solar differential rotation influenced by latitudinal entropy variations in the tachocline", Astrophys. J., 641, 618, doi: 10.1086/499621

Miesch, M. S., Elliott, J. R., Toomre, J., Clune, T. L., Glatzmaier, G. A., & Gilman, P. A. 2000, "Three-dimensional spherical simulations of solar convection. I. Differential rotation and pattern evolution achieved with laminar and turbulent states", Astrophys. J., 532, 593, doi: 10.1086/308555

Miesch, M. S., & Hindman, B. W. 2011, "Gyroscopic pumping in the solar near-surface shear layer", Astrophys. J., 743, 79, doi: 10.1088/0004-637x/743/1/79

Mihalas, D., Däppen, W., & Hummer, D. G. 1988, "The equation of state for stellar envelopes. II. Algorithm and selected results", Astrophys. J., 331, 815, doi: 10.1086/166601

Mihalas, D., Hummer, D. G., Mihalas, B. W., & Daeppen, W. 1990, "The equation of state for stellar envelopes. IV. Thermodynamic quantities and selected ionization fractions for six elemental mixes", Astrophys. J., 350, 300, doi: 10.1086/168383

Mirouh, G. M., Baruteau, C., Rieutord, M., & Ballot, J. 2016, "Gravito-inertial waves in a differentially rotating spherical shell", J. Fluid Mech., 800, 213, doi: 10.1017/jfm.2016.382

Moffatt, H. 1963, Magnetic field generation in electrically conducting fluids (Cambridge: Cambridge University Press)

Mordvinov, A. V., & Kitchatinov, L. L. 2004, "Active longitudes and North-South asymmetry of the activity the Sun as manifestations of its relic magnetic field", Astron. Rep., 48, 254, doi: 10.1134/1.1687019

Moreno-Insertis, F., Schuessler, M., & Ferriz-Mas, A. 1992, "Storage of magnetic flux tubes in a convective overshoot region", Astron. Astrophys., 264, 686

Moss, D., Brandenburg, A., Tavakol, R., & Tuominen, I. 1992, "Stochastic effects in mean-field dynamos", Astron. Astrophys., 265, 843

National Research Council. 2012, The Effects of Solar Variability on Earth's Climate (Washington, D.C.: National Academies Press), doi: 10.17226/13519

Nelson, N. J., Brown, B. P., Brun, A. S., Miesch, M. S., & Toomre, J. 2013a, "Buoyant magnetic loops generated by global convective dynamo action", Sol. Phys., 289, 441, doi: 10.1007/s11207-012-0221-4

Nelson, N. J., Brown, B. P., Brun, A. S., Miesch, M. S., & Toomre, J. 2013b, "Magnetic wreaths and cycles in convective dynamos", Astrophys. J., 762, 73, doi: 10.1088/0004-637x/762/2/73

Nelson, N. J., Featherstone, N. A., Miesch, M. S., & Toomre, J. 2018, "Driving solar giant cells through the self-organization of near-surface plumes", Astrophys. J., 859, 117, doi: 10.3847/1538-4357/aabc07

Neugebauer, M., Smith, E. J., Ruzmaikin, A., Feynman, J., & Vaughan, A. H. 2000, "The solar magnetic field and the solar wind: Existence of preferred longitudes", J. Geophys. Res., 105, 2315, doi: 10.1029/1999ja000298

Newton, H. W., & Milsom, A. S. 1955, "Note on the observed differences in spottedness of the Sun's northern and southern hemispheres", Mon. Not. R. Astron. Soc., 115, 398, doi: 10.1093/mnras/115.4.398

Nordlund, Å., Stein, R. F., & Asplund, M. 2009, "Solar surface convection", Liv. Rev. Sol. Phys., 6, doi: 10.12942/lrsp-2009-2

Norton, A. A., Charbonneau, P., & Passos, D. 2014, "Hemispheric coupling: Comparing dynamo simulations and observations", Space Sci. Rev., 186, 251, doi: 10.1007/s11214-014-0100-4

Norton, A. A., & Gallagher, J. C. 2010, "Solar-cycle characteristics examined in separate hemispheres: Phase, Gnevyshev gap, and length of minimum", Sol. Phys., 261, 193, doi: 10.1007/s11207-009-9479-6

Noyes, R. W., Hartmann, L. W., Baliunas, S. L., Duncan, D. K., & Vaughan, A. H. 1984, "Rotation, convection, and magnetic activity in lower main-sequence stars", Astrophys. J., 279, 763, doi: 10.1086/161945

Ogurtsov, M., Nagovitsyn, Y., Kocharov, G., & Jungner, H. 2002, "Long-period cycles of the Sun's activity recorded in direct solar data and proxies", Sol. Phys., 211, 371, doi: 10.1023/a:1022411209257

O'Mara, B., Miesch, M. S., Featherstone, N. A., & Augustson, K. C. 2016, "Velocity amplitudes in global convection simulations: The role of the Prandtl number and near-surface driving", Adv. Space Res., 58, 1475, doi: 10.1016/j.asr.2016.03.038

Orvedahl, R. J., Calkins, M. A., Featherstone, N. A., & Hindman, B. W. 2018, "Prandtl-number effects in high-rayleigh-number spherical convection", Astrophys. J., 856, 13, doi: 10.3847/1538-4357/aaaeb5

Palme, H., Lodders, K., & Jones, A. 2014, "Solar system abundances of the elements", in Treatise on Geochemistry (Elsevier), 15–36, doi: 10.1016/b978-0-08-095975-7.00118-2

Parker, E. N. 1955, "Hydromagnetic dynamo models.", Astrophys. J., 122, 293, doi: 10.1086/146087

Parker, E. N. 1970, "The generation of magnetic fields in astrophysical bodies. I. The dynamo equations", Astrophys. J., 162, 665, doi: 10.1086/150697

Parker, E. N. 1975, "The generation of magnetic fields in astrophysical bodies. X. Magnetic buoyancy and the solar dynamo", Astrophys. J., 198, 205, doi: 10.1086/153593

Parker, E. N. 1993, "A solar dynamo surface wave at the interface between convection and nonuniform rotation", Astrophys. J., 408, 707, doi: 10.1086/172631

Passos, D., & Charbonneau, P. 2014, "Characteristics of magnetic solar-like cycles in a 3D MHD simulation of solar convection", Astron. Astrophys., 568, A113, doi: 10.1051/0004-6361/201423700

Pedlosky, J. 1987, Geophysical Fluid Dynamics (New York: Springer), doi: 10.1007/978-1-4612-4650-3

Peristykh, A. N. 2003, "Persistence of the Gleissberg 88-year solar cycle over the last ∼12,000 years: Evidence from cosmogenic isotopes", J. Geophys. Res., 108, doi: 10.1029/2002ja009390

Petrie, G. J. D. 2015, "Solar magnetism in the polar regions", Liv. Rev. Sol. Phys., 12, doi: 10.1007/lrsp-2015-5

Pipin, V. V. 2012, "Advances in mean-field dynamo theories", Proc. Int. Astron. U., 8, 375, doi: 10.1017/s1743921313002810

Pipin, V. V., & Kosovichev, A. G. 2011, "The subsurface-shear-shaped solar $\alpha\omega$ dynamo", Astrophys. J. Lett., 727, L45, doi: 10.1088/2041-8205/727/2/l45

Plumb, R. A., & McEwan, A. D. 1978, "The instability of a forced standing wave in a viscous stratified fluid: A laboratory analogue of the quasi-biennial oscillation", J. Atm. Sci., 35, 1827, doi: 10.1175/1520-0469(1978)035<1827:tioafs>2.0.co;2

Proxauf, B., Gizon, L., Löptien, B., Schou, J., Birch, A. C., & Bogart, R. S. 2020, "Exploring the latitude and depth dependence of solar Rossby waves using ring-diagram analysis", Astron. Astrophys., 634, A44, doi: 10.1051/0004-6361/201937007

Prusa, J. M., Smolarkiewicz, P. K., & Wyszogrodzki, A. A. 2008, "EULAG, a computational model for multiscale flows", Comp. Fluids, 37, 1193, doi: 10.1016/j.compfluid.2007.12.001

Racine, É., Charbonneau, P., Ghizaru, M., Bouchat, A., & Smolarkiewicz, P. K. 2011, "On the mode of dynamo action in a global large-eddy simulation of solar convection", Astrophys. J., 735, 46, doi: 10.1088/0004-637x/735/1/46

Rädler, K.-H. 1986, "Investigations of spherical kinematic mean-field dynamo models", Astron. Nach., 307, 89, doi: 10.1002/asna.2113070205

Rast, M. P., Ortiz, A., & Meisner, R. W. 2008, "Latitudinal variation of the solar photospheric intensity", Astrophys. J., 673, 1209, doi: 10.1086/524655

Raynaud, R., & Tobias, S. M. 2016, "Convective dynamo action in a spherical shell: Symmetries and modulation", J. Fluid Mech., 799, doi: 10.1017/jfm.2016.407

Rempel, M. 2005, "Solar differential rotation and meridional flow: The role of a subadiabatic tachocline for the Taylor-Proudman balance", Astrophys. J., 622, 1320, doi: 10.1086/428282

Rempel, M. 2006, "Flux-transport dynamos with Lorentz force feedback on differential rotation and meridional flow: Saturation mechanism and torsional oscillations", Astrophys. J., 647, 662, doi: 10.1086/505170

Rempel, M. 2016, "Extension of the MURAM radiative mhd code for coronal simulations", Astrophys. J., 834, 10, doi: 10.3847/1538-4357/834/1/10

Rempel, M., & Cheung, M. C. M. 2014, "Numerical simulations of active region scale flux emergence: from spot formation to decay", Astrophys. J., 785, 90, doi: 10.1088/0004-637x/785/2/90

Rempel, M., Schüssler, M., & Knölker, M. 2009, "Radiative magnetohydrodynamic simulation of sunspot structure", Astrophys. J., 691, 640, doi: 10.1088/0004-637x/691/1/640

Rhines, P. B. 1979, "Geostrophic turbulence", Ann. Rev. Fluid Mech., 11, 401, doi: 10.1146/annurev.fl.11.010179.002153

Rhodes, E. J., Ulrich, R. K., & Simon, G. W. 1977, "Observations of nonradial p-mode oscillations on the Sun", Astrophys. J., 218, 901, doi: 10.1086/155745

Richardson, J. D., Paularena, K. I., Belcher, J. W., & Lazarus, A. J. 1994, "Solar wind oscillations with a 1.3 year period", Geophys. Res. Lett., 21, 1559, doi: 10.1029/94gl01076

Rieutord, M., Gergeot, B., & Valdettaro, L. 2001, "Inertial waves in a rotating spherical shell: attractors and asymptotic spectrum", J. Fluid Mech., 435, 103, doi: 10.1017/s0022112001003718

Rogers, F. J., Swenson, F. J., & Iglesias, C. A. 1996, "OPAL equation-of-state tables for astrophysical applications", Astrophys. J., 456, 902, doi: 10.1086/176705

Rogers, T. M. 2011, "On limiting the thickness of the solar tachocline", Astrophys. J., 733, 12, doi: 10.1088/0004-637x/733/1/12

Rossby, C.-G. 1939, "Relation between variations in the intensity of the zonal circulation of the atmosphere and the displacements of the semi-permanent centers of action", J. Mar. Res., 2, 38

Rossby, C.-G. 1945, "On the propagation of frequencies and energy in certain types of oceanic and atmospheric waves", J. Meteor., 2, 187, doi: 10.1175/1520-0469(1945)002<0187:otpofa>2.0.co;2

Rosseland, S. 1930, Handbuch der Astrophysik, ed. G. Eberhard, A. Kohlschütter, H. Ludendorff, E. A. Milne, A. Pannekoek, S. Rosseland, & W. Westphal (Berlin: Springer Berlin Heidelberg), doi: 10.1007/978-3-642-90705-0

Roxburgh, I. W. 1967, "Implications of the oblateness of the Sun", Nat., 213, 1077, doi: 10.1038/2131077a0

Roy, J. R. 1977, "The North-South distribution of major solar flare events, sunspot magnetic classes and sunspot areas (1955–1974)", Sol. Phys., 52, 53, doi: 10.1007/bf00935789

Rozelot, J. P., Kosovichev, A. G., & Kilcik, A. 2019, "Solar oblateness & asphericities temporal variations: Outstanding some unsolved issues", Proc. Int. Astron. U., 15, 232, doi: 10.1017/s1743921319009918

Rüdiger, G., & Hollerbach, R. 2004, The Magnetic Universe (Weinheim: Wiley-VCH), doi: 10.1002/3527603654

Scherrer, P. H., Schou, J., Bush, R. I., Kosovichev, A. G., Bogart, R. S., Hoeksema, J. T., Liu, Y., Duvall, T. L., Zhao, J., Title, A. M., Schrijver, C. J., Tarbell, T. D., & Tomczyk, S. 2011, "The Helioseismic and Magnetic Imager (HMI) investigation for the Solar Dynamics Observatory (SDO)", Sol. Phys., 275, 207, doi: 10.1007/s11207-011-9834-2

Schou, J. 2003, "Wavelike properties of solar supergranulation detected in Doppler shift data", Astrophys. J., 596, L259, doi: 10.1086/379529

Schou, J., Antia, H. M., Basu, S., Bogart, R. S., Bush, R. I., Chitre, S. M., Christensen-Dalsgaard, J., Mauro, M. P. D., Dziembowski, W. A., Eff-Darwich, A., Gough, D. O., Haber, D. A., Hoeksema, J. T., Howe, R., Korzennik, S. G., Kosovichev, A. G., Larsen, R. M., Pijpers, F. P., Scherrer, P. H., Sekii, T., Tarbell, T. D., Title, A. M., Thompson, M. J., & Toomre, J. 1998, "Helioseismic studies of differential rotation in the solar envelope by the solar oscillations investigation using the Michelson Doppler Imager", Astrophys. J., 505, 390, doi: 10.1086/306146

Schüssler, M., & Cameron, R. H. 2018, "Origin of the hemispheric asymmetry of solar activity", Astron. Astrophys., 618, A89, doi: 10.1051/0004-6361/201833532

Silverman, S. M., & Shapiro, R. 1983, "Power spectral analysis of auroral occurrence frequency", J. Geophys. Res., 88, 6310, doi: 10.1029/ja088ia08p06310

Smolarkiewicz, P. K., & Prusa, J. M. 2004, "Forward-in-time differencing for fluids: Simulation of geophysical turbulence", in Turbulent Flow Computation (Kluwer Academic Publishers), 279–312, doi: 10.1007/0-306-48421-8_8

Spergel, D. N., & Press, W. H. 1985, "Effect of hypothetical, weakly interacting, massive particles on energy transport in the solar interior", Astrophys. J., 294, 663, doi: 10.1086/163336

Spiegel, E. A., & Veronis, G. 1960, "On the Boussinesq approximation for a compressible fluid.", Astrophys. J., 131, 442, doi: 10.1086/146849

Spiegel, E. A., & Zahn, J.-P. 1992, "The solar tachocline", Astron. Astrophys., 265, 106

Spitzer, L. 1962, Physics of Fully Ionized Gases, 2nd Ed. (New York: Interscience Publishers)

Spruit, H. C., & van Ballegooijen, A. A. 1982, "Stability of toroidal flux tubes in stars", Astron. Astrophys., 106, 58

Starr, V. P. 1968, Physics of Negative-Viscosity Phenomena (New York: McGraw Hill)

Steigman, G., Quintana, H., Sarazin, C. L., & Faulkner, J. 1978, "Dynamical interactions and astrophysical effects of stable heavy neutrinos", Astron. J., 83, 1050, doi: 10.1086/112290

Stein, R. F., & Nordlund, Å. 2000, "Realistic solar convection simulations", Sol. Phys., 192, 91, doi: 10.1023/a:1005260918443

Stein, R. F., & Nordlund, A. 2006, "Solar small-scale magnetoconvection", Astrophys. J., 642, 1246, doi: 10.1086/501445

Stein, R. F., & Nordlund, Å. 2012, "On the formation of active regions", Astrophys. J., 753, L13, doi: 10.1088/2041-8205/753/1/l13

Stenflo, J. O., & Kosovichev, A. G. 2012, "Bipolar magnetic regions on the Sun: Global analysis of the SOHO/MDI data set", Astrophys. J., 745, 129, doi: 10.1088/0004-637x/745/2/129

Strugarek, A., Beaudoin, P., Charbonneau, P., Brun, A. S., & do Nascimento, J.-D. 2017, "Reconciling solar and stellar magnetic cycles with nonlinear dynamo simulations", Sci., 357, 185, doi: 10.1126/science.aal3999

Strugarek, A., Brun, A. S., & Zahn, J.-P. 2011a, "Magnetic confinement of the solar tachocline: The oblique dipole", Astron. Nach., 332, 891, doi: 10.1002/asna.201111613

Strugarek, A., Brun, A. S., & Zahn, J.-P. 2011b, "Magnetic confinement of the solar tachocline: II. Coupling to a convection zone", Astron. Astrophys., 532, A34, doi: 10.1051/0004-6361/201116518

Suzuki, Y. 1995, "Kamiokande solar neutrino results", Nucl. Phys. B - Proc. Supp., 38, 54, doi: 10.1016/0920-5632(94)00733-c

Svalgaard, L., & Wilcox, J. M. 1975, "Long term evolution of solar sector structure", Sol. Phys., 41, 461, doi: 10.1007/bf00154083

Sweet, P. A. 1950, "The importance of rotation in stellar evolution", Mon. Not. R. Astron. Soc., 110, 548, doi: 10.1093/mnras/110.6.548

Swinson, D. B., Koyama, H., & Saito, T. 1986, "Long-term variations in North-South asymmetry of solar activity", Sol. Phys., 106, 35, doi: 10.1007/bf00161351

Talon, S., Kumar, P., & Zahn, J.-P. 2002, "Angular momentum extraction by gravity waves in the Sun", Astrophys. J., 574, L175, doi: 10.1086/342526

Tanenbaum, A. S., Wilcox, J. M., Franzier, E. N., & Howard, R. 1969, "Solar velocity fields: 5-min oscillations and supergranulation", Sol. Phys., 9, 328, doi: 10.1007/bf02391655

Tassoul, J.-L., & Tassoul, M. 1986, "Meridional circulation in rotating stars. IX. The effects of an axisymmetric magnetic field in early-type stars", Astrophys. J., 310, 786, doi: 10.1086/164732

Thompson, M. J., Christensen-Dalsgaard, J., Miesch, M. S., & Toomre, J. 2003, "The internal rotation of the Sun", Ann. Rev. Astron. Astrophys., 41, 599, doi: 10.1146/annurev.astro.41.011802.094848

Tobias, S. M. 1997, "The solar cycle: Parity interactions and amplitude modulation", Astron. Astrophys., 322, 1007

Ulrich, R. K. 1970, "The five-minute oscillations on the solar surface", Astrophys. J., 162, 993, doi: 10.1086/150731

Ulrich, R. K. 2001, "Very long lived wave patterns detected in the solar surface velocity signal", Astrophys. J., 560, 466, doi: 10.1086/322524

Ulrich, R. K., & Tran, T. 2013, "The global solar magnetic field—Identification of long-lived ripples", Astrophys. J., 768, 189, doi: 10.1088/0004-637x/768/2/189

Unno, W., Osaki, Y., Ando, H., Saio, H., & Shibahashi, H. 1989, Nonradial oscillations of stars, Second Edition (University of Tokyo Press)

Usoskin, I. G. 2013, "A history of solar activity over millennia", Liv. Rev. Sol. Phys., 10, doi: 10.12942/lrsp-2013-1

Usoskin, I. G., Sokoloff, D., & Moss, D. 2009, "Grand minima of solar activity and the mean-field dynamo", Sol. Phys., 254, 345, doi: 10.1007/s11207-008-9293-6

Usoskin, I. G., Solanki, S. K., & Kovaltsov, G. A. 2007, "Grand minima and maxima of solar activity: New observational constraints", Astron. Astrophys., 471, 301, doi: 10.1051/0004-6361:20077704

van Ballegooijen, A. A. 1982, "The overshoot layer at the base of the solar convective zone and the problem of magnetic flux storage", Astron. Astrophys., 113, 99

van Driel-Gesztelyi, L., & Green, L. M. 2015, "Evolution of active regions", Liv. Rev. Sol. Phys., 12, doi: 10.1007/lrsp-2015-1

van Driel-Gesztelyi, L., Mandrini, C. H., Thompson, B., Plunkett, S., Aulanier, G., Démoulin, P., Schmieder, B., & de Forest, C. 1999, "Long-term magnetic evolution of an AR and its CME activity", in Astron. Soc. Pac. Conf. Ser., Vol. 184, 302–306

Vasil, G. M., Lecoanet, D., Brown, B. P., Wood, T. S., & Zweibel, E. G. 2013, "Energy conservation and gravity waves in sound-proof treatments of stellar interiors. II. Lagrangian constrained analysis", Astrophys. J., 773, 169, doi: 10.1088/0004-637x/773/2/169

Vögler, A., Shelyag, S., Schüssler, M., Cattaneo, F., Emonet, T., & Linde, T. 2004, "Simulations of magneto-convection in the solar photosphere", Astron. Astrophys., 429, 335, doi: 10.1051/0004-6361:20041507

Vogt, H. 1924, "Zum strahlungsgleichgewicht der sterne", Astron. Nach., 223, 229, doi: 10.1002/asna.19242231403

von Zeipel, H. 1924, "The radiative equilibrium of a rotating system of gaseous masses", Mon. Not. R. Astron. Soc., 84, 665, doi: 10.1093/mnras/84.9.665

Vorontsov, S. V., Christensen-Dalsgaard, J., Schou, J., Strakhov, V. N., & Thompson, M. J. 2002, "Helioseismic measurement of solar torsional oscillations", Sci., 296, 101, doi: 10.1126/science.1069190

Wang, H., Zirin, H., & Ai, G. 1991, "Magnetic flux transport of decaying active regions and enhanced magnetic network", Sol. Phys., 131, 53, doi: 10.1007/bf00151744

Wang, Y. M., Nash, A. G., & Sheeley, N. R. 1989, "Magnetic flux transport on the Sun", Sci., 245, 712, doi: 10.1126/science.245.4919.712

Warnecke, J., Käpylä, P. J., Käpylä, M. J., & Brandenburg, A. 2014, "On the cause of solar-like equatorward migration in global convective dynamo simulations", Astrophys. J., 796, L12, doi: 10.1088/2041-8205/796/1/l12

Watson, M. 1981, "Shear instability of differential rotation in stars", Geophys. Astrophys. Fluid Dyn., 16, 285, doi: 10.1080/03091928008243663

Webb, D. F., & Howard, T. A. 2012, "Coronal mass ejections: Observations", Liv. Rev. Sol. Phys., 9, doi: 10.12942/lrsp-2012-3

Weber, M. A., Fan, Y., & Miesch, M. S. 2013, "A theory on the convective origins of active longitudes on solar-like stars", Astrophys. J., 770, 149, doi: 10.1088/0004-637x/770/2/149

Weiss, N. O., & Tobias, S. M. 2016, "Supermodulation of the Sun's magnetic activity: The effects of symmetry changes", Mon. Not. R. Astron. Soc., 456, 2654, doi: 10.1093/mnras/stv2769

Wilcox, J., Schatten, K., Tanenbaum, A., & Howard, R. 1970, "Photospheric magnetic field rotation: Rigid and differential", Sol. Phys., 14, doi: 10.1007/bf00221311

Wolf. 1861, "Abstract of his latest results", Mon. Not. R. Astron. Soc., 21, 77, doi: 10.1093/mnras/21.3.77

Wood, T. S., & Brummell, N. H. 2012, "Transport by meridional circulations in solar-type stars", Astrophys. J., 755, 99, doi: 10.1088/0004-637x/755/2/99

Wood, T. S., & Brummell, N. H. 2018, "A self-consistent model of the solar tachocline", Astrophys. J., 853, 97, doi: 10.3847/1538-4357/aaa6d5

Yadav, R. K., Christensen, U. R., Morin, J., Gastine, T., Reiners, A., Poppenhaeger, K., & Wolk, S. J. 2015, "Explaining the coexistence of large-scale and small-scale magnetic fields in fully convective stars", Astrophys. J., 813, L31, doi: 10.1088/2041-8205/813/2/l31

Yadav, R. K., Christensen, U. R., Wolk, S. J., & Poppenhaeger, K. 2016, "Magnetic cycles in a dynamo simulation of fully convective M-star Proxima Centauri", Astrophys. J., 833, L28, doi: 10.3847/2041-8213/833/2/l28

Zahn, J. P. 1974, "Rotational instabilities and stellar evolution", in Stellar Instability and Evolution, ed. P. Ledoux, A. Noels, & A. W. Rodgers, Vol. 59, 185

Zahn, J. P. 1975, "Differential rotation and turbulence in stars", Mem. Soc. Roy. Sci. Liege, 8, 31

Zahn, J. P. 1992, "Circulation and turbulence in rotating stars", Astron. Astrophys., 265, 115

Zahn, J.-P., Talon, S., & Matias, J. 1997, "Angular momentum transport by internal waves in the solar interior", Astron. Astrophys., 322, 320

Zaqarashvili, T. 2018, "Equatorial magnetohydrodynamic shallow water waves in the solar tachocline", Astrophys. J., 856, 32, doi: 10.3847/1538-4357/aab26f

Zaqarashvili, T. V., & Gurgenashvili, E. 2018, "Magneto-Rossby waves and seismology of solar interior", Front. Astron. Space Sci., 5, doi: 10.3389/fspas.2018.00007

Zaqarashvili, T. V., Albekioni, M., Ballester, J. L., Bekki, Y., Biancofiore, L., Birch, A. C., Dikpati, M., Gizon, L., Gurgenashvili, E., Heifetz, E., Lanza, A. F., McIntosh, S. W., Ofman, L., Oliver, R., Proxauf, B., Umurhan, O. M., & Yellin-Bergovoy, R. 2021, "Rossby waves in astrophysics", Space Sci. Rev., 217, doi: 10.1007/s11214-021-00790-2

Zhao, J., & Kosovichev, A. G. 2004, "Torsional oscillation, meridional flows, and vorticity inferred in the upper convection zone of the Sun by time-distance helioseismology", Astrophys. J., 603, 776, doi: 10.1086/381489

Zhao, J., Nagashima, K., Bogart, R. S., Kosovichev, A. G., & Duvall, T. L. 2012, "Systematic center-to-limb variation in measured helioseismic travel times and its effect on inferences of solar interior meridional flows", Astrophys. J., 749, L5, doi: 10.1088/2041-8205/749/1/l5